The effects of pressure and thermal history on the crystallisation of cocoa butter

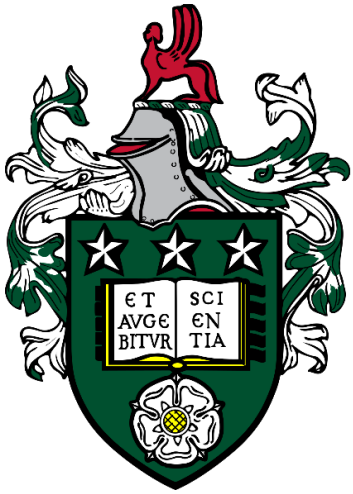

Marjorie Ladd Parada

Submitted in accordance with the requirements for the degree of

Doctor in Philosophy

University of Leeds

School of Food Science and Nutrition

Faculty of Mathematics and Physical Sciences

November 2018

Declaration

The candidate confirms that the work submitted is his/her own, except where work which has formed part of jointly-authored publications has been included. The contribution of the candidate and the other authors to this work has been explicitly indicated on the next page. The candidate confirms that appropriate credit has been given within the thesis where reference has been made to the work of others.

Part of the work in Chapter 3 appears in the manuscripts accepted for publication as follows:

> Sadeghpour, A., Ladd Parada, M., Vieira, J., Povey, M., Rappolt, M. Global Small-Angle X-ray Scattering Data Analysis of Triacylglycerols in the Molten State (Part I). 2018. (Accepted for publication in The Journal of Physical Chemistry B). DOI: 10.1021/acs.jpcb.8b06704
>
> Ladd Parada, M., Sadeghpour, A., Vieira, J., Povey, M., Rappolt, M. Global Small-Angle X-ray Scattering Data Analysis of Triacylglycerols in the α-Phase (Part II). 2018. (Accepted for publication in The Journal of Physical Chemistry B). DOI: 10.1021/acs.jpcb.8b06708

The diffusion studies presented in Chapter 4 appear in the published paper:

> M. Ladd-Parada, M. J. Povey, J. Vieira and M. E. Ries, *Molecular Physics*, 2018, DOI: 10.1080/00268976.2018.1508784, 1-8.

Further details of the jointly-authored publications and submitted manuscripts and to the work are included below:

Marjorie Ladd Parada: Conducted the experimental design and measurements, data analysis, data interpretation, drafted the two manuscripts where she is main author, and edited and provided feedback for the manuscript where she is second author.

Amin Sadeghpour: Drafted the manuscript where he is the main author, data interpretation, wrote the MATLAB code for data analysis (global fittings), and provided SAXS training.

Josélio Vieira: Helped to proofread the manuscripts.

Megan (previously Malcolm) Povey: Helped to proofread the manuscripts and commented on the final drafts, and contributed with the discussion of the structural models and CB crystallisation mechanisms.

Michael Rappolt: Helped to develop the structural models and supported their theoretical description, thorough editing and amending of the manuscripts.

Michael E. Ries: Helped with the experimental design, data analysis methods, and with the preparation of the manuscript.

Acknowledgements

First and foremost, I would like to thank my family, who have always believed in me, and inspired me to pursue a career in science. Without their unconditional love, I would not have been capable of undertaking this adventure; I hope I have made you proud. I particularly want to thank my sister who first inspired me to undertake a PhD, and who also helped me with my MATLAB® programming, and without whom, some of the data analysis would have taken longer.

Then, I would like to thank my supervisors at the University of Leeds, Prof Megan Povey and Prof Michael Rappolt, and my supervisors at Nestlé, Product Technology Centre, York, Dr Josélio Vieira, and Dr Peng-Siong Chong. They have taught me far more than the technical side of my PhD, and have encouraged, given advice, and motivated me when needed. But most importantly, I am very grateful for whilst always happy to give a hand, they taught me how to fly with my own wings, and find the scientist in me.

My sincere gratitude goes to Dr Amin Sadeghpour from EMPA, Switzerland, who was a post-doc here at the University of Leeds when I first started my PhD. He provided SAXS training and was part of invaluable discussions of technical nature and regarding the PhD journey. Afterwards, we had a closer collaboration when we wrote the two manuscripts on the nanostructure of triacylglycerols. His expertise in the analysis of SAXS data and in MATLAB® programming were key to make those two manuscripts a reality.

I would like to thank Dr Michael E. Ries from the School of Physics and Astronomy, here in Leeds University, who introduced me to the world of NMR, allowing me to perform my diffusion measurements in his lab, not to mention the discussions we had on the subject, leading to the preparation of the FFC-NMR manuscript. From the same school, Dr Helen Gleeson allowed me to use the polarised microscopes and Linkam stage in her Liquid Crystals laboratory. Additionally, Dr Daniel Baker provided training for the use of the two NMR techniques, and provided support when performing NMR and microscopy measurements.

I would like to extend a warm thank you to Dr Nicholas Brooks from Imperial College, London, who allowed me to perform the pressure microscopy studies in his laboratory, using the set-up he designed.

From Nestlé, Product Technology Centre, York, I would like to thank Dr Conor McKee for the triacylglycerol analysis of my cocoa butter, and Dr Stephanie Marty-Terrade who always provided encouraging words and advice.

This PhD could not have occurred without the financial support of various organisations. Firstly, the Consejo Nacional de Ciencia y Tecnología (CONACYT), México, who provided me a full scholarship covering tuition fees and living expenses. Secondly, Nestlé, Ltd, Switzerland, who provided financial support for the incurred experimental and conference expenses. Thirdly, COST Action CA15209 which allowed me to attend an FFC-NMR Training School, and SCI, London for the AJ Banks travel bursary which allowed me to attend the AOCS Annual Meeting 2018.

Finally, I would like to thank all of my friends. I thank the ones back home for their continuous support and encouragement and for always believing in me. I am also very grateful for those friends that I made along the way, for they gave me a home away from home.

Publications

M. Ladd-Parada, M. J. Povey, J. Vieira and M. E. Ries, Fast field cycling NMR relaxometry studies of molten and cooled cocoa butter, *Molecular Physics*, 2018, DOI: 10.1080/00268976.2018.1508784, 1-8.

Sadeghpour, A., Ladd Parada, M., Vieira, J., Povey, M., Rappolt, M. Global Small-Angle X-ray Scattering Data Analysis of Triacylglycerols in the Molten State (Part I). 2018. (Accepted for publication in The Journal of Physical Chemistry B). DOI: 10.1021/acs.jpcb.8b06704

Ladd Parada, M., Sadeghpour, A., Vieira, J., Povey, M., Rappolt, M. Global Small-Angle X-ray Scattering Data Analysis of Triacylglycerols in the α-Phase (Part II). 2018. (Accepted for publication in The Journal of Physical Chemistry B). DOI: 10.1021/acs.jpcb.8b06708

Conferences

EuroFed Lipid 2015 – poster ‘X-ray scattering studies of the effect of thermal pre-treatment on the crystallisation of cocoa butter’

EuroFed Lipid 2016 – poster ‘Calorimetry study of the effect of thermal pre-treatment on the crystallisation of cocoa butter’

BACG/CGOM 2016 – oral presentation ‘Studies of the effects of pressure and thermal pre-treatment on the crystallisation of cocoa butter’

ChocoTec 2016 – poster ‘Calorimetry study of the effect of thermal pre-treatment on the crystallisation of cocoa butter’

EuroFed Lipid 2017 – poster ‘Effect of thermal pre-treatments on the isothermal crystallisation of cocoa cutter’

Food Colloids 2018 – oral presentation ‘Evidence of two different memory effects on the crystallisation of cocoa butter’

Annual AOCS Meeting 2018 – oral presentation ‘Studies on the effect of thermal pre-treatment on the crystallisation of cocoa butter’

MRFood 2018 – oral presentation ‘Self-diffusion studies on cocoa butter using PG-NMR and FFC-NMR’

Manuscripts submitted and under preparation

Submitted

M. Ladd-Parada, M. J. Povey, J. Vieira and M. E. Ries, Fast Field Cycling and Pulsed NMR Relaxometry for Tracking the Early Stages of Crystallization of Fats. 2018. (Under review)

Under preparation

Pink, D.A, Ladd Parada, M., Mazzanti, G. Crystal memory near discontinuous triacylglycerol phase transitions: Models, metastable regimes and critical points.

Ladd Parada, A., Vieira, J., Povey, M., Rappolt, M. The effect of thermal pre-treatment on the crystallisation of CB.

Ladd Parada, A., Vieira, J., Povey, M., Rappolt, M. Polymorphism of cocoa butter as affected by pressure.

Ladd Parada, A., Povey, M., Rappolt, M., Vieira, J. Effect of seed concentration on the contraction behaviour of West-African cocoa butter.

Ladd Parada, A., Gregersen, S., Povey, M., Rappolt, M. Small angle X-ray scattering data analysis of triacylglycerols: Electron density profile calculation of their meta-stable polymorphs)

Abstract

Cocoa butter (CB) imparts most of the key sensory and stability characteristics in chocolate, when crystallised in the β-V form. However, current processing methods can still be improved, since they do not account for the inherent compositional variations observed in products from different origin. Therefore, in-depth knowledge of the nanostructure of CB, and the different parameters affecting CB crystallisation is indispensable for new technologies to be developed. Two of these parameters which remain, surprisingly, under-reported are the temperature at which CB is molten prior to its crystallisation and application of medium pressure (<1000 bar).

The nanostructure of the three main polymorphs of CB were determined from X-ray scattering experiments, and a novel structure in liquid CB is proposed. This is followed by the study of the effect of three thermal pre-treatments (50, 80 or 110 °C), using a multi-technique approach. Here, it was observed that by using a higher T_{imax}, the crystallisation of the meta-stable phases was delayed, whereas the formation of the β-V was enhanced, which is desirable for chocolate production. The differences between the 50 °C treatment and the other two treatments have been associated with the presence of crystallites of fully saturated TAG, DAG and MAG species, respectively.

The effect of pressure was analysed by applying 100 to 600 bar to CB, which was subsequently cooled to 24, 26 or 28 °C, respectively. Initial post-processing analysis showed encouraging results, as crystallisation of the β-V form appeared to be enhanced. However, these findings were not confirmed by *in-situ* experiments, where only the development of α-polymorphs was observed during pressurisation, which subsequently melted, to different extent, upon releasing the pressure. The observed differences might be caused by design-related issues of the pressure-treating machine used in the initial experiments.

Contents

List of Figures

List of Tables

List of Abbreviations

A	Arachidonic acid
CB	Cocoa butter
CNP	Crystal nanoplatelets
DAG	Diacylglycerol
DDF	Dynamic difference functions
DSC	Differential scanning calorimetry
EDP	Electron density profile
FA	Fatty acid
FFC	Fast field cycling
FID	Free induction decay
FT	Fourier transform
L	Linoleic acid
M	Myristic acid
NMR	Nuclear magnetic resonance
O	Oleic acid
P	Palmitic acid
PL	Phospholipid
PLM	Polarised light microscopy
P_{max}	Maximum pressure
POP	1,3-dipalmitoyl-2-oIeylglycerol
POSt	1-palmitoyl-2-oIeylglycerol-3-stearoylglycerol
SAXS	Small angle X- ray scattering
SFC	Solid fat content
St	Stearic acid
StOSt	1,3-distearoyl-2-oIeylglycerol
TAG	Triacylglycerol
T_{cryst}	Temperature of crystallisation
T_m	Melting temperature
T'_m	Experimentally observed melting temperature
T_{imax}	Maximum initial temperature
VFT	Vogel-Fulcher-Tamman
WAXS	Wide angle X-ray scattering

Chapter 1 Introduction and theoretical background

1.1 Chocolate: a brief history and today's processing

Cacao products have been highly desirable and valued throughout history. The cacao plant was domesticated ca. 1500 B.C. and used by Mayans to prepare a hot beverage with water. Eventually, it reached the Aztecs who used the cacao bean as currency and reserved the bitter beverage for the elite and important religious celebrations[1-4].

When Christopher Columbus first arrived to the Americas, he did not export the beverage, even if he did take some cacao beans with him back to Europe. It was not until Hernán Cortéz conquered what is now known as Mexico that the Spanish started including the cacao brew in their daily lives, making it more palatable by preparing it with milk rather than water, and adding sugar and other ingredients. By the 17th century, it had become a popular drink for the higher classes, not only in Spain, but also in England and the Netherlands. This led to the extension of the production of the cacao to Dutch colonies in Africa, where most of the world production comes from today[1, 2].

By the mid-19th century, Fry & Son's decided to develop a new type of confectionery based on the cacao bean, giving birth to the chocolate tablet. Regardless, it was not fully accepted until Daniel Peter added milk to the mix, making the product more palatable to the European. In addition, Lindt's development of a process called "conching" allowed for the chocolate tablet to have a smoother and less acidic flavour, thus giving the finishing touches to what we know today simply as "chocolate" [1-3, 5].

According to the Food Standards Agency[6], chocolate is

> … the product obtained from cocoa products and sugars which…contains not less than 35 percent total dry cocoa solids, including not less than 18 percent cocoa butter and not less than 14 percent of dry non-fat cocoa solids.

For manufacturing chocolate, a recipe has to be defined, i.e. the proportions of cocoa product, and sugars, in the case of dark chocolate. Then, the ingredients are weighed, mixed, and milled to ensure a uniform particle size that will prevent a gritty texture in the final product. After milling, the chocolate mass is conched [7, 8]. This process is based on continuous heating and shearing, and can be divided into three stages[7-9]:

1. Dry conching, where the water and undesirable volatile components are removed from the chocolate masse.
2. Pasty phase, where the chocolate masse is transformed into a thick paste, and the sugar particles are coated with fat. This ensures a smooth texture in the final product.
3. Liquid conching, which consists of the application of high-speed shearing and lower temperatures are used. Emulsifiers, such as lecithin, can be added to ensure the correct flow properties for the following stage.

Once a fluid chocolate mass is obtained, it can be used for enrobing or panning. However, if a chocolate tablet is to be produced, a final processing step is needed, i.e. tempering.

Tempering has as main objective to ensure that cocoa butter (CB) crystallises into the correct crystal form (β-V). The characteristics of good temper are high gloss, good mould release, good snap, cooling effect when melting in the mouth, and stability at ambient temperatures below 30 ºC. If other crystal forms are present, production, sensory, and stability problems arise, i.e. de-moulding problems, dull and/or a whitish surface (bloom), and room temperature melting point (20 °C - 25 °C).

Traditional tempering involves four steps[10]:

1. Melting of the chocolate (maximum of 50 °C).
2. Cooling to the crystallisation point.
3. Further decrease of temperature to favour crystallisation growth (26-29 °C).

4. Mild heating to melt the less stable polymorphs, so that only β-V crystals remain (29-32 °C).

After tempering, the chocolate is poured into moulds, cooled and stored to allow further crystal growth.

Note should be taken that traditional tempering, though being the industry standard method, is not completely efficient, hence, the development of bloom and other problems are still to be surmounted. This can be explained by tempering not giving consistent results as it is not easily adaptable to different chemical compositions of CB, thus resulting in products with different proportions of β-V and less stable crystals.

1.2 Challenges in the chocolate industry

Nowadays, chocolate is consumed worldwide with a particularly high demand from Western Europe. However, the consumption in this region seems to have reached its peak (between 7 and 9 kg/year/person) and is expected to stop growing or even decline. Regardless, emerging economies (MINT and BRIC countries) have started to increase their chocolate consumption, mainly due to the sales of more economic versions of the leading brands, in addition to the economic growth and/or large populations of such countries[11]. In fact, overall demand of cacao beans increased 13% between 2010 and 2015 [12, 13], and is expected to keep increasing as chocolate demand in Asia keeps growing[14].

Unfortunately, this increase in demand is not parallel to an increase in cacao bean production, but rather the opposite. As most of the world's production comes from West African countries such as Ivory Coast and Ghana, political instabilities heavily affect cacao bean availability. Moreover, the increase in world temperature has led to poor yield crops, and if the predicted annual 2°C increase continues[13], some countries will not be capable of producing cacao beans any longer. Problems with cacao bean production have already caused an increase in prices, and if the yield problems continue, farmers might switch to higher yielding, and more profitable crops, further decreasing cacao bean availability[13].

Moreover, CB composition varies according to the region of origin, thus resulting in softer CB from South America, harder CB from Asia and Oceania, and intermediate soft CB from Africa and North America[15-17]. The composition does not only affect the final consistency of the CB, but also the crystallisation times, the softer the CB, the slower it crystallises, and vice-versa. This suggests that growing cacao trees under different temperatures affects the physical characteristics of CB. Therefore, in addition to a declining production, the chocolate industry will need to adapt its chocolate processing methods to account for such differences.

1.3 Cocoa butter production and composition.

From the previous, the importance of cocoa butter (CB) in the chocolate industry context is evident. Namely, it is the key ingredient of chocolate (ca. 33%) that provides it with its characteristic gloss, brittle texture and its sharp melting profile when consumed[18, 19]. However, these properties can only be obtained when CB has crystallised in the sufficiently stable polymorphic structure i.e. in the β-V form. This form is usually obtained through tempering. However, it is complex, energy consuming, and not adaptable to current changes in CB's composition. Therefore, it is important to develop a deep understanding of the crystallisation of CB, so that the tempering process can be made more efficient.

CB is the fat component of the cacao bean (*Theobroma cacao)*. To obtain it, the beans are fermented, dried, roasted, and winnowed (i.e., the shell is separated from the rest of the bean) resulting in roasted cocoa nibs that have already developed the aromatic compounds necessary for a good flavoured chocolate product. The cocoa nibs are then ground into a cocoa mass or liquor that is then pressed to extract the CB. It can then undergo further processing to eliminate certain aromatic compounds that are not desirable for certain applications, such as for the processing of white chocolate [7].

Table 1.1 Lipid composition of CB (%) (adapted from [17]).

Triacylglycerols	Free Fatty Acids	Diacylglycerols	Phospholipids	Glycolipids
95.77-97.92	0.87-1.04	0.81-1.39	<0.1-0.3	0.3-1.5

CB is composed of a variety of lipids (Figure 1.1 and Table 1.1) of which the main species is triacylglycerols (TAGs). From these, three species represent 75 to 97%[15, 17]: 1-palmitoyl-2-oIeyl-3-stearoylglycerol (POSt), 1,3-distearoyl-2-oIeylglycerol (StOSt), and 1,3-dipalmitoyl-2-oIeylglycerol (POP). Though the previous TAGs are the largest contributors to CB's crystal behaviour, CB's minor components, in particular fully saturated TAGs, and phospholipids (PLs), also play an important role as will be discussed later in the thesis[20].

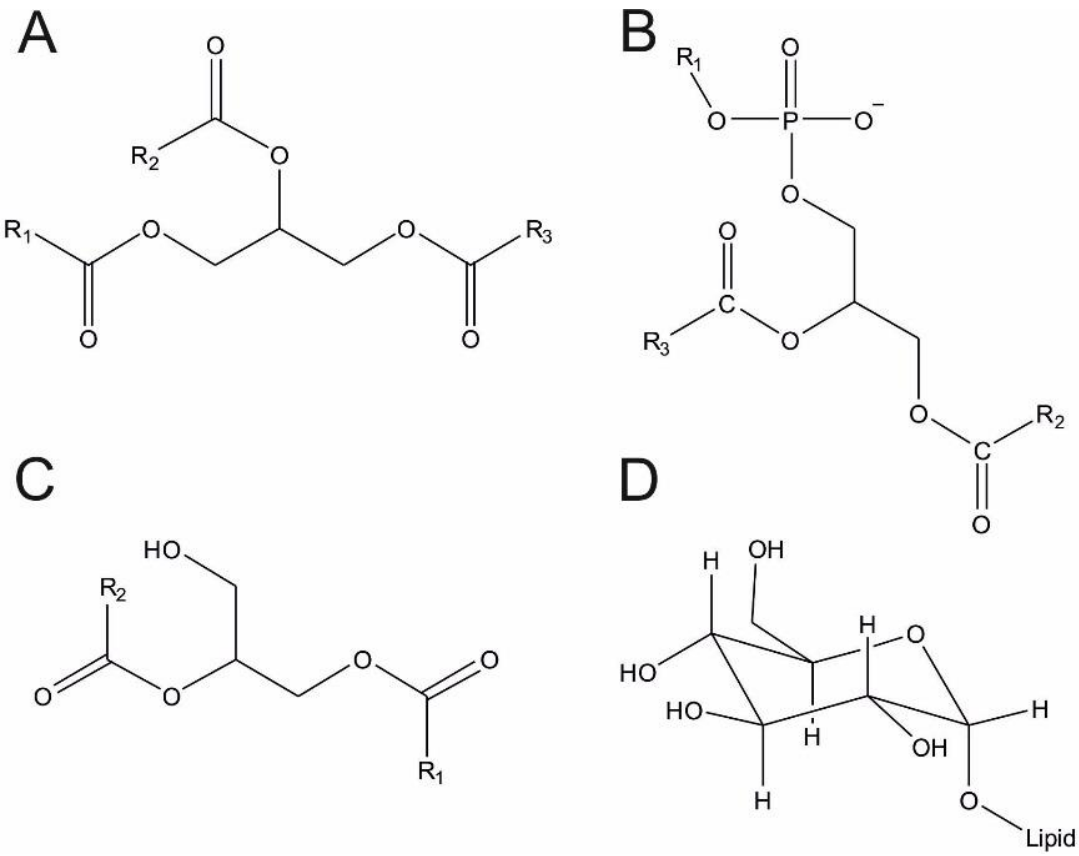

Figure 1.1 Basic molecular structures of A) triacylglycerols (TAGs), B) phospholipids (PLs), C) diacylglycerols (DAGs), where R1 to R3 represent different hydrocarbon chains, and D) glycolipids, where the lipid is most commonly an acylglycerol, a sphingolipid, or phosphatidylinositol.

1.4 Fundamentals of vegetable fat crystallisation

1.4.1 Crystal structures

Crystals are anisotropic solids formed by a series of particles arranged in a symmetric pattern. They are commonly described by four main units[21]:

Asymmetric unit: particle (molecules or atoms) from which the crystal is formed.

Space lattice: basic 3D structure of a crystal. It is an infinite series of points arranged in such a way, that the same "pattern" can be observed around any reference point[21]. Bravais postulated that only 14 lattices could be geometrically obtained, and they were grouped according to their symmetry, hence obtaining seven different groups (Table 1.2) which are described by the length of their axes and the angles between them (Figure 1.2). In addition, their capacity to interpenetrate lead to a total of 230 possible combinations[22]. Further, 32 sets of symmetry operations are used to characterize three-dimensional lattices (point groups). Including also translational symmetry operations 230 space groups can described[22].

Crystal structure: group of asymmetric units in a symmetric order, remaining the same for each lattice point.

Unit cell: the basic unit of a crystal containing all its symmetry elements. Through its translational displacement, the complete crystal can be formed.

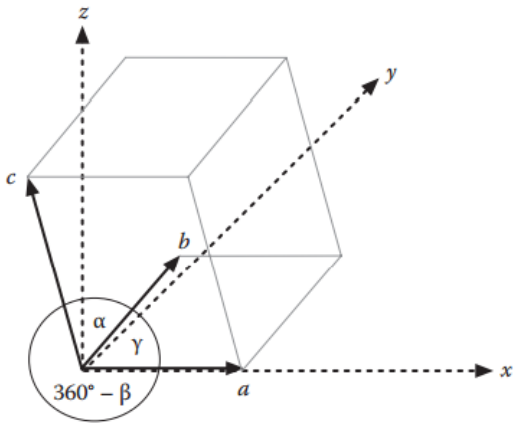

Figure 1.2 Diagram depicting the three crystallographic axes a, b, c, and the corresponding angles α, β, γ within a unit cell21.

Table 1.2 The seven crystal systems and Bravais lattices (adapted from Mullin and Marangoni [21, 22]).

Crystal System	Angles between axes	Length of axes	Lattice
Regular	α=β=γ=90°	a=b=c	Cube Body-centred cube Face-centred cube
Tetragonal	α=β=γ=90°	a=b≠c	Square prism Body-centred square prism
Orthorhombic	α=β=γ=90°	a≠b≠c	Rectangular prism Body-centred rectangular prism Rhombic prism Body-centred rhombic prism
Monoclinic	α=γ=90°≠β	a≠b≠c	Monoclinic parallelepiped Clinorhombic prism
Triclinic	α≠β≠γ≠90°	a≠b≠c	Triclinic parallelepiped
Trigonal	α=β=γ<120°≠90°	a=b=c	Rhombohedrum
Hexagonal	α=β=90°γ=120°	a=b≠c	Hexagonal prism

1.5 Crystallisation process

Fat crystallisation requires the occurrence of two main steps: nucleation and crystal growth [23]. As crystal growth continues, a crystal network is formed, obtaining a fully crystalline material.

This process can be described in both, thermodynamic and kinetic terms. The final solid is thermostable, if the temperature of the system is taken below T_m. Once energetic barriers are overcome, the diffusion of molecules in the different, apparent phases as well as their aggregation and arrangement need to be considered[23]. Both crystallisation steps affect the nucleating polymorph and potentially lead to compositional gradients within the crystals or to alterations in the packing of the components throughout the growing stage.

1.5.1 Nucleation

Nucleation is the critical step, for as long as a stable embryo (nucleus) is not formed, growth cannot occur. It can be described in both thermodynamic and kinetic terms. Thermodynamic terms are necessary, for when the melt is cooled down the solid phase is the most stable one. However, since the process is in principle slow, and the transition is not spontaneous, kinetic factors need to be considered [24] as they

determine which polymorph will be the first to nucleate, as will be discussed afterwards, the presence of composition gradients within the crystals, and the crystal perfection, i.e. the degree of defects in the lattice.

During nucleation, the melt organises in domains which, have a decreased energy across their volume, but due to the new interface between the crystal and the melt present a higher surface energy. Thus a critical nucleus size, where an energy balance is reached (equation. 1), is necessary for crystal growth to occur. Before this critical size is obtained, the particles are called embryos rather than nuclei, and they melt before the crystal can grow. However, if these embryos gain atoms in a rate that allows for them to grow, nuclei can be formed [24].

$$\Delta G_{nucleus} = 4\pi r^2\gamma + \frac{4}{3}\pi r^3 \Delta G_{\bar{v}} \quad (1)$$

where r is the radius of the cluster, γ the surface tension, and $\Delta G_{\bar{v}}$ is the decrease of free energy per unit volume due to the enthalpy of fusion.

The $\Delta G_{nucleus}$ term increases until the critical nucleus size (r*) is obtained, after that, higher r values decrease $\Delta G_{nucleus}$ making the crystal growth possible [23]. Considering that at r^* $\Delta G_{nucleus}$ is zero, and that $\Delta G_{\bar{v}} = \Delta_{\mu}/\bar{V}$, the activation energy barrier can be calculated through equation 2 for a spherical nucleus [23, 24].

$$\Delta G^*_{nucleus} = \frac{16\pi V^2\gamma^3 T_m^2}{3(\Delta H_m \Delta T^2)^2} \quad (2)$$

where T_m is the melting temperature of a specific polymorph, ΔH_m its enthalpy of fusion, T the crystallization temperature and V the molar volume of the nucleus.

However, whilst the previous provides information on the energy balances, the nucleation rate needs to be calculated as well, for the diffusion of molecules to the nucleus represents a barrier. Furthermore, the entropy loss due to the molecules incorporation into the nucleus, as well as the probability of a fraction (α) of a molecule to be in the correct conformation $\left(\frac{-\alpha\Delta S_i}{R}\right)$ need also be considered. These terms are all included in equation 3, which applies for homogeneous nucleation [24].

$$J = N\frac{K_B T}{h}\exp\left(\frac{-\alpha\Delta S_i}{R}\right) exp\left(\frac{-\Delta G^*_{nucleus}}{K_B T}\right) \quad (3)$$

where K_B is the Boltzman's constant, R the gas constant, T the crystallization temperature in K, h the Planck's constant, and $\Delta S_i = \frac{\Delta H_m}{T_m}$.

The previous equations are only valid for homogeneous nucleation. However, heterogeneous nucleation can also occur, and in fact, it is relatively more common due to the presence of impurities. These impurities help induce nucleation by acting as catalytic sites, thus reducing the energy barrier and the supercooling required[24].

1.5.2 Crystal Growth

As mentioned before, once stable nuclei are obtained, crystal growth can occur. This step is affected by a variety of factors, of which the chain length and mass transport rate are the most relevant. In terms of chain length, the longer TAGs fatty acids, the slower the growth rates. Regarding mass transport, as the solid fat content starts to increase, so does the viscosity, thus hindering the molecular diffusion towards the nuclei [23], which in turn decreases the growth rate. Therefore, crystal growth occurs at a faster rate in the initial stages and slows down as crystallisation progresses.

1.5.3 Polymorphism

Regardless of the type of nucleation and crystal growth rate, vegetable fats are known to have a polymorphic nature. This polymorphism causes high sensitivity to temperature differences, due to the range of melting points of each crystal form[23].

A polymorphic fat is defined as one that is capable of aggregating in different crystalline arrangements, whilst maintaining its chemical identity[22]. The three basic polymorphs are named α, β', and β. To identify them, X-ray scattering techniques are used. The sample is irradiated with an X-ray beam which then becomes scattered creating an interference pattern, which provides the orientation and distances between the atoms/molecules. The repetitive distances can be obtained in the case of constructive interference of scattered X-rays (diffraction), i.e. when Bragg's equation (equation 4) is fulfilled [25, 26].

$$2d \cdot sin\,\theta = n \cdot \lambda \qquad (4)$$

where d is the spacing between each layer of the crystals, θ is the angle of incidence, and λ the wavelenght of the x-rays as observed in Figure 1.3

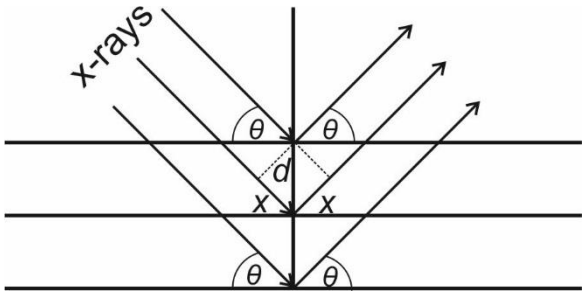

Figure 1.3 Diagram of the geometry of the reflection of X-rays from crystal planes, used for the derivation of Bragg's Law.

Due to the periodicity of crystal structures, characteristic patterns can be observed in the wide and small angle regions, which correspond to the short and long spacings, respectively. The long spacings in the case of TAGs relates to lamellar layering of the molecules with each layer extended over either two or three hydrocarbon chain lengths, also known as double (2L) or triple (3L) stacking (Figure 1.4B), while their short spacings indicate their sub-cell structure (Figure 1.4 A and Table 1.3). A more detailed description on X-ray scattering is provided in the following chapter, though for in-depth explanations, the reader is referred to the SAXS Guide provided by Anton Paar[26].

Table 1.3 Characteristic short spacings of the three basic polymorphs [23, 27].

Polymorph	Packing	Short spacing
α	Hexagonal (H)	Single at ca. 0.415 nm (s)
β'	Orthorhombic ($O_{\perp}$)	At least one at 0.38 nm (s) and one at 0.42 nm (s)
β	Triclinic ($T_{//}$)	0.46 nm (vs), and peaks in the range of 0.36 to 0.39 nm (s)

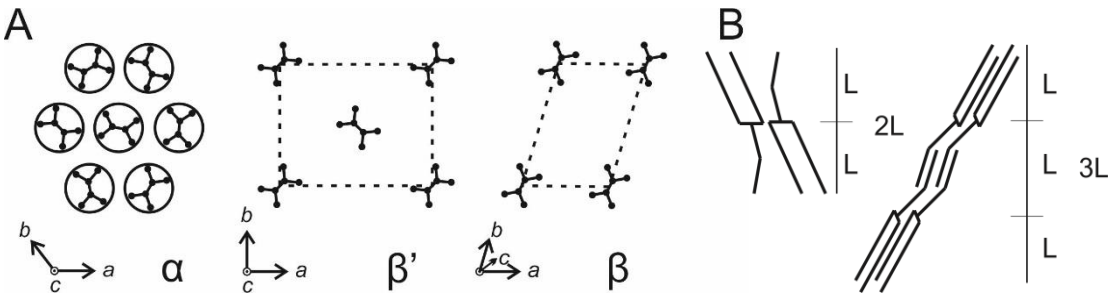

Figure 1.4 A) Packing of TAG polymorphs: hexagonal (α form), orthorhombic (β' form) and triclinic (β form) crystals. B) Stacking of TAGs, i.e. the thickness of the lamellar structure is either in the order of twice the length of one hydrocarbon chain (2-L) or roughly three times its length (3-L).

Usually, the metastable polymorphs (α- and β-phases) can be crystallised directly from the melt, and will eventually transform into the most stable polymorph via

solid-solid or melt-mediated transformations (Figure 1.5), with the last transition being irreversible[23, 28] as fats are of a monotropic nature. This means that at any given set of temperature or pressure conditions, only one phase (β-form) is the most stable one.

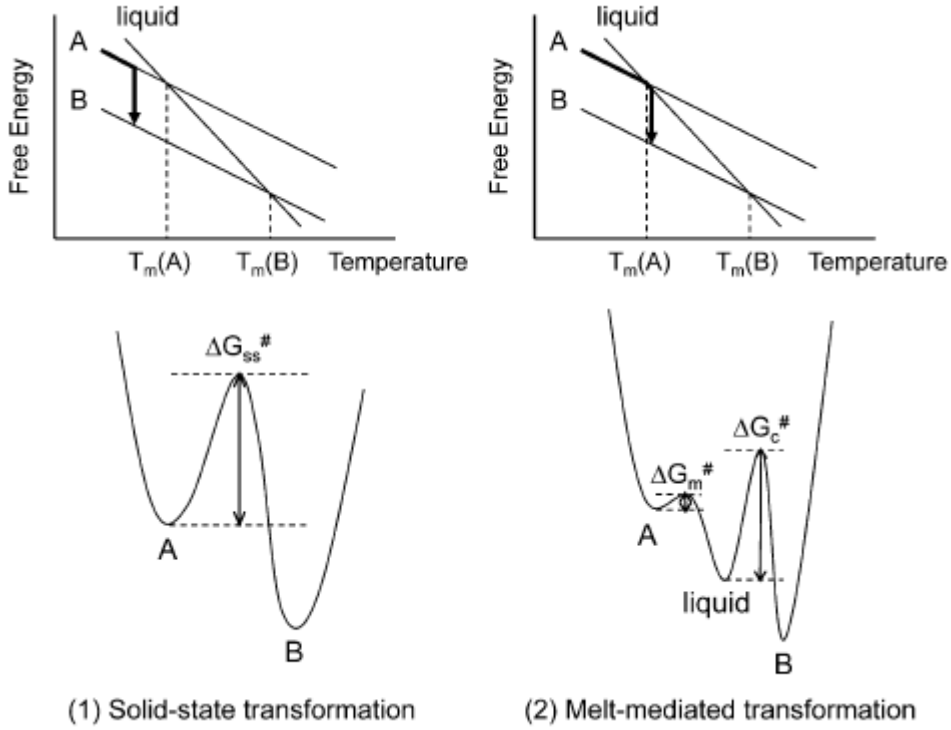

Figure 1.5 Relative stability of two polymorphic forms showing (1) solid-solid and (2) melt-mediated transformation pathways, and their corresponding transformation activation energies ($\Delta G^{\#}$). Adapted from reference[29].

The previous behaviour is the core of the Ostwald rule of stages[30], which states that the less stable polymorphs crystallise faster as they represent a local minima of free Gibbs energy (Figure 1.5), and will preferentially transform stepwise to more stable forms during storage. However, different external factors can have an influence on this behaviour, such as the crystallisation temperature, cooling rates, as by maintaining the temperature above that of the metastable phases, or using slower crystallisation rates, direct nucleation into more stable phases, such as the β', can be induced[31, 32]. However, this process can be expected to occur more slowly due to the larger energetic barrier, as observed in Figure 1.5, unless the sample is seeded with a specific polymorph, thus acting as a template for the developed crystalline structures[33]

Once the TAGs form lamellar structures, they are expected to stack forming what has been defined as crystal nanoplatelets (CNPs)[34] with a variety of size and shapes depending on the TAG composition and the specific process applied. These CNPs are thought to be mainly insoluble in the liquid oil (less than 0.1 mol fraction in the case of tristearin in triolein at approximately 47 °C[35] , which are coated either partially or totally, thus determining the way that CNPs can further aggregate. This aggregation is caused by Van der Waals forces, leading to the formation of cylindrical clusters named TAGwoods[36]. These TAGwoods then aggregate further, first by Diffusion Limited Cluster Aggregation, and then, if sufficient time is allowed, *via* Reaction Limited Cluster Aggregation resulting in uniformly distributed aggregates[36-41].

The full crystallisation process can be affected by a variety of factors such as cooling and heating rates, temperature of crystallisation, pressure, sonication, and shearing[32, 42] through mechanisms that have been extensively reviewed elsewhere[29]. The focus of this thesis lies on thermal pre-treatment, and pressure supported CB processing.

1.5.4 Effects of thermal treatment

Different cooling rates and crystallisation temperatures have been observed to alter lipid crystallisation strongly, from nucleation times and crystal growth (size) to morphology, polymorphism (both nucleating structures and posterior transitions), and ultimately, the crystal network. The effect of different thermal treatments has been widely studied in a variety of lipids, ranging from pure TAGs, fully saturated or mixed saturated-unsaturated, through binary mixtures [43-46, 47, 48], to natural fats from animal and vegetable origin [49-59].

The cooling rates studied so far range from 0.1 °C/min to 20 °C/min, and whilst the effects of specific cooling rates vary depending on the system under study, results are in agreement on the effects of slow (less than 1 °C/min) and intermediate, or even fast cooling rates (above 5 °C/min).

Slower crystallisation rates result in crystallisation starting at higher temperatures and subsequently into more stable forms, sometimes skipping altogether the α-polymorph, and frequently in a mix of β' and β-polymorphs [53]. The effect on polymorphism is not limited to the nucleating form, but also in later transformation

on heating. In addition, the induction time (time required for the first crystals to be detected[60]), crystallisation enthalpy (possibly related to the crystallisation of more stable polymorphs) and crystallisation rate are increased with slower cooling rates, as observable by small- and wide-angle X-ray scattering (SAXS and WAXS), polarised microscopy (PLM), solid fat content (SFC) determinations, and DSC measurements. At the lower rates slower nucleation processes have been observed to cause fractionation in complex systems such as lard and anhydrous milk fat [50, 51].

Related to the structural effects of the cooling rate, small, tightly packed crystals are frequently observed with higher cooling rates, whilst using slower cooling rates leads to a lower number of nuclei, which allow the formation of larger crystals, as observed by microscopy[55]. This is relatable to the observed effects on rheology and mechanic properties[50, 61]. With a faster cooling rate, the viscosity increases from the start due to the higher number of nuclei formed that reduce the amount of liquid oil present. Moreover, a higher final hardness is observed, which is related to the tighter packing, and more homogeneous structure of the crystals, as it is observed after several days[49, 50, 55, 62].

The increased nucleation rate during the faster cooling rates has been attributed to an increased crystallisation driving force due to higher supercooling levels reached in less time, i.e. due to the higher ΔT, thus reducing the energy barriers. This increased nucleation, as stated before, causes a rise in viscosity which reduces diffusion, and consequently the crystallisation rate and growth[29, 63].

The previous also explains why faster cooling rates result in less stable polymorphs. Given that lower temperatures are reached earlier on than in the slower rates, crystallisation can occur in a shorter time frame. Consequently, only structures with lower energies of activation, that is following the Ostwald rule, only metastable polymorphs (mainly α-form) can be obtained[32]. In contrast, when slower cooling rates are used, the sample is held for enough time at temperatures representing undercooling for the α-polymorph but supercooling for the more stable forms (β' and or β), hence overcoming the larger energy barriers of the latter[58].

Similarly to the application of very fast cooling rates, when using low crystallisation temperatures (<-15 °C) a mix of γ- and α-phases develop, whereas by increasing this temperature to up to 22 ° CB and milk fat has been observed to nucleate initially into

the α-form, and eventually transformed into the β' and β-phases[64-68]. However, on applying a higher temperature (22-26 °C) a behaviour parallel to that of slower cooling rates is observed, i.e. direct nucleation into the β' phase[56, 65-68]. The latter is expected as the temperatures lie above the T_m of the α-phase, i.e. the sample is not kept at the supercooling necessary for this polymorph to nucleate.

1.5.5 Effects of pressure

Most work on the effects of pressure on the structure and properties of lipids has been performed on FAs and DAGs. Though FAs lack the glycerol backbone which restrict the mobility of the hydrocarbon chains, their study still provides valuable insights into the potential effects of pressure on TAGs.

Kos *et al* [69], observed through light scattering studies that at approximately 300 bar the transmission of light reached a minimum. This happened alongside an increase in scattered light and an increase of temperature, which indicates either a phase change, or a "molecular collapse". However, when the sample was heated to 60 °C, such phase transition was no longer observed even when reaching 3000 bar [70]. Furthermore, it was not only during the increase of pressure that an effect was observed. Tefelski *et al.* [71] using particle image velocimetry, observed two phases: liquid and solid, during decompression. Also, Kościesza *et al.* [72] observed that although a phase transition was evident in oleic acid under pressurised conditions, the surface looked very irregular, suggesting a poorly packed crystal. Regardless, once decompression started, the surface of the crystal looked smooth suggesting that a better packing had been reached. The first phenomenon would be expected, for if crystallisation occurs faster when applying pressure, there would not be enough time for molecules to arrange in a perfect packing, but rather are "immobilised" or compressed in a similar arrangement to the liquid form. Once decompression occurs, molecules might recover some mobility, allowing them to arrange into a more energetically favourable packing, through a solid-solid transformation.

To gather further insights on the phase transition in DAGs, Kiełczyński *et al*. [73] measured the viscosity at different pressures (up to 5000 bar). They applied pressure using a piston, which was then locked in a specific position. Once it was locked, the pressure initially remained constant while viscosity increased. This behaviour was

followed by a decrease of pressure, accompanied with an almost constant viscosity, which was related to a phase transition. Eventually, the pressure stabilised once more suggesting the end of the phase transition. Interestingly, the transition was slower at higher temperatures, confirming what had been previously observed in oleic acid, i.e. the use of high temperatures can hinder the phase transitions promoted by pressure[70].

In another paper, the isothermal and adiabatic compressibility of DAGs under pressures up to 6000 bar was studied [74]. It was observed that both types of compressibility decrease with increasing pressure. In addition, through adiabatic compressibility they obtained the bulk modulus, which increased with pressure and approaches values characteristic of solid materials after the phase transition observed through sound velocity measurements

The effect of pressure in TAGs and vegetable oils has also been studied in terms of their physicochemical properties and of crystallisation. When observing the effect of pressure (up to 8000 bar) on the viscosity of triolein[75, 76], a similar behaviour to that of DAGs was evident, i.e. at a certain point the pressure dropped and the viscosity kept increasing, suggesting a phase transition. Moreover, the specific volume, isothermal compressibility and thermal expansivity of olive oil and sunflower oil have been studied[77] at pressures up to 3500 bar. The three parameters decrease as pressure increases, similar to what was observed in DAGs[74]. Finally, the melting temperature of TAGs increase with pressure, at least up to 450 MPa[78, 79]. In terms of crystallisation, it has been observed that when applying 1500 to 7500 bar, triolein and trilaurin crystallise and the measured induction times decreased with increasing pressure [78, 80]. Contrariwise, the crystal growth rate decreased with applied pressure[79].

From the previous, it can be concluded that pressurisation helps induce crystallisation in TAGs in low specific volume forms due to the pressure-volume product contributing to the energy barrier to nucleation. Smaller (more negative) values of this product favour nucleation. This is in agreement with Le Chatelier's principle[81] which states that an increase in pressure results in a decrease of volume in the system. In most cases the solid is the state with a lower specific volume, hence the equilibrium shifts from the liquid phase to solid (crystalline) phase, thus raising

the melting point (T_m)[81]. This increase of the T_m is further explained by the Clausius-Clapeyron Equation (equation 5) where it is evident that ΔP and ΔT are directly proportional.

$$\frac{\Delta T_m}{\Delta P} = \frac{\Delta V}{\Delta S} \quad (5)$$

where ΔT_m is the change in melting temperature as pressure is increased, ΔP is the pressure change, ΔV the molar volume change, and ΔS is the change in entropy both expected to be positive as they decrease upon solidification [82, 83]. As long as $\Delta V > 0$, when pressure is applied the thermodynamic barrier decreases due to $\delta\sigma/\delta P < 0$ (where $\delta\sigma$ is the change in specific interface energy) and an increased chemical potential driver ($\Delta\mu$), as extensively discussed by various authors [82, 84, 85].

However, pressurisation also hinders molecular transport, as observed in self-diffusion simulations that showed that this parameter decreased with increasing pressure[86], and by the increased viscosity at higher pressures[73], in other words, the kinetic barrier is increased. Therefore, though increasing the pressure induces the onset of crystallisation, crystal growth rate, and potentially polymorphic transformations are hindered under pressurised conditions. This then suggests that there is a maximum of pressure that can successfully be applied to facilitate nucleation, as if pressure surpasses this value, the kinetic barrier can surpass the thermodynamic drive[82, 84]. In fact, this is already partially observable in the results of Ferstl *et al.*[87] where the slope of the inverse induction time vs pressure considerably decreases on reaching approximately 275 MPa.

Little research has been done regarding the effects of high pressure on vegetable fat crystallisation. Nevertheless, similar effects to those in TAGs have been observed, i.e. it promotes nucleation[78, 87, 88]. In addition, when pressure is released, the less stable polymorphs melt, hence favouring the presence of the more stable polymorphs. These small crystals are thought to then serve as seeds for the remainder of the lipid to nucleate[29].

More specifically, two studies have been carried out on CB. The first one by Yasuda and Mochizuki [89] who observed that, by holding CB at 30 °C and applying 1500 bar two times for five minutes, it was possible to obtain the β-V polymorph directly. Additionally, it was possible to arrange a continuous system where pressure was only applied once, but some of this partially crystallised material had been returned to the

original holding vessel, and therefore was acting as a seeding agent. This is in accordance with the previously discussed studies of Ferstl *et al.*[78, 87].

The second paper involved the application of 3000 bar for half an hour to CB, at 60 °C, which was then allowed to crystallise at 21 °C for 1 h and 21 h [90]. Unlike the previous studies, after 1 h of crystallisation, they only observed the presence of β'-IV, whereas the non-pressurised treatment had already crystallised into the β-V polymorph. However, after 24 h, all samples were clearly identified as crystallised in the β-V polymorph. The latter is not unexpected as it is known that the β'-IV is a metastable polymorph, therefore it eventually transforms into β-V form. Nevertheless, the fact that this transformation occurs more slowly in the pressurised CB, suggests that by applying pressure the structures formed are more stable, i.e. the FA chains have an increased *trans* or antiperiplanar conformation[91] -torsion angle between ± 150° and 180°-. This translates into a reduced mobility of the molecule, thus hampering polymorphic transformation. Nevertheless, it is remarkable that the application of pressure at a temperature above the melting point of CB has such a strong effect even after depressurisation.

The previous studies have shown promising results for the application of pressure for the crystallisation of fats. However, from discussions with Dr Josélio Vieira (Nestlé, Product Technology Centre, York, UK), it is evident that industry is more interested in the application of lower pressures, below 1000 bar. Therefore, there is a need of understanding if and how crystallisation is promoted under such conditions.

1.6 Crystallisation of the main cocoa butter triacylglycerols and pure cocoa butter

StOSt, POP, and POSt (St-stearic acid, O-oleic acid, P-palmitic acid) are the three main TAGs present in CB, thus the three main components governing its crystallisation. However, PStSt and StStSt might be the first TAGs involved in seed formation. Consequently, their specific crystallisation behaviours must be kept in mind when studying CB.

1.6.1 1,3-Distearoyl-2-oleoyl-glycerol (StOSt) and 1,3-Dipalmitoyl-2-oleoyl-glycerol (POP)

StOSt crystallises in at least five different polymorphs [92], although a transient form, called δ, was also identified in a study using DSC [93] (Table 1.4).

Table 1.4 StOSt polymorphs and their corresponding chain length and melting points.

Polymorph	Chain length	T'_m (°C) [92]	T'_m (°C)[94]
α	Double	23.5	22.4
γ	Triple	35.4	
δ	Triple		36.2
Pseudo-β'**	Triple	36.5	
β_2	Triple	41.0	
β_1	Triple	43.0	44.3

**It is a deviation of β' for it presents a triple chain length structure, instead of the typical double, but maintains its O⊥ packing [93]

The α polymorph, though easily identified through its short spacing ca. 4.2 Å, was observed to present two peaks in the long spacing area, when crystallising without annealing. In contrast, only one peak is observed when annealing, suggesting that this step is critical for enabling the saturated and unsaturated chains to arrange into a more energetically favourable conformation. The two peaks observed when no annealing was present [95] have been explained as the presence of an "imperfect α" which exists as two domains with different interchain packing (Figure 1.6).

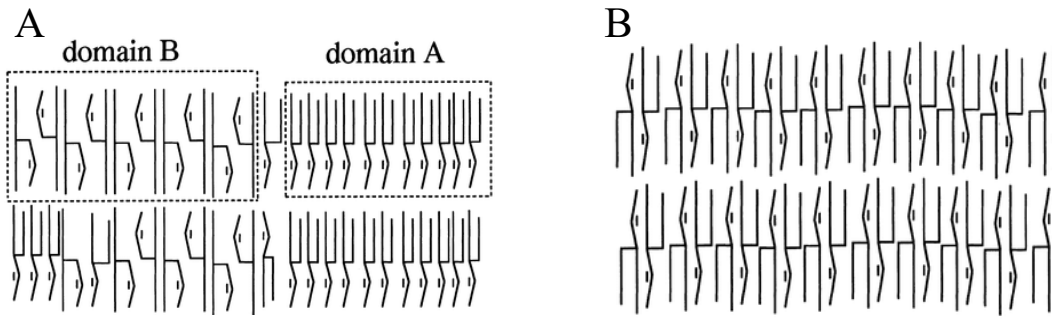

Figure 1.6 Proposed structures for a) imperfect and b) perfect α polymorph packing [95].

Further research on the α-polymorph [96, 97] led to the discovery of two different polymorphs, called α_2 and α_1. The α_1-phase presented the typical 2L structure, previously described, where both saturated and unsaturated chains are parallel, and arranged in a hexagonal packing. In contrast, the FA chains in the α_2-phase (Figure

1.7) are expected to be arranged in a twisted structure, i.e. they have a higher degree of *gauche* or synclinical conformations[97] (torsion angle between 30° to 90° or –30° to –90°). As crystallisation continued, the α_2-phase was observed to transform into a mixed 2L-3L structure, as evidenced by an observed broad peak corresponding to a d-spacing of 12 nm, which represents the sum of 2L and 3L spacings (5.2 and 7.1 nm respectively)[97, 98]. This transient structure further transformed into the α_1-, γ- or even the β'-form[98].

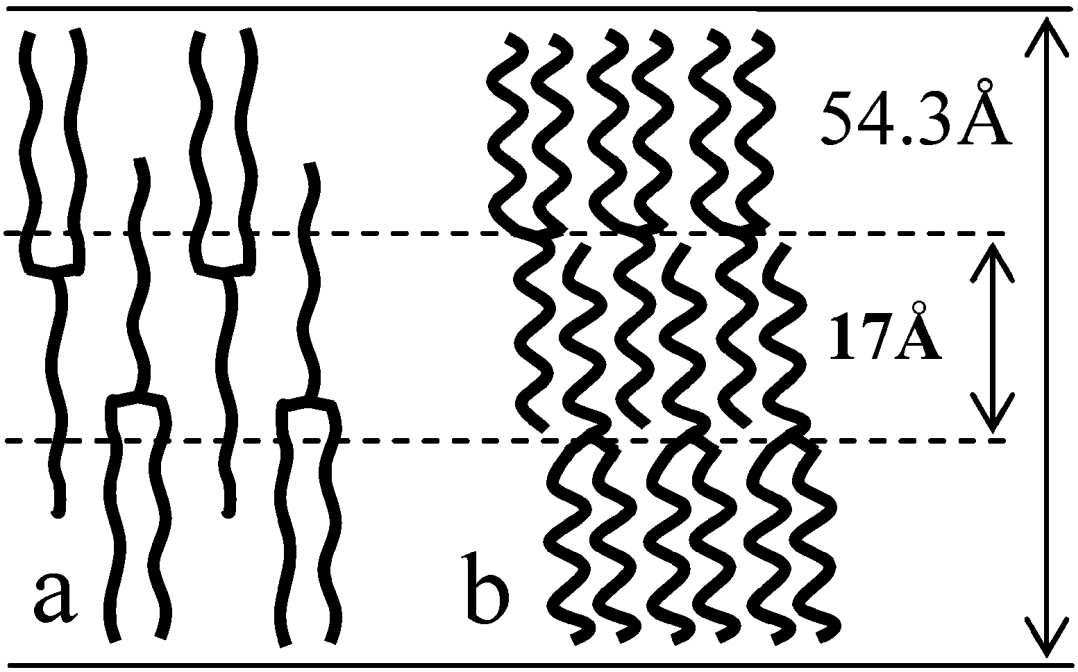

Figure 1.7 Proposed structures for the α_2-phase of StOSt (Taken from reference[97]).

Moreover, StOSt also presents a different polymorph from the classical three: the γ-phase, which is more stable than the α-phase and presents a triple chain length with an orthorhombic parallel sub-cell packing. After a slight supercooling of the melt [99], the α-phase is observed. It then transforms into the γ-phase which still presents a loose packing of chains. Afterwards, the sub-cell packing is stabilised first through lamella-lamella interactions[95] and then through lateral chain-chain interactions. This stabilisation leads to the formation of the β'-form and avoids the steric hindrance between oleic and stearic chains. Finally, the β-form is obtained through the tilt of the chains [92] which is evident through the short spacings in X-ray diffraction studies.

Finally, Ueno *et al.* [95] observed that when StOSt is crystallized at 30 °C and 33°C, through a melt mediated process and without annealing, the α-form transformed into the β'-phase via an apparent liquid crystal (long spacing present without a short

spacing), rather than via the γ-phase. The liquid crystal has its origin in the high mobility of the fatty acid chains.

POP polymorphism is quite similar to that of StOSt (Table 1.5), but with one important exception: the pseudo-β' polymorphs are double chained rather than triple chain, which indicates that its polymorphic transformation is more complex, following the sequence double → triple → double → triple chain length [92, 100]. Thus, it has been proposed that the pseudo-β' structures, though having the oleic and palmitic chains within the same lamella, the steric hindrance is reduced by the oleoyl chains being present in a conformation which allows a straighter chain structure, such as that observed in cholesteryl oleate [92] .

In addition, it should be noted that the triple→double transformation from the γ-phase to the pseudo-β'-forms, indicates that the initial triple structure is highly unstable. This can be caused by the FA chains still having high mobility, though it is also likely that an imperfect triple structure is formed, i.e. where not all oleoyl chains are present in the same layer but containing some of the fully saturated fatty acid chains.

Table 1.5 POP polymorphs and their corresponding chain length and melting points[100].

Polymorph	Chain length structure	T'_m (°C)
α	Double	15.2 ± 1.0
γ	Triple	27.0 ± 0.3
Pseudo-β_2'	Double	30.3 ± 0.3
Pseudo-β_1'	Double	33.5 ± 0.3
β_2	Triple	35.1 ± 0.3
β_1	Triple	36.7 ± 0.3

1.6.2 1-Palmitoyl-2-oleoyl-3-stearoyl glycerol (POSt)

Between three and four different polymorphs have been identified in POSt (Table 1.6). It is important to note that the 'intermediate' phase was only identified by DSC measurements, suggesting a volume and a heat transfer effect. All forms could be obtained through melt-mediated transformation. However, the pseudo-β'-form (identified as the β'-form by Lutton[101]) and β-forms were also obtained via solid-state transformation of the β'-phase[102].

Table 1.6 POSt polymorphs and their corresponding chain-length and melting points [17, 95, 101, 102].

Polymorph	Chain-length structure	T'_m (°C)[92]	T'_m (°C)[101]	T'_m (°C)[103]
α	Double	19.5 ± 1.0	18.2	18.2
δ	Triple	28.3 ± 0.3		
Intermediate	Triple	29.8 ± 0.3		24.5
Pseudo-β'	Triple	31.6 ± 0.3	33.0	33.0
β	Triple	35.5 ± 0.3	38.0	37.4

Furthermore, POSt has certain unique characteristics. For instance, it presents a δ-phase instead of γ-phase (StOSt or POP) possibly due to the different chain lengths of the palmitic and stearic acids. Moreover, this difference evidently effects the packing of all polymorphs as observed by the lower melting temperatures of the α- and β-forms, when compared to StOSt. Additionally, POSt only develops one β-polymorph, in contrast with CB, POP and StOSt, which present two different ones[102], thus reinforcing the idea that a more closed packing is only feasible when the chain lengths are equal.

1.6.3 1-Palmitoyl-2,3-distearoyl-glycerol (PStSt) and 1,2,3-tristearoyl-glycerol (StStSt)

These two TAGs differ from the ones previously described as they only consist of fully saturated FA. This characteristic causes them to crystallise solely in the three basic polymorphs (α, β', and β), all of them with double chain structures (Table 1.7). Additionally, their melting points are higher, due to their higher saturation levels which allow for a better packing.

Table 1.7. StStSt and PStSt polymorphs and their corresponding chain length and melting points [44].

Polymorph	Chain-length	StStSt T'_m (°C)	PStSt T'_m (°C)
α	Double	54	51
β'_1	Double	66	56.7
β'_2	Double		61.3
β	Double	73.4	65.2

Bouzidi and Narini (2012) observed that the long spacing of PStSt (52.3 Å) is smaller than that of StStSt (55.7 Å), suggesting that palmitic acid, due to its shorter chain length, interferes with the interactions at the methyl-end group.

Unfortunately, isothermal crystallisation was not considered in these authors' research, therefore it is difficult to compare with studies of other TAGs. Regardless, the different cooling rates used (from 0.1 to 25 °C/min) allowed them to observe the appearance of the different polymorphs under different supercooling conditions. For example, PStSt crystallised into the β'-phase under slow cooling rates, and into the α-phase under quick cooling rates, which could be compared to using higher and lower temperatures for isothermal crystallisation. In contrast, StStSt though it crystallised into the α-form at higher cooling rates, it crystallised directly into the β-phase at 0.1 and 0.2 °C/min, and not into the β'-form. As such, β' might only be obtained through melt-mediated or isothermal crystallisation. Furthermore, even when the α-phase was the nucleating polymorph, followed by transformation into the β'-phase, it quickly transformed into the β-phase, indicating that the β'-form is an unfavourable conformation.

Bouzidi and Narine [44] also studied binary systems of the two TAGs discussed in this section. Such systems are of interest if the seed crystals are mainly composed of StStSt and PStSt as observed by Davis and Dimick [104]. Interestingly, they found that the structure, the phase development, and the crystallisation process in these mixtures, is mainly influenced by PStSt, rather than StStSt due to the mismatch chain lengths.

1.6.4 Compound crystals of mixed TAGs

Whilst most studies on triacylglycerols have been performed on pure samples, a few studies have been done concerning binary mixtures of fully saturated species, such as StStSt, PStSt and PPP[44, 47, 105], as well as mixed composition TAGs: PPO, POP, POO, OPO and their equivalents substituting the palmitic acids with stearin[94, 106-109].

In the case of the fully saturated fatty acids, when combining tristearin and tripalmitin, in the α- and β' phases, a solid solution (two components being miscible at all concentration rations in the solid phase[110]) was formed, whereas in the β-phase a eutectic behaviour has evident[105], whilst retaining a T'_m above 60 °C. A similar behaviour was observed with mixtures of PStSt and StStSt, though the difference in chain-length in PStSt hindered the transformation into the β-phase, thus suggesting the formation of a molecular compound (mixed crystal occurring only at defined

compositions through specific molecular interactions[110-112]) as it shows that it is interacting directly with StStSt, poisoning the crystal structure, not allowing a closer packing.

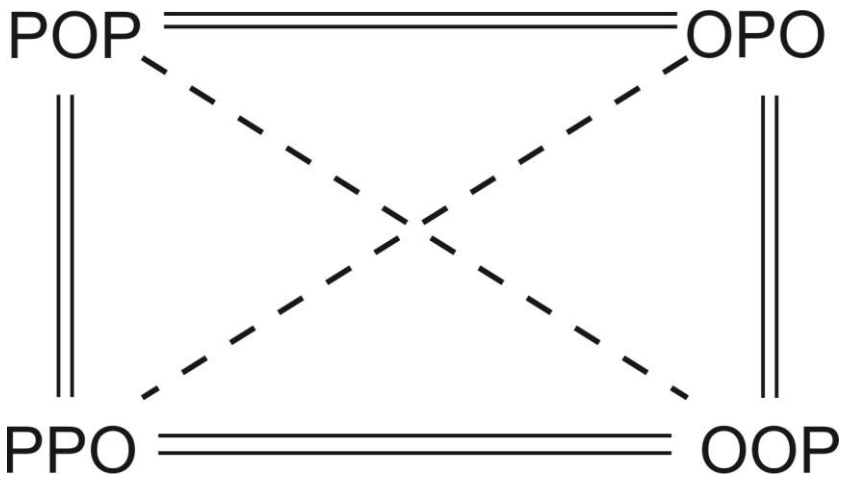

Figure 1.8 Diagram of binary mixture systems of POP, OPO, PPO, and POO. Dashed lines indicate eutectic behaviour, double lines indicate the formation of molecular compounds (based on reference[108]).

In the case of the mixed composition TAGs, an updated figure (Figure 1.8) of that presented by Bayés-García, *et.al*[108] summarises their interaction which is mainly through the formation of molecular compounds, except for the mixtures of POP/OOP, and PPO/OPO where a eutectic behaviour has observed. Most interestingly, however, is that in all cases, the β-phase was not 3L as is typically observed, but rather a 2L structure. This led to the molecular compounds slight instability after 17 months. Similar behaviour has been observed with mixtures of OOSt and StOSt[107].

In CB, however, POP and StOSt are both present in larger amounts than OOP or OOSt[113, 114]. Thus, their interaction needs to be considered as well. They have been observed to form solid solutions in the β-phases with complete miscibility, thus it is likely that they will retain similar interactions with the other mixed TAGs present as in the binary mixtures described above.

Whilst most of this work comprises mixtures of different TAGs, it is important to consider that mono and diacylglycerols can initially attach themselves to growing TAG crystals due to their similar structure, creating defects, or stunting crystal growth. However, they have also been observed to become excluded from the crystalline structure, overtime. Hence, it is possible to say that these compounds

affect the early stages of crystallisation, creating defected crystals, which perfect as time progresses[56, 115-120]. In other words, the crystals of a fat allowed to mature for a long time, are expected to have a more homogeneous composition.

1.7 Cocoa butter crystallisation

CB's polymorphic nature and how it is affected by different factors such as the cooling rate, crystallisation temperature and composition, has been studied since the 1960's. Nevertheless, due to the differences in the methodologies used, most studies are not directly comparable, and often present contradictory results, suggesting that the crystallisation of CB is more complicated than it was originally thought.

Table 1.8 Main long and short spacings of CB [121].

Form	**I (sub-α)**	**II (α)**	**III (β'-III)**	**IV (β'-IV)**	**V (β-V)**	**VI (β-VI)**
Long Spacings (Å)	55.10	49	49	45	63.1	63.1
Short Spacings (Å)	4.19	4.24	4.25	4.35	4.58	4.59
				4.15		
			3.86		3.98	
	3.70				3.67	3.70

Wille & Lutton (1966) identified six different polymorphic forms (I-VI) via their XRD "fingerprint region" (3-6 Å) (Tables 1.8 and 1.9). Since then, more studies have led to the hypothesis that CB might only crystallise into four or five polymorphs, more commonly identified by the Greek alphabet nomenclature[122], which is the one used in this paper. The lower amount of polymorphs is supported by forms β'-III and β'-IV having different melting ranges, but similar XRD patterns[122]. The same is proposed by for the β-V and β-VI forms.

Table 1.9 Melting point of CB's polymorphs (adapted from references[121-123]).

Form	**Melting point (°C)**
Sub-α	-5.0 - 5.0
α	17.0 - 22.0
β'-III	20.0-25.5
β'-IV	25.6-27.5
β-V	29.0-33.8
β-VI	32.3-36.3

Furthermore, as evidenced by their melting points (Table 1.9), the α- and sub-α- forms are the least stable, as in most TAGs. Interestingly, the sub-α form presents a β'-sub-cell (similar short-spacings), but its chains are packed more loosely, as evidenced by broad lines in the long spacing area [124, 125]. Whereas the α-, β'-, and β- forms present their typical sub-cells (A) Packing of TAG polymorphs: hexagonal (α form), orthorhombic (β' form) and triclinic (β form) crystals. B) Stacking of TAGs, i.e. the thickness of the lamellar structure is either in the order of twice the length of one hydrocarbon chain (2-L) or roughly three times its length (3-L).a) [23].

The nucleating polymorph depends on the cooling rate and final crystallisation temperature [20]. At very slow static cooling rates (0.017 °C/h -0.25 °C/min) or higher static crystallisation temperatures (~26 °C) the β'-form is the first to nucleate. In contrast, when higher cooling rates and lower crystallisation temperatures are used, either the α- (0.5 - 1 °C/min) or the sub-α forms (4 - 360 °C/min and/or temperatures below-20 °) are the first to nucleate [122].

1.7.1 Compositional Effects

Though CB's components are the same independently of its origin, the ratios in which they are present does vary, modifying the hardness and the velocity at which it nucleates (Table 1.10) [15-17]. It has been observed that the higher the amount of POO and StOO and lower StOSt content, the CB crystallises more slowly and into a softer product. Whereas higher levels of trisaturated and monounsaturated TAGs have the opposite effect [15-17].

Table 1.10 Classification of CB

Hard/Quick	**Medium**	**Soft/Slow**
Asia and Oceania	West African and North American	South American

DAGs also have an impact on CB's crystallisation. CBs with a higher content of these species presented increased secondary nucleation induction times, resulting in lower total crystallisation[15, 126]. Contrastingly, when DAGs were rich in stearic acid, CB nucleated more quickly during dynamic crystallisation. Therefore, it is not possible to generalise the effect of DAGs on CB crystallisation, for it depends on the DAGs specific composition.

Regarding phospholipids (PLs), their addition has been found to reduce induction rates, but hinder crystal growth and secondary nucleation[15, 127]. However it is important to note that not all PLs display this behaviour, for example, Savage[128] observed that CB's with a higher content of phosphatidylcholine did crystallise more quickly, but when a higher amount of phosphatidylinositol was present, the opposite occurred. Therefore, the effect of PLs on crystallisation is likely dependent on the type and their relative amount in the fat.

As a final comment, though not intrinsic of CB composition on its own, other materials such as small particles originated from processing, such as pieces of the husk or residues coming from the processing machinery (mills) can also induce crystallisation, acting as heterogeneous nuclei.

1.7.2 Seed crystals and the effect of melting temperature on the crystallisation of cocoa butter

As mentioned earlier, though CB's crystallisation is mainly directed by its TAG composition, it is also influenced by some of its other components, e.g. PLs and DAGs. In fact, several researchers propose that CB has seed crystals composed of a core of PLs present in an inverse ribbon phase [129], and surrounded by high-melting (T'_m > 60 °C) acylclycerol species[104, 130-132] (Figure 1.9). The inverse ribbon phase can be described as inverse micelle, where the phospholipid headgroups face inwards surrounding the few water molecules present in CB, and the FA chains facing outwards, due to the media being primarily hydrophobic, i.e. non polar. The FA of the inverse phases are then expected to serve as scaffolding for TAG crystals to form. The higher melting TAG species are thought to be the first ones to crystallise due to their having a stronger crystallisation driving force. This force comes from a higher degree of super-cooling (T_m-T) at any given temperature, in comparison to the lower-melting species (those with unsaturations). Whilst the previous could be considered as one of the ways in which crystallisation begins in vegetable fats, the proposed model (Figure 1.9) shows different lipid species (TAGs, FAs, DAGs) interdigitating with the FA chains of the PLs. However, this is only thought to be possible during the initial stages, where the FA chains still retain a large degree of mobility which could help avoid or resolve any steric hindrance. Similarly to the way TAGs have

been observed to interdigitate in PL membranes, which eventually phase separate due to the increased strain on the membrane, and the repulsion experienced by contact with the polar headgroups[133]. In contrast, once crystallisation starts, the increase presence of antiperiplanar conformations would be expected restrict the interaction between the chains. Hence, it is likely that rather than interdigitations, only methyl end interactions would be energetically favourable, thus acting as the start of the crystalline lamellar structures.

The exact composition of these crystals cannot be specified due to the different isolation methodologies used by different researchers [104, 124, 134]. Regardless, a general trend is evident in all cases: seed crystals present a higher concentration of PLs and stearic acid (as a component of DAGs or TAGs), when compared to the CB from which they were extracted. This suggests that a fractionation occurs during the crystallisation of CB as fully saturated TAGs crystallise first, especially stearin containing species.

These seed crystals are thought to be of approximately 0.09 - 0.28 μm in size [135], and represent less than 0.1 % of CB [136]. Given that their melting temperature is higher than the temperature at which chocolate is commonly melted prior to tempering (ca. 50 °C), they are expected to remain solid at this stage of processing, thus serving as nucleating sites.

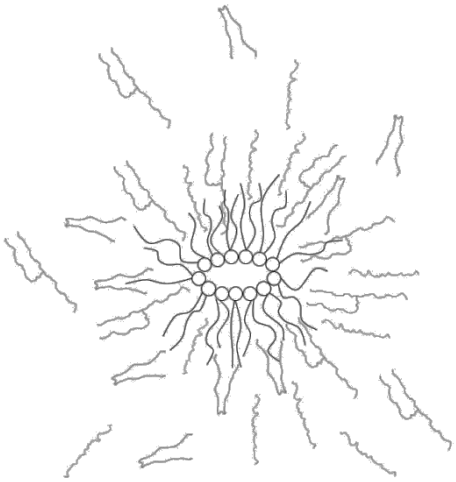

Figure 1.9 Proposed structure for a seed crystal with a phospholipid core surrounded by high melting acylglycerol species (based on [136]).

There is, however, a study by Toro-Vazquez *et al.* [127] who removed PLs through solid phase extraction. In this study, the crystallisation onset of the phospholipid-free

CB was delayed but both the polymorphic transformations and the end of crystallisation happened faster. Therefore, it is thought that while phospholipids act as seeds, accelerating the start of crystallisation, they might hinder the correct structuring of CB TAGs by creating defects in the crystal structure. Notably, though, they found through rheology studies, that the onset of crystallisation is at 59.8 ± 3.7 °C in CB, supporting the hypothesis that 60 °C are insufficient to fully melt it, as such temperature already represents sufficient supercooling for crystallisation to occur. This seemingly contradicts the findings of Foubert[137], who did not observe any difference in the crystallisation kinetics of CB melted at either 65 or 80 °C. However, she used a different cooling rate, not to mention, she only performed these studies using DSC, which, according to the previous authors, is not as sensitive as rheometry. Therefore, it is possible that these events were present but not detected. Moreover, she based her conclusion on comparing only the second crystallisation event, rather than the first, which is not necessarily as sensitive for it can be related to transformation and crystal growth enthalpies. Lastly, it is notable that she only used a longer holding time for the 65 °C treatment, and not for the 80 °C treatment, which could have proved more insightful.

Regardless of the previous results, it is important to remember that it is only one study, and it was not performed in-depth. This is relevant, for the understanding of the impact of this initial melting temperature is of interest as CB seed crystals have higher melting points than those attributed to CB [136], not only because of the proposed phospholipid core but because of the tristearin content, and also, based on a study performed on oleic acid [138], which showed that the induction time for the crystallisation of the α-form increased along with the initial maximum temperature. The previous suggests that even with a simpler and more homogeneous system, the initial maximum temperature is critical, suggesting that this may also be true for a complex system like CB.

Finally, in the more recent work by Wang[139], the β-memory effect (direct crystallisation into the β-polymorph) was studied in pure, fully-saturated TAGs and their mixtures. The main conclusion drawn from the experiments was that not more than 6 °C above the T'_m, as determined by DSC, were needed to melt the TAGs to fully erase the β-memory effect. Nevertheless, what is particularly interesting is the

computational simulation performed by Mazzanti, through which the time-temperature combination required for the molten crystal cluster (of a mix of TAGs) to reach the same molecular distribution as that of the original, "memory-free" liquid. The resulting recommendation was the application of 93-103 °C for 10 min, which is considerably higher than the experimental values

1.7.3 Pre-nucleating structures

In addition to the seed model which has been proposed as the initiator of crystallisation, different pre-nucleating structures have been proposed for TAGs, independently of their origin and the presence or absence of minor components. Three main structures have been put forward: lamellar, nematic and discotic.

Lamellar (smectic)

Based on the combination of a diffuse small-angle diffraction maxima, and a short-spacing of approximately 4.5 Å observed in XRD [140], Larsson (1992) proposed a model of loosely stacked lamellar structures which do not possess a long-range order. He proposes that this model is strengthened further by the similarity to the XRD pattern of L_2-phases of polar lipids [141].

Nematic

This structure differs from the others [142] for it was inferred from Neutron Diffraction studies, rather than XRD. This method was chosen for its capability to contrast match different molecular moieties. Given that it identifies different isotopes of hydrogen, if different parts of a molecule are deuterated, their diffraction is then enhanced, making changes in packing more evident. This last characteristic was exploited by the authors, for they selectively deuterated either the glycerol section (LLL-DH), or the FA section (LLL-HD) of trilaurin.

The basis to their proposed structure is the presence of a shift in the low-angle region from (001) to between 15-25 Å, which is attributed to more tightly packed glycerol molecules. Furthermore, they observed a reduction of the high angle features at $2\theta \approx 60$ ° in the LLL-DH, when compared to the LLL-HD. They suggested that the

long spacings between solid and liquid fractions are different [142]. This is the main evidence which they find contradicts Larsson's[141] hypothesis. Nevertheless, Larsson[141] considers the observed behaviour is expected due to molecular movements which make atoms "invisible" to the neutron or X-ray beam.

Discotic

This model was proposed by Corkery, *et al.* [140] based on the presence of "molecular aggregates". They assume that the preferred structure of TAGs in such a free state as a liquid crystal is Y-shaped rather than h-shaped, as both Larsson and Cebula propose. This structure is expected to reduce the free energy, for the chains are thought to be at approximately 120° from each other. Furthermore, these Y-shaped molecules are presumed to be contained in disc-like volumes (hence the discotic term) which would present a thickness determined by the mobility of the molecules.

The diameter of the disc-like volumes is thought to be 15-22 Å, which is very close to what Larsson and Cebula found, hence they considered this data as support to their hypothesis. Even though they admit that the discotic model might be a way of reconciling both Larsson's and Cebula's proposed structures by considering the three of them as a sequence of arrangements, they propose that the most likely chain conformation would be the Y-shaped, due to the lower free energy state it would represent, as supported by theoretical modelling[143]. Nevertheless, it is important to mention that, though this structure might be more energetically favourable, it is unlikely for these discs to present a long-range order as only reduced van der Waals forces are present, which are not considered to be sufficient to support this complex assembly.

Similar to the discotic model, Lin proposed the Loose Multimer Model[144], where the glycerol backbones are surrounded by their folded fatty acid chains[145], i.e. similar to the Y-shaped proposed by Corkery *et al.* but allowing for deformation of the chains, rather than expecting them to be stiff and fully extended. Therefore, each loose multimer is assumed to be dodecahedral, allowing for space filling arrangements to be preserved.

Importantly, the previous models only consider two possible conformations: the Y-shape (120 °) and the h-shape or chair conformation. This is likely to be derived from

only considering fully saturated TAGs which do not display the same steric hindrance occurring in TAGs with unsaturated FA chains. However, even in this case, a third conformation could be expected to form, i.e. the tuning fork, as described below.

More recently, Tascine *et al.*[146] performed molecular dynamics simulations on liquid sebum TAGs at body temperature, observing that TAG molecules form elongated clusters with the glycerol backbones grouped together. These elongated clusters eventually merge, forming a single continuous network. Importantly, they also evaluated the different conformations of the TAG molecules. Previous workers had suggested that the most favourable conformation was the "propeller" (Y-shaped), i.e. where all the chains are at 120 ° in respect of each other; however, in Tascine's work, the largest population corresponded to the tuning fork, where the sn-2 FA is pointing in the opposite direction to the sn-1 and sn-3 FAs which are parallel to each other. Considering that these studies were performed with mono-acid TAGs, it is likely that in systems with mixed TAGs, like CB, the proportion of TAGs in tuning fork conformation is even larger as the unsaturated FA is expected to be.

Regardless of which liquid crystalline arrangement is present, what seems to be applicable in every case, and even in more complex TAG systems, is that a pre-nucleation structure is present. Studies of trisaturated TAGs in vegetable oils have shown evidence that pre-nucleation interactions occurred due to short-range van der Waals forces. Furthermore, the oil should present TAGs with at least one palmitic acid chain[147, 148]. This is of relevance, for even though CB crystallisation is thought to be mainly directed by StOSt, other TAGs like POP and POSt might prove to be essential in forming pre-nucleating structures, and possibly, its observed memory effect after melting [149].

1.8 Justification and aims of this thesis

CB crystallisation has been studied for several decades[29, 63, 150, 151]; however, there is still no consensus regarding its pre-nucleating/liquid structure, and there are certain factors that have not been fully explored and might have an impact. One of these factors is the temperature at which CB is melted prior to crystallisation. Work in this

area comprises only three serious studies[152-154], of which only one compares the use of temperatures above 60 °C[154]. However, in the latter study, only two temperatures were compared, namely 65 and 80 °C. Furthermore, the only technique used was differential scanning calorimetry (DSC), which does not always allow for conclusive assertions[155]. The lack of studies in this area is surprising as conching temperatures can reach temperatures above 80 °C[8]. Moreover, CB is known to have fully saturated triacylglycerol (TAG) species with melting points above 65 °C which would need temperatures of at least 105 °C to be fully molten, based on the observation of Hernqvist[156] that order in the melt is retained up to 40 °C above the melting point. Additionally, a study on oleic acid[138] demonstrated that by heating it to 60 °C above its melting point, the induction time for crystallisation increased, as compared to using an initial temperature of only 7°C above the melting point. This could be ascribed to either self-diffusion (random motion of molecules driven by internal thermal energy)[157, 158] or changes in the liquid structure. This raises the question if a similar effect is expected in TAGs, thus motivating the investigation of the effect of what is called in this thesis as initial maximum temperature (T_{imax}) on the crystallisation of CB.

More recently, further justification for this work was found in a thesis by Wang[139]. Here it was determined that to avoid direct crystallisation into the β-form, long holding times were required when heating a TAG at its determined melting temperature (T'_m) or temperatures between 1.3 and 6 °C above this T'_m, depending if the system was composed of a single TAG or a blend of TAGs. However, based on molecular diffusion simulations made by Prof Mazzanti, also reported in Wang's thesis, temperatures between 93 °C and 103 °C, held for 10 minutes, would be required for the melt of mixed TAG crystals (trimystirin and tripalmitin) to reach the same TAG distribution as the rest of the liquid. This would suggest that self-diffusion plays an important role in crystallisation as the temperature applied to melt the crystals will determine whether the liquid has a homogeneous composition, or if clusters or with different composition gradients are present. These regions would then have the potential to crystallise at earlier stages if having a larger proportion of the higher melting TAGs.

In addition to the T_{imax}, pressure also remains an under-studied parameter in terms of crystallisation of TAGs and its potential use for processing fats. As has been

described in section 1.5.5, several studies have been performed in acylglycerols, relating to their physical properties such as compressibility[76, 86, 159-161]. In terms of TAG crystallisation, however, only few studies have been performed, and more importantly, they have not allowed the determination of the crystallised polymorphs *in-situ*, though they have shown that pressurising CB promotes crystallisation[69, 79, 87, 90, 159, 162-164]. Nevertheless, most of these studies have applied pressures above 1000 bar, which is above that which the chocolate industry desires to use (J. Vieira, personal communication, 2015). Moreover, preliminary studies in chocolate hinted towards an induced crystallisation into the β-V form when treated at pressures between 200 and 400 bar (J. Vieira, personal communication, 2014). Hence, it is evident that studies are needed to determine if crystallisation of pure CB is also promoted when pressures below 1000 bar are applied, and if so, to identify which polymorphs form under controlled pressure conditions.

1.8.1 Aim

To enhance fundamental understanding of the crystallisation and polymorphic transformations of CB crystals under different pressure and thermal processing conditions.

1.8.2 Objectives

1. Understand how the isothermal crystallisation kinetics, polymorphic transformations and morphology of CB are affected by the use of different T_{imax}.
2. Evaluate the role of self-diffusion on the crystallisation of CB as effected by the use of different T_{imax}.
3. Evaluate if the application of pressures below 1000 bar induces the crystallisation of CB.
4. Determine if the initial melting temperature has an effect on the pressure-induced crystallisation of CB.

1.9 Structure of this thesis

For the accomplishment of the objectives different experimental approaches and techniques were used, which are fully described in the materials and methods chapter. This section was kept separate and independent of the results chapters as similar techniques were used, even if the specific equipment or experimental protocols differed due to the different parameters studied (T_{imax} and pressure). Briefly, for the first objective, a multi-technique approach was undertaken. Well-established techniques were applied to determine the kinetics of crystallisation, such as differential scanning calorimetry (DSC), solid fat content (SFC), and X-ray scattering, the latter being useful in determining the developing polymorphs and their transitions. Polarised light microscopy (PLM) studies were also performed to gather insights regarding the changes in morphology.

For the second objective, the obvious measurements to be performed were those of self-diffusion. Measurements were undertaken using both the standard pulse gradient nuclear magnetic resonance (NMR) method, and a more recent, alternative method named fast field cycling NMR. These studies were performed on both heating and cooling ramps of CB, and were complemented by speed of sound measurements. The latter, though not directly related to diffusion, were used to calculate the compressibility of a material, and hence, can provide insights regarding the degree of liquid or solid behaviour[165] of a material.

For the third objective, two approaches were taken, one performing post-processing analysis of pressure treated CB, which led to inconclusive results, thus motivating *in-situ* studies. Initially PLM studies were performed, helping determine the induction of crystallisation under pressurised conditions (<1000 bar), followed by X-ray scattering measurements at a Synchrotron Light Source, through which the developed polymorphs were identified. Within these *in-situ* measurements, an additional set was performed, where a T_{imax} of 100 °C was applied prior to cooling and applying the pressure treatment, for the fulfilment of the fourth objective.

The methodology section is then followed by a short chapter, where a description of the different lamellar organisations in CB is provided in the form of electron density distribution maps calculated from the characteristic X-ray scattering patterns of CB.

It is important to notice that this chapter does not only present the different crystal forms of CB, but also proposes a new structure for its liquid phase. This is described in great detail in the attached manuscript[166] .The results and their analysis are then presented in two chapters, one dealing with the effects of T_{imax} and the other one describing the effects of pressure (< 1000 bar) on the crystallisation behaviour of CB. The effect of thermal pre-treatment is presented first, allowing the reader to become better acquainted with crystallisation kinetics, and the different techniques used. However, given that differences were obtained between the different treatments, and considering the behaviour simulated by Prof Mazzanti[139], the bulk self-diffusion and speed of sound results are presented as well as an attempt to elucidate the mechanisms behind the observed behaviour in the crystallisation process. The second results chapter describes the effects of pressure on the crystallisation of CB. This starts with the post-processing analysis of CB pressure-treated using a be-spoke machine, followed by the *in-situ* measurements, including those dealing with the combined effects of an increased T_{imax} and pressure.

Chapter 2 Materials and methods

This thesis comprises the study of how two different parameters affect the crystallisation of CB: T_{imax} and medium pressure, defined as that being above 1 and below 1000 bar.

For the first parameter, three temperatures were selected: 50, 80 and 110 °C. 50 °C was used as a baseline for it is closer to that which industry uses for chocolate production, 80 °C was used as an intermediate temperature that is still above the melting point of the β-form of tristearin (73 °C)[167, 168] and 110 °C as the highest temperature based on the experiments by Hindle, *et al.* [134, 135]. In the latter, this temperature was selected in an attempt to fractionate CB, and because it is more than 30 °C above the melting point of tristearin, which is suggested in literature as it erases crystal memory [169].

The main methodologies used for understanding the effects of T_{imax} on crystallisation were SAXS/WAXS, differential scanning calorimetry (DSC), polarised light microscopy (PLM), and solid fat content (SFC). In addition, nuclear magnetic resonance (NMR) studies were performed to evaluate if self-diffusion was the key factor driving the differences between treatments. Regarding the liquid phase of CB, in addition to the diffusion studies, the compressibility of CB as a function of temperature was also calculated using density and speed of sound measurements.

For the study of the effect of pressure on the crystallisation of CB, two main sets of experiments were performed. The first one consisted of off-line DSC and SAXS/WAXS measurements of pressure-treated CB samples. However, as such off-line measurements do not allow the tracking of crystallisation during pressurisation or de-pressurisation, *in situ* measurements were required. These allowed to determine, if the determination of the effects occurring during either of the processes and if they were related to external factors. The measurements consisted of simultaneous SAXS

and WAXS measurements at Diamond Synchrotron Facility and pressure PLM at the Chemistry Department of Imperial College, London.

Finally, two more methods are described: TAG composition, and oxidative stability. The first is necessary to identify, if the CB here used is in the range of the soft and slow-crystallising CBs or the hard and fast crystallising ones as observed by Foubert and Chaiseri and Dimick [15, 170].

2.1 X-ray scattering

Small- and wide-angle X-ray scattering (SAXS and WAXS) measure the interaction of a sample, when it is irradiated with X-rays. Four basic elements are needed: an X-ray generating equipment, a collimation system through which the beam size is shaped, the sample, and a beam stop with a detector.

Once the sample is irradiated, it absorbs and scatters the incident X-rays. The scattered rays will then undergo either constructive (described by Braggs law, $2dsin\theta = n\lambda$) or destructive interference Figure 2.1 B) depending on whether the waves are in or out of phase with each other.

Note, that the scattering angle 2θ has the disadvantage that it depends on the wavelength which varies between X-ray instruments. Because of this, it is common practice to present the scattering patterns as a function of q, also known as a scattering vector (equation 6) [26] thus allowing a more direct transformation into "real-space" distances, d.

$$q = \frac{4\pi}{\lambda} \sin(\theta) = \frac{2\pi}{d} \quad (6)$$

It is relevant to mention that in this thesis, X-ray powder diffraction is used, rather than single crystal, as is common practise in fat crystallisation studies[32]. This is, because crystallisation kinetics measurements require to be performed in the bulk, thus resulting in a multitude of small crystallites. Secondly, single-crystal measurements in fats are not feasible in the case of the meta-stable polymorphs due to their low melting points, and more importantly, because of CB's monotropic nature. Thirdly, the main objective of the X-ray scattering measurements was to follow the crystallisation of CB, particularly polymorphic transformations, rather than obtain detailed structural

information. This, in fact, outlines the main difference between single crystal and powder X-ray diffraction, i.e. the former provides detailed structural information, whereas the latter does not.

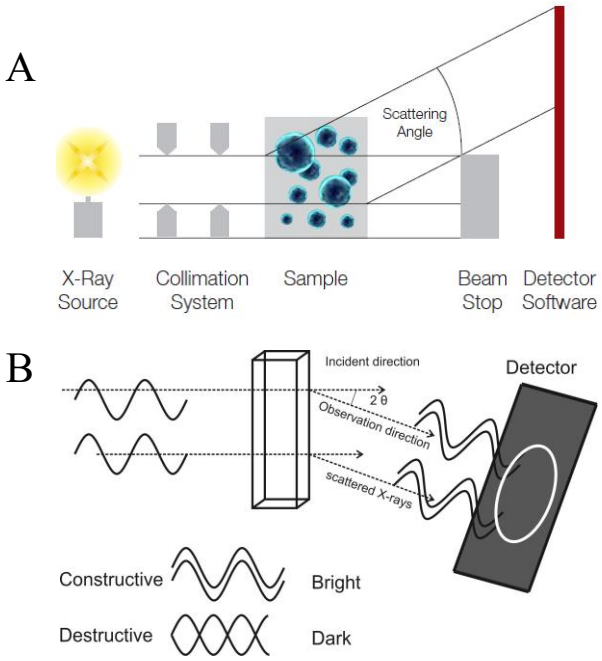

Figure 2.1 A Shows the components of an X-ray scattering instrument[26] from the X-ray source to the detector. Panel B shows how the scattered rays are at an angle from the incident direction, and how only X-rays creating constructive interference lead to bright areas in the detector.

Single crystal diffraction relies on generating one pure crystal which is then rotated so that it can be measured at different, well-described angles. Thus, the location of all the lattice points can be identified, thus allowing for the description of the crystal structure at atomic level. Powder diffraction, on the other hand, measures a mix of small crystallites, hence there is no need for rotating the sample. By having a large number of crystallites, information of the different planes are simultaneously measured[171]. However, the intensities of the peaks are usually broadened mainly due to imperfections of the crystallites, not to mention that the obtained peaks are an average of all the different planes. This leads to loss of resolution, especially in the wide angle region, as there is an overlap of peaks caused by reflections that are close to each other, or because of a systemic overlap of the lattice points of different planes, for example the (100) and (110) planes of a face-centered cubic lattice [21]. Hence, whilst information of the d-spacing, i.e. the overall stacking, can be obtained, the full description of the unit-cell is not attainable through powder diffraction[172].

2.1.1 SAXSpace specifications

In this work, simultaneous SAXS and WAXS measurements were performed with a SAXSpace instrument (Anton Paar GmbH, Graz, Austria) equipped with a Cu-anode that operates at 40 kV and 50 mA ($\lambda = 0.154$ nm). The instrument is equipped with Peltier elements (TCStage 150, Anton Paar, Graz, Austria) for temperature control in a range from -30 to 150 °C (± 0.1 °C).

The scattering vector q was calibrated with silver-behenate. The sample-detector distance (SDD) used was 317 mm allowing the measurement of scattering vectors of $0.1 \leq q \geq 18$ nm^{-1}. The 1D scattering patterns were recorded with a Mythen micro-strip X-ray detector (Dectris Ltd, Baden, Switzerland). All measurements were made with an exposure time of 10 minutes.

2.1.2 Sample preparation

West African cocoa butter (CB) provided by Nestlé, Product Technology Centre, York, U.K. was used without additional refining. 1.5mm quartz disposable capillaries were filled with molten CB (at 50 °C), and sealed with wax and epoxy glue. The samples were then allowed to cool at room temperature, and kept under this condition for at least two weeks to ensure the presence of the β-V polymorph. Its formation was confirmed through a preliminary SAXS/WAXS measurement taken with an exposure time of 5 minutes.

2.1.3 Thermal protocols

As mentioned before, three maximum melting temperatures (T_{imax}) were selected: 50, 80, and 110 °C. Additionally, it is known that the cooling rate applied has an important effect on the crystallisation. In this work, a constant rate of 3 °C/min was used. A faster cooling rate was not applied, as this is uncommon in industry given the larger volumes used.

The samples were left to equilibrate at 20 °C in the sample stage for 5 min, after which they were heated to 50 °C for 10 minutes. This was followed by either direct cooling to 20 °C, or an additional heating step to 80 or 110 °C for 10 minutes prior to the cooling ramp. Once the 20 °C were reached, 5 minutes were allowed for thermal

equilibration prior to the start of measurements, which were performed continuously for at least 20 h, with an exposure time of 10 minutes. After 24 h, samples were kept in a temperature-controlled room, and were measured daily for a week, then at weekly intervals for a total of four weeks, and finally once every month for six months.

Note that the holding times for thermal equilibration were selected from a preliminary experiment using a larger sample (25 mL) in a glass container.

2.1.4 Data Analysis

All the scattering patterns were corrected with respect to the position of the primary beam using SAXStreat software (Anton Paar, Graz, Austria). All data was further transmission-corrected by setting the attenuated scattering intensity at $q = 0$ to unity using SAXSQuant software (Anton Paar, Graz, Austria). Background subtraction was performed by considering the empty capillary scattering profile, using SAXSQuant.

The different polymorphs developed by each sample were identified during their thermal treatment by comparing the obtained d-spacings in the SAXS regime, and the peak positions in the WAXS region to those reported in literature[20, 121, 123]. Note should be taken that for the identification of polymorphs, no de-smearing procedure was required as smearing mainly effects the FWHM and shape of the peaks, rather than their position[26].

As a first approach, to determine the time ranges within which each identified polymorph was present, contour plots were used to evaluate the first 24 h of crystallisation. For further analysis in the SAXS region, a Matlab® (Mathworks, Massachussets, U.S.A.) code was written to find the peak positions of the first, and second or third order peaks (for the α, β'-III, and β-V polymorph identification, respectively). However, this programme was only helpful in the analysis of the 50 and 80 °C treatments, as the 110 °C treatment at its initial stages presented undefined broad peaks that could not be assigned to a specific polymorph. Thus, for the 50 and 80 °C treatments, the start and end of crystal transformation was easily tracked, but for the 110 °C treatment, detailed visual inspection was used to determine at what point in time these broad peaks developed by comparing them to the first frame. Moreover, the transition between the α- and β'-IV forms had to be confirmed visually by comparing to a frame where only the α-form was observable. This is because the first-order peak

positions of both metastable forms are quite similar, thus overlapping in the initial stages, and their third-order peaks have a low intensity, thus resulting in an inaccurate determination of the start of the transition.

For the first 24 h, the WAXS region was analysed through a combination of dynamic difference functions ($DDF_{(j,k)}$, where j and k are two different patterns) and visual inspection, as described by van Malssen, *et al.*[20]. However, given the large similarities between the β-V and the β-VI forms, this transition could only be visually.

Briefly, the DDF method consists of determining the overall squared difference of the corresponding channel intensities (I) between two patterns (j and k) as described in equation 7.

$$\Delta_{(j,k)} = \sum_{i=p}^{q} \left[I_{(j,i)} - I_{(k,i)} \right]^2 \quad (7)$$

For the transition between α and β'-IV, $DDF_{(j,1)}$ was used, as the α-form WAXS peak developed from the start, whereas for the transition into the β-V form $DDF_{(j,65)}$ and $DDF_{(j,115)}$ were used for the 50 and 80 °C treatments, respectively. These two frames were selected (65 and 115 min for the 50 and 80 °C treatment, respectively) as they showed no evidence of the alpha phase neither in the SAXS more the WAXS region.

Representative diffraction patterns of the main three polymorphs, α-, β'- and β-phase, were selected from the lab-based (β'- and β-phase) and the Diamond synchrotron (α-phase) SAXS measurements for further analysis. Diffraction patterns were treated as mentioned earlier. It must be added, however, that in the case of lab-based SAXS measurements, these were performed using a line-focus collimation system which is known to cause smearing of the peaks[26]. Therefore, de-smearing process was applied beforehand in an automated manner using SAXSQuant software (Anton Paar, Graz, Austria).

Afterwards, the diffraction peaks were fitted to a Lorentzian distribution function using OriginPro9.5® (OriginLab, Northampton, MA). The intensities were further Lorentz corrected [173], and the form factor values, F_h, were obtained from the square root of corrected intensities.

Considering that TAGs are centrosymmetric structures, similarly to phospholipid bilayers, the electron density profile (EDP) can be estimated using the FT analysis of

the electron density contrast by the summation of cosine terms only[174] as described in equation 8:

$$\Delta\rho(z) = \sum_{h=1}^{h\,max} \alpha_h\, F_h cos\left(\frac{2\pi z h}{d}\right) \quad (8)$$

where $\Delta\rho(z)$ is the electron density contrast, h the Miller index (diffraction order), α_h, the phases (either +1 or -1) of the form factors, F_h, and d denotes the lattice spacing, $d-spacing = \frac{2\pi}{q}$.

Note, that as the form factors are obtained from the squared roots of the corrected intensities, it is necessary to determine the correct phases, α_h, of the amplitudes, F_h, for the application of equation 8, which for centrosymmetric structures is reduced to the task of deciding if a given contrast should be considered positive or negative, respectively. The correct phase combinations for the α and β-V polymorphs were taken, and verified, from the work by Mykhaylyk *et al.* due to the similarities between the structures of StOSt and CB. In the case of the β'-form, all possible phase combinations were checked and confronted with *a priory* strip model of the β'-form EDP to determine the correct phase combination.

In addition to the EDPs of the different crystalline structures, in collaboration with Dr Amin Sadeghpour, a new model for the liquid state of CB was proposed (see attached manuscript[166]). Briefly, TAG assemblies are expected to be immersed in an isotropic medium. The TAGs in these assemblies are thought to have their glycerol backbones at the centre and their FA chains facing outwards (Figure 2.2 A). TAG molecules from the isotropic medium are then expected to attach to the outer layer of FA chains as temperature decreases (Figure 2.2 A), thus serving as scaffolding for the formation of crystalline lamellar structures, similarly what has been proposed with the PLs present in CB by Dimick and others [136, 175].

The electron density distribution (Figure 2.2 B) is then described by the summation of three Gaussian terms: a positive one at the centre, representing the glycerol backbone, followed by a smaller negative one representing the averaged position of the methyl ends of the FA chains, and finally, a small positive term representing the glycerol backbone of the TAG molecules attached to the base structure (Figure 2.2 B)

$$\rho_{III}(z) = exp\left(-\frac{z^2}{2\sigma_G}\right) - \rho_r \sum_{j=1,-1} exp\left(-\frac{(z-jz_C)^2}{2\sigma_C}\right) + |\rho_{shell}| \sum_{j=1,-1} exp\left(-\frac{(z-jz_{shell})^2}{2\sigma_{shell}}\right) \quad (9)$$

where σ_G, σ_C and σ_{shell} represent the distribution breadth of the glycerol backbone, FA chains and the second layer of TAGs, respectively; z_C represents the position of the methyl groups (CH_3); $\rho_r = |\rho_C/\rho_G|$ indicates the electron density contrast between the CH_3 groups (ρ_C) and the glycerol backbone (ρ_G); $|\rho_{shell}|$ is the relative electron density contrast betweem the lower concentrated glycerol regions of the second TAG layer and the glycerol backbone; and jz_{shell} represents the position of the former along z-axis.

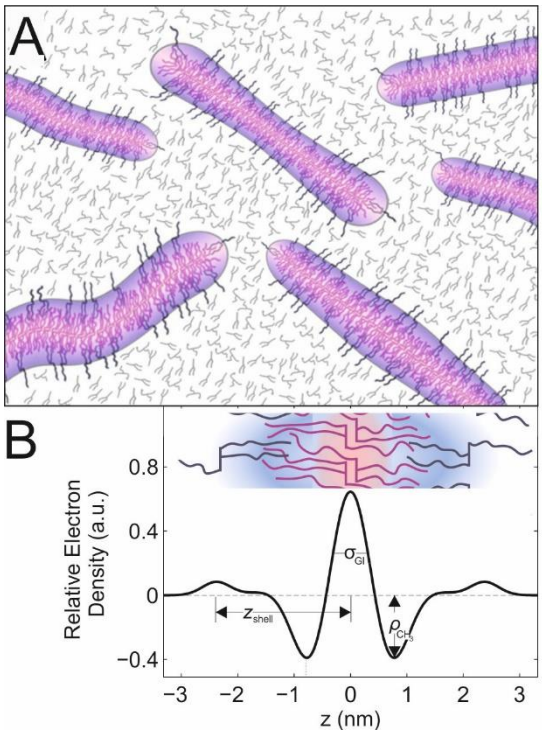

Figure 2.2 Lamellar TAG assembly model. (A) Schematic sectional representation of the lamellar TAG assembly model. The TAGs back-to-back assemblies are treated as 2D-lamellar double layers (red-purple) with a loosely attached outer layer of TAGs (black). Note, that the lateral extension of the assemblies are assumed to be practically infinite, when compared to the thickness of the lamellae. Non-assembled TAGs are shown in light grey. (B) Electron density profile modelled with three Gaussian distributions identifying (i) the high density centred glycerol backbone region, (ii) the low density hydrocarbon chain regions (methyl group rich) and (iii) low density glycerol backbone regions (loosely attached second layer)[166].

2.2 Differential scanning calorimetry

In differential scanning calorimetry (DSC) the heat flow released or absorbed by a sample is measured during either isothermal or temperature change profiles. In practice, a heat flow DSC instrument measures the power needed to maintain either the set temperature or the temperature change rate (cooling or heating), and comparing such power to a reference furnace[176]. This makes the method ideal for isothermal crystallisation studies by providing an accurate measurement of the heat released during such processes, as well as for determining melting ranges of the final polymorphs, through heating profiles.

2.2.1 Sample preparation and thermal protocols

Samples of molten CB (1.35 ± 0.2 mg) were weighed, transferred into a 30 μL aluminium pan, and sealed with the appropriate aluminium cover. It was then put inside a Diamond DSC (Perkin Elmer, Massachusetts, USA) where samples were held at either 50, 80 or 110 °C for 10 minutes, and cooled down to 20 °C at 3 °C/min, as in the X-ray scattering experiments. Once this temperature was reached, it was held for four hours as this was sufficient to observe the initial phases of crystallisation that could not be tracked by lab-source X-ray measurements, as they do not allow time-resolved measurements during the cooling ramps, nor the first 15 min of crystallisation due to the longer required exposure times.

After the isothermal period, samples were heated to 50 °C at 50 °C/min to determine the polymorphs present through the observed melting peaks and comparing them to the values reported in literature [17, 20, 121, 124, 169, 177, 178].

All measurements were performed in triplicate at Nestlé, Product Technology Centre, York.

2.2.2 Data analysis

For the analysis of the cooling ramps, when a crystallisation event was evident, i.e. an exothermic curve, the onset of the transition was determined as the point where the curve started deviating from the baseline.

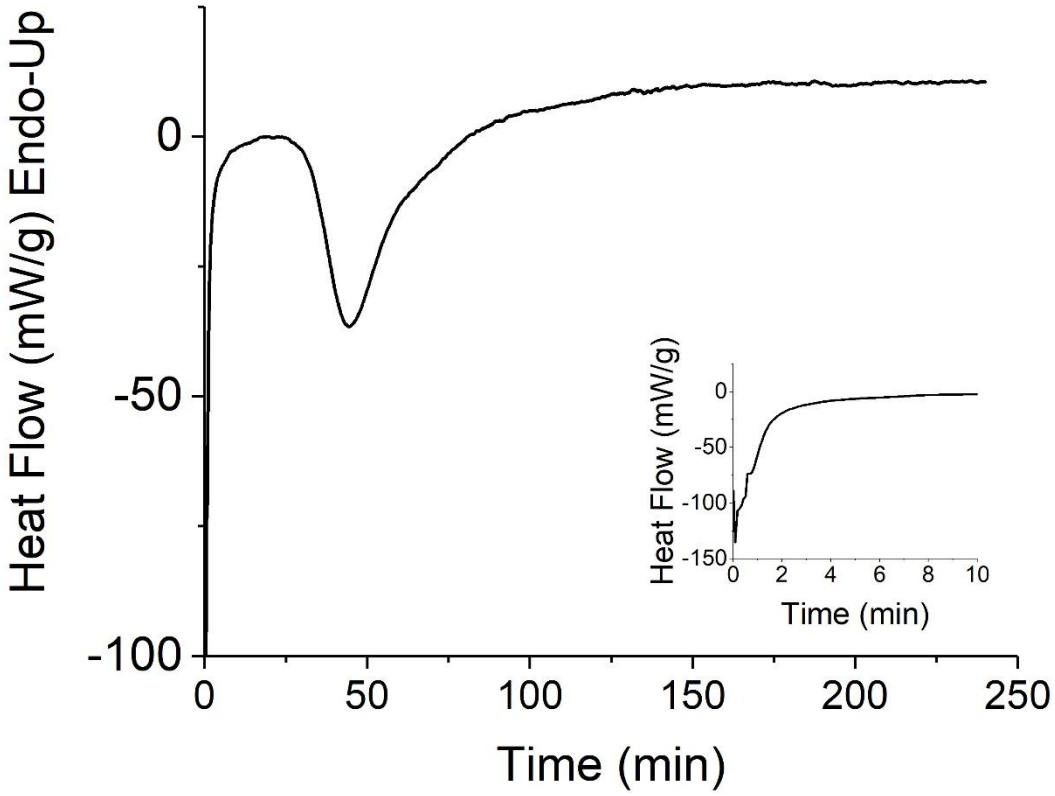

Figure 2.3 Example of DSC isothermal thermogram, corresponding to one of the repetitions of the 110 °C treatments. The inset shows the first crystallisation event, which in this case can be considered a combination of multiple small events occurring on reaching isothermal conditions.

During the isothermal period, usually two crystallisation events were observed. The first transition temperature (assumed α-phase formation) peak tended to be too close to the first recorded data point, thus not allowing for the analysis of the turnover. However, global analysis was possible for the second crystallisation event (β' phase formation). Here, the partial areas of the crystallisation peaks were calculated at 5 min intervals, plotted, and further fitted (Figure 2.4) with the modified Gompertz model for crystallisation kinetics[179] equation 10:

$$f(t) = m \cdot exp\left(-exp\left(\frac{\mu e}{m}(\lambda - t) + 1\right)\right) \quad (10)$$

where f is the fraction solid fat content at time t (%), or in this case the area under the DSC curve; m is the maximum heat of crystallisation (mW/g); μ is the maximum increase rate in crystallisation (the tangent to the inflection point of the crystallisation curve), and λ is a measure for the induction time in minutes (intercept of the tangent at the inflection point with the time-axis) and e equals 2.7183. This fitting was performed using an in-house Matlab R0215A® (MathWorks Inc., Massachusetts, USA) programme with 95% confidence levels. The resulting parameters were then analysed

using ANOVA and t-tests to determine significant differences with a critical p-value of 0.05.

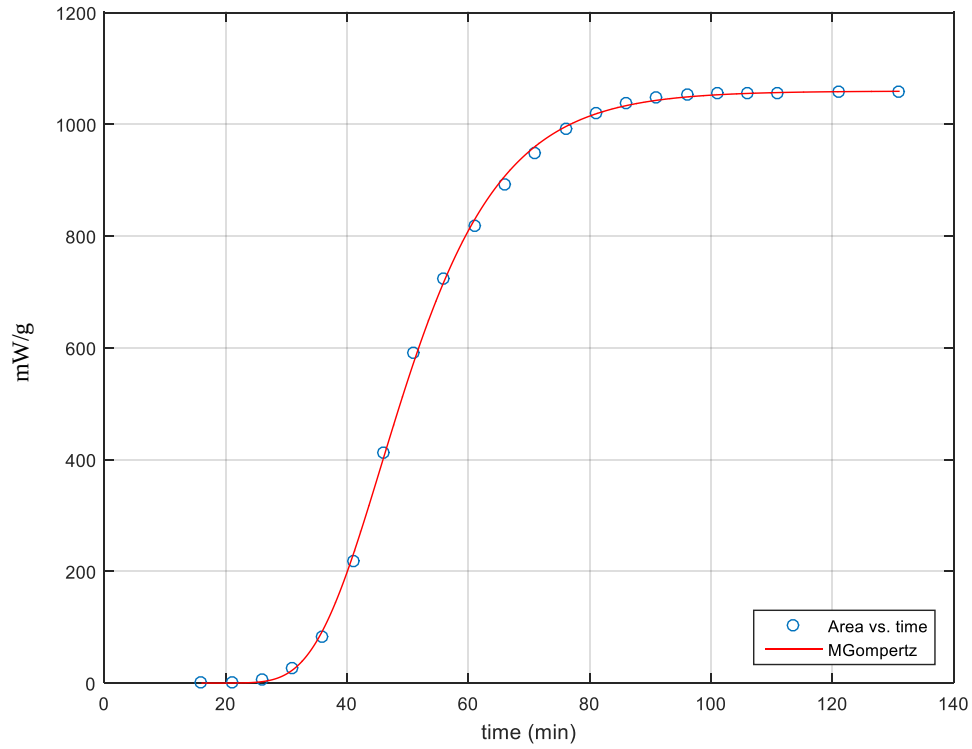

Figure 2.4 Partial areas of the second isothermal peak of the 110 °C treatment of CB, plotted as a function of time. The blue circles correspond to experimental data, and the red continues line represents the fit with the modified Gompertz model.

2.3 Polarised light microscopy measurements

Polarised light microscopy (PLM) is a specimen enhancement technique that involves the use of two polarisers, before and after the sample. It is useful in the study of birefringent materials as it extinguishes the light that has not suffered a change in polarisation angle[180, 181].

Birefringence occurs only in anisotropic materials[180, 181]. This results in different refractive indices. That is, light is refracted in two different directions and velocities on crossing the sample. One of the rays, termed the ordinary ray, follows the law of normal refraction, thus its propagation can be described as a spherical wavefront as it travels at the same velocity in all directions. The other ray is termed extraordinary ray, and it can be described as an elliptical wavefront as its velocity depends on the direction of the crystal (Figure 2.5). In this case, the maximum velocity corresponds to that

parallel to the long axis, and the slowest at the short axis. If the ordinary and extraordinary rays coincide at the major axis then the extraordinary refractive index is larger, thus resulting in a positive birefringence, and the opposite leads to a negative birefringence.

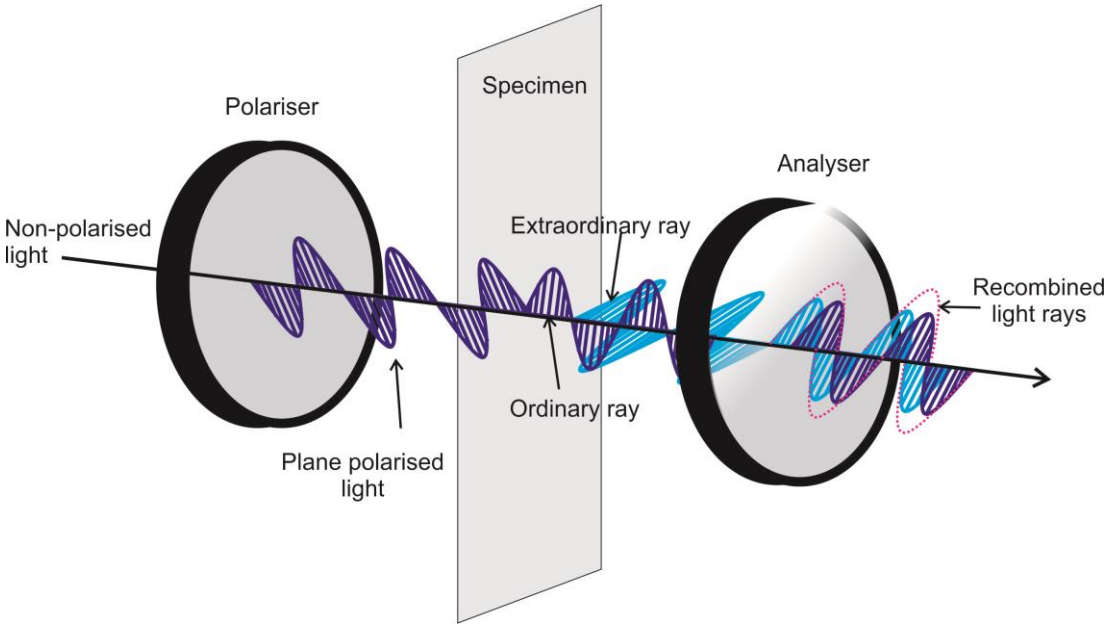

Figure 2.5 Polarised light optics configuration describing how non-polarised light is affected by both the cross-polars (combination of polariser and analyser) and the birefringent specimen (adapted from references[180, 181]).

Moreover, as one wave is retarded with respect to the other, destructive and constructive interference occurs, causing different wavelengths to be affected or extinct at different parts of the object. Therefore, different parts of the spectrum will be visible at given areas resulting in different colours as observed in Figure 2.6. Of the full spectrum shown here, the most sensitive area is that of the first order red at approximately 550 nm, as a slight change causes a shift towards cyan or yellow[182]. Therefore, a wave retardation plate can be used to add further enhancement, thus allowing to determine further structure differences, both quantitative and/or qualitative.

In the specific case of spherulites, a wave plate is particularly useful as it allows the determination of their sign. Here, positive spherulites are evidenced by having a blue colour in the first and third quadrants, whilst the opposite applies for negative spherulites (Figure 2.7)[183-185].

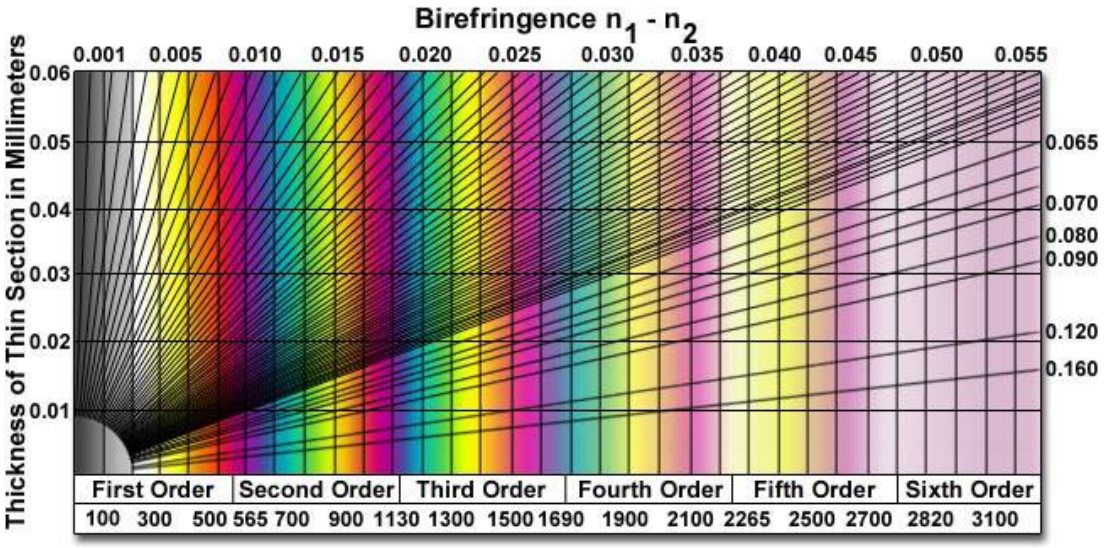

Figure 2.6 Michel-Levy birefringence chart[182].

Samples were observed with a Leica Microscope DM2700P (Leica Microsystems, Cambridge, UK) equipped with a Linkam LTSE 120 (Linkam Scientific, Tadworth, UK) hot stage and temperature controller (±0.1 K). A Nikon Camera D7100 (Nikon, Japan) was used to take single frames at variable intervals during the cooling ramp, isothermal period, and melting ramp.

20x and 50x objective lenses were used to obtain more in-depth visualisation of the crystals. Transmitted light was always preferred. A wave plate was used when differentiating between structures was not possible with standard polarised lenses, and to render full melting events of structures clearer.

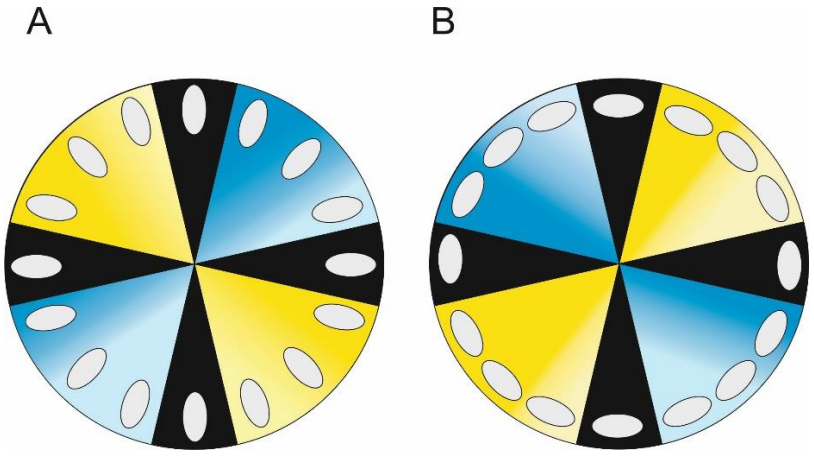

Figure 2.7 Maltese cross pattern exhibited by positive (A) and negative (B) birefringent spherulites viewed through polarised microscopy. Positive spherulites have the largest semi-axis in a radial direction, whilst negative spherulites have the long axis in the tangential direction.

2.3.1 Sample preparation and thermal protocol

One drop of molten CB (at 50 °C) was put on top of a glass slide and covered with a square coverslip, which was allowed to crystallise at ambient temperature for at least 2 weeks.

A similar thermal protocol to that of the SAXS studies was followed; however, samples were only allowed to crystallise for 1 h in the Linkam stage, as this permitted the observation of the initial stages of crystallisation, as well as the development of a crystal network stable enough to allow for transportation to an incubator. Pictures were taken every 10 s during the cooling ramp, and every 30 s during the isothermal period. The samples were then transferred to a temperature-controlled incubator set at 20 °C, for two weeks. Samples were photographed daily for at least three consecutive days, then on days seven and fourteen. On the last day, samples were melted at 1 °C/min to 40 °C. During the melting protocol, pictures were taken every 10 s.

2.4 Solid fat content measurements

Solid fat content (SFC) measurements were performed in a Minispec-mq_{one} SFC analyser (Bruker BioSpin, GmbH, Rheinstetten, Germany), using the direct method AOCS Cd 16b-93[186] applying equation 11.

$$SFC\ (\%) = \frac{f(s'-l)}{l+f(s'-l)} \cdot 100 \qquad (11)$$

where *l* is the free induction decay (FID) of the liquid, *s* the FID of the solid, and *s'* the FID the FID of the solid after a dead time (Figure 2.8)

This method relies on NMR measurements of the free induction decay (FID) of a given sample after applying an electromagnetic 90° pulse. When such a pulse is applied, the nuclear spins align to the magnetic field, but once the pulse finishes, they slowly return to their original equilibrium resulting in a decaying signal. Because of the high mobility of molecules in the liquid (*l*), their return to the initial equilibrium is slower than in the solid (*s*). In fact, after 70 μs the only observable signal is that of the liquid (*l*). However, *s* is not directly measurable as there is an inherent dead time of the receiver, thus, *s'* is measured instead [187-189]. This value is corrected by a factor of *f*, which has already been

established for a variety of fats. Once all the previous values are obtained, the SFC values are easily determined automatically by the NMR software according to reference [190].

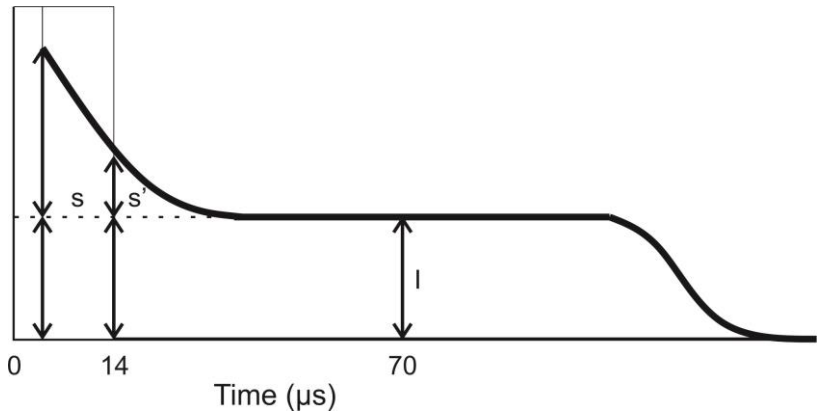

Figure 2.8 Schematic of the signal of a partially crystallised sample after a 90 ° pulse, where s represents the combined signal of the solid and liquid fractions, s' essentially represents the same as s, but after the inherent dead time, and l represents the signal of the liquid fraction only.

2.4.1 Sample preparation and thermal protocol

Glass NMR tubes were filled with approximately 1.5 mL of molten CB (50 °C). Similarly, to the X-ray protocols, samples were heated to 50 °C for 10 minutes, and then, depending on the treatment, they were heated to 80 or 99 °C (maximum temperature allowed by the heat blocks of the equipment) and held isothermally for 10 minutes. Once the samples had equilibrated at the corresponding temperature, they were cooled down to a crystallisation temperature of 20 °C. When this temperature was reached, it was held for 2 h, and measurements were taken at variable intervals.

Given the limited amount of heating blocks present in the MiniSpec, as well as software limitations, it was not possible to obtain a continuous cooling ramp as in the DSC, and SAXS/WAXS protocols. Rather, a step-wise approach was utilised. For the 50 °C treatment, after thermal equilibration the samples were cooled down directly to 41 and 35 °C, and finally to 20 °C in 3 °C steps. The 80 °C sample had to be cooled down initially in larger steps. Samples were first cooled down to 60 and 40 °C, after which the same protocol of the 50 °C treatment was followed, starting from 35 °C. Finally, for the 99 °C treatment, the sample was initially cooled down to 80 °C, after which the

same temperature protocol of the 80 °C sample was followed. In all cases, the holding times corresponded to 1 minute per degree decreased, thus simulating a cooling ramp of 1 °C/min. Once the sample reached 20 °C, it was held for 3 min prior to the beginning of measurements for temperature equilibration.

Final isothermal plots of SFC vs. time were made and fitted with the modified Gompertz equation (Equation 5) using the same Matlab® code as before.

2.5 NMR for diffusion measurements

NMR techniques help investigate the dynamical properties of molecules, such as self-diffusion, through the measurement of spin-lattice relaxation rates (R_1=1/T_1). These rates correspond to the time necessary for the nuclear magnetization to approach thermal equilibrium (Boltzmann equilibrium) after being perturbed by a magnetic field. This process is mediated by an exchange of energy between the nuclear spin energy and the system (i.e. the lattice) [191,192].

Diffusion can be defined as the translational motion of molecules resulting from their own internal thermal energy, in the absence of molecular mixing [193-195]. It is usually described by the diffusion coefficient (m^2/s). It reflects the mean square displacement of molecules per unit of time. As this value increases, the molecules are expected to move, or diffuse faster, whilst when lower values are observed the molecules are expected to diffuse at a slower rate.

The diffusion coefficient depends primarily on temperature, viscosity, and the size of the molecules. Diffusion tends to increase alongside temperature, as molecules become more mobile. The opposite effect is observed with viscosity and molecular size, to which diffusion is inversely proportional, as described by the Einstein-Stokes relation for spherical particles (equation 12)

$$D = \frac{K_B T}{b\pi\eta r_s} \quad (12)$$

where K_B is the Boltzmann constant, b relates to the boundary conditions, and is usually either 4, for large volume molecules, or 6, for small volume molecules, η is viscosity and r_s is the radius of the molecule.

2.5.1 Pulse gradient spin echo NMR (PGSE-NMR)

The "Golden standard" for measuring diffusion coefficients is the spin-echo (SE) pulse field gradient (PG) technique[194]. This technique is based on a single SE technique. This relies on first applying a 90° pulse along the *x* direction so that it shifts towards the *xy* plane, in the *y* axis (Figure 2.9). Once the pulse is removed, the fields begin to de-phase, some clockwise, and some anti-clockwise, depending on their magnetisation. After a time of de-phasing, τ, a 180° pulse is applied so that the spins are re-orientated on the *y* axis (Figure 2.9). Because the spins keep precessing at the same frequency as before, they cluster once more at time 2τ forming an echo (Figure 2.9). If a 180° pulse is continuously applied, a decay is observed caused by what is known as T_2 relaxation, which stops the spins from dephasing fully. Therefore, the SE technique can be used for measuring T_2 [157, 194, 196, 197].

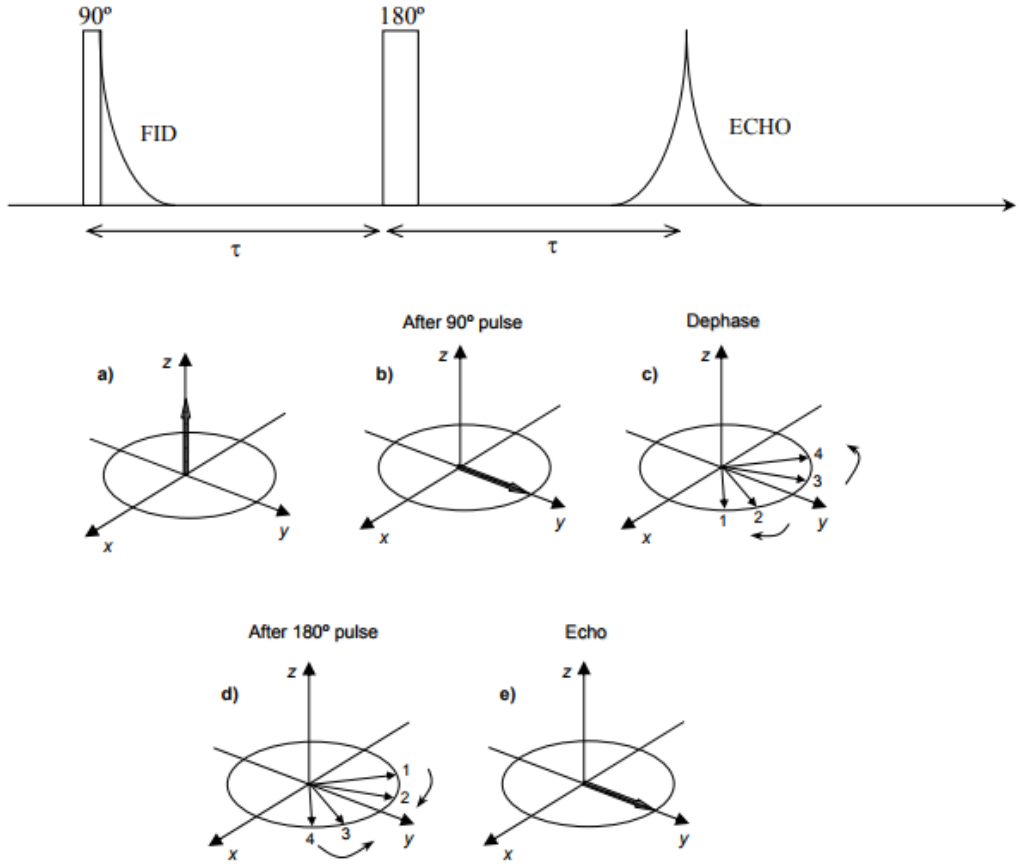

Figure 2.9 Spin echo pulse sequence. An initial 90° pulse is performed to de-phase the spins, and after a time τ, a 180° pulse is applied to invert the position of the spins, but not the direction in which they travel. This eventually generates an echo, after τ, as the spins once more realign on the +y axis [158].

However, diffusion is best estimated when the measured decaying amplitude of the echo is only caused by a pulse gradient, PG, rather than T_2. Thus, instead than continuously applying 180° pulses after a time τ (ms), a pulse gradient of amplitude g (50 G/cm/A), and duration δ (ms), is applied after the 90 and 180° pulses (Figure 2.10). Furthermore, all the delays, including the time between the two pulse gradients (ms), Δ, are kept the same, so that the attenuation effect of T_2 is only observed as a constant factor (Figure 2.9 and 1.8).

The observed decay in the echo amplitude (signal decay) is described by the Stejskal-Tanner Equation[198] (equation 13):

$$S_g = S_0 e^{-D\gamma^2 g^2 \delta^2 \Delta - \frac{\delta}{3}} \quad (13)$$

where S_g represents the signal as affected by diffusion, S_0 the initial signal, D the diffusion factor, and γ the gyromagnetic ratio of hydrogen. The previous equation can then be fitted to the experimental results, thus allowing the determination of D (Figure 2.11).

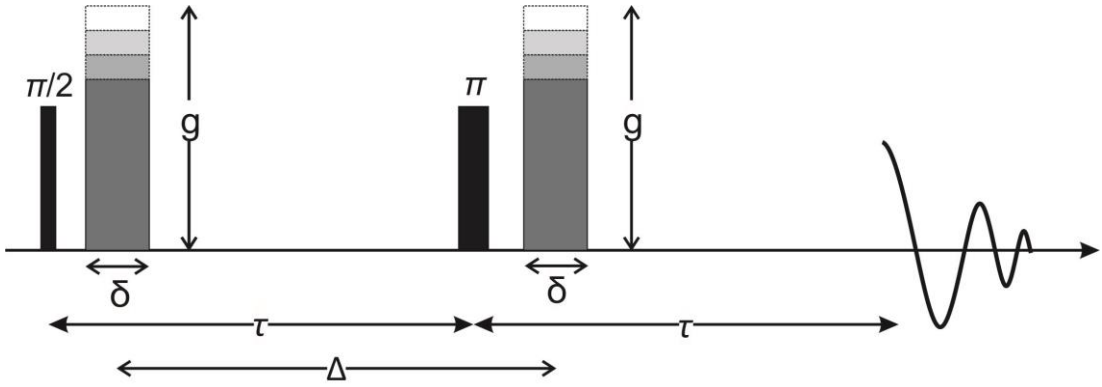

Figure 2.10 Pulse field gradient spin echo (PGSE) sequence (adapted from reference [158]).

PGSE-NMR Experimental protocol

For temperatures below 50 °C, 5 mm glass NMR tubes were filled with approximately 1 cm of molten CB (50 °C), which was then allowed to solidify for at least a week at ambient temperature. For treatments above 50 °C, a glass capillary of 2 mm inner diameter was filled with 0.5 cm of molten CB. This capillary was sealed and inserted in a 5 mm glass NMR tube. This set-up was necessary to reduce convection, which causes an over-estimation of the diffusion coefficient[199, 200].

Self-diffusion coefficients were measured on a Bruker Avance II 400 MHz with a diffusion probe (Diff50). The diffusion time, Δ, was 60 ms, and the pulse gradient duration, δ, was 4 ms for all measurements. Measurements were taken at 35, 37, 40, 50, 60 and 70 °C. The samples were left to equilibrate for 10 min prior to measurements. Temperature was controlled with an accuracy of ±0.1 °C.

Data Analysis

The signal attenuation as a function of gradient, was fitted using the Stejskal-Tanner equation (Equation 11), as shown in Figure 2.11[157, 194, 201]. Diffusion coefficients were determined from the signal intensity measured as the area of the strongest peak in the spectrum, which represents the CH_2 groups within the fatty acid chain (Figure 2.12).

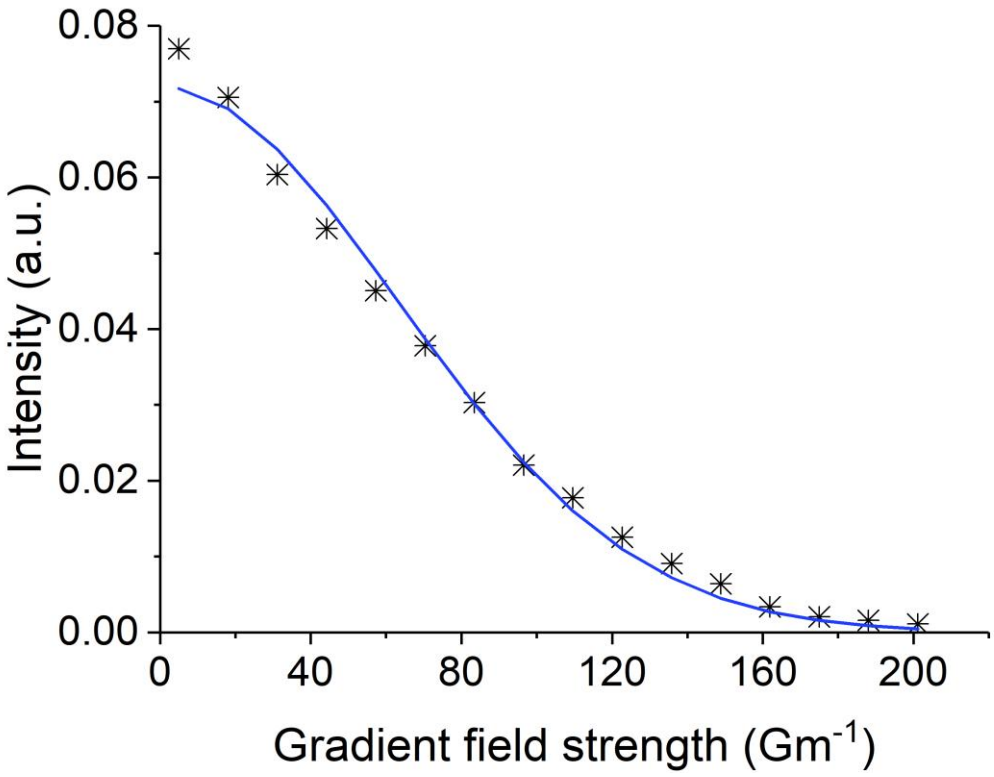

Figure 2.11 Integral intensity vs gradient field strength curve of the ^{1}H-NMR CH_2 peak of cocoa butter at 60 °C. The blue filled circles represent the experimental values, whilst the blue continuous curve represents the fit using equation 11.

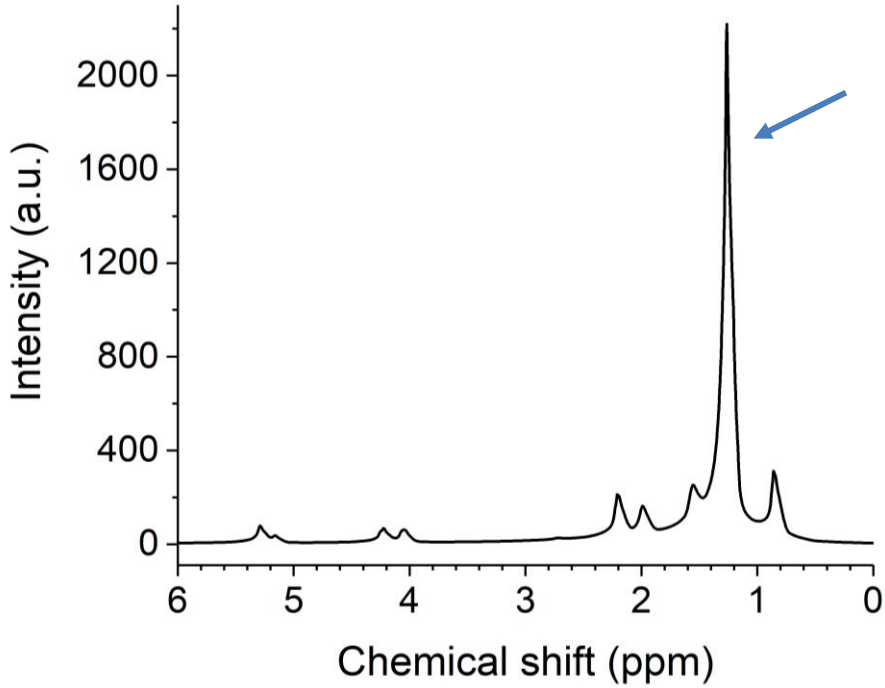

Figure 2.12 ^{1}H-NMR spectrum of CB at 50 °C. The arrow indicates the peak related to the CH_2 groups of the FA chain.

2.5.2 Fast field cycling NMR (FFC-NMR)

An alternative method to measuring diffusion is by the analysis of relaxation data, this was previously hard to achieve as most NMR machines only allow measurements at one specific field, usually above 2 MHz. This is far from ideal as slower molecular motions can only be observed at magnetic strengths of a few kHz. FFC-NMR then presents a solution to this problem as it not only allows for changes in the applied field, but also covers a range from kHz to hundreds of MHz[191, 192, 202].

A standard FFC NMR experiment consists of cycling the Zeeman field, B_o, applied to the sample through three different values (Figure 2.13). First, a high magnetic polarization field, B_{pol}, is applied to pre-polarise the sample to increase signal intensity by achieving magnetization saturation. Then, the sample relaxes in a second field, B_{relax}, for a period τ, allowing the magnetization to reach a new equilibrium. Thirdly, the field is set to a detection value, B_{acq} (acquisition field), that allows the observation of the magnetisation and the FID[191, 202-204] .

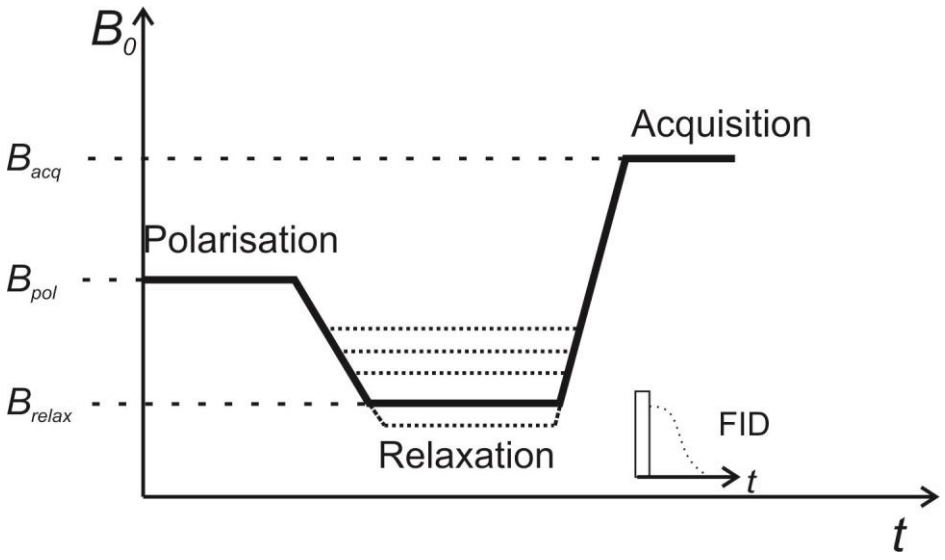

Figure 2.13 Typical FFC-NMR experimental set-up (adapted from [205] and [191]).

It is during the second step that the key processes needed for diffusion measurements occur. As mentioned before, when the field is switched to B_{rel} new equilibrium conditions are reached after the ^{1}H magnetisation decreases in time. This decay is usually exponential, with a time constant referred as the spin-lattice relaxation time T_1. The spin transitions are induced by the fluctuations of magnetic dipole-dipole interactions of both intramolecular and intermolecular proton sites. As such, the measured R_1 is the sum of both contributions.

On the one hand, the intramolecular relaxation is associated with molecular rotation, which changes the vector orientation between the nuclei (protons) within a molecule with respect to the external magnetic field. On the other hand, the intermolecular relaxation the dipole interactions are associated with molecular translation. The previous causes changes in the internuclear axis, as well as in the separation between the different molecules [206].

Previous work applying FFC NMR on edible oils has been limited, and in fact has not explored diffusivity or the impact of temperature, making this experiment the first one of its kind.

Sample preparation and thermal protocol

Glass NMR tubes of 0.8 mm inner diameter were filled with approximately 2.5 cm of West African CB previously molten at 50°C. Samples were then allowed to solidify

for at least a week at ambient conditions prior to measurements. ^{1}H NMRD profiles (R_1 vs. proton Larmor frequencies) were obtained on a Stelar Smartracer FFC NMR Relaxometer (Stelar s.r.l., Mede, PV, Italy) using different thermal treatments as described below.

Samples were heated from 22 °C (minimum temperature reached by the FFC-NMR equipment) to 25, 27, 30, 35, 37 and 40 °C and subsequently to either 50 or 110 °C in 10 °C steps. The sample was then cooled down to 22 °C, following a reversed protocol in cooling direction. Samples were allowed to equilibrate to each temperature for at least 10 minutes on heating, and at least 15 minutes on cooling, prior to any measurements.

The proton spins were submitted to a B_{pol} corresponding to a Larmor frequency ($\nu_L = \omega_L/2\pi$) of 7 MHz for a period of polarization (T_{pol}) of about five times the T_1 estimated at this frequency. Afterwards, the magnetic field was switched to the necessary value (B_{relax}) corresponding to ν_L in the range 0.01–10.0 MHz for a period τ. FIDs were recorded following a single ^{1}H 90° pulse applied at a B_{acq} of 7 MHz. Field-switching time was 2.5 ms, while the spectrometer dead time was 15 to 20 µs. A recycle delay of 0.5 s was always used. A non-polarized FFC sequence was applied when the relaxation magnetic fields were in the range of 10.0-1.6 MHz. A polarized FFC sequence was applied in the proton Larmor frequencies B_{relax} range of 1.6–0.01 MHz.

Data Analysis

Diffusion calculations could only be done above 35 °C during the heating ramp, as below this temperature samples remained solid. This helped to establish the presence or absence of hysteresis in the measured diffusion values between heating and cooling events. Moreover, as the sample did not crystallise immediately on reaching 22 °C after either thermal treatment, it was possible to calculate the diffusion value of CB at such low temperature, and thus, compare the two different treatments.

Diffusion factors were calculated from the obtained R_1 values[206] applying equation 14.

$$R_1(\upsilon) \cong R_1(0) - B\sqrt{\upsilon} = R_1(0) - N\left(\frac{\mu_0}{4\pi}\gamma_H^2\hbar\right)^2\left(\frac{\sqrt{2}+8}{30}\right)\left(\frac{\pi}{D}\right)^{\frac{3}{2}}\sqrt{\upsilon} \quad (14)$$

where υ is the frequency, N the number of nuclei (in this case hydrogen), μ_0 is the magnetic constant, γ_H is the gyromagnetic factor of hydrogen, $\hbar$ is the reduced Planck's constant, and D is the diffusion factor in m^2/s.

From equation 14, it is evident that from the slope of the curve of R_1 vs$\sqrt{\upsilon}$, B can be estimated (Figure 2.14) . From this value, D was estimated using a minimum squares refinement. However, additional information was needed, as N is not available in literature and is defined in equation 15 as

$$N = \rho n/M \quad (15)$$

where ρ is the density, n is the number of hydrogens and M the molar mass. For the last two parameters, an average of the values of the three main TAGs in CB were used, whereas for the density, measurements were performed as described in the following section.

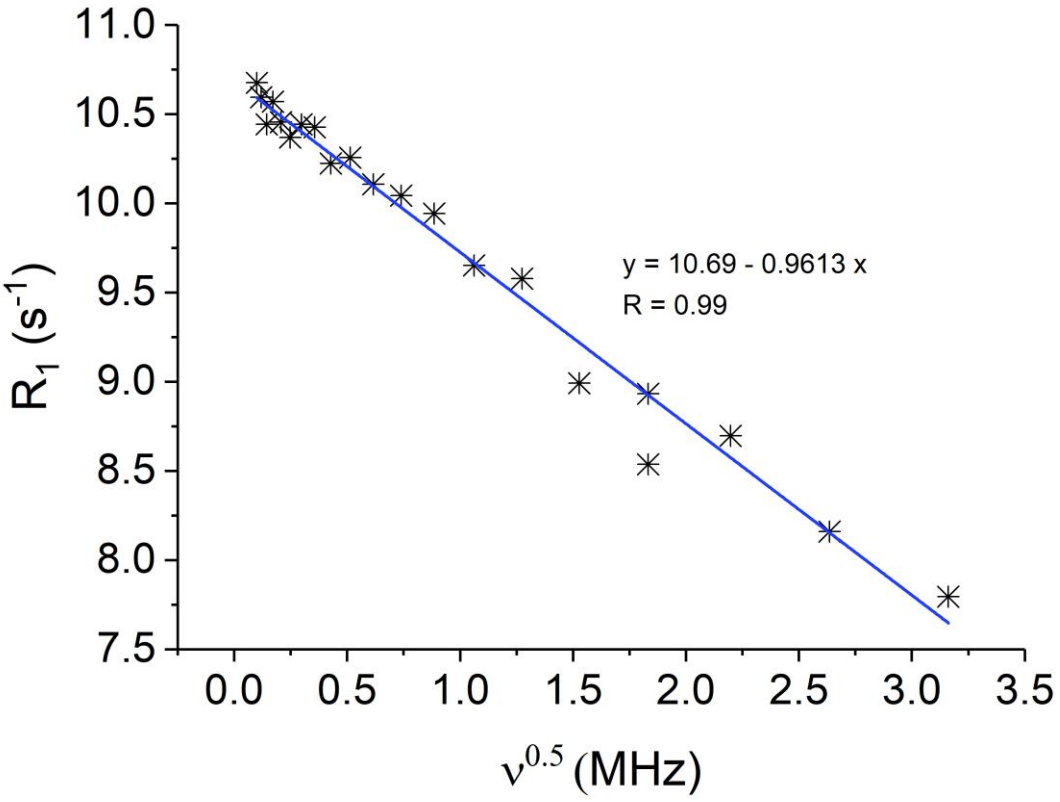

Figure 2.14 R_1 vs $\sqrt{\upsilon}$ of cocoa butter at 35 °C. The full circles correspond to the experimental values, while the solid blue line corresponds to the linear fitting.

Finally, all diffusion factors were plotted against temperature and fitted according to the linearized version of the Arrhenius equation[207] (16):

$$\ln D = \ln D_0 - \frac{Q_d}{RT} \quad (16)$$

where D_o is the pre-exponential factor (m^2/s), which is independent of temperature, Q_d is the activation energy, and R is the ideal gas constant, and to the Vogel-Fulcher-Tammann (VFT) equation (17):

$$\ln D = \ln D_0 - \frac{B}{(T - T_0)} \quad (17)$$

where D_o is the pre-exponential factor (m^2/s), which is independent of temperature, B is a material dependent parameter that can be associated to the activation energy, and T_o is usually interpreted as the ideal glass transition or crystallisation temperature[208, 209].

2.6 Density

As mentioned before, density measurements were indispensable for the calculation of the diffusion factor and compressibility calculations. Hence, the density of CB was measured in a DMA 4500 vibrational density meter (Anton Paar, GmbH, Graz, Austria) at different temperatures: 25, 27, 30, 35, 40, 45, and 47 °C, and from 50 °C to 100 °C in 10 degree steps.

2.7 Speed of sound

Measurements were performed using a ResoScan® instrument (TF-Instruments, Heidelberg, Germany). The ResoScan® system operates based on the resonance technique. It consists of two independent cells with a path length of 7.0 mm. They are embedded into a metal block which is temperature controlled by a Peltier system with a precision of 0.001 °C. Each cell consists of a small cylindrical cavity with a lithium-niobate piezoelectric transducer at each end. One of the transducers transforms the electrical signal into a mechanical force, generating a sound wave, which then travels through the sample and is received by the other transducer. This second transducer has a double function: it transforms the sound wave into an electrical signal, and it also reflects the wave, thus establishing a standing wave pattern (Figure 2.15) [210].

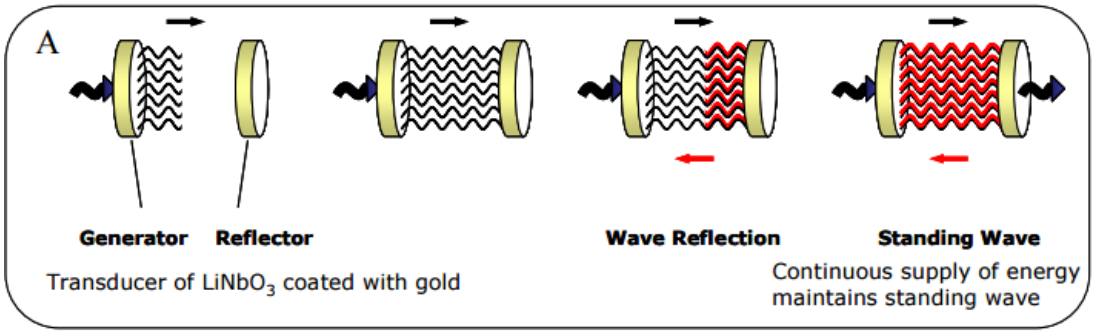

Figure 2.15 Establishment of standing wave between transducers[211].

During initialisation, a frequency range of 7-8 MHz is used, and the amplitudes of the resonance peaks generated are recorded. From these peaks the system automatically selects the optimal "master peak" which is then used as a reference to calculate the ultrasonic velocity and attenuation of the sample. Prior to measurements, the instrument was initialised at 85 °C with a 0.2 mL sample of molten CB. The sample was then cooled down to 25 °C at 300 mK/min, taking measurements every 10 s, using an input of 18 dB.

From these measurements, the compressibility of CB was calculated from the relationship[212] in equation 18:

$$c = \sqrt{\frac{B}{\rho}} \qquad (18)$$

Where c is the speed of sound, B is the bulk modulus defined as the reciprocal of the bulk modulus, and ρ is the density of the material.

It is known that whilst both liquids and solids are not highly deformable, the former are more susceptible to deformations than the latter. Therefore, measuring the compressibility gives an idea of changes in the susceptibility to deformation, even in the liquid, therefore, small structural differences can be inferred from these measurements[165].

2.8 Oxidative stability index

Given that 110 °C is more than twice above the average temperature at which CB is usually melted, it was necessary to check its oxidative stability at such temperature.

This was evaluated through the oxidative stability index (OSI) method, using a Rancimat 743 (Metrohm, AG, Switzerland).

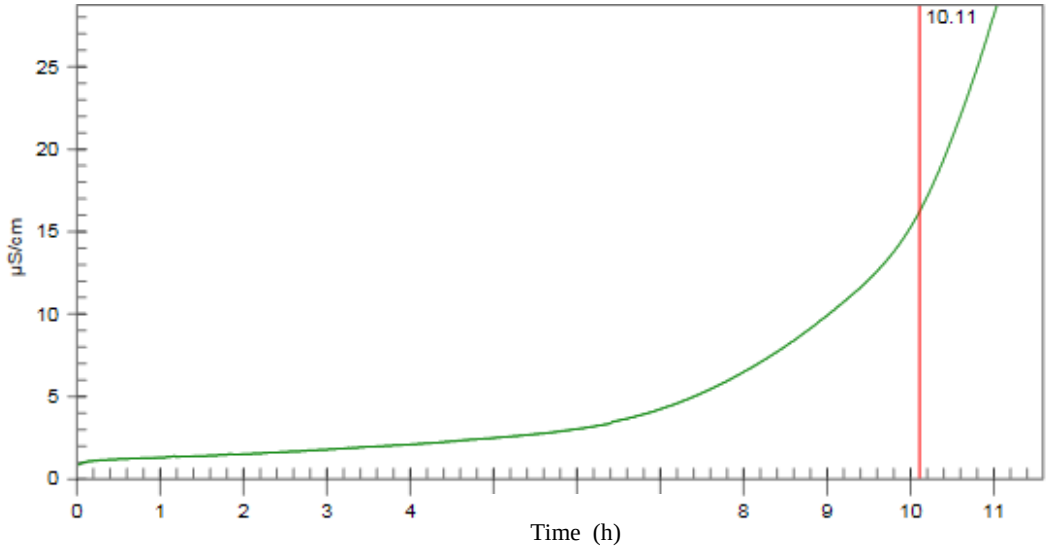

Figure 2.16 Sample curve of OSI determination (conductivity *vs*. time) where the turning point is identified automatically by the Rancimat's software as the maximum peak of the second derivative.

The OSI method [213] relies on heating a sample (3 g ± 0.5 g) of oil or fat through which purified air is pumped at a constant rate (20 L/h). The air coming out of the sample tube is collected and transferred to a container with deionised water, of which the conductivity is monitored continuously. As oil oxidation processes arise and develop, a variety of volatile components, such as formic acid, are formed. These then solubilise with the deionised water, thus changing its conductivity (Figure 2.16). The turning point is then determined through the maximum peak of the second derivative of the conductivity vs. time curve. This point is an indication of the life-time of the product at the conditions used.

2.9 Triacylglycerol analysis

TAG analysis was performed by gas chromatography (GC) by and at Nestlé, Product Technology Centre, York according to the AOAC official Method 986.19 in a GC Agilent 6890 with a FID detector, and an Agilent DB17-hT column (30 m, 0.25 mm, 0.15 µm).

Briefly, the fat samples were initially dissolved in hexane in a 5 mg/mL concentration, from which a 20 µL sample was injected. The temperature protocol used was as

follows: starting from an initial temperature of 200 °C, the temperature was then increased to 325 °C, at a rate of 5 °C/min, and held for 10 min, always maintaining the injector and detector temperatures of 330 and 360 °C, respectively. Identification and quantification of each TAG was performed by comparing the obtained chromatographs (retention times and peak area) to those of the standards.

2.10 Off-line measurements of pressure-treated CB

2.10.1 Sample preparation

For the off-line measurements, CB was treated in a bespoke high-pressure machine with pending patent approval (Figure 2.17). Briefly, it consists of two main connected vessels. The first one is for containing the molten CB, which is then pumped into the heat exchanger, where CB is cooled to the desired temperature, and where hydrostatic pressure can be applied. After the temperature-pressure treatment is finished, the processed CB is pumped out.

The machine was initially heated to 50 °C for at least an hour to melt any remaining solid CB. The cooling vessel was then set at the desired temperature. Once this was reached, approximately 100 g (capacity of heat exchanger) of CB were pumped out, to ensure that only non-treated CB was used for the pressure treatment:

1. Melting of CB at 50 °C in the holding vessel.
2. Pumping of the CB into the heat exchanger pre-set at the crystallisation temperature (T_{cryst}) of 26 or 28 °C, allowing one minute for temperature equilibration.
3. Pressurising of CB to a P_{max} of 100, 200, 400 bar or 600 bar and holding for 1 minute. An additional non-pressurised treatment was performed by holding the CB for an additional minute at the stated T_{cryst}.
4. De-pressurisation.
5. Sampling.

Samples were received in rectangular moulds, from which a sub-sample was taken to fill quartz disposable capillaries, which were then sealed using the same protocol as before. Both sets of samples were transferred to a temperature-controlled incubator

kept at 18 °C for 30 minutes. The capillaries were then immediately put inside the freezer, whereas the moulds had to be left inside a refrigerator at 4 °C for 15 min, so that the samples could be de-moulded and then frozen to prevent polymorphic transformation.

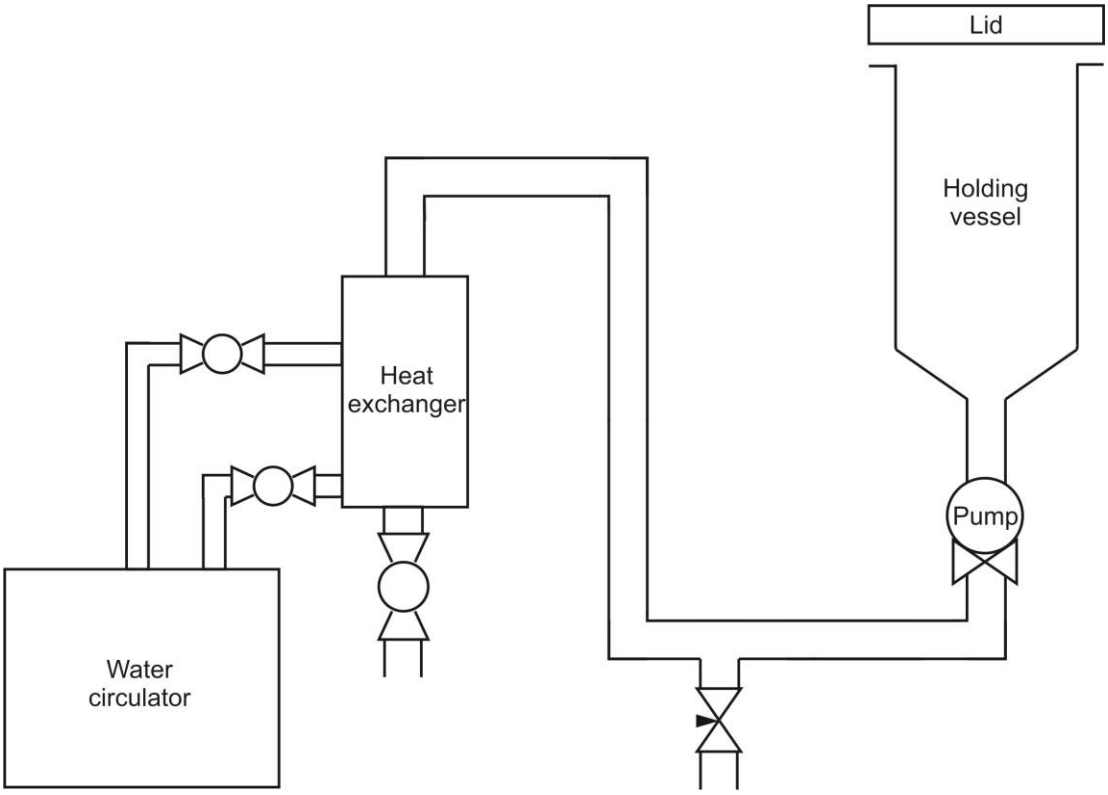

Figure 2.17 Diagram of bespoke temperature/pressure machine, where the holding vessel contains and melts the CB to be further pressure and temperature treated in the heat exchanger.

2.10.2X-ray scattering protocols

Measurements were performed in a SAXSpace machine, as described earlier using the same SDD, and following the same data treatment regarding correction, normalisation and background subtraction.

The frozen capillaries were measured using SAXS/WAXS at 15 °C allowing for 5 minutes to equilibrate in temperature. The exposure time used was of 10 minutes. The resulting X-ray profiles were used to identify the polymorphic structures present in each treatment, based on literature values[20, 121, 123].

2.10.3 DSC protocol and sample preparation

The melting profiles of all samples were analysed using a Diamond DSC with Hyper DSC (Perkin Elmer, UK). Samples of 1.350 ± 0.002 mg sealed between two 30 µL pans were heated from -30 °C to 70 °C at a rate of 50 °C/min. The high heating rate, in comparison to the work of Nightingale *et al.* and Hachiya *et al.*[130, 214], was chosen for being the one currently used in industry to avoid the transition from unstable to stable polymorphs during heating[214]. The melting points were determined from the peak maxima of the thermograms.

2.11 Pressure microscopy

Pressure microscopy studies were performed at the Department of Chemistry of Imperial College London.

Samples were observed with a Nikon Eclipse TE2000-E (Nikon Instruments, Japan) Microscope equipped with a high pressure set-up similar to that used for the pressure cell at Diamond Synchrotron Light Source [215]. However, instead of using a capillary, 0.9 µL of molten CB were placed in a diamond cell with a glass coverslip (Figure 2.18 and 1.16). The temperature was controlled through the circulating water which was also used to pressurise the system. Pictures were taken with an Andor Zyla sCMOS camera (Andor Technology Ltd, Belfast, Northern Ireland) during the pressurising, isobaric, and de-pressurising periods.

Two sub-sets of experiments were performed. The first set was performed following a protocol based on that of the off-line measurements. Molten CB was directly put in the diamond cell, pre-set at one of two crystallisation temperatures (T_{cryst}), 26 or 28 °C. It was then pressurised to one of five different P_{max}, namely atmospheric conditions, 100, 200, 400 or 600 bar and held isobarically for one minute prior to depressurisation. Both pressurisation, and de-pressurisation ramps were applied manually.

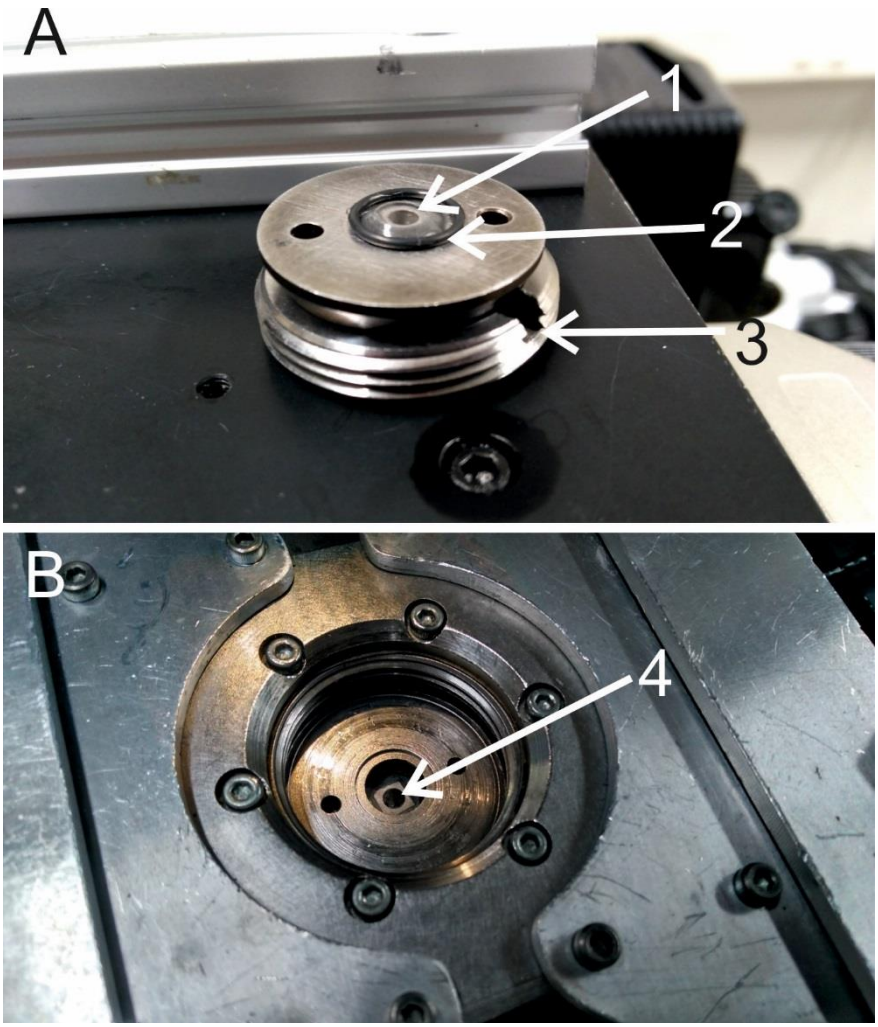

Figure 2.18 Photographs of the pressure sample holder. Figure A shows the upper diamond window, where 1 is the diamond, 2 is the O-ring separating the sample from the pressurising water, and 3 is the fixating ring. Figure B shows the bottom diamond window where the sample is placed on top of the diamond window (4)

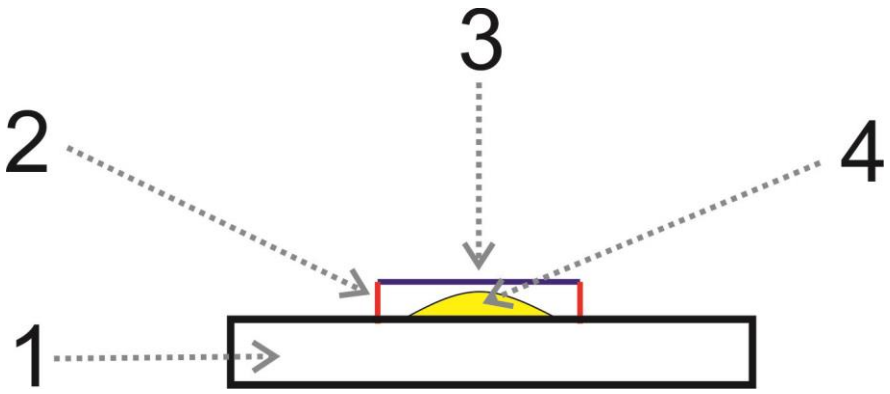

Figure 2.19 Schematic of the sample set-up in the lower diamond window, showing the diamond (1), the double sided sticky tape (2) that is used to hold the glass coverslip (3), and the droplet of sample (4).

It was noticed that manual de-pressurisation took longer than the one observed in the bespoke machine. Therefore, it was decided to perform further experiments where the de-pressurisation was performed with a "jump", i.e., by the opening of a computer-controlled valve that allowed to either drop the pressure completely or to a pre-set value. This allowed to observe the effect of an almost adiabatic de-pressurisation, rather than isothermal de-pressurisation as in the first set.

For this second set, the focus was on the use of a T_{cryst} of 26 °C and a P_{max} of 400 bar. This temperature was selected to ensure a liquid sample from the start, whilst avoiding small crystal generation as would be expected from the use of 24 °C. The 400 bar were selected as it is the maximum pressure expected to be used industrially.

The first experiment consisted of treating the sample at 26 °C and pressurising it to 400 bar and holding the pressure for 2 minutes, followed by depressurisation to ambient temperature. The second experiment consisted of applying a cooling ramp down to 20 °C after pressurising the sample, and finally depressurising the sample. Given that the morphology of a crystal cannot be directly associated with a specific polymorph [67], the crystals obtained after cooling to 20 °C were melted both, before and after the release of pressure, thus permitting the comparison of the effect of pressure on the melting points of the obtained crystal polymorphs.

2.12 *In-situ* X-ray scattering at Diamond Synchrotron Light Source

Simultaneous small- and wide-angle pressure X-ray scattering measurements were undertaken on beamline I22 at Diamond Light Source (DLS) using a wavelength of 0.69 Å.

2 mm disposable capillaries were filled with molten CB (50 °C) and mounted in the custom-built high-pressure cell described elsewhere [215]. Briefly, the cell consists of a stainless-steel body with chemically vapour deposited diamond windows (1 mm thick, 5 mm diameter) which can hold up to 5000 ± 10 bar. Temperature was controlled to ± 0.2 °C using a jacket connected to an external circulator. Temperature in the cell was measured with an accuracy of ± 0.05 °C. An empty disposable capillary was measured at different pressures and used for the background scattering subtraction.

2.12.1 Pressure protocol

A first set of experiments was undertaken using 50 °C as $T_{imax,}$ and three different T_{cryst} were used: 24, 26 and 28 °C, as well as three different P_{max}, 200, 400 and 600 bar, which coincide with the different pressure levels that can be successfully applied with the pressure rig described earlier. Additionally, it was decided to determine if some crystalline memory was retained in the liquid after depressurisation. This was achieved by cooling the fully de-pressurised sample to 15 °C, thus allowing it to re-crystallise. As before, an additional treatment was performed were no pressure was applied, but where the sample was held at the selected T_{cryst} for the equivalent time of the 200 bar treatment.

Prior to starting any experiments, the pressure cell was set at the selected T_{cryst}. Once equilibrium was reached, the capillary, which had been previously held at 50 °C, was inserted and left to equilibrate for 10 min. Then, the pressure was raised in 50 bar steps to the corresponding P_{max}, and held isobarically for 80 s before depressurising in 50 bar steps down to 50 bar. Frames were taken at each pressure step and continuously during the isobaric period, with an exposure time of 1 s. Pressure was then completely released and the temperature of the water circulator was set to 12 °C, resulting in a cooling rate of approximately 0.8 °C/min. Frames were taken with an exposure time of 1 s, every 5 s.

A second set of experiments was performed following a similar protocol as the one described above. Here, the main objective was to determine the impact of using a higher T_{imax} (100 °C) on the pressure-induced crystallisation of CB. For this matter, the same three T_{cryst} as before were studied, but only one P_{max} was selected, i.e 600 bar, as it was identified as the pressure that enhanced crystallisation the most.

A third and final set was undertaken to determine the melting point of the developed crystalline structures. Therefore, the 50 °C treatments using the same three T_{cryst} as before, and 600 bar as P_{max}, were repeated. However, no further cooling was applied in these treatments, but rather the samples were heated to 50 °C with a heating rate of approximately 0.5 °C/min prior to the release of pressure

Chapter 3 Nanostructures of the α-, β'-, β-phases and TAG clusters in the molten state

This chapter has as main objective to familiarise the reader with the different types of lamellar assemblies of CB, depending on the crystalline form – α_1-, α_2-, β'- or β – in which it is present. These smectic lamellar structures are best characterized through the calculation of electron density profiles (EDPs) from selected SAXS patterns of the different polymorphs. However, it should be noted that, as described in the introduction, a level of structuring is also expected in the molten state. Hence, a new model is proposed here which fits the experimental data. Whilst a general description of the model is provided, the reader is referred to the attached manuscript for further details[166].

The α_1-phase EDP was calculated from an X-ray diffraction pattern obtained at Diamond Light Source synchrotron, where five peak orders were observed (Figure 3.1), which is more than what has been previously reported in literature[20, 123, 216], even for pure TAGs such as StOSt[96, 98]. This permitted obtaining a high-quality EDP (Figure 3.2), where the two positive electron density contrast correspond to the glycerol backbones, and the negative one to the methyl trough region of the 2L-layer structure.

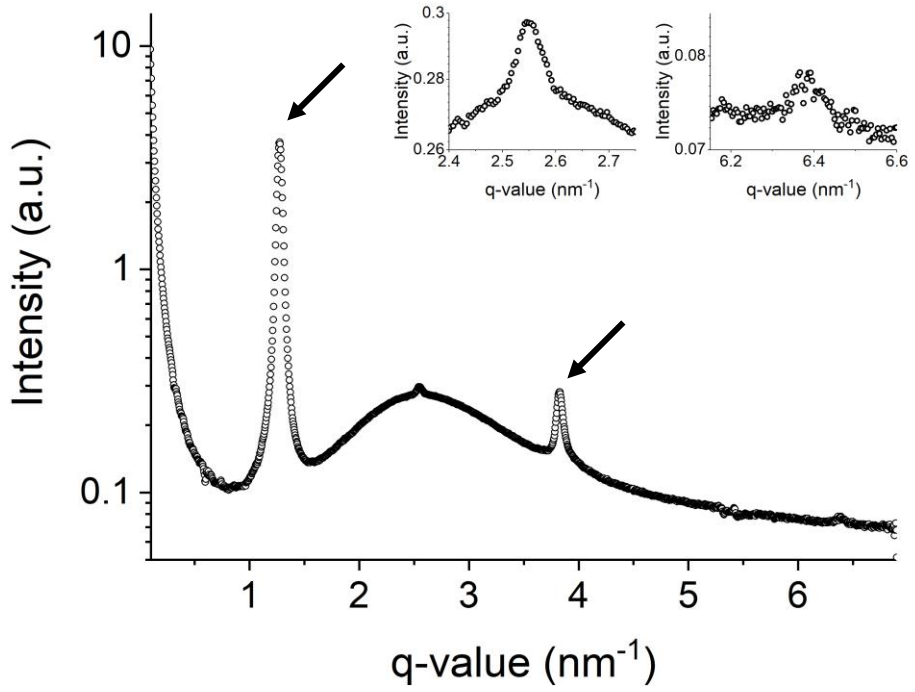

Figure 3.1 Diffraction pattern of the α_1-phase of CB obtained from measurements, where the characteristic 1st and 3rd order peaks are clearly visible (identified by arrows), as well as the 2nd and 5th order (see insets). Adapted from [217].

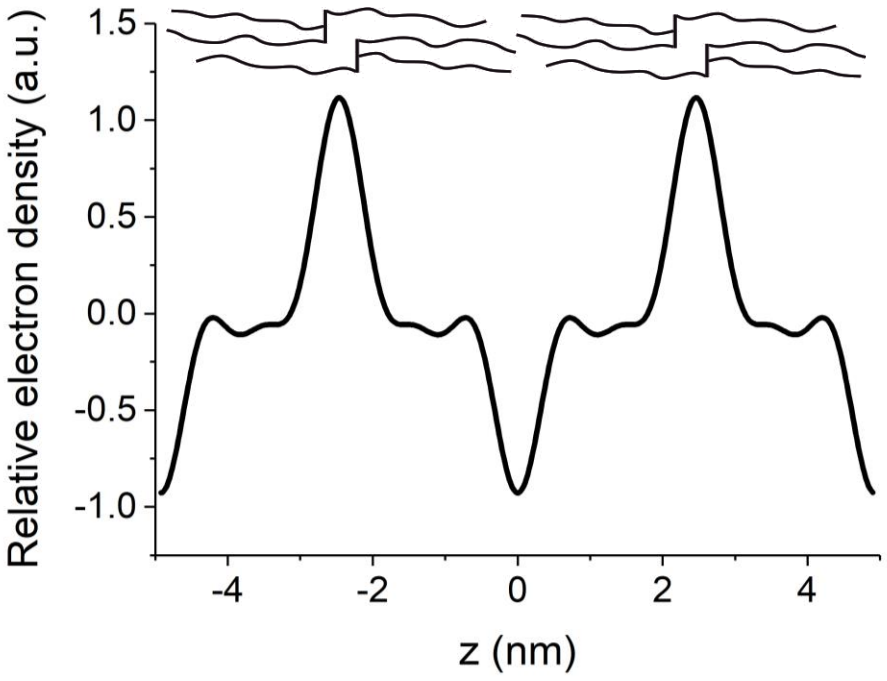

Figure 3.2 Electron density profile of the alpha-1 form. Adapted from [217].

The α_2-phase EDP was calculated from an X-ray diffraction pattern obtained at Diamond Light Source synchrotron, where four peak orders were observed (Figure 3.3), similarly to what has been reported for StOSt[96, 98]. The derived EDP differs from the α_1-phase. It retains a negative electron contrast describing the methyl trough. However, two positive electron contrasts are present, describing the two glycerol backbone regions separated by the oleic acid chain region. Since the oleic acid chains of adjacent TAGs are interdigitating in this regime, the electron density contrast is small as compared to the methyl trough region (Figure 3.4).

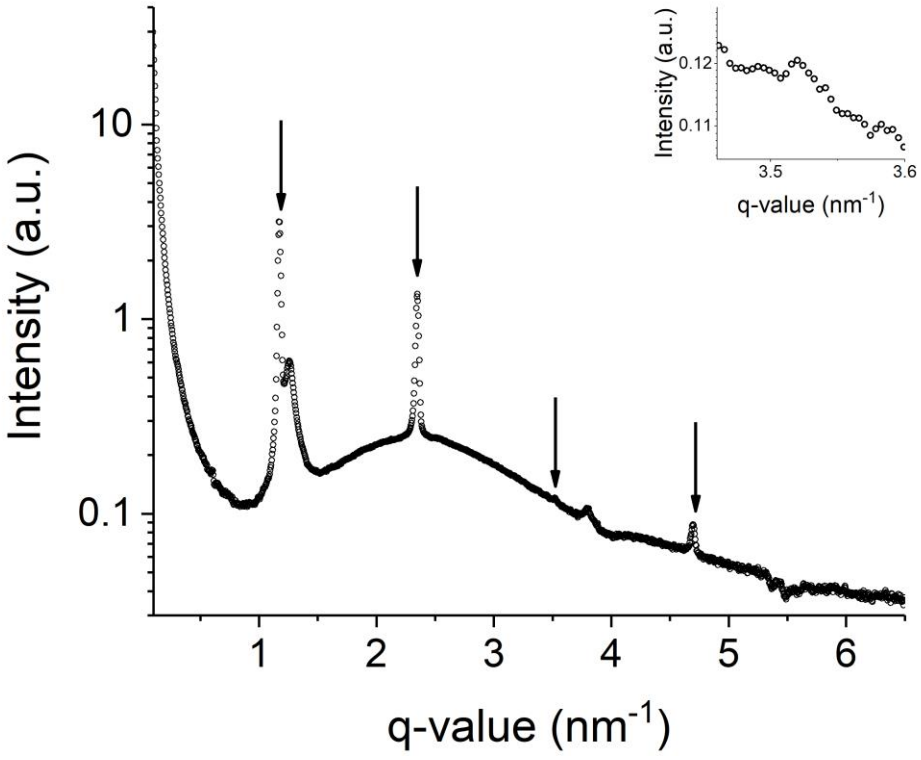

Figure 3.3 Diffraction pattern of the α_2-phase of CB obtained from measurements where the characteristic 1st, 2nd and 4th order peaks are clearly visible (identified by arrows), as well as a small 3rd order peak as shown in the inset.

In the literature[97], it is suggested that either a slightly interdigitated 3L structure of partially molten TAGs or a mixed 2L/3L structure compose the α2-phase of StOSt. However, whilst slight interdigitations could be expected in a fully molten state due to the largely dynamic state of the molecules, as they start self-assembling, the FAs are expected to retain less mobility, thus reducing the possibility of interdigitation. In the case of the mixed 2L/3L structure, the problem lies in the good definition of the α_2-peak, if a mixed layering were too occur, a broadening would be observable,

instead of a well-defined Bragg peak with clear higher order reflections. Therefore, here it is proposed that the TAGs are arranged in a 3L structure, though highly tilted (46.34 ° calculated from the α_1-phase as the only structure with no tilt) with a large amount of synclinical bonds. It is noted that a high degree of tilt would be surprising at this stage of crystallisation; however, this phase is highly unstable, thus allowing the possibility of such transient arrangement.

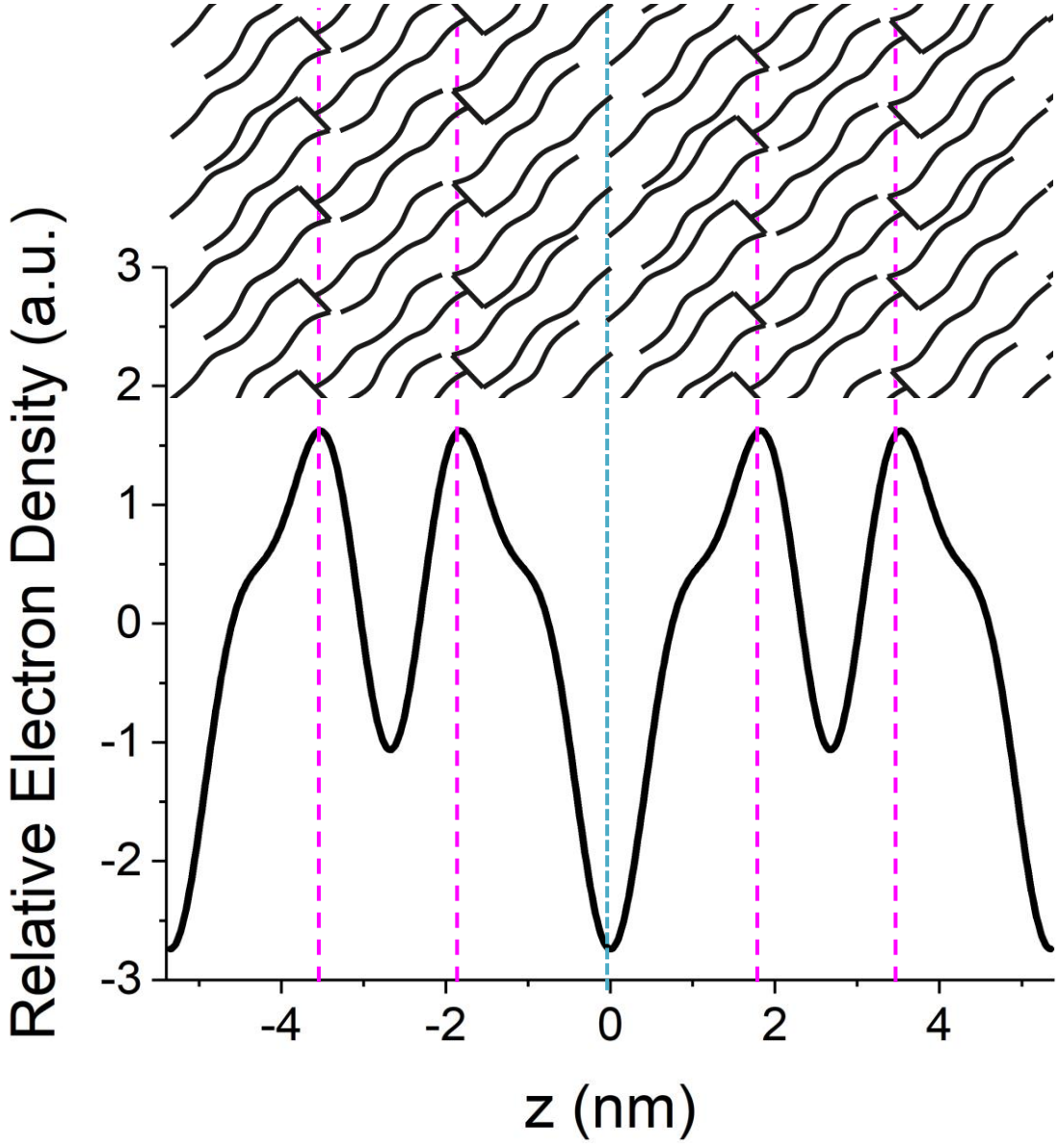

Figure 3.4 Electron density profile of the α_2-phase.

In the case of the β'-phase, only three peak orders were observable, 1st, 3rd, and 5th orders (Figure 3.5). Note, the second and fourth order Bragg diffraction peak being practically zero, signifies a very low electron density contrast at a repeat distance of *d*/2 and *d*/4, respectively. Figure 3.5). Whilst this is usually deemed insufficient for

the application of a standard Fourier Transform approach[174], in reality, it is considered that the scattering pattern actually provides information of four peak orders, rather than three, hence making the application of this method possible. This is inferred from the α-phase pattern, which has a considerably higher resolution and still does not show a 4th order peak, thus confirming that this 4th order truly has a form factor of zero. Given the strong similarity between the α- and β'-form lamellar structures, it is possible to assume that the same applies for the β'-form.

The resulting EDP is essentially the same as that of the α-phase (Figure 3.6), though the *d*-spacing is smaller (4.46 nm *vs.* 4.93 nm of the α-phase), as expected from the tilting of the TAG molecules in the β'-phase. From the *d*-spacing of a non-tilted lamellar structure, 4.93 nm (α-phase), it derives that the TAG molecules in the β'-phase are tilted at an angle of 25°.

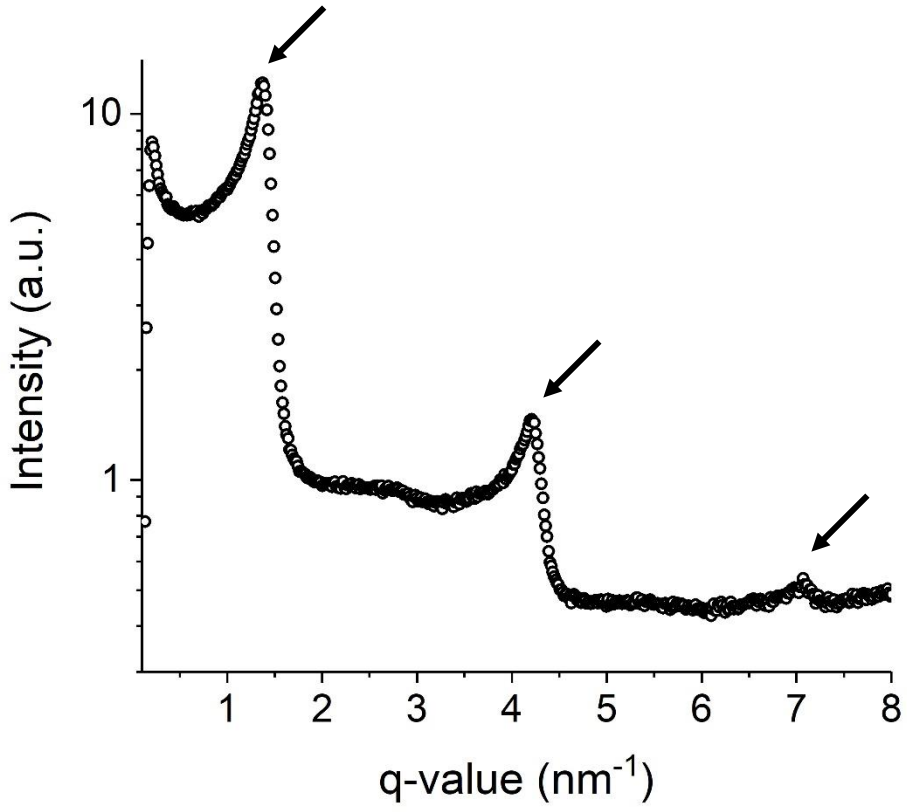

Figure 3.5 Diffraction pattern of the β'-phase of CB obtained from measurements where the characteristic 1st, 3rd and 5th order peaks are clearly visible (identified by arrows). Note, that regardless of the de-smearing procedure, this is not perfect and still modifies the shape of the peaks.

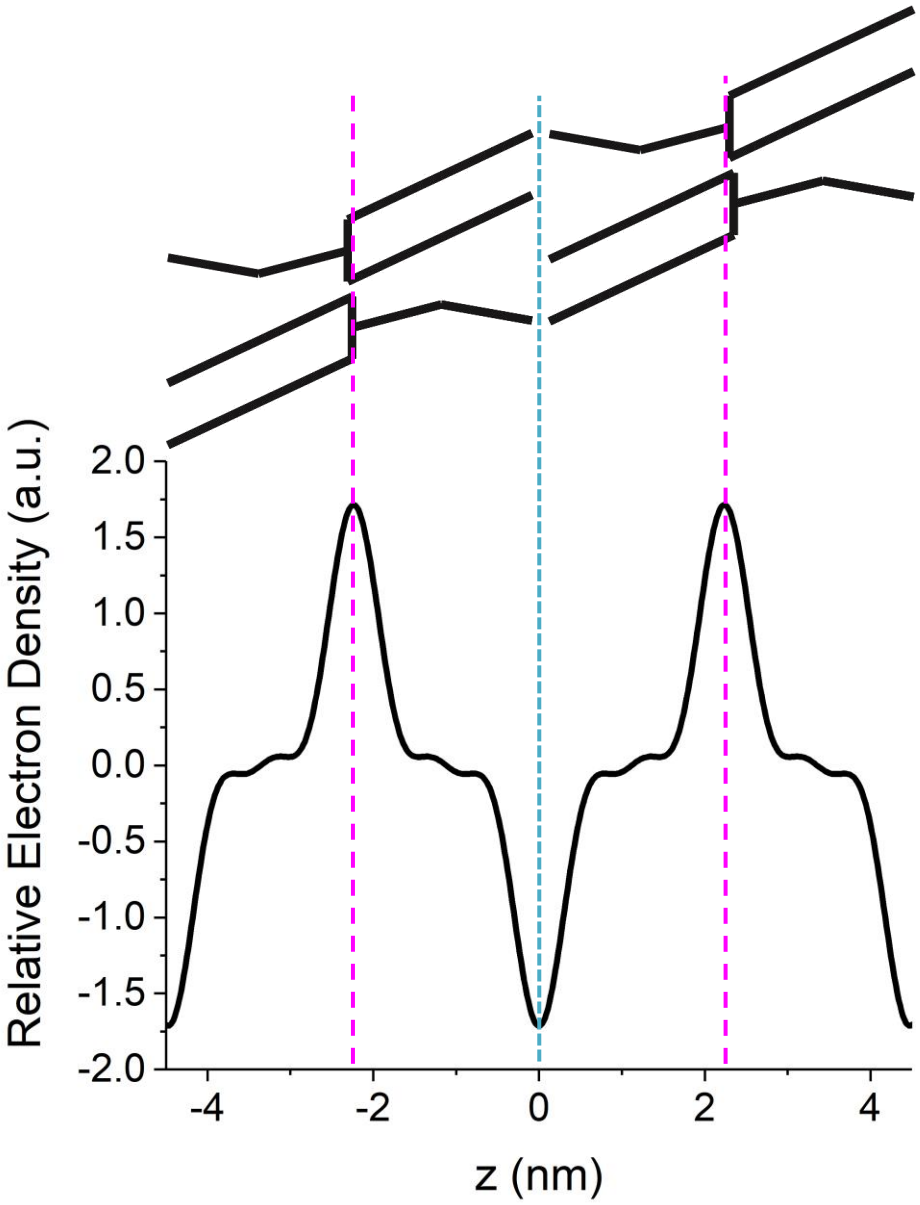

Figure 3.6 Electron density profile of the β'-form. At the top of the EDP the arrangement of the TAG molecules is displayed with their, in correspondence with their electron density.

In the case of the β-phase, more diffraction peaks were observable, as would be expected from its stability derived from a perfected crystalline structure (Figure 3.7). The derived EDP differs from the α_2- and β'-phases, as its lamellar structure corresponds to a 3-L structure. This EDP retains a negative electron contrast describing the methyl trough. However, similarly to the α_2-phase, two positive electron contrasts are present describing the two glycerol backbone regions separated by the oleic acid chain region. Since the oleic acid chains of adjacent TAGs are interdigitating in this regime, the electron density contrast is small as compared to the methyl trough region (Figure 3.8).

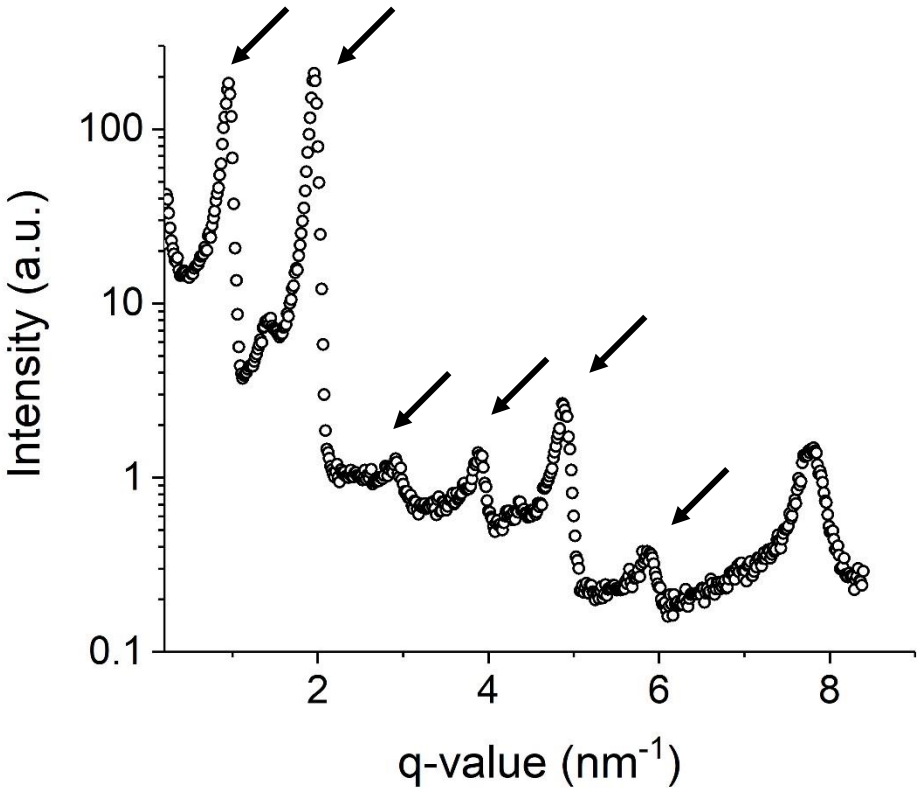

Figure 3.7 Diffraction pattern of the β-V form of CB. The characteristic peaks are identified with arrows. The peak between the 1st and 2nd orders is expected to be caused by remaining 2L structures of either the β'-form or, more likely, the fully saturated TAG species[97]. Note that regardless of the de-smearing procedure, this is not perfect and still modifies the shape of the peaks.

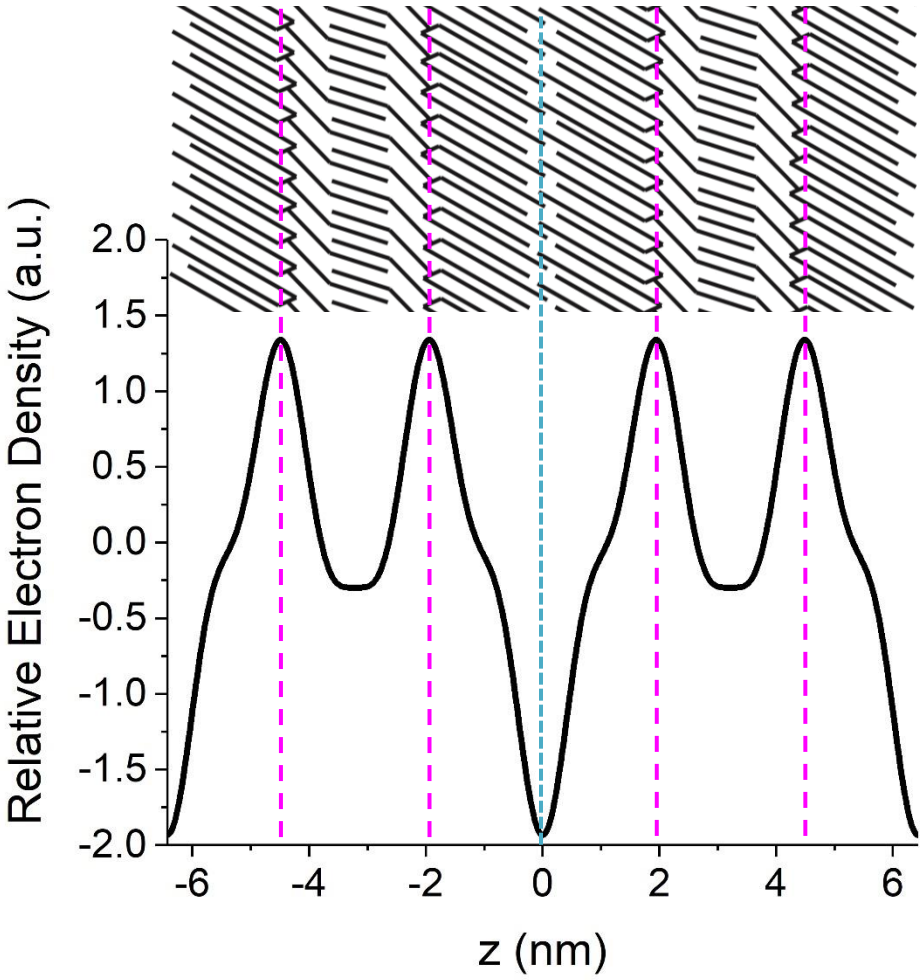

Figure 3.8 Electron density profile of the β-V form of CB. At the top of the EDP the arrangement of the TAG molecules is displayed, in correspondence with their electron density. The TAG structure is presented with its characteristic tilt of 63-66 ° (saturated FA chains), and an angle of 32-39 ° for the oleoyl chain (on the side of the glycerol backbone)[218].

All obtained form factor values and their corresponding phases of the α- β'- and β-phases are summarized in Table 3.1.

Table 3.1 Normalised form factors calculated from the peak intensities of the Bragg peaks of the three main cocoa butter polymorphs.

h	α_h^{217} (α_1)	F_h/F_1^{217} (α_1)	α_h (α_2)	F_h/F_2* (α_2)	α_h (β')	F_h/F_1 (β')	α_h (β)	F_h/F_2* (β)
1	-1	1.0000	-1	0.7421	-1	1.0000	-1	0.6871
2	+1	0.1724	-1	1.0000	---	---	-1	1.0000
3	-1	0.6326	+1	0.1196	-1	0.5332	+1	0.1234
4	---	---	-1	0.4116	---	---	-1	0.1159
5	-1	0.2376	---	---	-1	0.1800	-1	0.2534

* Note that for the α_2- and β-phases, it is the second order peak having the highest intensity.

As mentioned before, the best combination of phases for the first three peak orders of the α-phase, and for all the peak orders of the β-phase were taken from[97]. For the β'-phase, only three peak orders were obtained, and the assigned phases are equivalent to those of the α-phase, which is not surprising given the similarity between the two structures.

From the EDPs above, different parameters can be obtained (Figure 3.9 and Table 3.2) such as the *d*-spacing, the density ratio (ρ_R) between the density of the glycerol backbones (ρ_c) and the methyl trough (ρ_G), as well as the distribution breadth of both electron density contrasts, σ_c and σ_G for the methyl trough and glycerol backbone, respectively, as shown in Figure 3.9.

Table 3.2 Deduced structural parameters of the different phases of CB at 20 °C.

Parameter	**α_1-phase[217]**	**α_2-phase**	**β'-phase**	**β-phase**
d-spacing (nm)	4.93±0.01	5.35±0.06	4.46±0.01	6.43±0.09
z_G (nm)	2.47±0.005	1.83±0.005	2.23±0.005	1.95±0.005
σ_G (nm)	0.28±0.11	0.25±0.10	0.27±0.13	0.33±0.15
σ_C (nm)	0.24±0.10	0.33 ±0.12	0.25±0.12	0.36±0.15
ρ_R	0.82±0.10	0.59±0.01	1.00±0.10	0.69±0.10

As mentioned earlier, the α- and β'-phases have very similar *d*-spacings, the small difference being caused by the FA chains being slightly tilted (25 °) in the β'-phase. The β-phase, as expected, has the largest *d*-spacing, as it corresponds to a 3-L structure. These results are in good agreement with the estimated values of StOSt by Mykhaylyk97, 98 who observed a *d*-spacing of 6.45 nm, and an inter-glycerol distance, Z_{GG}, of 2.36 nm for the β-phase. In addition, the β-phase has the lowest ρ_R of all treatments, which is expected, as its ρ_G results from one glycerol backbone only.

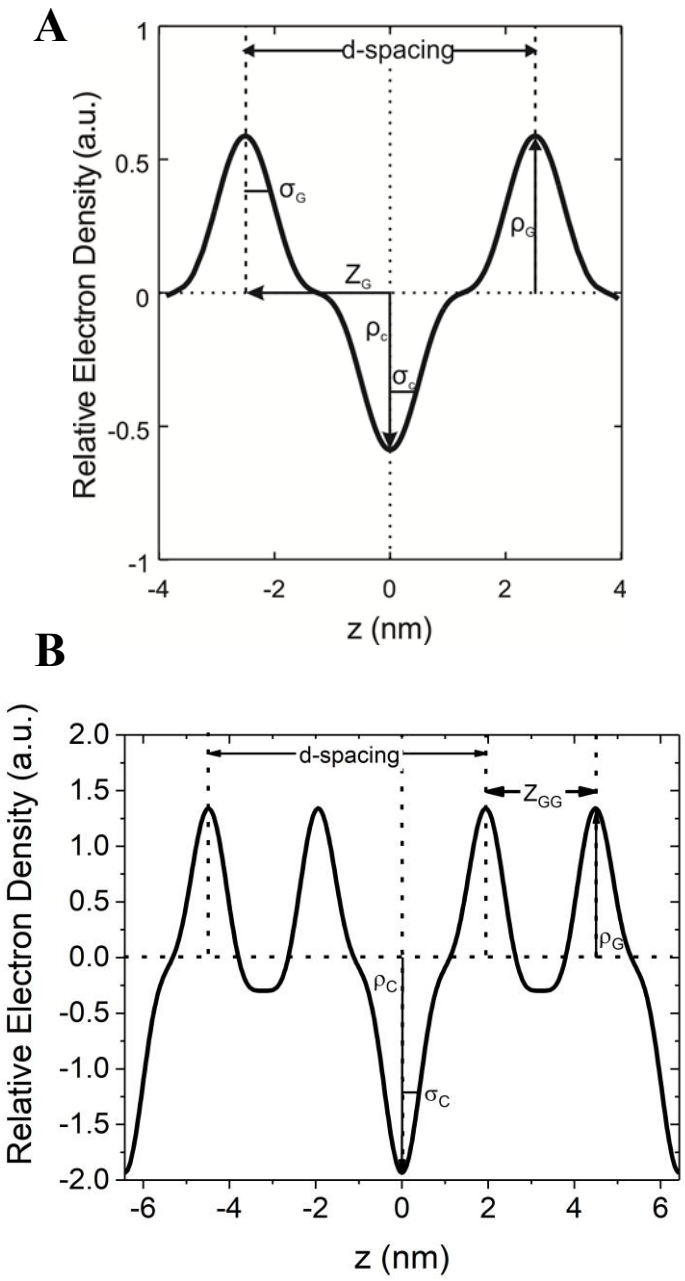

Figure 3.9 Parameters describing a two-Gaussian EDP model of the (A) α- and β'-polymorphs of CB. The 'positive' Gaussian at position $\pm z_G$ (width σ_G) with an amplitude of ρ_G represents the glycerol backbone region and the 'negative' Gaussian (width σ_C) centred at zero models the hydrocarbon chain region (taken from reference [217]). Figure B shows the EDP of the β-polymorph, which again could be described by a two-Gaussian model, with the difference, however, the neighbouring glycerol backbone regions are not overlapping but separated by the distance Z_{GG}. In this respect note, that the electron density contrast of the glycerol backbone region in the β-phase is reduced, when compared to the β'-phase.

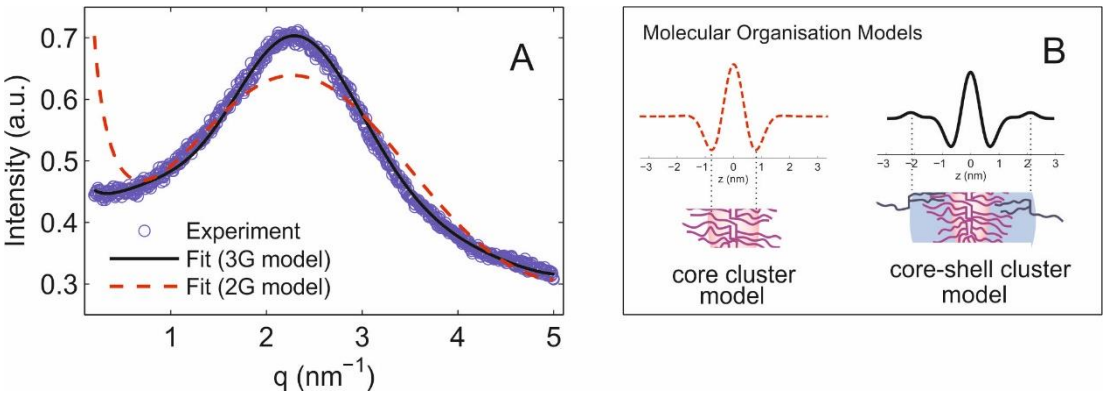

Figure 3.10 A) Experimental SAXS pattern from molten TAGs at 110 °C (blue circles) and the simulated scattering profile with 2-Gaussian (dashed line and left hand diagram in B) and 3-Gaussian form factor model (solid line and right hand diagram in B). B) the electron density distribution curves are represented together with the corresponding molecular cluster model schemes. Taken from ref. [166]

Lastly, we draw attention to model the liquid phase of CB. As can be seen in Figure 3.10 A (black curve), our proposed TAG cluster model fits the experimental data perfectly (see details in Materials and Methods). Moreover, it is noted that an additional model was also attempted which retained the core cluster of TAGs, but without considering loosely attached TAG molecules which are represented by the 3rd Gaussian term in the final model (Figure 3.10 B, left hand side). This model does not fit the experimental data well, resulting in a depressed intensity of the broad peak, and an excess intensity in the area below 0.5nm^{-1} (Figure 3.10 A dashed red line). This strengthens the hypothesis that the clusters have an additional layer or "shell" of loosely attached TAGs.

This outer shell is expected to lead to the crystallisation of CB, as it increased its coverage as temperature decreased[166]. Thus, if insufficient temperature is applied, it could contribute to the memory effect, defined as the presence of small crystallites that promote nucleation, but are too small to be detectable by experimental techniques, or even templating of the crystalline structure. However, under adequate heating conditions, the degree of occupancy is expected to decrease to such extent that templating would not be present, and the memory effect reduced, but rather would only act as heterogeneous nuclei. In other words, the liquid structures would then help reduce the surface energy barrier, but as they are not considered crystalline material, then they cannot be considered as promoters of crystal memory.

Chapter 4 Effect of thermal pre-treatment on the isothermal crystallisation of cocoa butter

4.1 Results

4.1.1 Triacylglycerol analysis

Table 4.1 Triacylglycerol composition (g/100g) of the West African CB used in this work, compared to a similar West African CB, a fast (Malaysia) and a slow (Brazil) crystallising CBs[154].

TAG	This work	West African	Malaysia	Brazil
POSt	40.15 ± 0.49	41.3	40.7	38.7
StOSt	28.55 ± 0.49	25.5	25.9	23.8
POP	16.15 ± 0.07	17.7	17.8	17
PLSt	2.85 ± 0.21	2.86	2.67	2.97
StOO	2.5 ± 0.28	3.01	2.82	5.96
POO	1.8 ± 0.10	2.29	2.38	5.02
PLP	1.6 ± 0.14	1.61	1.84	2.18
StOA	1.1 ± 0.14	1.21	1.32	1.1
PStSt	0.8 ± 0.0	0.65	1.03	0.32
PPSt	0.7 ± 0.0	0.89	0.84	0.58
MOP	0.3 ± 0.14	0.22	0.20	0.21
StStSt	0.3 ± 0.0	0.78	0.56	0.24
PLO	0.25 ± 0.07	0.43	0.49	0.34
PPP	0.2 ± 0.0	0.22	0.22	0.26
StLS+OOO+StLO	1.8 ± 0.1	1.33	1.29	1.38

P – palmitic acid; O – oleic acid; St – Stearic acid; M – myristic acid; L – linoleic acid; A – arachidonic acid

Overall, the CB used in this thesis is similar to that used by Foubert *et al.* [154] However, it has a slightly higher content of StOSt and PStSt, and a lower content of di-unsaturated TAGs (StOO, POO, and PLO). Therefore, it is likely that its crystallising

behaviour is closer to faster crystallising CBs[17, 154, 170] such as that from Malaysia. Nevertheless, it is not possible to disregard the relevance of minor components which were not analysed in this thesis, but would help obtain a further understanding of the mechanisms at play in the crystallisation of CB. These minor components are primarily free FAs, and phospholipids. The former has already been observed to affect the crystallisation kinetics of CB by Foubert [15], fully saturated FAs result in faster induction times, whilst the opposite is observed for higher concentrations of unsaturated FAs. The effect of phospholipids inherent to CB is not yet fully understood, partially because most literature only focuses on the analysis of phosphorus, and it has been made evident by Arruda and Dimick[131], that the type of phospholipid and FA composition is relevant, rather than the amount in which they are present.

4.1.2 X-ray scattering measurements

From the contour plots in Figure 4.1 it is possible to observe that both the 50 and 80 °C treatments behaved in a similar fashion following the usual step-wise crystallisation: first crystallising into the α-form (within the first 15 min), followed by transformation into β'-IV form, which eventually started transforming into the β-V. Contrariwise, the 110 °C treatment started crystallising after approximately 115 min (Figure 4.2), time at which a broad hump appeared covering the range of the three different spacings of the different polymorphs. Importantly, whilst the behaviour of the first four hours was confirmed by at least one repetition (± 10 min), the long-term behaviour was only performed once, therefore, further repeats would be advisable to confirm the transformation into the β-VI polymorph.

Whilst a general behaviour of the treatments could be obtained through the contour plots, a more detailed analysis (see Methods section) was required to obtain more accurate times of appearance and disappearance of the different polymorphs (Figure 4.2). This is particularly important for the identification of the β-VI form as it has a diffraction pattern very similar to that of β-V (Figure 4.2). From this more detailed analysis, minor but relevant differences between the 50 and 80 °C treatments were observed. Firstly, in the small-angle, the α-form of the 80 °C treatment had a longer life-time. Secondly, in the wide-angle regime, the 50 °C treatment developed the

characteristic α-phase peak within the first 15 minutes, whilst the 80 °C treatment, displayed a short delay and only started developing such peak after 25 minutes. Whilst the differences between the 50 and 80 °C treatments, at this stage, could be attributed to the stochastic nature of CB crystallisation, it is not the case of the 110 °C which presented a different behaviour to both 50 and 80 °C treatments, therefore raising the question of the mechanisms behind it.

By pre-treating CB to 110 °C, the development of well-defined Bragg peaks was delayed considerably, appearing only after more than an hour. Nevertheless it should be noted that almost from the first frame, a low intensity, broad hump that covered the range of the three main polymorphs was evident, suggesting a large variability of stackings. This hump eventually resolved into two peaks corresponding to the α- and β'-forms. In the WAXS region, no evidence of the α-phase was found, but rather direct formation of the β'-phase orthorhombic subcell was observed, which is not expected at this temperature[20, 154, 219]. Nevertheless, given that the α-phase peak (4.24 Å) is very close to one of the β'-phase (4.25 Å) it is possible that the higher intensity of the latter does not allow the correct visualisation of the former.

In the 50 °C treatment the β'-form SAXS peaks developed within the hour, whilst in the 80 °C treatment they appeared after 75 minutes. In both cases, the WAXS peaks developed alongside those in the SAXS region, in contrast with the 110 °C treatment, where the WAXS peaks developed at a later stage.

Interestingly, the development of the β-V form followed a different behaviour than that of the other polymorphs. Here, the treatment that developed this phase the fastest, in both the SAXS and WAXS regimes, was the 110 °C treatment, followed by the 80 °C one, and finally the 50 °C one. In the case of the 110 °C treatment, the WAXS peaks developed at a similar time to the SAXS ones, whilst the 50 and 80 °C treatments showed a slight delay, thus indicating that for the development of the sub-cell of the β-V, the 3-L lamellar arrangement must first be stabilised, and a higher amount of the other (2-L) phases hinders such sub-packing. Moreover, the development of the β-VI form was depressed when a T_{imax} above 50 °C was used, especially on applying 80 °C.

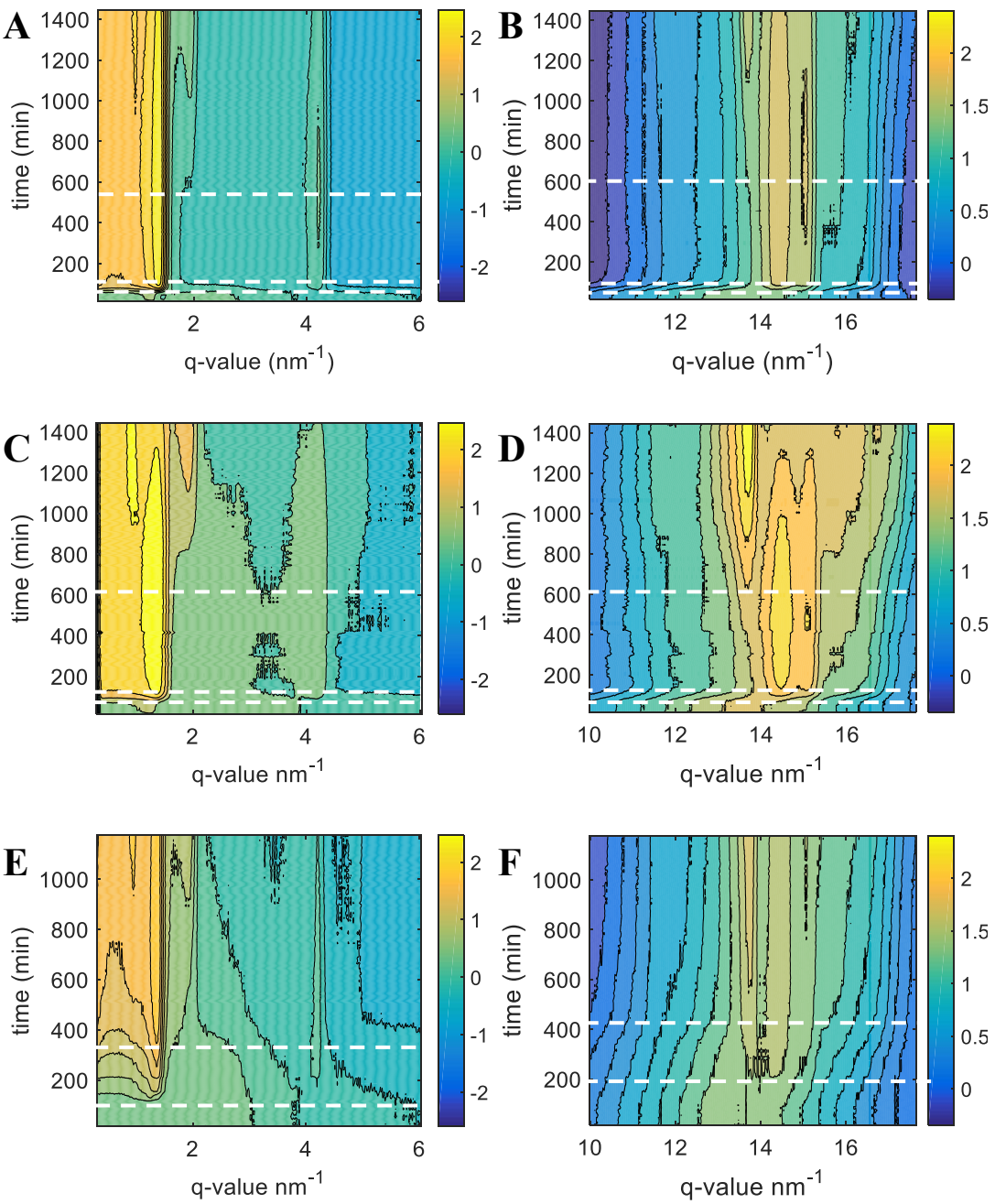

Figure 4.1 Contour plots of the isothermal crystallisation SAXS (A, C, E) and WAXS (B, D, F) scattering patterns of the three treatments: 50 (A, B), 80 (C, D) and 110 °C (E, F). The intensity of the patterns is in the z axis and is represented in the log scale. In the 50 and 80 °C, the dashed white lines divide the plot in four main areas, indicating the presence of the α-form, a mix of the α- and β'-forms, the β'-form, and a mix of the β'- and the β-V form, from top to bottom. In the case of the 110 °C treatment, the first region corresponds to the liquid phase, followed by a mix of the α- and β'-phases, and finally a mix of the β'- and β-V phases.

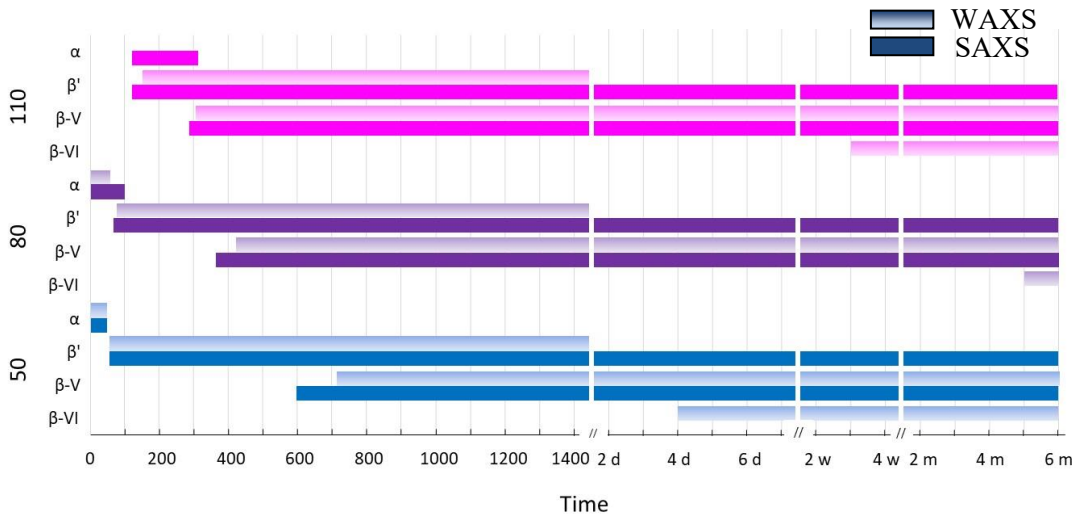

Figure 4.2 Time ranges of presence of the different polymorphs as observed by SAXS (filled rectangles) and WAXS (gradient rectangles) in the three different T_{imax} treatments: 50 (blue), 80 (purple) and 110 °C (pink). Note should be taken that for the β-VI polymorph, the SAXS peak is not being reported as it cannot be distinguished from that of the β-V. Time is represented in minutes in the first section of the graph, d represents days; w, weeks; m, months.

Overall, there was a difference in the induction of crystallisation and polymorph transformation between the three different treatments. When higher temperatures were used, an increased time of induction of the metastable phases and the β-VI polymorph was obtained, as evidenced by the slower appearance and/or definition of both the SAXS and WAXS region peaks. In contrast, the β-V developed faster with higher T_{imax}, resulting in an increased stability of such form, thus slowing down the development of the β-VI polymorph.

Besides the crystallisation times and polymorphic transformations, the changes of the d-spacings (calculated from the first-order peak position) of the three main polymorphs was tracked through the isothermal period (Figure 4.3). Note should be taken that no differentiation is made between different β'- or β-forms, because only the β'-IV was observed in these treatments, whilst the β-V and β-VI share the same d-spacing.

In all treatments the α-phase had a consistent spacing, the slight decrease observed particularly in the 80 °C treatment (Figure 4.3 C) is likely caused by the strong overlap between the α- and β'-form peaks. The β'-form peak decreased slightly through time, possibly due to tilting. Regarding the small fluctuations observed after 24 h, they are thought to be caused by the capillary having slightly different positions at each measurement. Yet, in all cases, values were of approximately 4.6 nm after one day,

whilst after a month they were closer to 4.4 nm (Figure 4.3 B, D and F). This behaviour is similar in all different treatments.

In contrast, the d-spacing of the β-form had a different behaviour depending on the T_{imax} used. The first observable difference between treatments is that the initial d-spacing increased along with the $T_{imax.}$ Moreover, the d-spacing of the 50 and 80 °C treatments (Figure 4.3 A-D) increased as crystallisation progressed, until an average value of 6.6 nm was reached. In the 110 °C treatment (Figure 4.3 E and F), however, the initial value was close to 6.6 nm and remained constant as crystallisation continued.

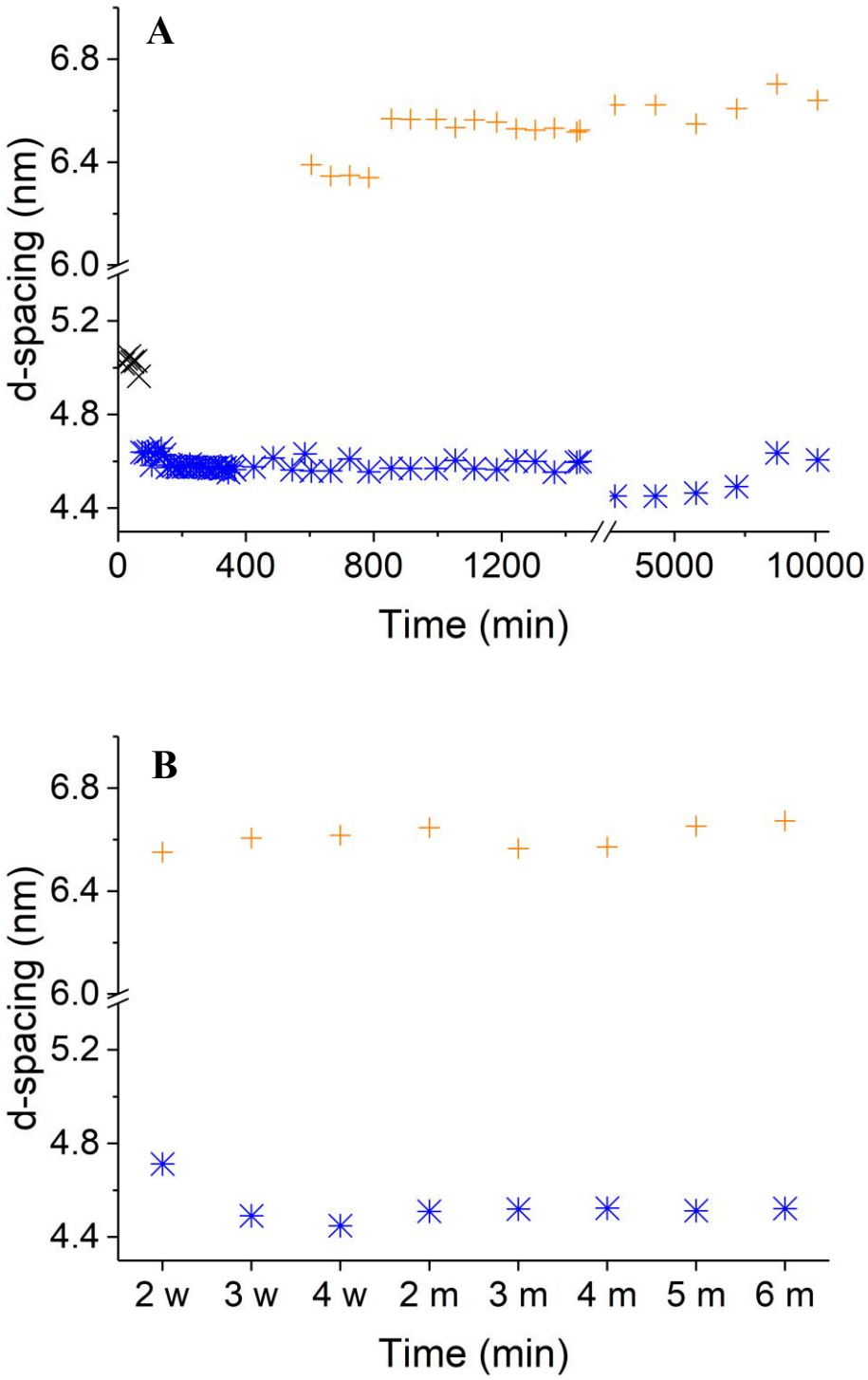

Figure 4.3 d-spacings of the three main polymorphs observed during the isothermal crystallisation of thermally pre-treated CB at 50 °C during the first week (A) and from two weeks to six months (B). Colour key: α-phase –black (X), β'-blue (*), β-orange (+).

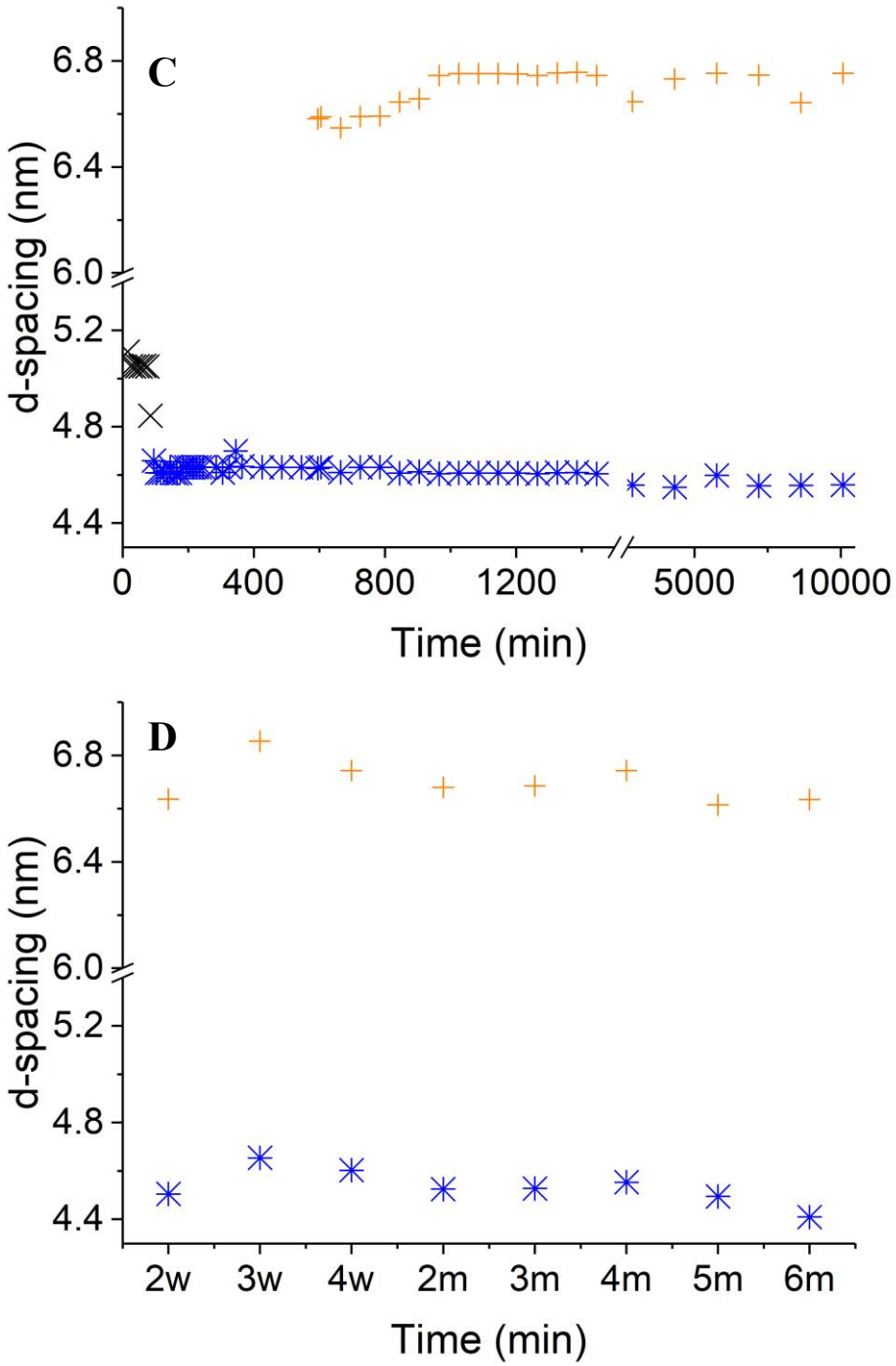

Figure 4.3 (Cont.) d-spacings of the three main polymorphs observed during the isothermal crystallisation of thermally pre-treated CB at 80 °C during the first week (C) and from two weeks to six months (D). Colour key: α-phase –black (X), β'-blue (*), β-orange (+).

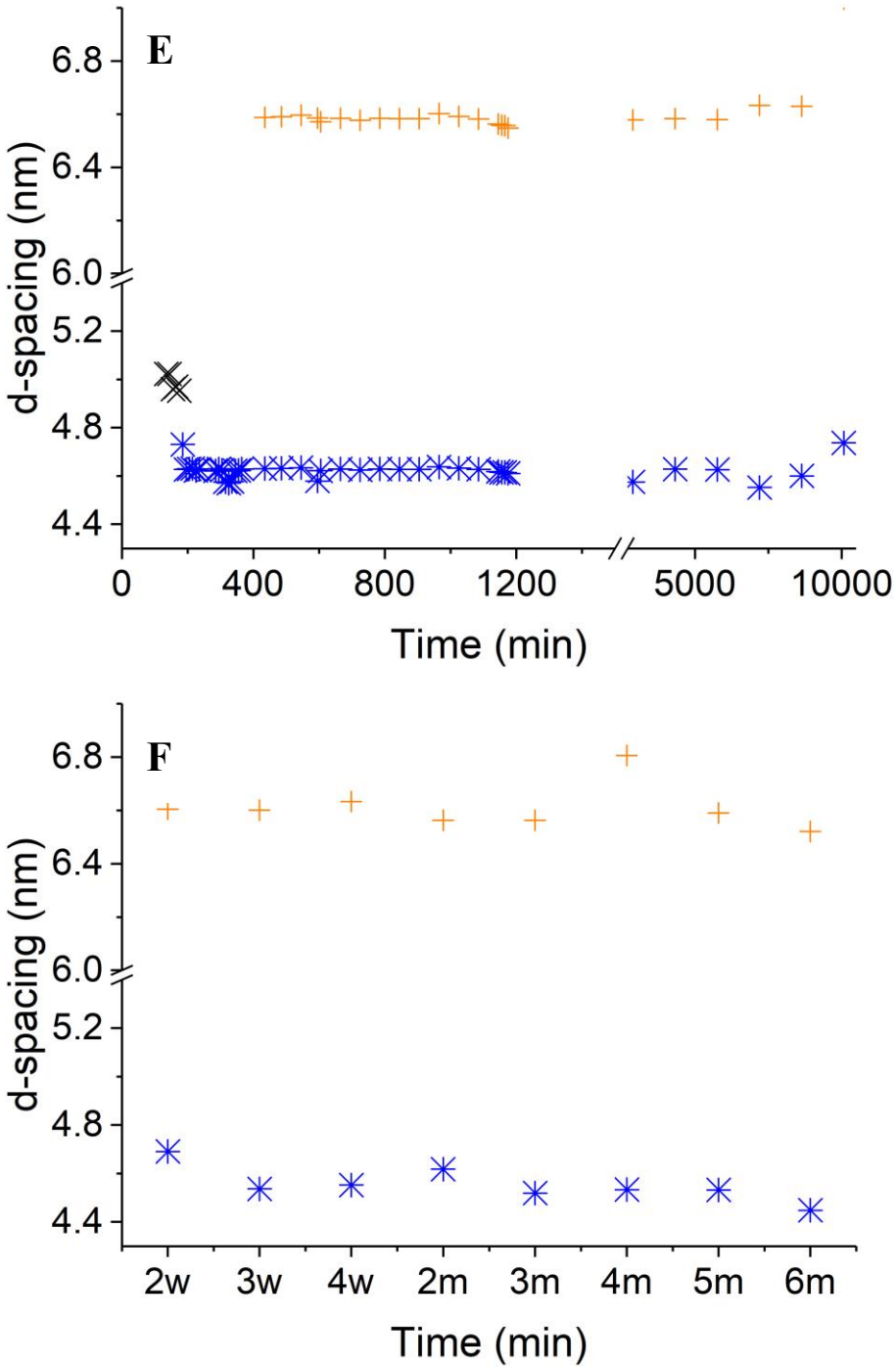

Figure 4.3 (Cont.) d-spacings of the three main polymorphs observed during the isothermal crystallisation of thermally pre-treated CB at 110 °C during the first week (E) and from two weeks to six months (F). Colour key: α-phase –black (X), β'-blue (*), β-orange (+).

4.1.3 DSC measurements

The advantage of performing DSC measurements is that they allow time-resolved experiments, hence the observation of the cooling curve and the first few minutes of the isothermal treatment was possible. Neither of these were recorded with our lab-based X-ray machine.

From the cooling curves it was made evident that the 50 and 80 °C treatments started crystallising prior to reaching the isothermal temperature of 20 °C, at approximately 23 °C (Figure 4.4A), in agreement with previous studies[154, 216, 219]. However, the 110 °C treatment crystallised at a later stage during the cooling ramp, or on reaching 20 °C.

During the isothermal period (Figure 4.4B), all samples showed three main exothermic events, the first one happening within the first 2 minutes (see inset). This did not allow for the calculation of the area under the curve, which is necessary if any kinetic models are to be applied for estimation of induction times and crystallisation rates. The second and third peaks overlapped in all treatments, though more strongly in the case of the 110 °C treatment where, additionally, the peak maximum of the largest peak occurs at a later stage. Because of this overlap, it was decided to calculate the area under the curve between 15 and 120 minutes, in fractions of 5 minutes. The resulting mW/g vs time plots were then fitted using the modified Gompertz equation, as described in the Methods section, thus obtaining the following parameters: λ which represents the induction time, μ which is the maximum rate of crystallisation, and m which is the maximum amount of exothermic energy.

The 110 °C treatment caused a longer induction time (Figure 4.5 A) of the second crystallisation event, whilst the maximum rate of crystallisation (Figure 4.5 B) and maximum amount of exothermic energy (Figure 4.5 C) were reduced. There was no significant difference observed between the 50 and 80 °C treatments in agreement with similar treatments performed by Foubert[154].

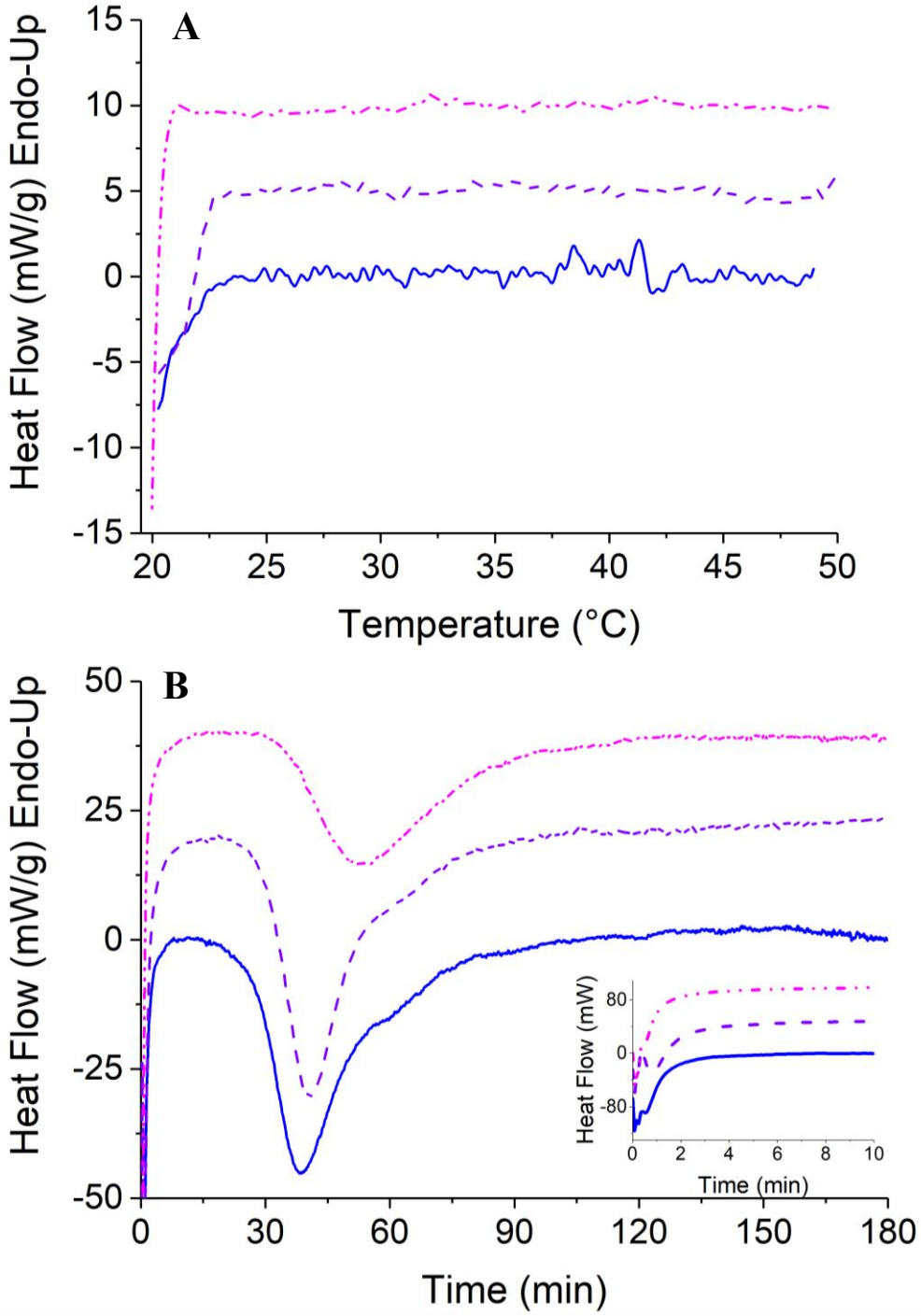

Figure 4.4 Characteristic thermograms of CB on cooling (panel A) from 50 (blue), 80 (purple) or 110 °C (pink) to 20 °C at 3 °C/min, followed by an isothermal period (panel B) of the samples to 50 °C at a rate of 50 °C/min. For ease of view only the first three hours are shown here.

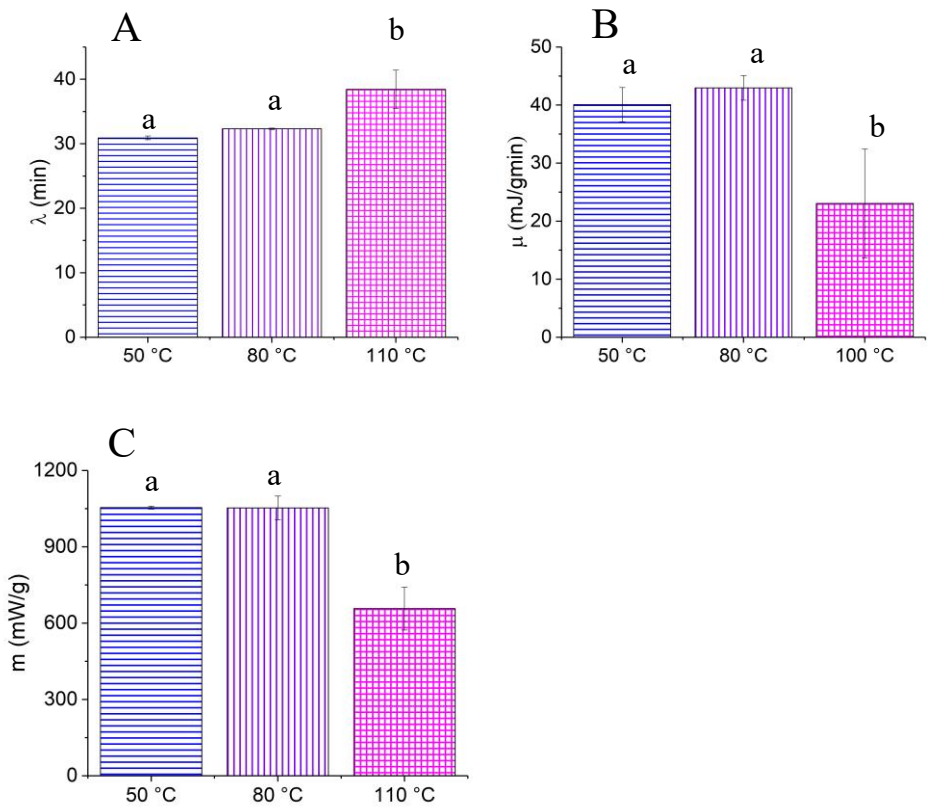

Figure 4.5 Modified Gompertz fit parameters of the partial areas of the second isothermal crystallisation peaks of the three different temperature treatments – 50 (blue horizontal lines), 80 (purple vertical lines-), and 110 °C (pink squares). Panel A shows the values obtained for lambda, representing the induction time, panel B showsμ, which relates to the maximum crystallisation rate reached, and panel C shows m which is the maximum crystallisation reached (as represented by released heat). Statistically different treatments are indicated with a different letter (t-test with p-value of 0.05).

Regarding the melting profiles (Figure 4.6), all treatments displayed two main peaks, one centred at 20 °C and another at approximately 32 °C. This suggests that the different treatments, though they crystallised at different times, developed the same polymorphs: the α-form, and the β'-form in combination with β-V-form, identified by the second endothermic peak ending at almost 40 °C.

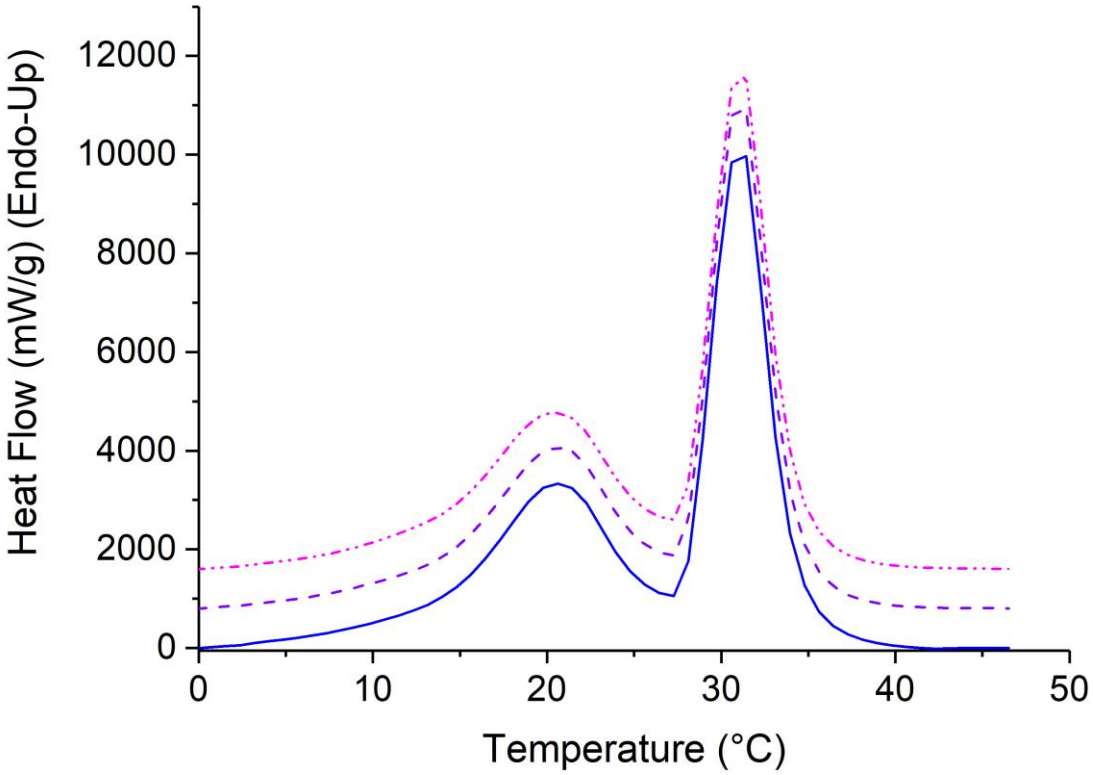

Figure 4.6 Melting thermograms of CB pre-treated to one of three temperatures, 50 (blue continuous line), 80 (purple dashed line) or 110 °C (pink dash-dot-dot line) and crystallised at 20 °C.

4.1.4 Polarised microscopy measurements

From the polarised microscopy images, it was evident that crystallisation occurred prior to reaching 20 °C, in agreement with the DSC results, in the form of small spherulites and individual crystals across all the visual field (Figure 4.7 A-B, E-F, I-J) as defined by Manning and Dimick[220]. After 1 hour, all treatments exhibited a granular morphology and no more clustering was observable suggesting that a crystal network now covered the visual field due to the different clusters growing into each other, similar to what has been observed by previous authors[21, 221].

After one day, only the 110 °C treatment had developed new structures, i.e. spheres with a granular centre, but with larger crystals in the periphery. After two days (Figure 4.8), all treatments had developed similar structures, although the periphery crystals in the 110 °C treatment had grown further and started developing in the centre of the spheres.

By the third day (Figure 4.9), these spheres continued to form, grow in size, and the longer crystals started to occupy larger portions. Moreover, all treatments started

developing new morphologies. The 50 °C developed crystals similar to the spiney rosettes observed by Davis and Dimick[220], whilst the 80 °C and the 110 °C treatments developed larger feather-like dendritic spherulites, which would sometimes grow from the side of the original circular clusters or their centre.

After four days not only was crystal growth evident, but also the development of new morphologies. In the 50 °C sample (Figure 4.10 B) clustering of the longer crystals was evident, without any sign identifiable by the use of the wave plate. In the 80 °C treatment (Figure 4.10 D) some spherulites either developed from the centre of larger ones, or were enveloped by them. Moreover, some branches started growing from the edges of the spherulites in the 50 and 80 °C treatments (Figure 4.10 B and D). In addition, it was possible to observe that some of the original spherulites formed at 50 and 110 °C (Figure 4.10 C and E) have a positive sign, i.e. that molecules are parallel to the radial direction[222, 223]. However, the spiney crystals surrounding them are negative. In the 110 °C treatment, clusters of spiney crystals were also evident, close to some of the spherical morphologies with long crystals in their periphery. These clusters, unlike those surrounding well-developed spherulites, did not develop a specific sign, similarly to the 50 °C treatment.

After a week (Figure 4.11), a few new morphologies still developed. In the 50 °C treatment feather-like spherulites had nucleated and grown (Figure 4.11 D), whilst in the 110 °C treatment the new spherulites tended to be more irregular in morphology, whilst still presenting distinct colouring (Figure 4. G). Importantly, the clusters of thin crystals surrounding spherulites developed feather-like, longer structures in the periphery, some of them with distinct colouring (Figure 4.11 B and K).

After two weeks (Figure 4.12), growth continued across all treatments and crystal morphologies, to the point where some of the spherulites started to impinge on each other (Figure 4.12 E). Moreover, some of these structures developed a border of longer feather-like structures, with either distinct or mixed colouring (Figure 4.12 E, H and L). Finally, new petal-like crystals also developed, which on occasion seem to have nucleated independently (Figure 4.12 I), whilst other developed from some of the initial circular structures with longer crystals in the periphery (Figure 4.12 F).

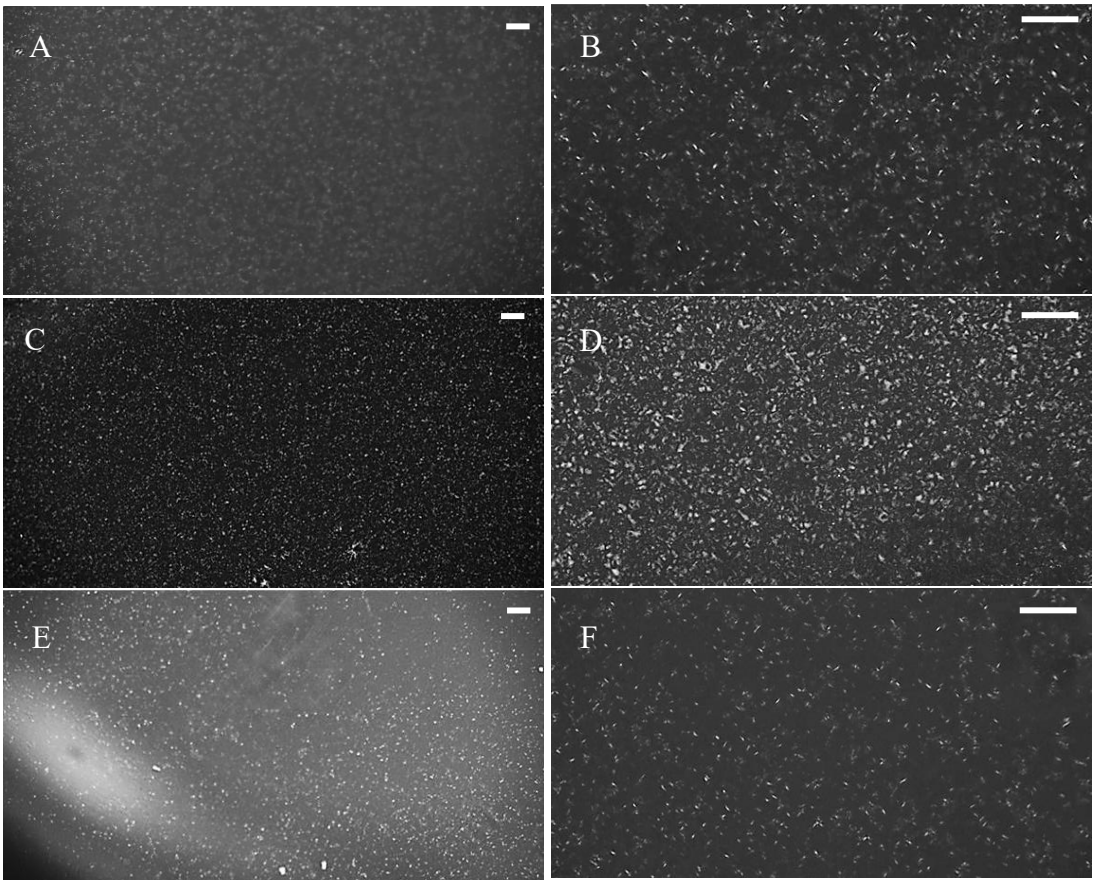

Figure 4.7 Polarised microscopy of CB heated to 50 (A-D), 80 (E-H), or 110 °C (I-L), cooled down to 20 °C at 3 °C/min and held isothermally for one hour. Panels A, E, and I correspond to the start of the isothermal period; panels B, F, and J, correspond to approximately 10 min of the isotherm using a 50x objective; panels C, G, and K are observations made after 1 hour using a 20x objective; panels D, H, and L are observations made after 1 hour using a 50x objective. All the bars indicate 50 μm.

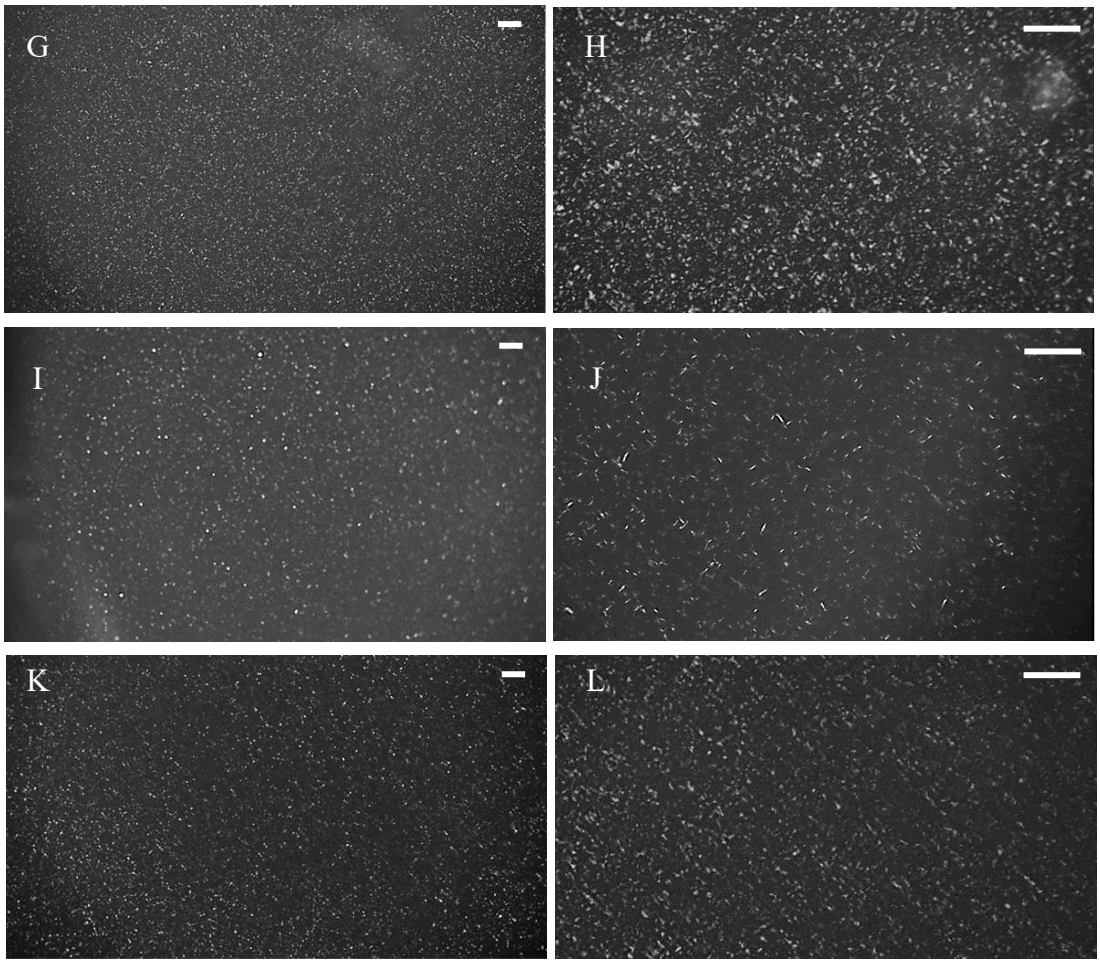

Figure 4.7 (Cont.) Polarised microscopy of CB heated to 50 (A-D), 80 (E-H), or 110 °C (I-L), cooled down to 20 °C at 3 °C/min and held isothermally for one hour. Panels A, E, and I correspond to the start of the isothermal period; panels B, F, and J, correspond to approximately 10 min of the isotherm using a 50x objective; panels C, G, and K are observations made after 1 hour using a 20x objective; panels D, H, and L are observations made after 1 hour using a 50x objective. All the bars indicate 50 μm.

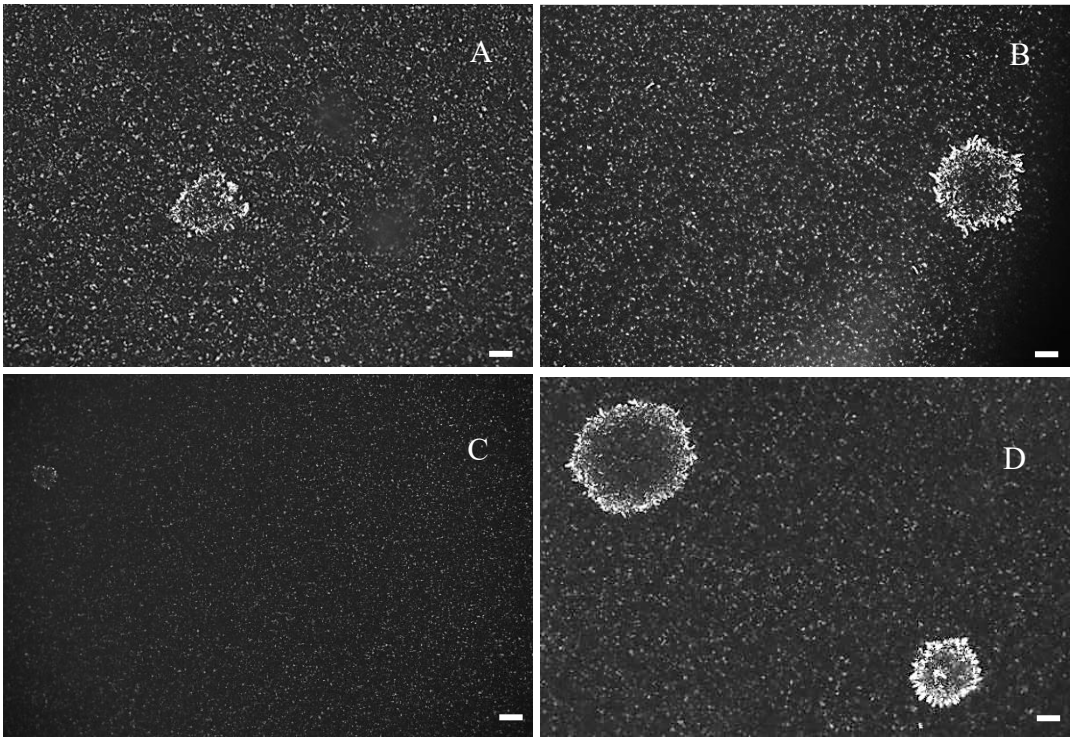

Figure 4.8 Polarised microscopy, of CB crystallised at 20 °C. Panel A refers to the 50 °C treatment after 48 h, panel B to the 80 °C treatment after 48 h, panel C to the 110 °C treatment after 24 h, and panel D to the 110 °C treatment after 48 h. All the bars indicate 50 μm.

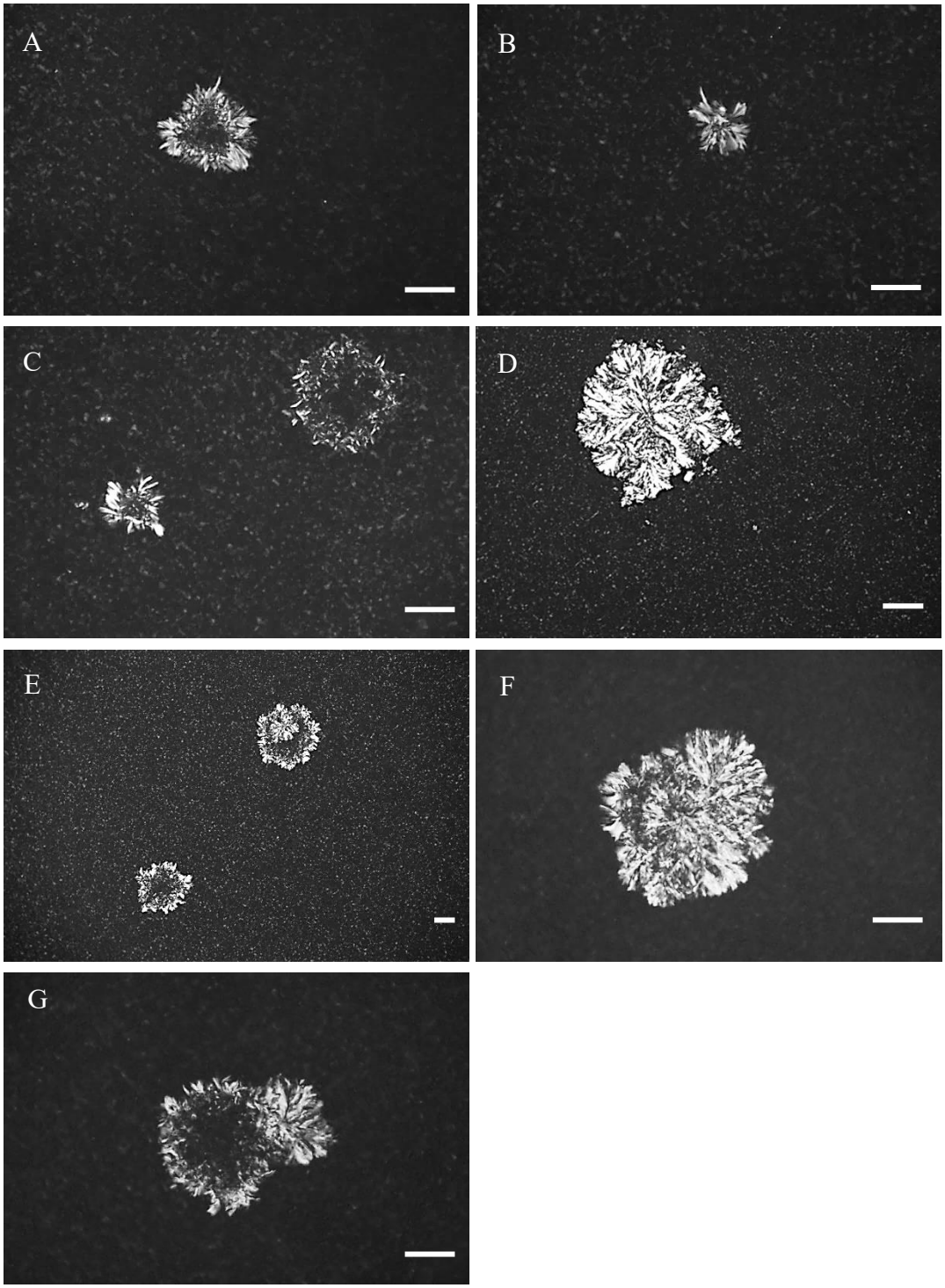

Figure 4.9 Polarised microscopy, of CB crystallised at 20 °C after three days. Panels A and B refer to the 50 °C treatment, panels C and D to the 80 °C treatment, and panels E to G are images from the 110 °C treatment. All images were taken using a 50x objective, except for image E. All the bars represent 50 μm.

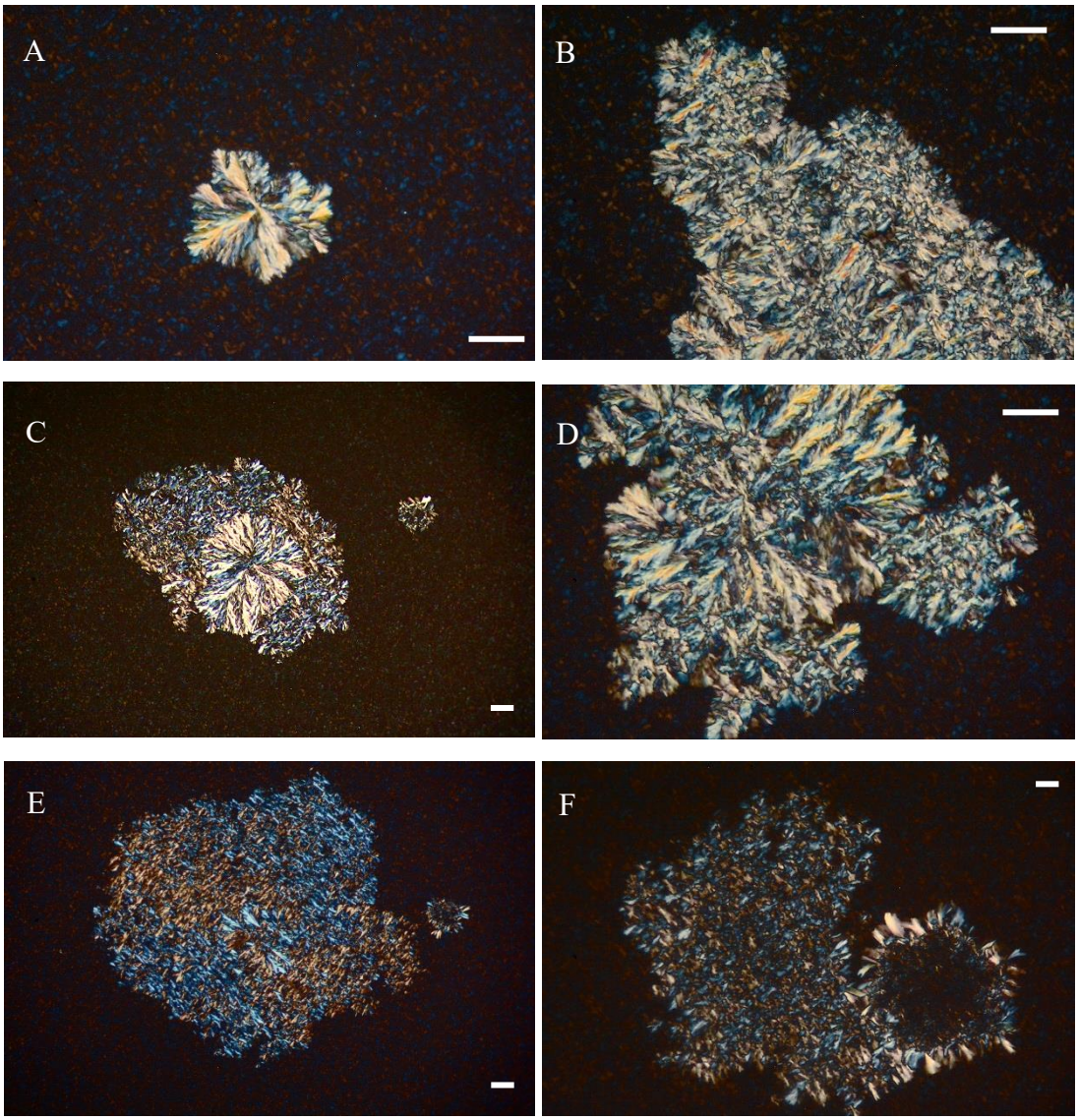

Figure 4.10 Polarised microscopy, of CB crystallised at 20 °C after four days. Panels A to C refer to the 50 °C treatment, panel D to the 80 °C treatment, and panels E to F are images from the 110 °C treatment. Images A, B, and D were taken using a 50x objective, the rest were taken using a 20x objective. All the bars represent 50 μm.

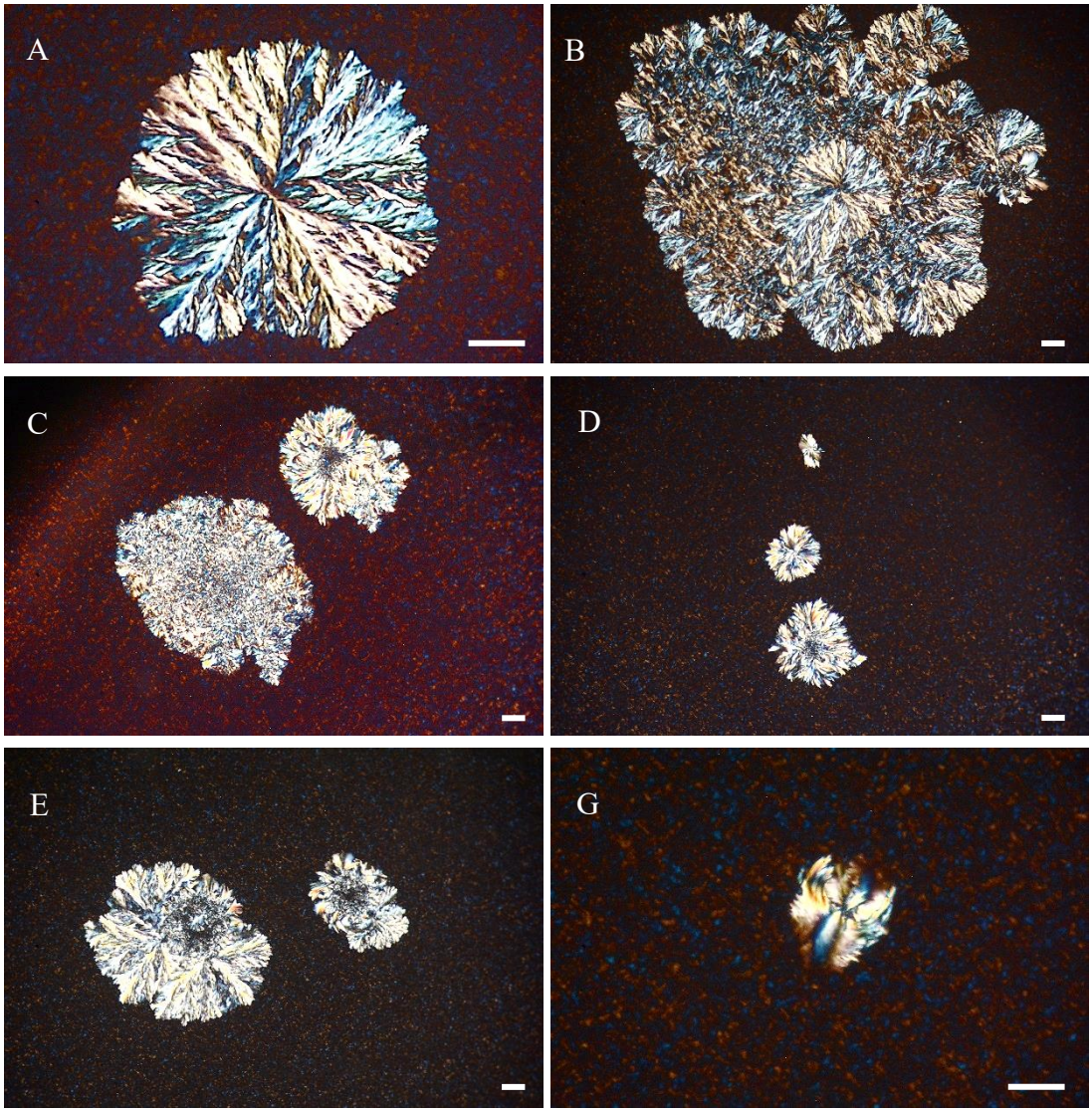

Figure 4.11 Polarised microscopy, of CB crystallised at 20 °C after one week. Panels A-D show images of the 50 °C treatment and panel E, the 80 °C treatment. Images in panels A and G were taken using a 50x objective, the rest are 20x images. The bars represent 50 µm.

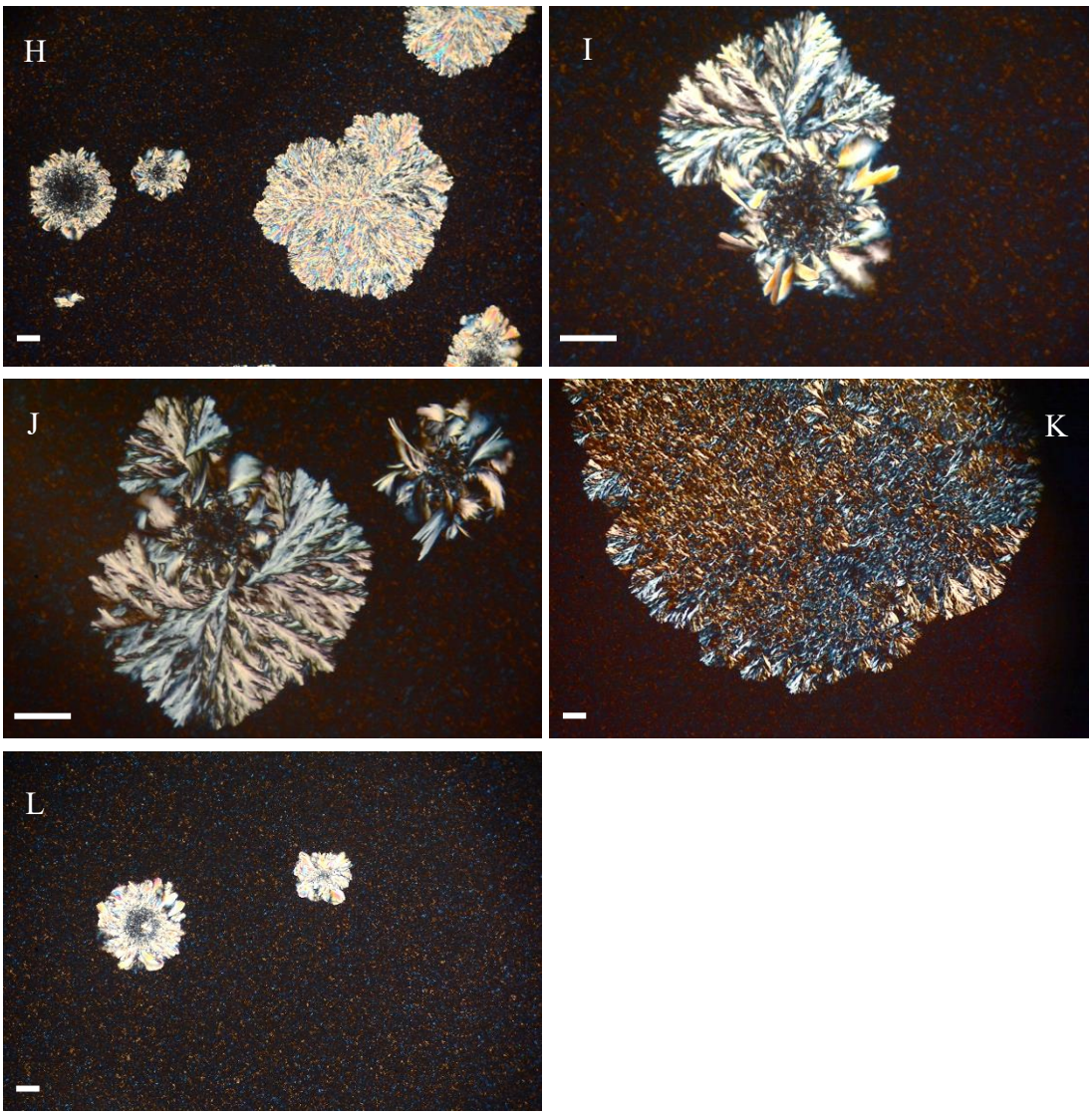

Figure 4.11 (Cont.) Polarised microscopy, of CB crystallised at 20 °C after one week. Panels H-L show the the 110 °C treatment. Images were taken with a 20x objective, except I and J. The bars represent 50 µm.

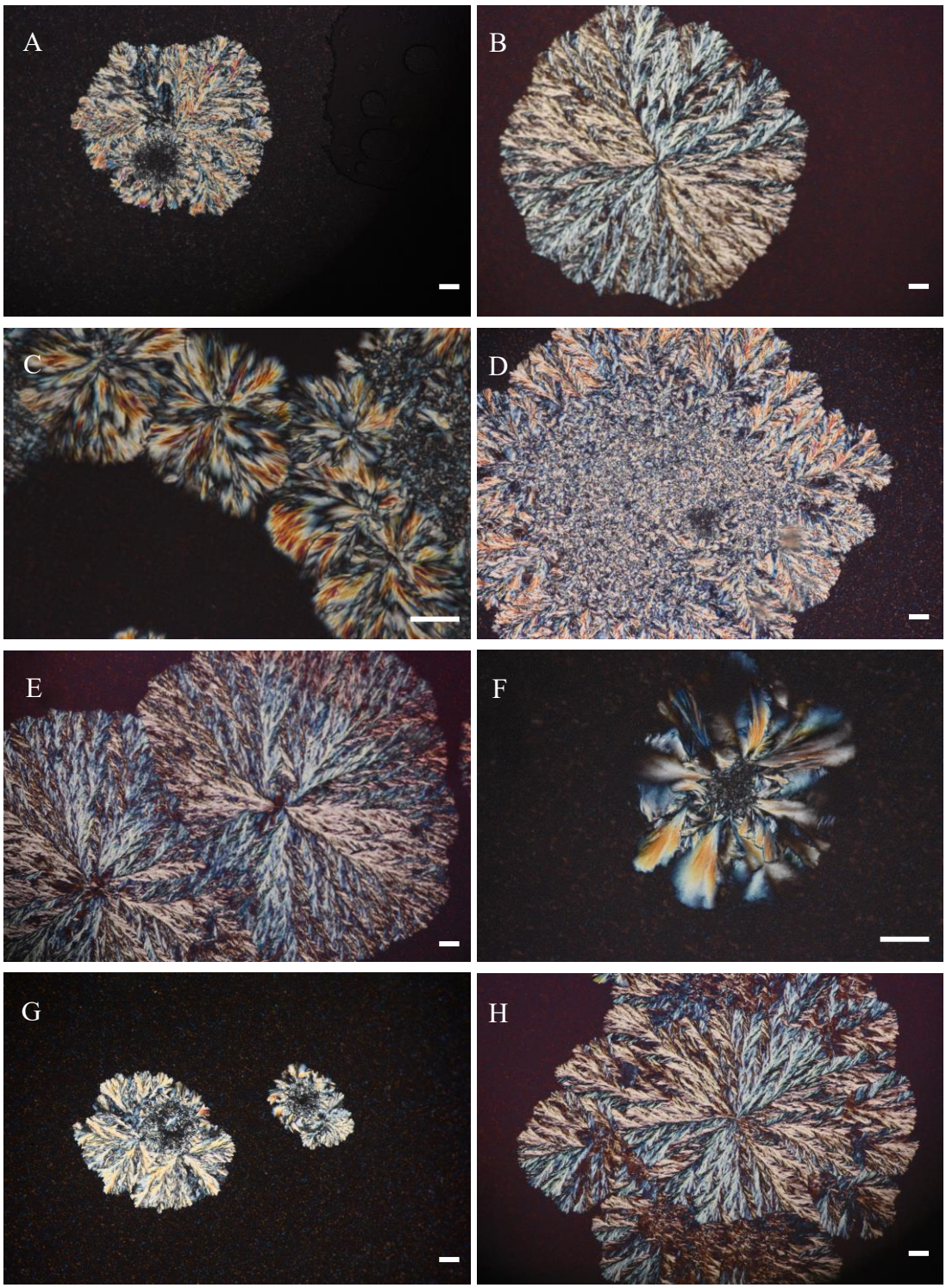

Figure 4.12 Polarised microscopy, of CB crystallised at 20 °C after two weeks. Panels A to E show images of the 50 °C treatment, and F to H, the 80 °C treatment. Images in panels C, and F were taken using a 50x objective, the rest are 20x images. The bars represent 50 µm.

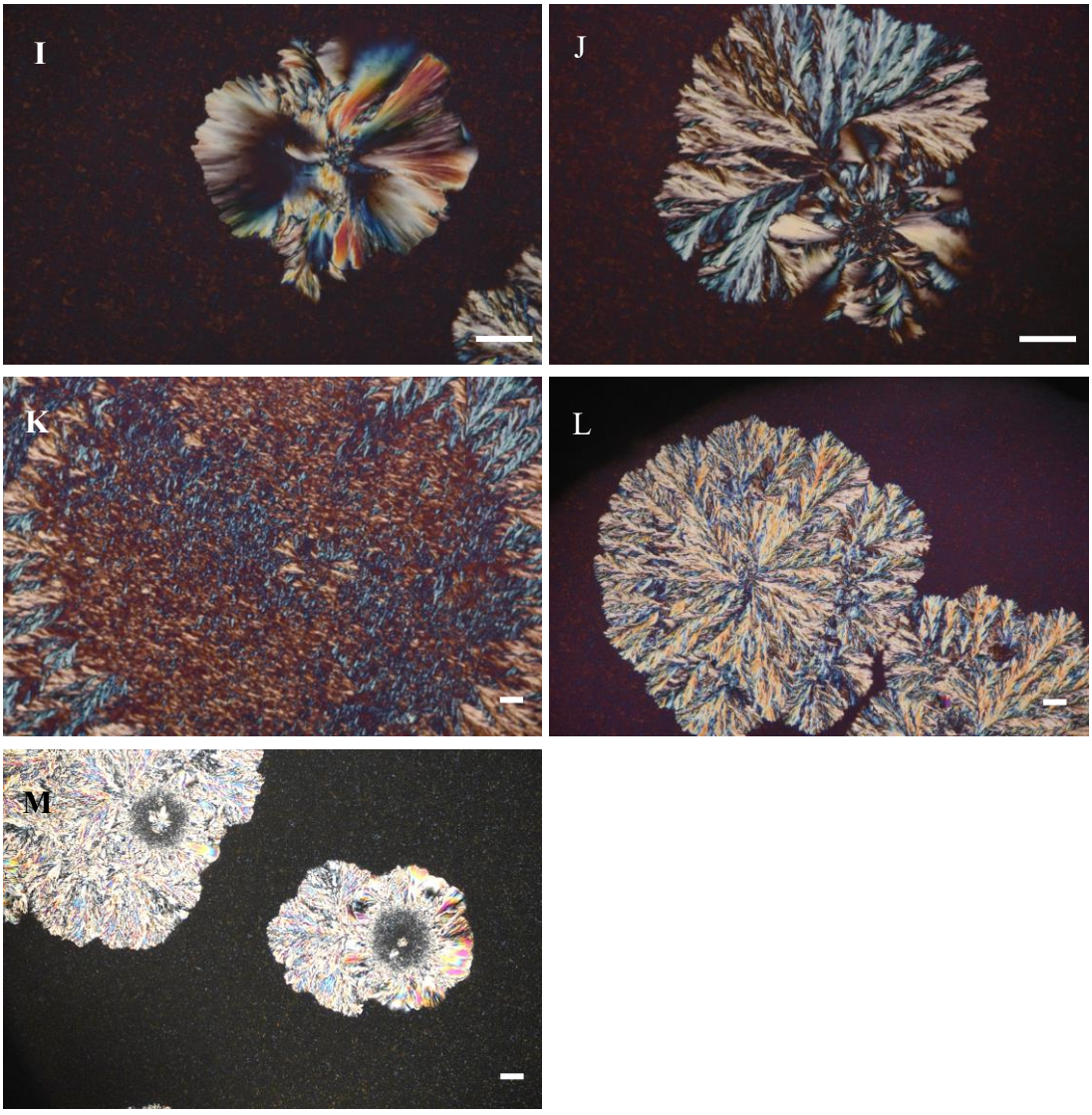

Figure 4.12 (Cont.) Polarised microscopy, of CB crystallised at 20 °C after two weeks. Panel I corresponds to the 80 °C treatment, and J to M the 110 °C treatment. Images in panels I and J were taken using a 50x objective, the rest are 20x images. The bars represent 50 µm.

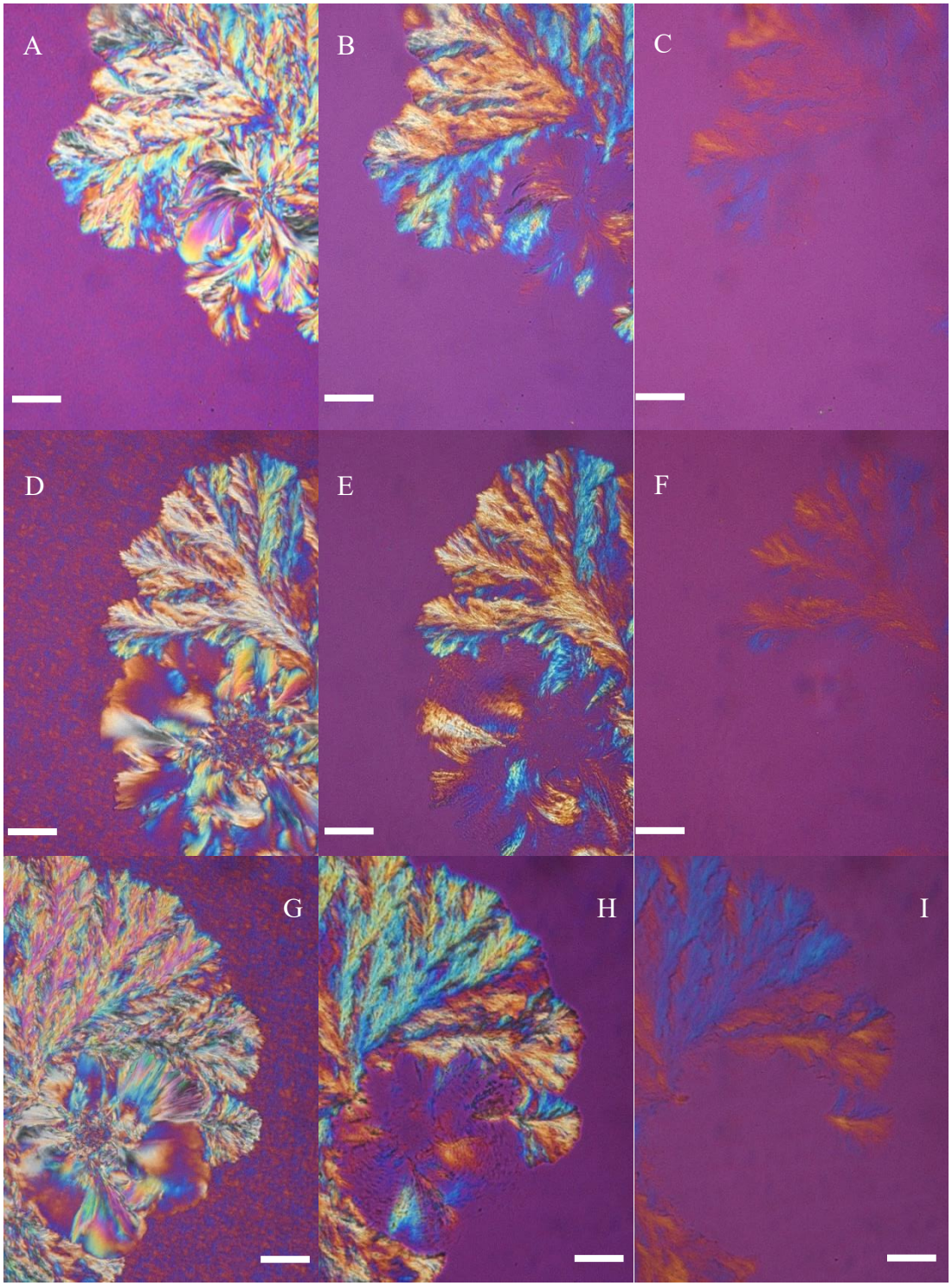

Figure 4.13 PLM images of CB crystallised at 20 °C for two weeks and melted at 1 °C/min. Panels A, D and G are the images prior to the heat treatment (20 °C), panels B, E and H (at ca. 31 °C) show the petal-like structures disappearing after the background, whilst panels C, F and I (at ca. 33 °C) show how after the petal-like crystals have disappeared completely, the feather like structures remain present. Panels A-C are from the 50 °C treatment, and panels D-F from the 80 °C treatment. The bars represent 50 µm.

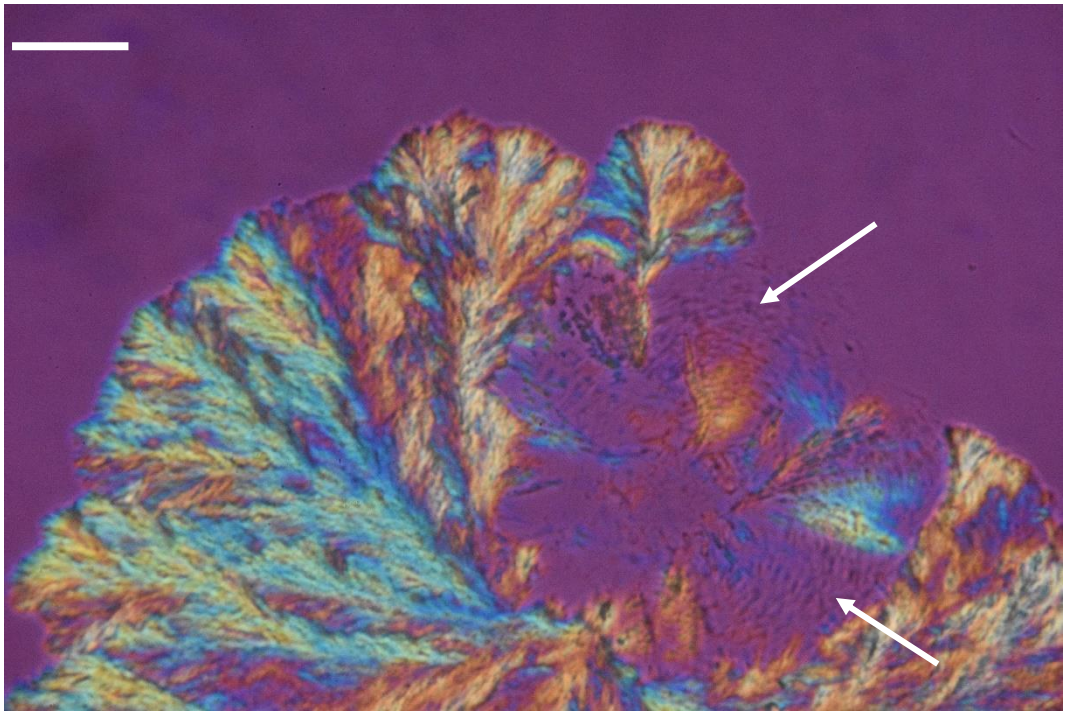

Figure 4.14 Polarised microscopy image of the melting crystals (at 31.14 °C) of the 110 °C treatment. The arrow indicates some of the areas where the concentric rings, or darker lines are observed. The bar represents 50 μm.

On melting, the wave plate was used again as it made it easier to detect the point at which crystals fully disappeared. The melting occurred in stages, starting from when the small spherulite granular background melted, followed by the start of the disappearance of the petal structures (Figure 4.13 B, E and H) and finalised when the feather-like crystals eventually disappeared (Figure 4.13 C, F and I). Interestingly, the feather crystals initially displayed mixed colours, suggesting a lack of specific alignment. However, as melting progressed, distinct yellow-orange and blue colouring areas were revealed. This evidenced that the organisation of these feather-like structures changes across their thickness. Moreover, the petal structures, during melting, displayed dark lines similar to the concentric rings (Figure 4.14) that have been related to twisted chains, and screw dislocations[183, 184, 224, 225].

Regarding the melting temperature ranges (Table 4.2), the granular background behaves in a similar fashion in all treatments, melting between 25 and 28 °C. These temperatures coincide with the melting temperatures of forms β'-III and β'-IV. The next morphology to melt was that of the petals, in the range between 28 and 33 °C corresponding to the β-V form, and finally, the feather-like structures melt in a range that sits between the melting temperatures of the β-V and β-VI forms (29.4 to 35 °C).

Furthermore, both the petal and feather structures increased in melting temperatures alongside the T_{imax} used.

Table 4.2. Range of melting temperatures (°C) of the three main crystal morphologies observed by polarised microscopy in the three different T_{imax} treatments of cocoa butter crystallised at 20 °C.

Morphology	50 °C	80 °C	110 °C
Granular background	25.12 - 27.88	25.04 - 27.90	25.05 - 28.09
Petals	28.60 - 32.85	28.11 - 32.97	29.33 - 32.96
Feathers	29.41 - 34.05	29.93 - 34.59	30.12 - 34.99

4.1.5 SFC measurements

Similarly to the DSC results, all treatments displayed two crystallisation events in the SFC curves. The first one occurring from the start of the isothermal period until approximately 30-35 minutes, followed by a second stronger one, that only started reaching stability after two hours. Here, the modified Gompertz equation was also used to fit the experimental data (Figure 4.15). It is important to mention that time zero was assigned to the first measurement at 20 °C, which, in principle, allowed for the fitting of the first crystallisation event, giving it an advantage over the DSC measurements. However, the 50 and 80 °C treatments started crystallising prior to reaching 20 °C, resulting in negative times of induction. The 99 °C treatment was the only one with a positive induction time. Nevertheless, differences were still observable between the 50 and 80 ° treatments (Figure 4.16 A), the latter resulting in a longer induction time (less negative) than the 50 °C one. Similarly, the induction times of the second crystallisation event significantly increased alongside temperature, though differences are smaller than to the DSC values (Figure 4.5), attributable to the lower sensitivity of SFC measurements.

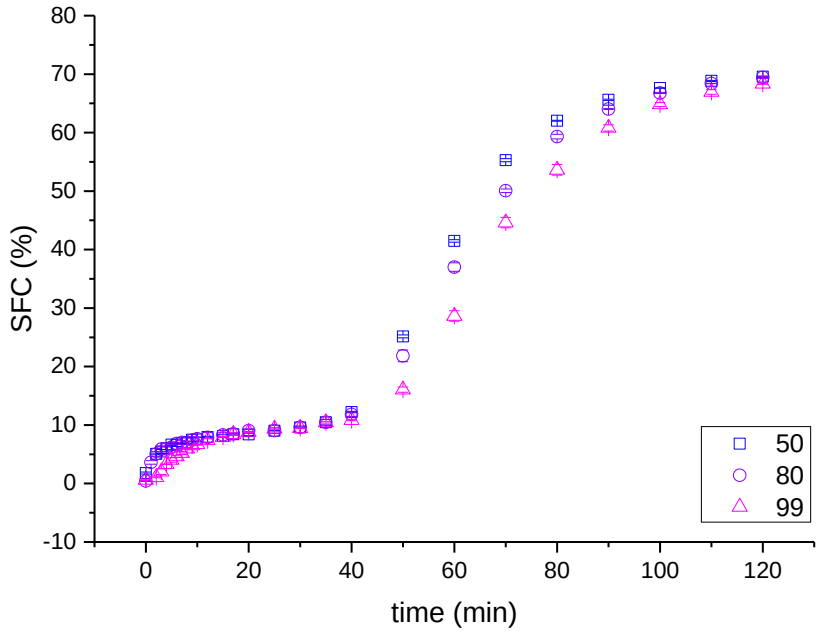

Figure 4.15 SFC measurements during isothermal crystallization at 20 °C. Blue squares refer to a T_{imax} of 50 °C; purple circles to 80 °C, and pink upward triangles to 99 °C. The error bars represent the standard deviation of n=2.

Regarding the maximum rate, there were no significant differences (p-value > 0.05) between the three treatments during the first crystallisation event. However, in the second event, this rate decreased significantly for the 99 °C treatment, similarly to the DSC results.

In the maximum SFC (Figure 4.16 E and F), a decreasing trend with increased T_{imax} is observed during the first crystallisation event, although it is not statistically different, mainly due to the larger error observed in the 50 °C treatment.

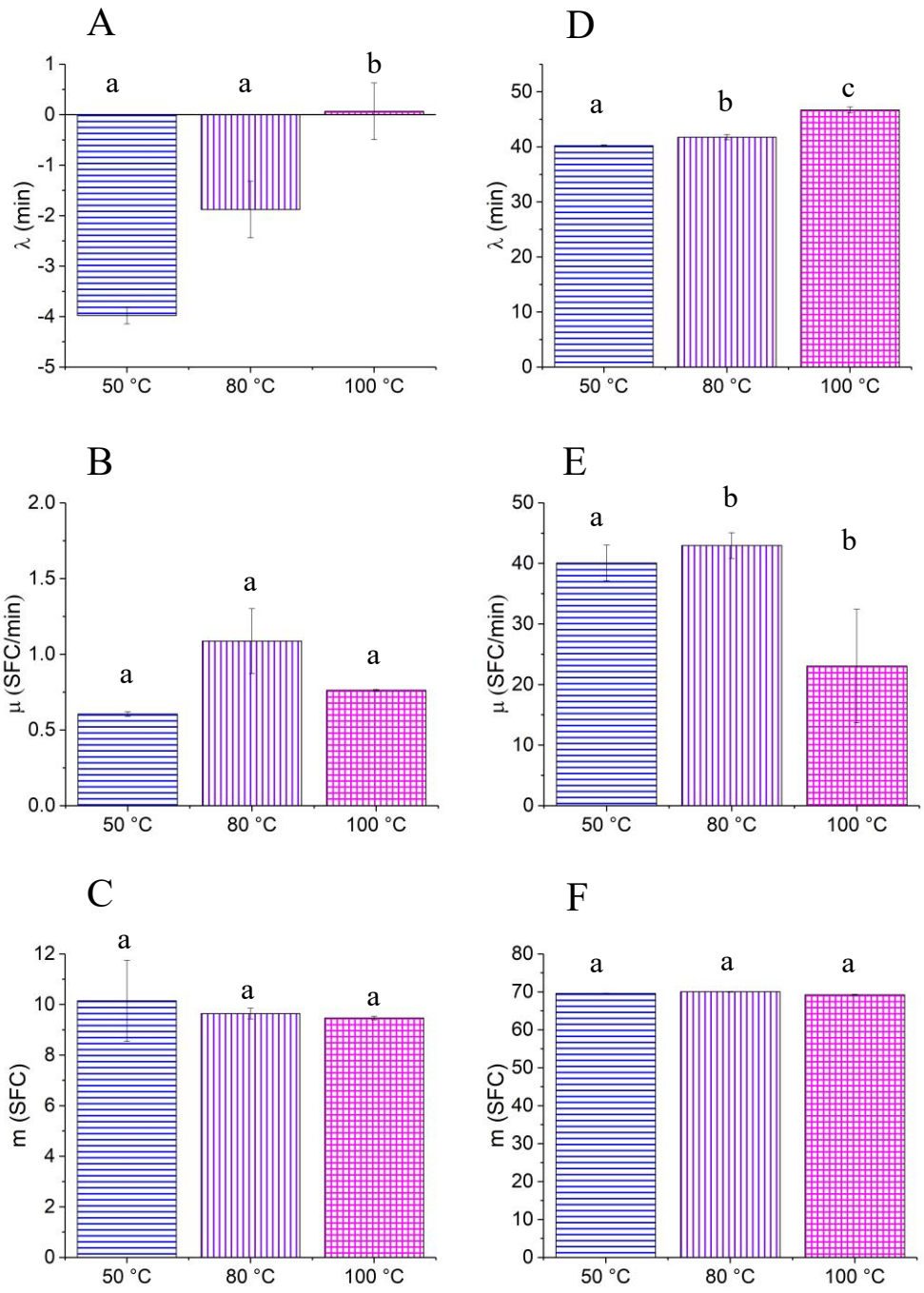

Figure 4.16 Fitting parameters from the two crystallisation steps observed by SFC measurements of the three different T_{imax} treatments: 50 (blue horizontal lines), 80 (purple vertical lines) and 100 °C (pink crossed). Panels A-C are the values obtained for the first event (first 30 min), and panels D to F are the values for the second event (40 to 120 min). Statistically different treatments are indicated with a different letter (t-test with p-value of 0.05).

4.1.6 Comparison between the three main techniques

Table 4.3 Times of the start of the development of the SAXS peaksα- and β'-forms determined from the X-ray scattering patterns; temperatures at which the first DSC peaks began to develop and the time of induction (λ) of the second isothermal event; temperatures at which SFC started to increase in the first sigmoidal region, and the time of induction (λ) of the second crystallisation event detected in the same SFC measurements.

Treatment (°C)	**SAXS**		**DSC**		**SFC**	
	α-form (min)	β'-form (min)	1st event (°C)	2nd event (λ - min)	1st event (°C)	2nd event (λ - min)
50	<15	55	≤ 25	30.91 ± 0.30	>20	40.21 ± 0.13
80	<15	65	≤ 25	32.31± 0.12	> 20	41.76 ± 0.49
100/110	115*	115*	≤ 21	68.43 ± 2.96	20	46.70 ± 0.56

*These are marked with an asterisk because crystallisation, or lamellar organisation was observable from the first frame as broad humps (Figure 4.1), but well defined peaks were only evident after almost two hours.

Regarding the first crystallisation event, all three techniques are in agreement, as crystallisation began, in most cases, before reaching 20 °C, or in the case of the 110 °C treatment, it would began upon reaching 20 °C or only slightly before.

There is a large discrepancy between the times of the second crystallisation event, presumably the transformation/nucleation into the β'-form. Both the DSC, and the SFC have earlier induction times than the SAXS, in particular the former.

4.1.7 Diffusion measurements

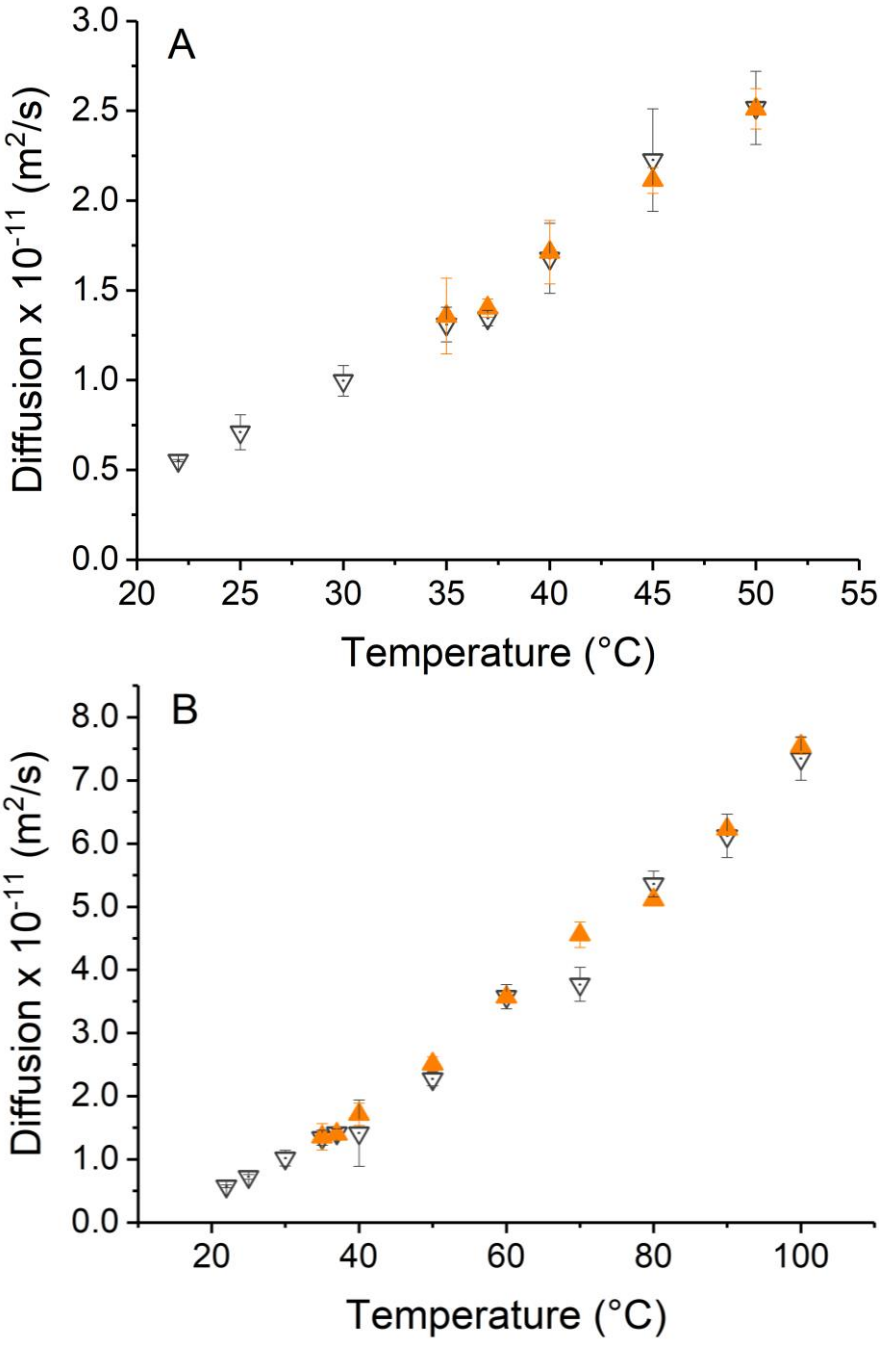

Figure 4.17 Diffusion factors calculated using FFC-NMR vs. temperature of the 50 (A) and 100 °C (B) treatment. The orange upward triangles symbolise the factors calculated during the heat treatment, only values from 35 °C are shown as prior to this temperature the sample was too solid for diffusion calculations. The grey downward triangles represent the values obtained on cooling the sample. Here it was possible to calculate diffusion factors down to 22 °C as crystallisation is not immediate. Both heating and cooling treatments were performed step-wise, allowing for at least 10 min for temperature equilibration (taken from reference[226].). The error bars correspond to the standard deviation of at least n=2.

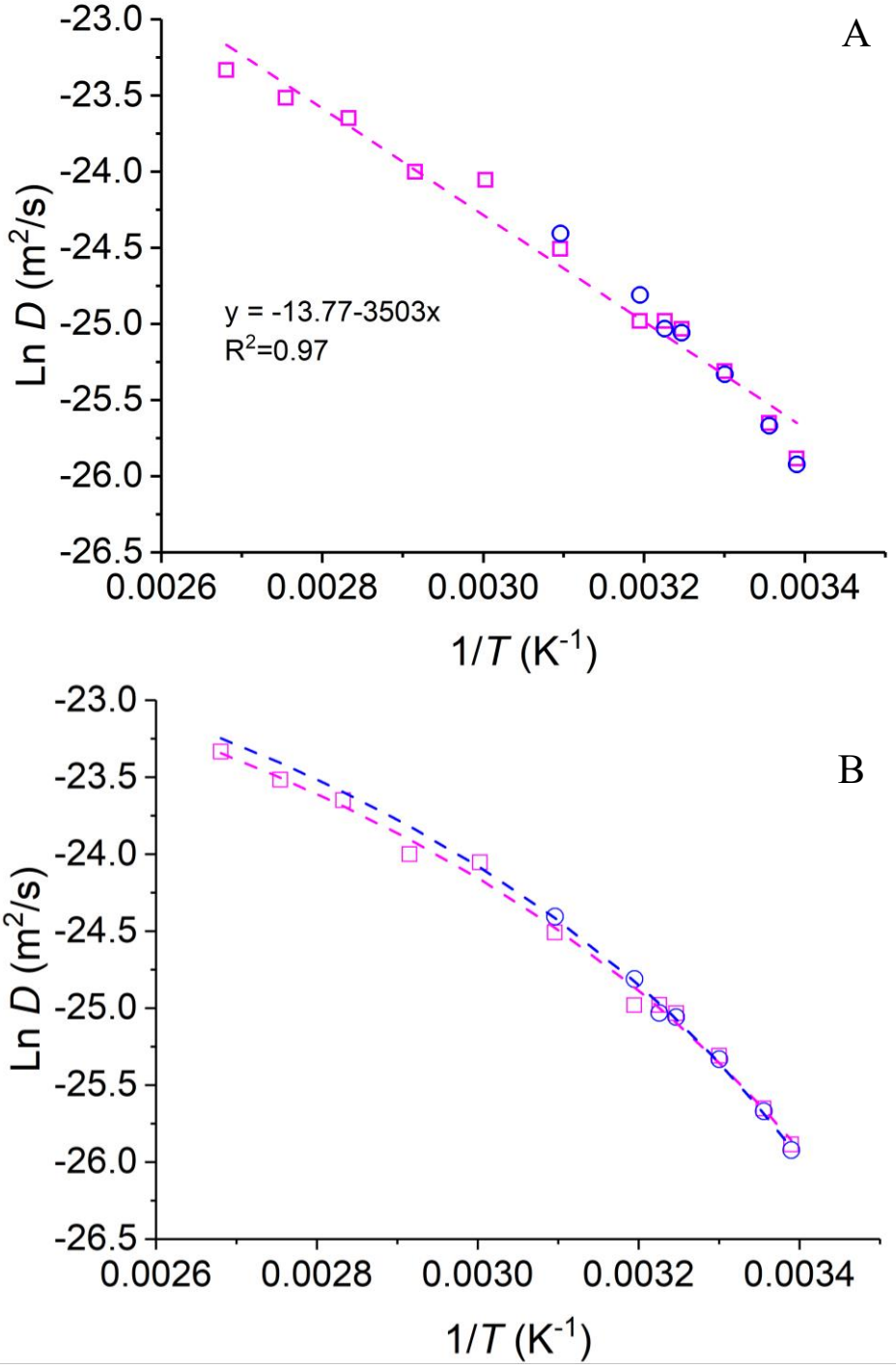

Figure 4.18 Arrhenius plots of diffusion factors during the cooling ramp for both, the 50 (blue circles) and the 100 °C (pink squares) treatments. A linear (Arrhenius) function was fitted through linear regression to the 100 °C values (A), from which the activation energy was estimated. However, as the diffusion curve does not follow a linear trend, a VTF curve was also fitted to both temperature treatments (B) (dashed blue and pink lines, corresponding to the 50 and 100 °C treatments, respectively). Taken from reference[226].

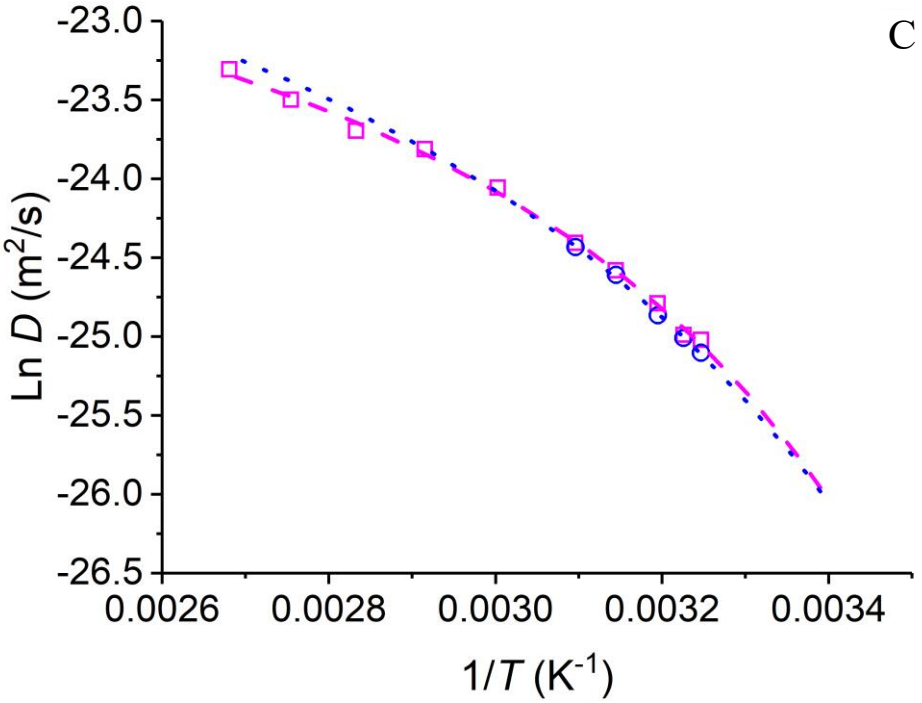

Figure 4.18 (Cont.) Ln of diffusion values of CB upon heating from 35 °C to 50 (blue circles) or 100 °C (pink squares) and their corresponding VTF fits (dotted blue and dashed pink lines, corresponding to the 50 and 100 °C treatments, respectively). Taken from reference[226].

No hysteresis was observable in the heating-cooling steps in the 50 °C treatment (Figure 4.17 A), whilst in the 100 °C treatment (Figure 4.17 B), at 70 °C, a deviation was observed upon cooling. Surprisingly, during the cooling ramp, a slightly lower diffusion factor was observable in comparison to the heating ramp, which, if significant, would suggest a transition in the organisation of the molecules such as the crystallisation of fully saturated TAGs, hindering molecular motion.

From Figure 4.18 A, two main conclusions are reached. Firstly, there is no difference between the 50 and 100 °C treatments, in terms of the diffusion factors. Secondly, the diffusion factors do not follow a linear trend, as there is a change in the slope between 40 and 70 °C. Because of this, it was decided to apply the VTF equation (Figure 4.18 B), which is commonly used for glass-forming and crystalline materials, such as polymers[227-232], as their behaviour is variable throughout different temperature regimes[207, 233]. This resulted in a better fit.

Table 4.4 Parameters from the fitted VFT and Arrhenius equations from the three different thermal treatments[226]. The values shown for tristearin (StStSt) and triolein (OOO) were taken from reference[234].

Fitted Parameter	Heating 35-50 °C	Cooling 50-22 °C	Heating 35-100 °C	Cooling 100-22 °C	StStSt	OOO
D_0 (m^2s^{-1}) (VFT)	$6.99x10^{-10}$ $\pm6.5x10^{-11}$	$6.48x10^{-10}$ $\pm6.8x10^{-11}$	$3.59x10^{-10}$ $\pm9.1x10^{-11}$	$5.89x10^{-10}$ $\pm4.8x10^{-11}$	---	---
B (A.U.)	294.91±7.3	289.98±7.5	200.132±8.5	299.61±7.1	---	---
T_0 (°C)	-38.2±7.6	-39.0±2.9	-25.5±1.0	-31.80±1.9	---	---
D_0 (m^2s^{-1}) (Arrhenius)	$1.21x10^{-5}$ $\pm2.4x10^{-7}$	$2.71x10^{-4}$ $\pm5.4x10^{-6}$	$3.01x10^{-7}$ $\pm6.0x10^{-9}$	$1.04x10^{-6}$ $\pm2.0x10^{-8}$	$4.7x10^{-7}$	$9.3x10^{-7}$
Activation energy (kJ/mol)	35.61±0.74	43.26±0.86	25.43±0.50	28.66±0.57	27.0	28.1

The calculated D_0 and activation energy values from both the Arrhenius and VFT fits (Table 4.4) are dependent on the T_{imax} and the ramp (cooling or heating) at which the measurements were taken. Overall, the 50 °C treatment led to an overestimation of both values, in comparison to literature values[234]. However, it should be kept in mind that this temperature is below the melting temperature of the β-form of tristearin and tripalmitin, both of which are present in CB. In the case of the 100 °C treatment, the values were expected to lie between those of StStSt and OOO. However, on heating, the D_0 (Arrhenius) was slightly lower than that of StStSt, whilst on cooling, it is closer to OOO. These differences can arise from the approach used for measurements, as we have shown here. Fitted values are different depending on whether measurements are taken on cooling or heating, and the temperature ranges used. Therefore, the D_0 values are still considered to be within literature ranges.

Whilst the overall trends of D_0 obtained by either the VFT or Arrhenius equations are comparable, the actual values differ considerably. It is thought that the Arrhenius equation leads to an overestimation of the D_0 as it does not take into account the reduction in the rate of diffusion increase alongside temperature. Hence, the VFT values are considered more representative. Furthermore, the VFT equation also allows the estimation of T_0 which is related to either the glass or crystallisation temperature[207]. Here, the heating treatments resulted in higher values than the cooling ramps, and so did the 50 °C treatment when compared to the 100 °C one. Moreover, all T_0 are below 0 °C, which can be associated with the formation of the γ-form which is only observed

on quenching CB to temperatures below zero[121, 123, 124], thus suggesting that these temperatures could be referring to the transition to this polymorph.

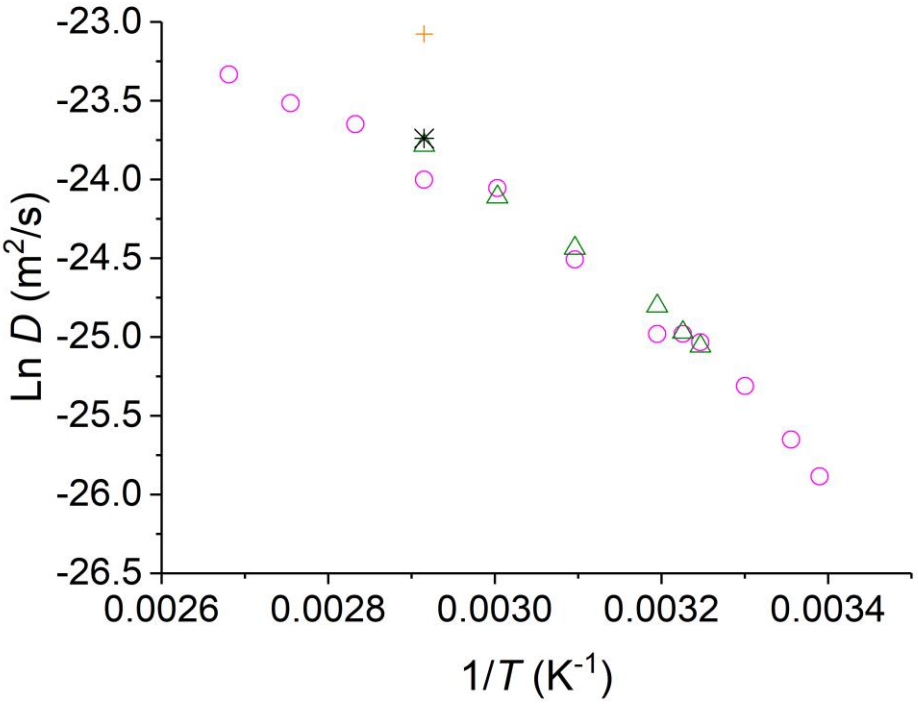

Figure 4.19 Diffusion factors of CB using different techniques. The green triangles represent the values obtained from a PG-SE sequence, and the pink circles those calculated from FFC-NMR measurements upon cooling. Additionally, values for tristearin (black star) and triolein (orange cross) were taken from literature[234] for reference (taken from reference[226]).

As mentioned in the methodology section, FFC-NMR is not a technique frequently used for diffusion measurements, therefore, the results obtained needed to be validated. This was achieved by performing measurements with a standard PGSTE sequence. The results obtained were in agreement not only between the two different techniques, but also with literature values, as shown in Figure 4.19, thus validating our results. Notably, the diffusion values of CB are considerably closer to those of tristearin than those of OOO, which is related to the TAG molecules having two saturated chains, and only one oleoyl chain.

4.1.8 Compressibility

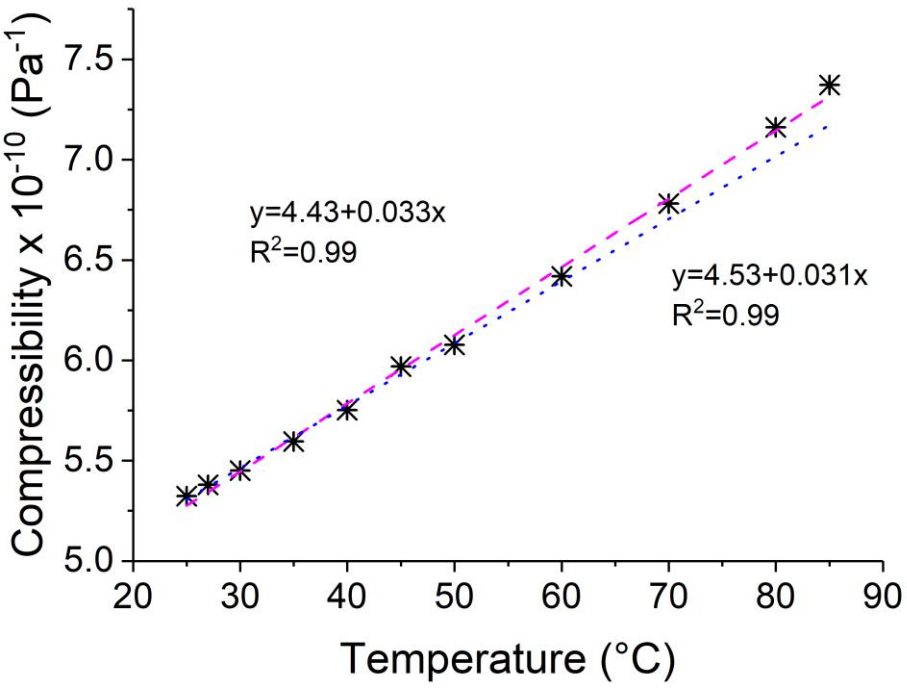

Figure 4.20 Compressibility of CB as a function of temperature as calculated from velocity of sound measurements. The pink dashed line represents the linear fit obtained from the fitting of all the data, whereas the blue dotted line represents the extrapolated of the fit in the range of 25 to 50 °C.

An overall linear behaviour (pink dashed line) is observed in the compressibility of liquid CB. As expected, with increased temperature, compressibility rises as well, as molecules are more mobile and thus more deformable. Note should be taken that a small increase in the slope of the curve is present after 50/60 °C have been reached, as evidenced by the blue dotted line.

4.1.9 Oxidative stability determination

The OSI (110 °C) value of CB was of 14.74 ± 4.4 h, i.e. it is expected to remain stable for at least 10 h when held isothermally at 110 °C. Therefore, the 10 min used here as thermal pre-treatment are not thought to cause extensive oxidative damage.

4.2 Discussion

The results obtained by the different techniques used, although differing in the specific values of induction times and crystallisation rates, showed a consistent trend between the different T_{imax} treatments. This is particularly relevant regarding the SFC measurements, for they demanded the largest volume and did not follow a continuous cooling ramp, but rather a step-wise cooling. The SFC results confirmed the observations made with the other techniques and show that the overall effect of the T_{imax} is independent of the method of cooling, with the caveat that specific transitions and nucleation times are dependent on the latter.

In the 50 and the 80 °C treatments, crystallisation occurred as a two-step process within the first two hours of the isothermal period (Figure 4.2), in agreement with previous research[20, 177, 216]. Here, the first step was the nucleation into the α-form, followed by the transformation and further nucleation into the β'-IV form, until eventually the α-form disappears. From the SFC (Figure 4.16) and DSC (Figure 4.5) analyses, it was possible to determine that in these treatments the first crystallisation event occurred during the cooling ramp prior to reaching the 20 °C (i.e. at ca. 23 °C) in agreement with literature[137, 154, 235].

The development of the α-form prior to the β'-IV form gives evidence to the 50 and 80 °C treatments following the Ostwald rule of stages[30], which states that the first polymorphic form to nucleate will be the least stable one (α-form) as it is the one with the lowest energetic barrier. Furthermore, it also indicates that these two T_{imax} are sufficient to erase β-polymorphic memory, as defined by van Malssen *et al.*[169], for the sample was in the β-V form prior to melting. However, in the 50 °C treatment, it is unlikely that the more stable TAGs (tristearin and tripalmitin) were completely molten as their T_m is higher than 60 °C[104, 113, 168]. Also, they are not expected to have dissolved entirely in the liquid oil based on observations made by Norton and Fletcher[168, 236], where, tristearin crystals displayed a lower solubility in triolein than calculated, potentially due to the steric hindrance with the oleic acid double bond, therefore they can act as heterogeneous nuclei[104, 113, 168]. This is supported further by the onset of crystallisation occurring during the cooling ramp. It can be argued that if tristearin crystals have not melted at 50 °C, they are present in the β-form, leading to

crystallisation into the β-V rather than the α-form. Yet, it should be kept in mind that tristearin is a fully saturated TAG, therefore, its β-form is organised in a 2-L lamellar structure, which is not the ideal conformation for the main TAGs of CB as they contain an unsaturated oleic FA, thus requiring a 3-L arrangement for the β-V form to develop. Furthermore it is noted that the lack of crystallographic evidence of the β-form of tristearin during the initial stages of crystallisation is not detrimental to the hypothesis here presented, as its content in CB is very low, thus making it practically impossible to be detected by SAXS[237], especially when using a lab-based source.

In contrast to the previous two treatments, the 110 °C sample crystallised at a later stage, and even though the DSC and SFC measurements show a two-step crystallisation process within the first two hours, the SAXS and WAXS measurements showed a different behaviour, suggesting that the second event might be related to crystal growth or further nucleation. The difference between the different techniques can be attributed to heat transfer differences due to changes in the sample size, as well as surface area in contact with the cooling medium. In the case of the DSC, the bottom of the pan is in direct contact making heat transfer more efficient. In the NMR, a larger sample (mL) is used and only the walls of the tube are in contact with the cooling medium. Finally, in the SAXS, only the two edges of the capillary are in contact, but a smaller sample (μL) is used, hence heat transfer is expected to lie between the other two treatments.

Moreover, in the 110 °C treatment, no well-defined Bragg peaks could be observed within the first two hours, thus showing a similar behaviour to that observed in oleic acid by Yoshimoto and Sato[138]. Also, crystallisation did not start directly into the α-form, but rather a broad peak developed in the SAXS regime covering the positions of all three main polymorphs, thus not allowing it to be assigned to a specific form. Nevertheless, it eventually refined into a less broad peak mainly covering the spatial regime of the α- and β'-forms. Nucleation into multiple polymorphs was previously observed by van Malssen, *et al.*[20, 177], when using a T_{imax} of 60 °C and a cooling rate of 0.25 °C/min, suggesting that the increase of the T_{imax} used has a similar effect to that of applying a very slow cooling rate, thus allowing for a better packing of the TAGs from the start, without requiring to organise only in a step-wise manner.

In the wide-angle region, it took longer for peaks to develop, which were subsequently identified as those belonging to the β′-IV polymorph. The previous observation indicates that TAGs arrange into a lamellar structure prior to the FA chains organising into a specific sub-cell, as observed by Ueno *et al.*[238] in StOSt. This may be explained by the the orthorhombic sub-cell of the methyl chains requiring a certain degree of tilt of the lamellar structure to develop an increased amount of *trans* conformers.

The 110 °C treatment led not only to a later crystallisation onset, but also to a prolonged presence of the long-scale diffraction peaks of the α-phase. This could initially be considered a disadvantage, because a higher proportion of the metastable forms could lead to undesirable sensory characteristics and a reduced stability in chocolate[214, 239]. However, considering that in the wide-angle only peaks corresponding to the β'-IV form were observed, it is likely that rather than indicating a continuous presence of the α form because of an increased stability, these peaks are an indication of newly formed 2-L lamellar stacks which tilt and pack into an orthorhombic sub-cell giving rise to β'-IV crystals.

Regardless, even if there were a prolonged presence of the α-form in the early stages, its potential detrimental effects are overcome by the earlier development of a more stable β-V polymorph as determined by the melting points observed by polarised microscopy (Figure 4.8). This result is remarkable, for it was also observed in the 80 °C treatment. Such behaviour could be explained in the 110 °C treatment by the earlier development of the β'-form, thus helping the development of the β-V, in accordance to the Ostwald rule of stages[30]. Another possibility is that by presenting a lower amount of crystallised material, there is an increased molecular mobility, which allows for an easier re-arrangement of the FA chains. This hypothesis is supported by the 110 °C treatment developing new morphologies and more crystal growth than the other two treatments. However, the 80 °C treatment did not present the initial simultaneous formation of 2-L and 3-L structures, as the 110 °C treatment did, and reached similar crystallisation levels to the 50 °C treatment, as observed by DSC and SFC measurements (Figure 4.5 and Figure 4.16). Therefore, the earlier development of the β-V is thought to be directly related to the use of a higher T_{imax} and enhanced by the differences in the amount of crystalline seed material. This could be related to a fractionation of the fat in its different species (fully saturated and mono-unsaturated),

thus generating crystals with a more homogeneous composition, and a consequent higher stability. The latter is supported by the slightly higher melting points observed by PLM and by the different morphologies observed in it.

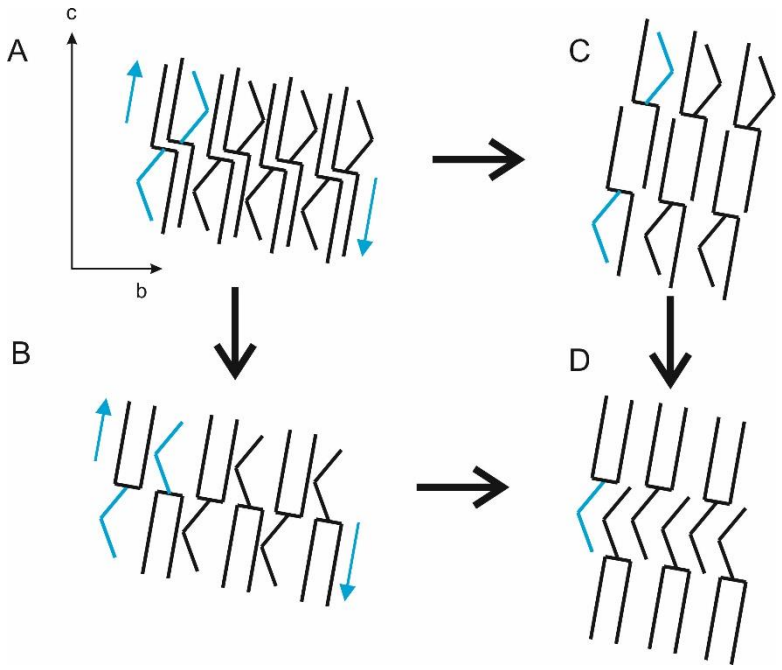

Figure 4.21 Proposed transformation pathways from a 2-L (A and B) to a 3-L (C and D) lamellar arrangement. From A to C TAG molecules only shift in the c axis to create the 3-L structure, which is not stable as the oleic acid (marked in blue) still causes steric hindrance by being next to a fully saturated chain. This is then followed by a flip of the oleic acid and one of the saturated chains so that all oleic chains lie next to each other (C to D). Alternatively, this last step can occur first (A to B) and then followed by the shift in the c axis (B to D).

The earlier transformation into β-V, although dependent on the actual T_{imax} applied, might also affect molecular arrangements through intramolecular motions, depending on the FA chain mobilities. Whilst intermolecular shifts are still needed to transform from a 2-L to a 3-L lamellar structure, it is plausible that the FA chains have a higher amount of *synclinical* conformations, in comparison to fully-extended antiperiplanar conformations[240], i.e. they retain a higher freedom of mobility, even when in the β'-IV form. This allows them to arrange more easily into a triclinic sub-cell. This is supported by the behaviour of the β-V-form WAXS peaks, which, whilst always developing after the SAXS peaks, appear after a shorter period of time when a higher T_{imax} is used (Figure 4.2). In addition to the larger amount of *synclinical* conformations present in the FA chains, the conformation of the TAG molecule is also relevant. Whilst Tascini *et al.*[146] through computational simulations have determined that the tuning-fork conformation is the one present in higher proportion, other conformations, such as the

chair, are also present. This is not particularly relevant in mono-acid TAGs, but it is in mixed saturated-unsaturated TAGs as is the case of CB. If a tuning-fork conformation is present, for a 2-L to a perfected 3-L structure transition to occur, only a shift in the c-axis is required (Figure 4.21 B to D). Instead, for the chair conformation the first and second FA need to flip to transform into the trident conformation (Figure 4.21 A transitioning into B, or C into D) to avoid the steric hindrance caused by the oleic acid's unsaturation.

Further evidence towards the delayed crystallisation, and enhanced β-V transformation not being related to higher intermolecular motions, at least not in the bulk, is found in the diffusion measurements. Here, no difference was observed between the values obtained from CB cooled down from either 50 or 100 °C, therefore a similar behaviour would be expected also on cooling from 80 °C. Nevertheless, there might be local diffusion, micro-viscosity changes due to the proposed shifts in the c-axis described above. Further studies in this area might prove more insightful as they could show inhomogeneities in the molecular motion that could help explain the observed behaviour[241, 242]. This is motivated by the preliminary studies performed by Dibildox-Alvarado and co-workers who observed an increase in the microviscosity of TAGs containing at least one palmitic acid[149]. Not only this, but to understand the process of 2-L to 3-L transformation, ^{13}C-NMR studies would be recommended, to determine which sections of the chain have a higher mobility.

From the diffusion measurements, also relevant information about the energy of activation was obtained. The estimated energy and D_0 values were only comparable to those in literature, when a temperature of 100 °C was used. Further supporting that heating CB to 50 °C is not sufficient for fully melting CB, based on the hypothesis of fully saturated TAGs (tristearin and tripalmitin) crystallising separately from the rest, forming crystal structures with melting points above 50 °C[104, 124, 136]. Additionally, CB did not display a typical Arrhenius behaviour, but was better fitted with a VFT model[207], which describes a variable rate of diffusion increase alongside temperature. Such behaviour would not be expected, if full melting had occurred at about 50 °C, as the system's diffusion would keep increasing monotonically with temperature after reaching this temperature. However, it is around 50 °C that the rate first starts to level off, but after 70 °C are reached, it starts increasing again slightly (Figure 4.17). This

behaviour was observable, though at a lower degree, in the compressibility measurements (Figure 4.20), thus suggesting that the assumed liquid has a higher degree of structuring below such temperature. From this it is clear that more detailed measurements are required in this range of temperatures.

The differences between the 50 °C and the other two treatments are thus explainable from the diffusion measurements, due to the change of slope at 70 °C, as well as the high melting points of the fully saturated TAGs in CB. Whilst tristearin has a melting point above 70 °C, when in the presence of tricaprin (T_m<40 °C), at temperatures between 40 and 50 °C, it is soluble in concentrations up to 1 %[236]; however, this is less than the total amount of fully saturated TAGs in this CB (2%). Also, in the presence of triolein, Norton *et al.*[168] found that tripalmitin and tristearin, at mole fractions below 0.04, have a lower solubility than expected as determined by the higher melting points (50-60 °C) exhibited by the mixtures, in comparison to the theoretical predictions. Thus supporting the hypothesis presented here that 50 °C are not sufficient to fully melt or promote solubilisation of the fully saturated TAG species.

Contrastingly, the 80 and 110 °C treatments are expected to ensure the melting of the fully saturated TAGs, hence, these cannot can be used to explain the observed differences in kinetics (Figure 4.1). Regardless, it must be kept in mind that CB has other fully saturated minor components[104, 114, 177, 243, 244] with melting points of approximately 80 °C, such as glycolipids, di- and monoacylglycerols[245-247]. Therefore, if the work by Wang[139], where it was observed that TAGs need to be heated up to 6 °C above their melting temperature to avoid crystal memory, is extrapolated to these minor components, the ideal melting temperature of CB would be of approximately 86 °C. Thus reinforcing the need to perform further experiments in the temperature range between 80 and 110 °C.

By thermally pre-treating CB to higher temperatures, the minor components, which can serve as heterogeneous nucleation sites when not properly heated[120, 248-250], melt, thus delaying the onset of crystallisation. However, as mentioned before, the increase of T_{imax} also caused the transformation into the β-V-form to be enhanced. This is also thought to be related to the minor components, which during the cooling ramp can be expected to crystallise separately, thus limiting their ability to act as fillers of the

defects in the crystal lattice[120] or to create compound crystals. Therefore, they would no longer hamper polymorphic transformation into the β-V-form.

The previous hypothesis is considered to be more plausible than that of a melt- or strong crystal-memory effect as observed in polymers. Firstly, because it has been reported by Davis and Dimick[104] that the first crystallisable fraction of CB, after heating to 110 °C, has a higher proportion of the aforementioned minor components and saturated TAG species than the bulk. Secondly, the melt-memory effect is only observable when melting a crystal above its equilibrium melting temperature[231, 251, 252]. In this regard, only one study has been found where the equilibrium melting temperature of fats (T_m) has been determined. This T_m is defined as the temperature at which an infinite stack of extended chain crystals have reached an equilibrium state with the normal liquid, so that surface effects are negligible[252]. Toro-Vázquez *et al.*[253] estimated, using the linear Hoffman-Weeks method, that palm stearin has a T_m of 70.82 °C, which is almost 20 °C above its reported T'_m of 53 °C [254]. However, they used the the linear approach[252] which has been observed to underestimate the T_m for approximately 30 °C[255], thus making the non-linear Hoffman-Weeks method[255, 256] the most accurate. Importantly, the linear method assumes that the difference between the temperature of crystallisation and the T'_m is only caused due to a continuous thickening of the lamellae. However, differences also arise from enhanced thickening originated from secondary nucleation and kinetic factors[255].

Consequently, CB's the equilibrium T_m can be expected to be of approximately 87 °C, if considering an experimentally determined T_m of 37 °C for the β-VI polymorph[127]. This would make the 110 °C treatment the only treatment above the equilibrium melting temperature. However, further evidence is required to determine if this is the case. Such measurements would need to take into consideration that CB is a polymorphic fat, therefore, the presence of a single polymorph (β-VI) would be needed to ensure that all observed melting points at the different crystallisation temperatures are comparable.

An additional comment is needed on what has been termed in literature as "seed crystals"[104, 136, 170]. These seeds, as mentioned in the introduction, are thought to be composed of PLs in an inverse phase, having a melting point above 200 °C[129]. Therefore, even the maximum temperature used in this work (110 °C) would not be

expected to melt them. Hence, all studies here refer to a CB where, at best, all acylglycerol molecules will have melted, whilst most of the PLs will remain solid, thus acting as heterogeneous nuclei, reducing the times of induction. Note, though some PLs in their inverse phase have displayed such high melting points, other lipids, such as DSPC, at low hydration (< 10 %), have transition temperatures between 80 and 90 °C[257]. Thus, reinforcing that 80 °C are still not enough to fully melt all lipidic structures within CB, and suggesting that they will also play an important role in its nucleation.

Furthermore, considering the persistence of high melting acylglycerol species at temperatures above 50 °C, and that tristearin has been observed to nucleate at similar temperatures upon cooling[47, 168, 258], then, diffusion (Figure 4.17) and compressibility measurements (Figure 4.20) at temperatures below 50 °C would be representative of a mix of liquid CB and small crystallites, presumably in the α-form. However, it should be kept in mind that these measurements represent the bulk, thus, given that the diffusion and compressibility at temperatures below 50 °C still follow the main trend of liquid CB, then it is considered that these small crystallites do not have a large impact on the behaviour of the bulk.

So far, the focus of the discussion has been related to the polymorphs developed during the first 24 h, where an earlier appearance and more stable variant of the β-V-form was observed, when CB was pre-treated at higher T_{imax}. This is desirable in chocolate production, as the β-V-form is the key polymorph responsible for some of the characteristic sensory properties of chocolate[7]. Nevertheless, the development of the β-VI-form is also relevant. The transformation into this form, contrariwise to the β-V-form, is not desirable for it has been related to the presence of bloom and a waxy texture in the mouth[7, 214, 259].

Here, by increasing the T_{imax} used, a beneficial effect has been observed once more, as it delayed the transformation into this polymorph (Figure 4.2), though the 80 °C treatment had a stronger effect in this respect than the 110 °C. This was unexpected as the latter developed the β-V-form at an earlier stage and did not suffer variations in its d-spacing, suggesting a higher degree of stability. Regardless, the difference between these two treatments might be attributed to the 110 °C treatment having a lower amount of crystallised material during the earlier stages, as evidenced by the lower peak

intensity in the small-angle and lower SFC values. The remaining liquid material is then expected to crystallise overtime either by attaching itself to other crystals, hence helping them grow, or by nucleating separately, as observed in the PLM studies. It is this material that is then expected to accelerate the transformation into the β-VI-form, as this would lead to purer crystals, i.e. less formation of compound crystals, with a higher capacity of transformation.

Whilst the melting of minor components of CB is considered to be the main driver behind the differences between the different temperature treatments, it is important to keep in mind the proposed structure of CB in the molten state[166]. As mentioned in Chapter 4 TAGs are thought to associate in clusters in a back-to-back arrangement. TAGs from the isotropic medium are then thought to attach to these clusters, thus forming the first layer of the known lamellar structures of CB crystals. From the work of Sadeghpour *et al.* [166]it was observed that the degree of TAG occupancy of this layer decreases with temperature. Therefore, by melting CB at a higher temperature, more vacant spaces would need to be filled before crystallisation can start from these sites, thus delaying the onset of crystallisation.

A final comment is required to explain why the X-rays display evidence of crystallisation at a much later stage in the 110 °C treatment. While certain differences between techniques are expected, the delay of almost two hours observed through X-ray scattering, in comparison to the other techniques, is remarkable. This, however, suggests that though some crystallisation has occurred, crystallite sizes (number of lamellae) might be too small to give rise to Bragg diffraction peaks. There are two main explanations for this. First, that the degree of overall crystallisation is lower in the 110 °C treatment in comparison to the other two, thus not being detectable, which is supported by the SFC measurements. Second, that CB is truly nucleating into different lamellar structures, both 2- and 3-L, with and without a tilt, thus resulting in a large variability of the lamellar length which cannot be picked up by the X-rays, or at least is not easily detectable with a lab-based source.

The first explanation can be easily probed mainly via DSC and SFC measurements, though both present certain difficulties in the unambiguous analysis of their results. DSC measurements have the problem that the heat released on crystallisation is not only relatable to the amount of crystals produced, but also to the polymorph being

developed[123, 176]. Therefore, a higher enthalpy is not a direct indication of the percentage of crystallised material, especially in this case, where it has been established that polymorphs with higher stability (β'- and β-V-phase) crystallise simultaneously. This would explain the sharp increase in heat release observed in the 110 °C treatments on cooling, in comparison to the other two treatments (Figure 4.5 A). This observation leads to a second problem with the DSC measurements, i.e. the first thermal peak evolves during either the cooling ramp or upon reaching the isothermal temperature. As mentioned earlier in the results section, this does not allow for enthalpy (area under the curve) calculations. However, on comparing the second crystallisation event within the first two hours (Figure 4.7), it was evidenced that the maximum enthalpy was lower in the 110 °C treatment, even with the development of more stable polymorphs. The previous supports the hypothesis of such treatment presenting a decreased amount of overall crystallisation during the first two hours. Therefore, though with certain downsides, DSC analysis still helped to elucidate the main differences between treatments.

Finally, it was not only the 110 °C treatment were differences were observed. In Table 4.3, it is evident that the second crystallisation event was detected at an earlier stage using DSC and SFC, than with the X-rays. This suggests that this second crystallisation event is likely to be more closely related to secondary nucleation, and/or crystal growth, than to polymorphic transformation.

4.3 Conclusions

Using a variety of techniques, it was observed that pre-treating CB to either 50 or 80 °C results in a similar crystallisation behaviour during the first two hours, i.e. a two-step crystallisation, first nucleating into the α-phase, followed by transformation, and possibly nucleation, into the β'-IV-phase. Contrastingly, the 110 °C treatment seemed to crystallise directly into a mix of the α- and β'-IV phases. More importantly, though, both the 80 and 110 °C treatments resulted in a delayed transformation/nucleation into the β'-IV, but enhanced transformation into the β-V polymorph, in comparison to the 50 °C treatments. These effects are particularly strong in the 110/100 °C treatments.

The differences between the 50 and 80 °C treatments can be attributed to 50 °C not being sufficient for the complete melting or solubilising of crystals composed of fully saturated acylglycerol species. Differences between the 80 and 110 °C treatments are thought to be related to 110 °C being the only temperature at which the minor components (DAGs and MAGs, and potentially some PLs) are fully molten and/or solubilised. This hypothesis is thought to be more likely than T_{imax} having an effect on the overall molecular mobility, as no difference was observed in the diffusion measurements of the different treatments. However, local viscosity and diffusion changes cannot be discarded.

Chapter 5 Effect of pressure on the crystallisation behaviour of cocoa butter

For the studies of the effect of pressure on the crystallisation of CB, two main sets of experiments were performed, as previously described in the methodology. The first one consisted in pressurising CB (previously cooled to either 26 or 28 °C), followed by moulding and cooling. The obtained crystallised CB was then evaluated both by X-ray Scattering and DSC. However, such measurements only provide information post-treatment, and once the sample has been allowed to mature, i.e. for crystals to grow. Thus, they do not allow for the understanding of the mechanisms through which the application and/or removal of pressure effects the crystallisation behaviour of CB. Consequently, the second set of experiments was performed, involving in-situ measurements (X-ray scattering and PLM) during pressurising, isobaric, and de-pressurising processes.

The second set of experiments was then sub-divided into three subsets. The first one involved PLM observations of CB temperature and pressure-treated under the same conditions as in the first set of experiments. Based on the obtained results, for the second subset, which consisted of X-ray scattering measurements, the 100 bar treatment was not considered, and an additional temperature of 24 °C was included to help promote crystallisation. After de-pressurising the sample, they were cooled down to 14 °C. Additional experiments were performed at all three temperatures, but only applying 600 bar, followed by heating to 60 °C whilst still pressurised, to determine the stability of the formed structures. Finally, the third subset also involved PLM observations, but rather than applying a slow de-pressurisation protocol, pressure was decreased through pressure jumps in the range of ms. This

subset was performed with the objective of obtaining an insight into the effect of an almost adiabatic de-pressurisation.

5.1 Results

5.1.1 Post-processing studies of pressure-treated CB

All pressure treatments at 28 °C developed β'-IV and β-V polymorphs peaks in both the SAXS and WAXS regions, whereas when no pressure was applied, only a mixture of α and β'-polymorphs could be observed (Figure 5.1). However, it is notable that the 600 bar treatments developed less intense β-V peaks than the rest of the treatments.

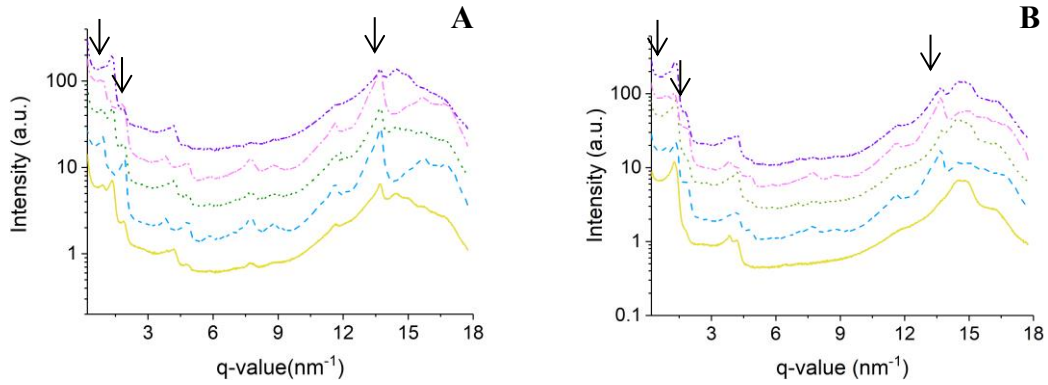

Figure 5.1 X-ray scattering patterns of pressure treated CB. Figure A corresponds to the samples cooled to 26 °C, and figure B to those cooled to 28 °C. The main peaks corresponding to the β-form are identified with arrows. The yellow pattern corresponds to ambient pressure, the blue (dashed) to 100 bar, the green (dotted) to 200 bar, the pink (dash-dot) to 400 bar and the purple (dash-dot-dot) to 600 bar.

The DSC thermograms showed that all treatments mainly developed a broad peak centred at ca. 36 °C corresponding to the β-V form (Figure 5.2). This peak, however, is not symmetrical and starts developing at approximately 20 °C, but increases drastically in intensity at roughly 28 °C, which suggests a small presence of the α-form, originated by the initial cooling to -30 °C, and a stronger one of the β'-IV form. In addition, from ambient pressure to 200 bar, at both temperatures, the centre of the peak shifted slightly towards the right. Regardless, it is not considered significant as at 400 and 600 bar the peak centre shifts back to the right.

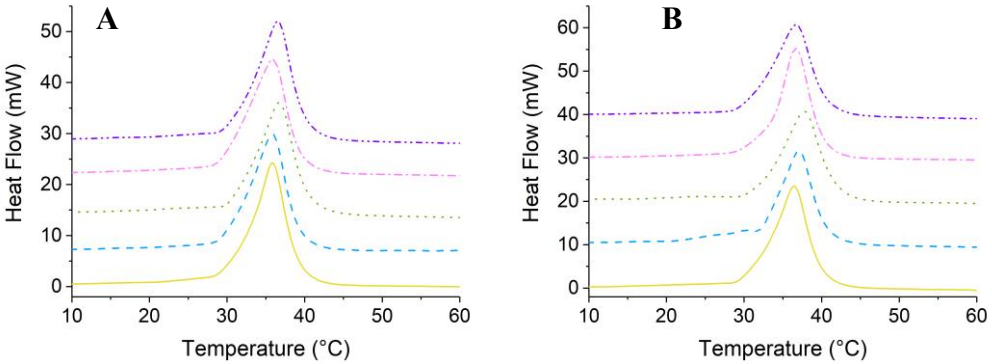

Figure 5.2 Melting thermograms of pressure treated CB. Figure A shows CB treated at 26 °C, and figure B CB treated at 28 °C. The yellow pattern corresponds to ambient pressure, the blue (dashed) to 100 bar, the green (dotted) to 200 bar, the pink (dash-dot) to 400 bar and the purple (dash-dot-dot) to 600 bar.

5.1.2 Pressure PLM

PLM allowed the observation of either the presence or absence of crystallisation. Here, it was possible to observe that none of the treatments crystallised at 100 bar (Figure 5.3), and only the 26 °C displayed evidence of crystallisation at the end of the isobaric period at 200 bar. CB, quenched at either 26 or 28 °C, and pressurised to either 400 or 600 bar crystallised. However, whilst the 400 bar treatment required the pressure to be held for a few seconds before developing crystalline material, the 600 bar treatment had already started to crystallise prior to reaching the set pressure. Regardless of the previous, all crystals, in all treatments, melted on releasing the pressure (Figure 5.4), suggesting the melting points of the crystalline forms is of 26 °C or even lower, i.e. they correspond to the α-polymorph.

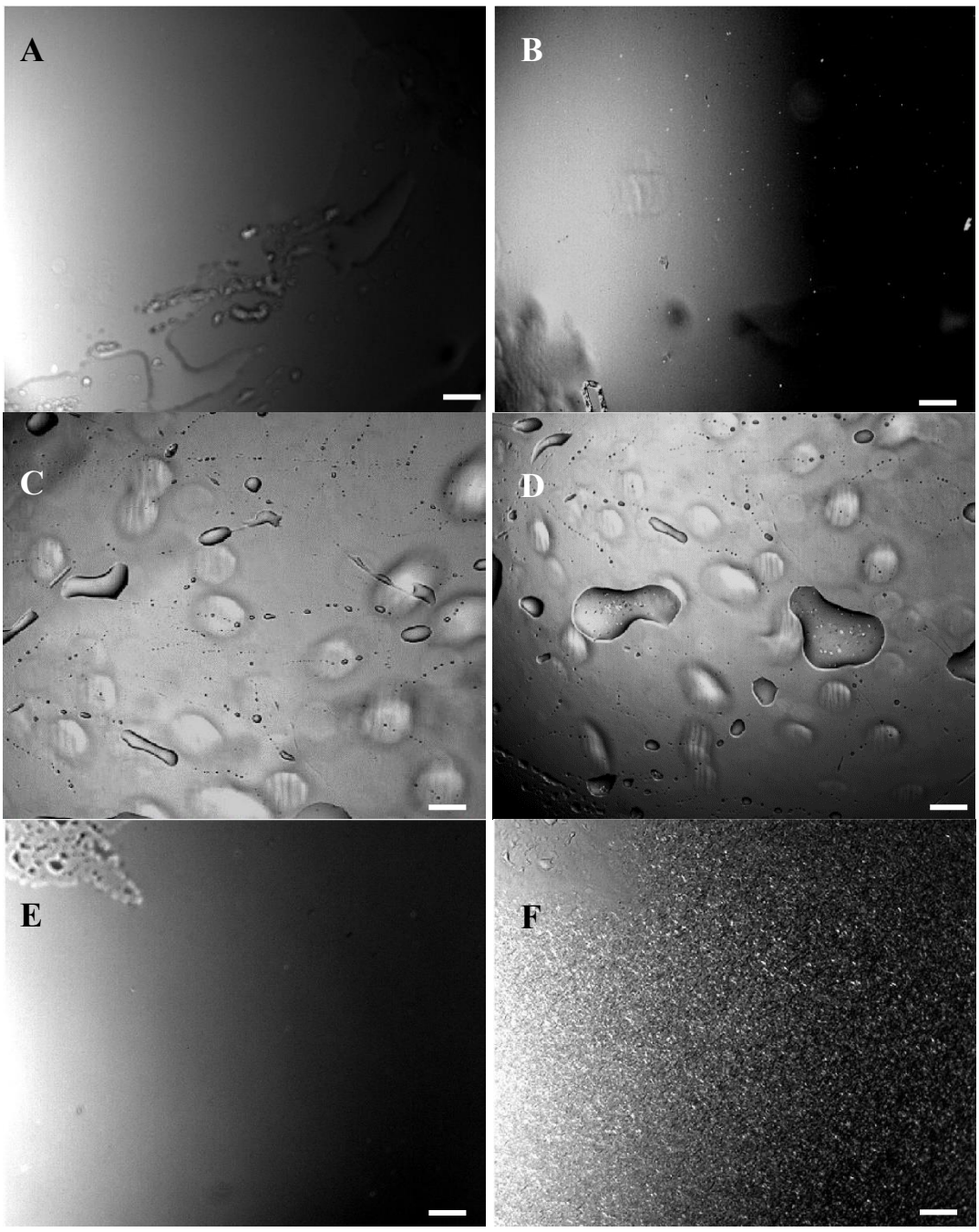

Figure 5.3 PLM images of CB quenched at different temperatures followed by a pressurisation, isobaric treatment, and de-pressurisation. Panels A-F represent treatments at 26 °C treated at 100 (A, B), 200 (C, D), 400 (E, F) bar. In all cases, the panel on the left is the first image taken on reaching the selected pressure, and the panel on the right corresponds to the last image of the isobaric treatment.

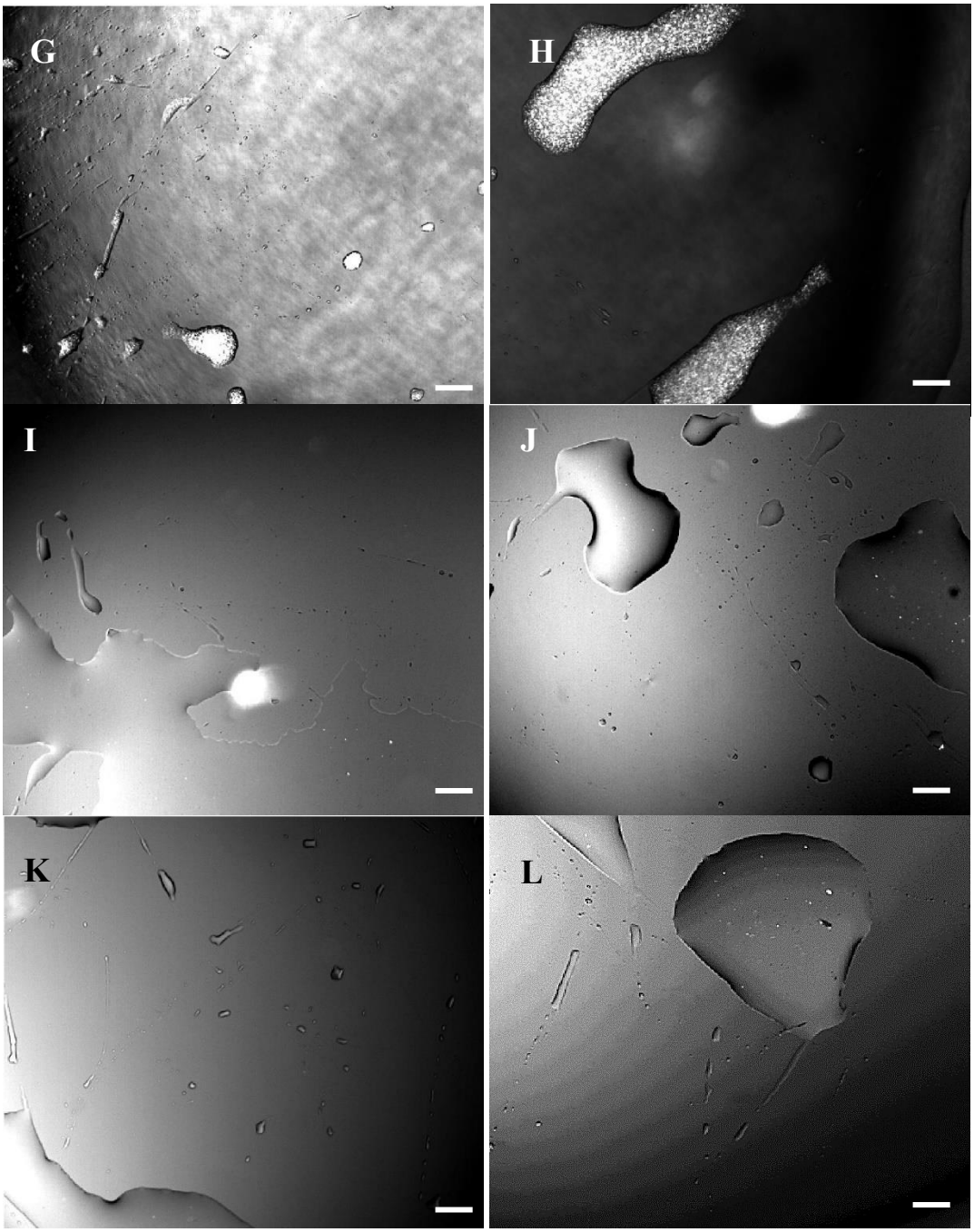

Figure 5.3 (cont). PLM images of CB quenched at different temperatures followed by a pressurisation, isobaric treatment, and de-pressurisation. Panels G-H represent treatments at 26 °C treated 600 bar. Panels I-L represent treatments at 28 °C treated at 100 (I, J), and 200 bar (K, L). In all cases, the panel on the left is the first image taken on reaching the selected pressure, and the panel on the right corresponds to the last image of the isobaric treatment.

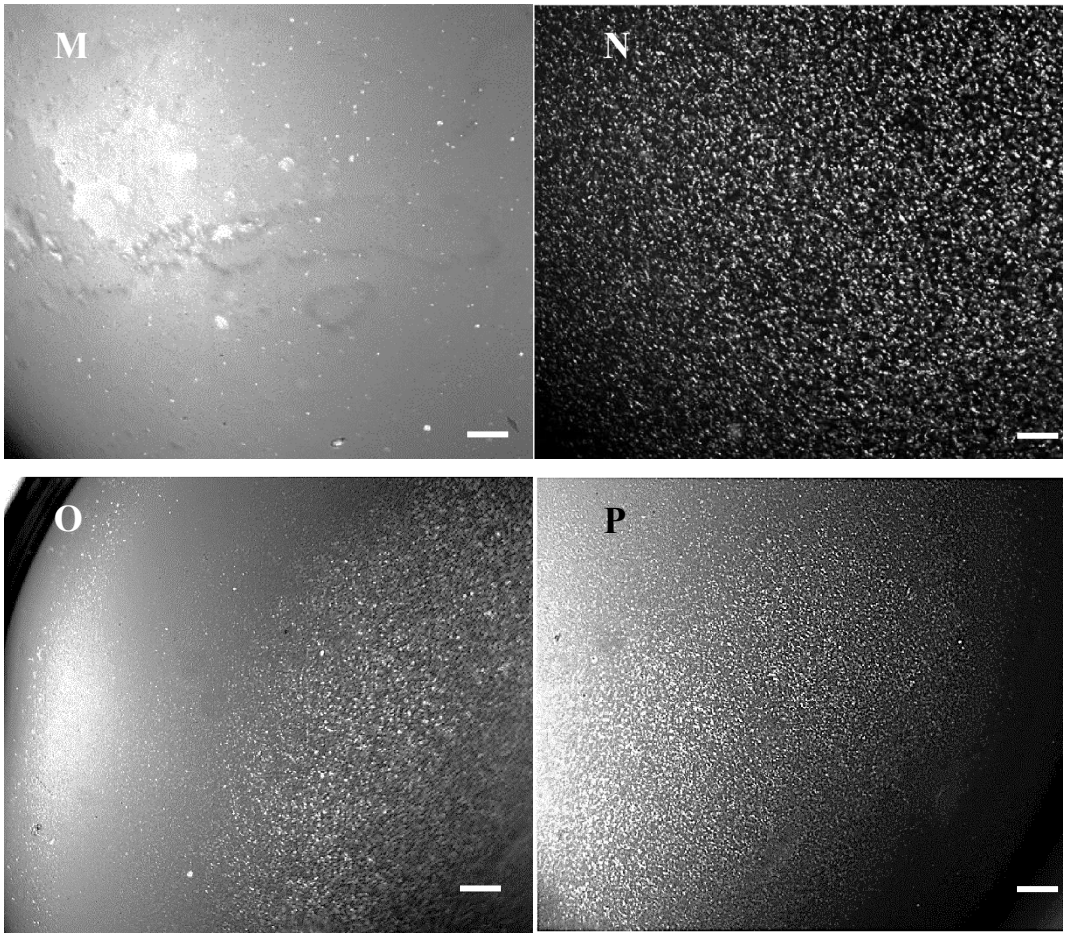

Figure 5.3 (cont.) PLM images of CB quenched at different temperatures followed by a pressurisation, isobaric treatment, and de-pressurisation. Panels M-P represent treatments at 28 °C treated at 400 (M,N) and 600 bar (O, P). In all cases, the panel on the left is the first image taken on reaching the selected pressure, and the panel on the right corresponds to the last image of the isobaric treatment.

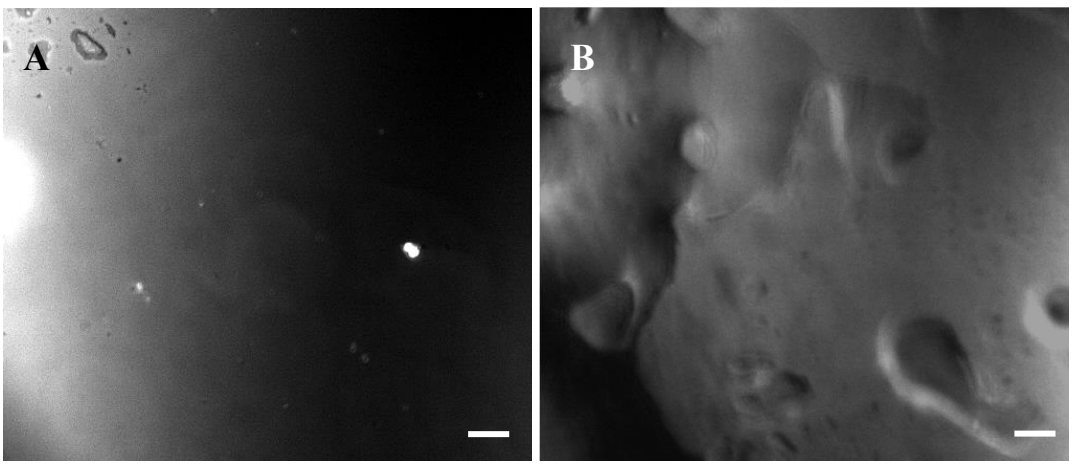

Figure 5.4 PLM images of thermally and pressure-treated CB after releasing the pressure back to atmospheric conditions. Both panels are 400 bar treatments, panel A at 26 °C, and panel B at 28 °C. Not all treatments are shown for due to the large similarity between them.

As in the first set of experiments the release of pressure was performed manually by, it was considered that the observed melting of the crystals could be related to an isothermal pressure-release, and it is presumed that the machine used for the preliminary experiments releases the pressure in an almost adiabatic manner for it occurs in less than a second. Therefore, for the second set of experiments pressure-jumps were used. However, as can be seen in Figure 5.5 C, the crystals melted once more after returning to ambient conditions.

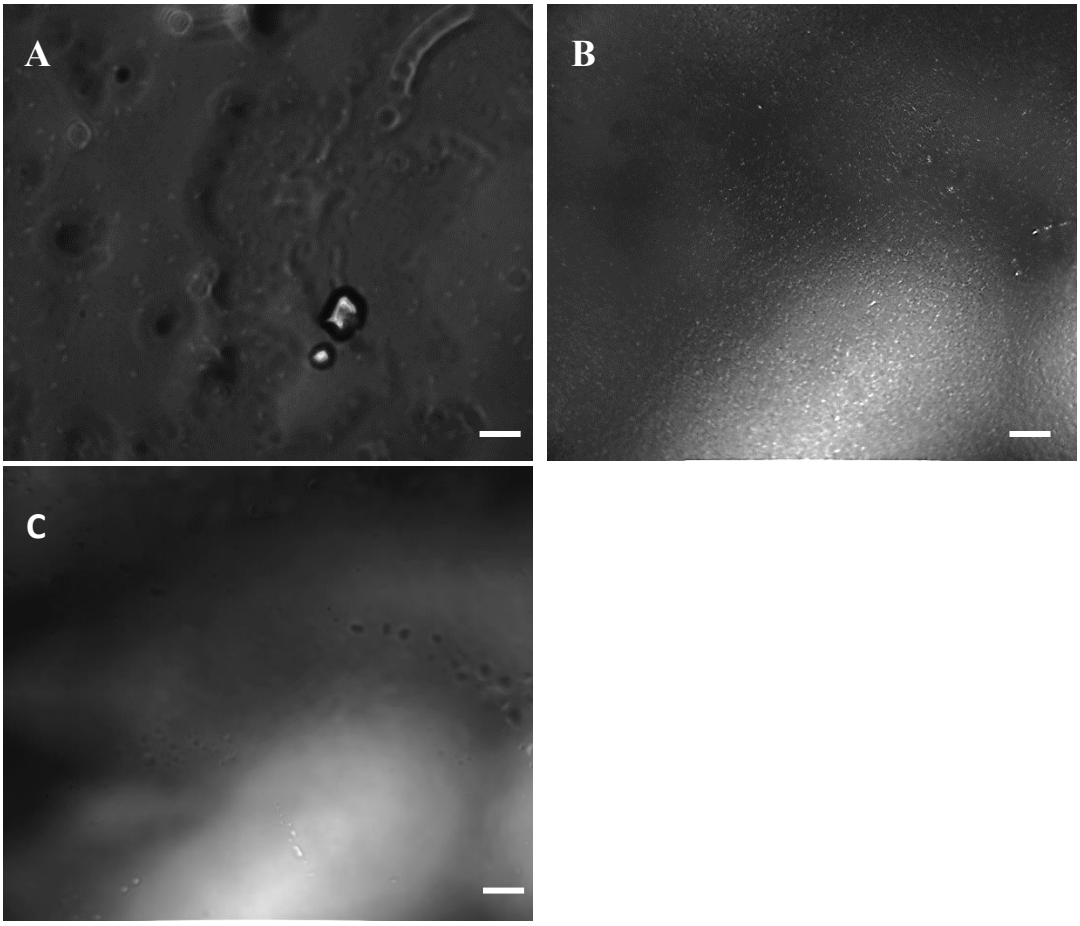

Figure 5.5 PLM images of CB quenched to 26 °C (panel A), pressurised to 400 bar and held isobarically for 2 min (panel B) and de-pressurised, using a pressure-jump, to ambient conditions (panel C).

During the cooling experiments, on decreasing the temperature down to 20 °C, crystallisation progressed as evidenced by the increase of intensity of the white specks across the field of vision. This was expected as in the isothermal experiments crystallisation started even before reaching such temperature (Chapter 4). Furthermore, these crystals did not melt on releasing the pressure, which allowed the determination of their melting point, and suggested that the generation of these crystals is primarily driven by the cooling rather than the pressure.

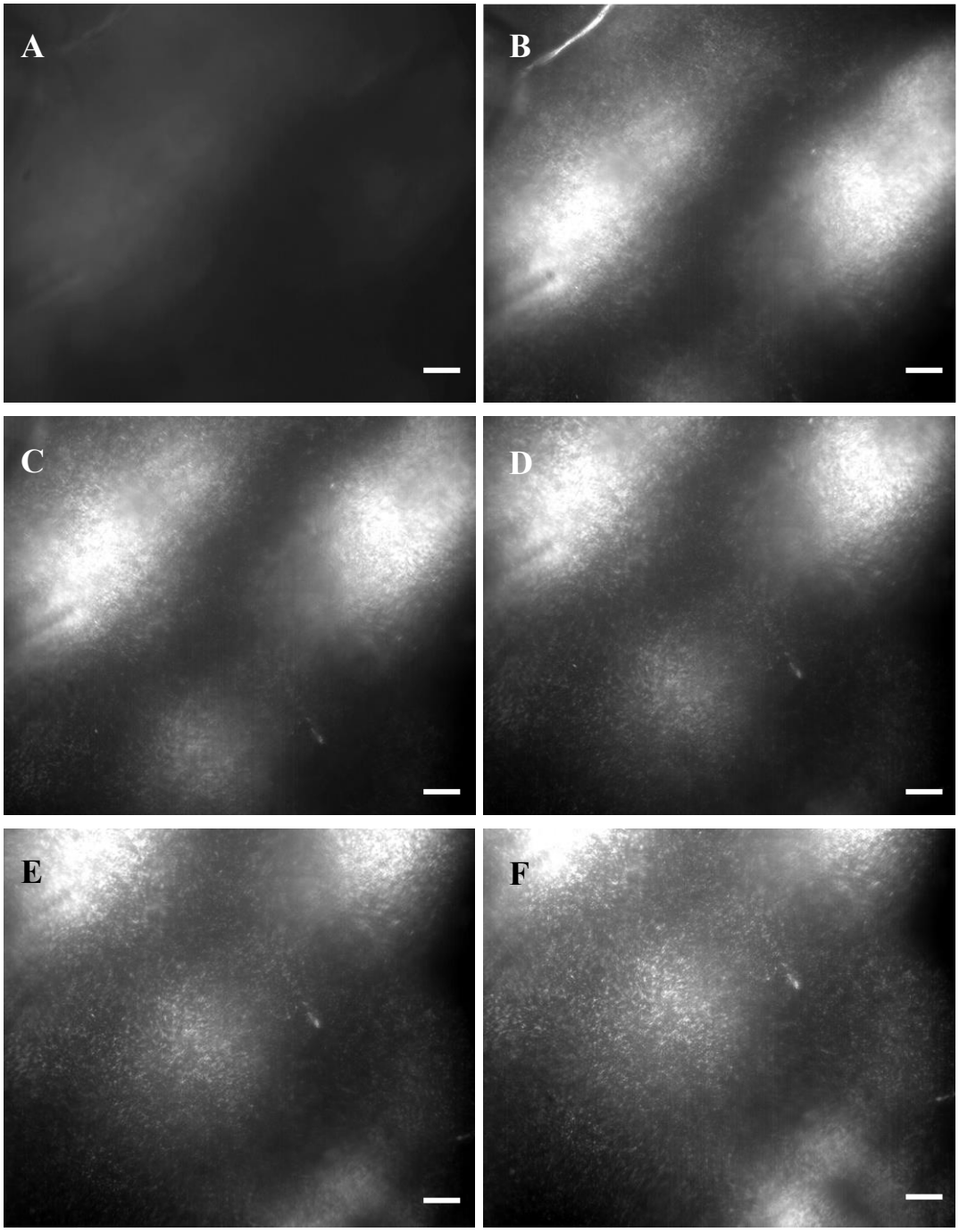

Figure 5.6 PLM images of CB quenched to 26 °C (panel A), pressurised to 400 bar, and held isobarically for 2 min (panel B), followed by a cooling ramp down to 20 °C. Panels C-F show CB on reaching 25, 24, 23, and 22 °C, respectively.

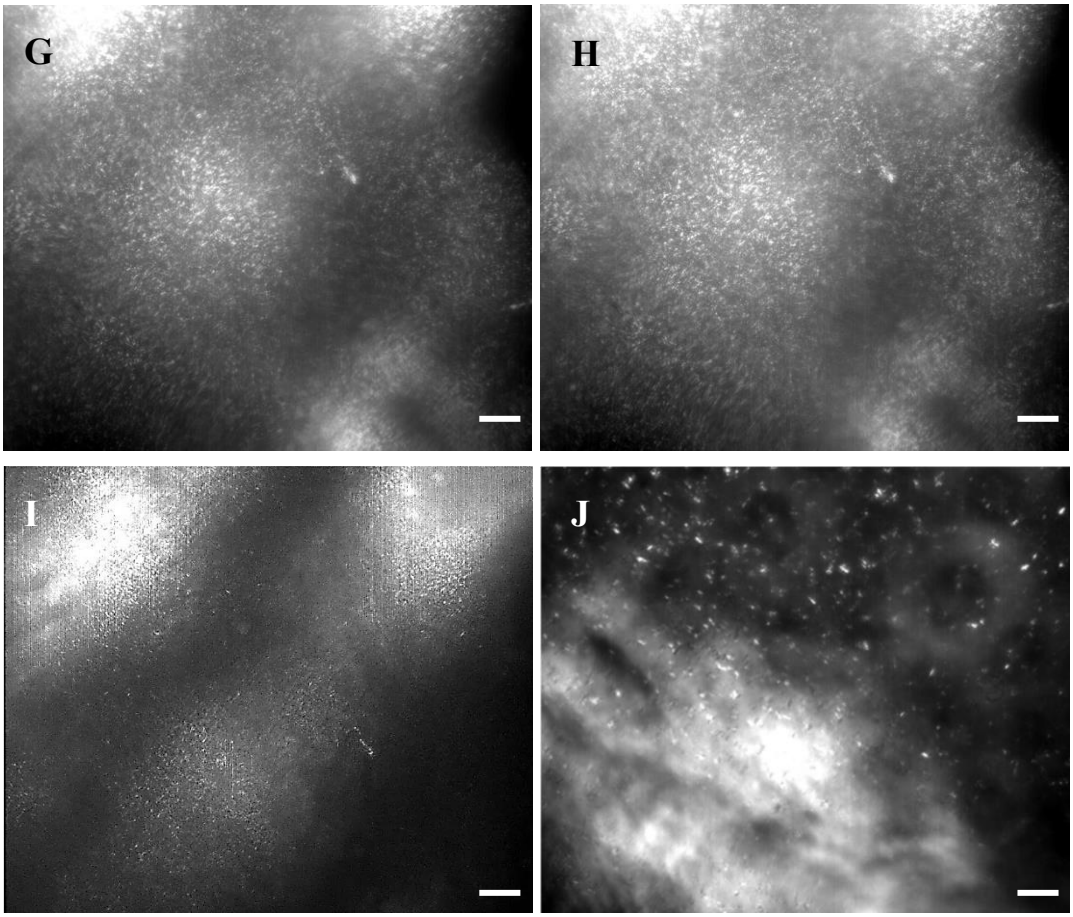

Figure 5.6 (cont.) PLM images of CB quenched to 26 °C, pressurised to 400 bar, and held isobarically for 2 min, followed by a cooling ramp down to 20 °C, and de-pressurisation to ambient conditions (panel I) . Panels G and H show CB on reaching 21 and 20 °C, respectively. Panel J shows the image of a non-pressurised treatment that followed the same thermal treatment.

After the pressure was released, re-focusing was necessary, hence, the area of observation was shifted (Figure 5.6 I). Nevertheless, it is possible to observe that the change in pressure did not melt the crystals formed after cooling, which allowed for the visual determination of their melting ranges. From Figure 5.6 , it is possible to observe that without the application of pressure, crystallisation was also induced but to a lesser extent, as individual needle-like crystals are observable.

Melting ranges of crystals cooled to 20 °C

Table 5.1 Comparison of the melting ranges of the crystalline structures developed during isobaric (400 bar) crystallisation of CB thermally treated from 26 to 20°C.

Condition of measurement	Start temperature (°C)	End temperature (°C)
400 bar	29.97	34.52
Atmospheric	24.05	28.10
Atmospheric (no pre-treatment)	22.55	28.29

The melting temperatures at 400 bar were approximately 6 °C above that of those measured at atmospheric pressure, which agrees with the values reported by Grenier *et al.*[86, 260]. The effect of pressure on the melting point of CB also agrees with that obtained by using the empirical equation deduced by Yasuda *et al.* $T = 0.14P + 26.6$[89], where T is in °C and P in MPa. Therefore, if we consider that the slope remains the same, and only the offset is different (24.05), then at 400 bar, a melting temperature of 29.65 °C would be expected, which is quite close to the one here observed.

In the case of the end of melting temperature, the difference between the estimated value, 33.4 °C, and that measured, 34.52 °C, is larger. However, it should be considered that PLM is not the most precise method of determining melting points and more importantly, that the model applied is empirical. Consequently, the experimental and theoretical melting points are still considered to be in good agreement.

Independently of the observed temperature increase under pressurised conditions, it is notable that the temperature ranges at ambient pressure correspond to those of the β'-form rather than the α-form, even if the morphology observed is usually related to the latter. Moreover, in both determinations at atmospheric pressure, the end of the melting process was at 28 °C. Whilst this temperature is higher than would be anticipated, it can be related to the slow heating rate (ca. 0.8 °C/min) used, which based on literature, can induce polymorphic transformations [29, 45, 261-263].

5.1.3 Synchrotron source X-ray Scattering measurements

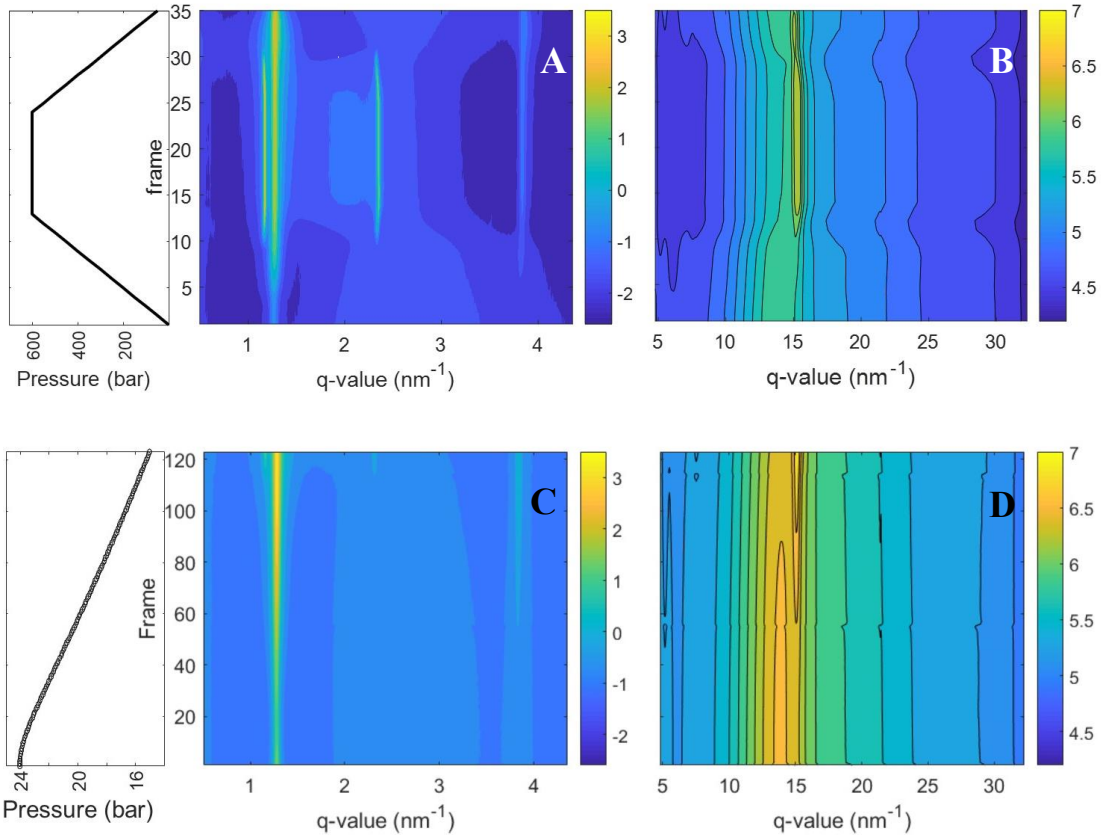

Figure 5.7 Contour plots of SAXS (A and C) and WAXS (B and D) of CB quenched to 24 °C during pressurisation to 600 bar held for 80 s and de-pressurised to atmospheric conditions, and the subsequent cooling to 13 °C (C and D). Panels A and C only show depressurisation down to 50, as the diffraction pattern at ambient pressure was measured during the cooling protocol.

The evolution of the crystallisation peaks was initially followed by contour plots, such as the ones portrayed in Figure 5.7 (See Appendix A for all treatments). In these, it was possible to observe that treatments developed a maximum of two structures in the SAXS region, identified from their peaks, at 1.27 nm^{-1} (49.5 Å) and 1.117 nm^{-1} (56.2 Å), as the α_1- and α_2-forms, respectively. When both forms developed, the α_2-form was the second one to crystallise and was the least stable of the two, as evidenced by its faster disappearance on depressurisation or heating. In the WAXS region, only one peak developed positioned at approximately 15 nm^{-1} (4.19 Å). For ease of visualisation, the information regarding the conditions under which the different peaks were present is summarised in Table 5.2.

Table 5.2 Ranges in which the different crystalline peaks were observable at the different P_{max} and T_{cryst}, and T_{imax} treatments. The ranges indicate the pressure (bar) at which peaks started developing, and were no longer observable. In cases where the peaks only developed during the isobaric period, the time of appearance is identified between brackets in seconds. '---' is used to identify where no peaks developed, 'atm' indicates the presence of the peaks at amospheric pressure.

Pressure (bar)	Polymorph	24 °C	26 °C	28 °C
Atmospheric	α_1	atm – atm	---	---
	WAXS	---	---	---
200	α_1	200 (16 s) – atm	200 (39 s) – atm	---
	WAXS	200 (57 s) – atm	200 (75 s)* – atm*	---
400	α_1	50 – atm	400 (14 s) – atm	400 (26 s) – atm*
	α_2	400 – 200	---	---
	WAXS	300 – atm	400 (44 s) – atm*	400 (60 s) – 50*
600 (T_{imax}50 °C)	α_1	atm – atm	600 (28 s) – atm	500 – atm *
	α_2	550 – 300	600 (70 s) – 50	550 – 250
	WAXS	450 – atm	600 (52 s) – atm*	500 – 50
600 (T_{imax}100 °C)	α_1	atm – atm	400 – atm	550 – atm*
	α_2	400 – 300	550 – 400	---
	WAXS	400 – atm	500 – 50	500 – 50

* In these treatments the peaks were very broad, not allowing for the calculation of spacings.

From the previous table, it is evident that at 24 °C crystallisation started even within the first 10 minutes of equilibration at ambient pressure, which contrasts with what was observed van Malssen *et al.* [20], who only observed crystallisation after four hours. However, these authors only looked at the WAXS region, and in this work, crystallisation was made evident solely in the SAXS region, thus underlining the importance of always analysing both regions of the scattering pattern during crystallisation studies.

More particularly, at 26 °C, the α_1-form developed during the isobaric period regardless of the P_{max} used, when using a T_{imax} of 50 °C. In addition, when the pressure increased from 200 to 400 bar, crystallisation occurred at an earlier stage. Surprisingly, though, the 600 bar treatment took longer to crystallise than at 400 bar.

Contrastingly, at a higher T_{imax}, in the 600 bar treatment peaks developed during the pressure ramp period, rather than during the isobaric time. In all cases, the SAXS peaks remained after reducing the pressure to ambient conditions.

When the T_{cryst} was increased to 28 °C, the SAXS peak only developed after holding the sample at 400 bar isobarically or on increasing the pressure to at least 500 bar, the latter being the only condition at which the WAXS peak developed. Overall, this wide-angle peak developed at a later stage than the SAXS peak, irrespective of the T_{cryst} used. Once more, evidence of crystallisation in the SAXS region was evident upon the release of pressure, though the peaks were too broad for fitting.

The α_2-form required either higher pressures or longer isobaric times than the α_1-form to crystallise. In the 24 °C treatment, its SAXS peak developed at either 400 or 550 bar and disappeared on depressurisation to 200 or 300 bar, depending on whether the sample had been treated at 400 or 600 bar, respectively. At 26 °C, it only developed on applying 600 bar for 28 s, and remained stable on reducing the pressure to 50 bar. In contrast, at 28 °C it started developing at a slightly lower pressure, 550 bar, but disappeared earlier during depressurisation, at 250 bar. As a final comment, on increasing the T_{imax}, however, the α_2-form did not develop. Hence, the α_2-form is considered an unstable and transient form.

The different peaks developed were not only analysed in terms of their time and pressure of appearance and disappearance, but also their positions were identified, from which d- and short-spacings were calculated and plotted (Figure 5.8 and Figure 5.10). Given that the α_2-form was only present fleetingly, and in a few of the treatments, its d-spacings were plotted independently of those of the α_1-form (Figure 5.10). In the case of the latter, for ease of view, its spacings were summarised in Figure 5.8, as it was present in all treatments, and in a larger proportion of the pressure protocol. This figure then shows only the values at the start of the crystallisation (initial), at the end of the isobaric treatment at P_{max} (isobaric), and the one after decreasing the pressure to 50 bar.

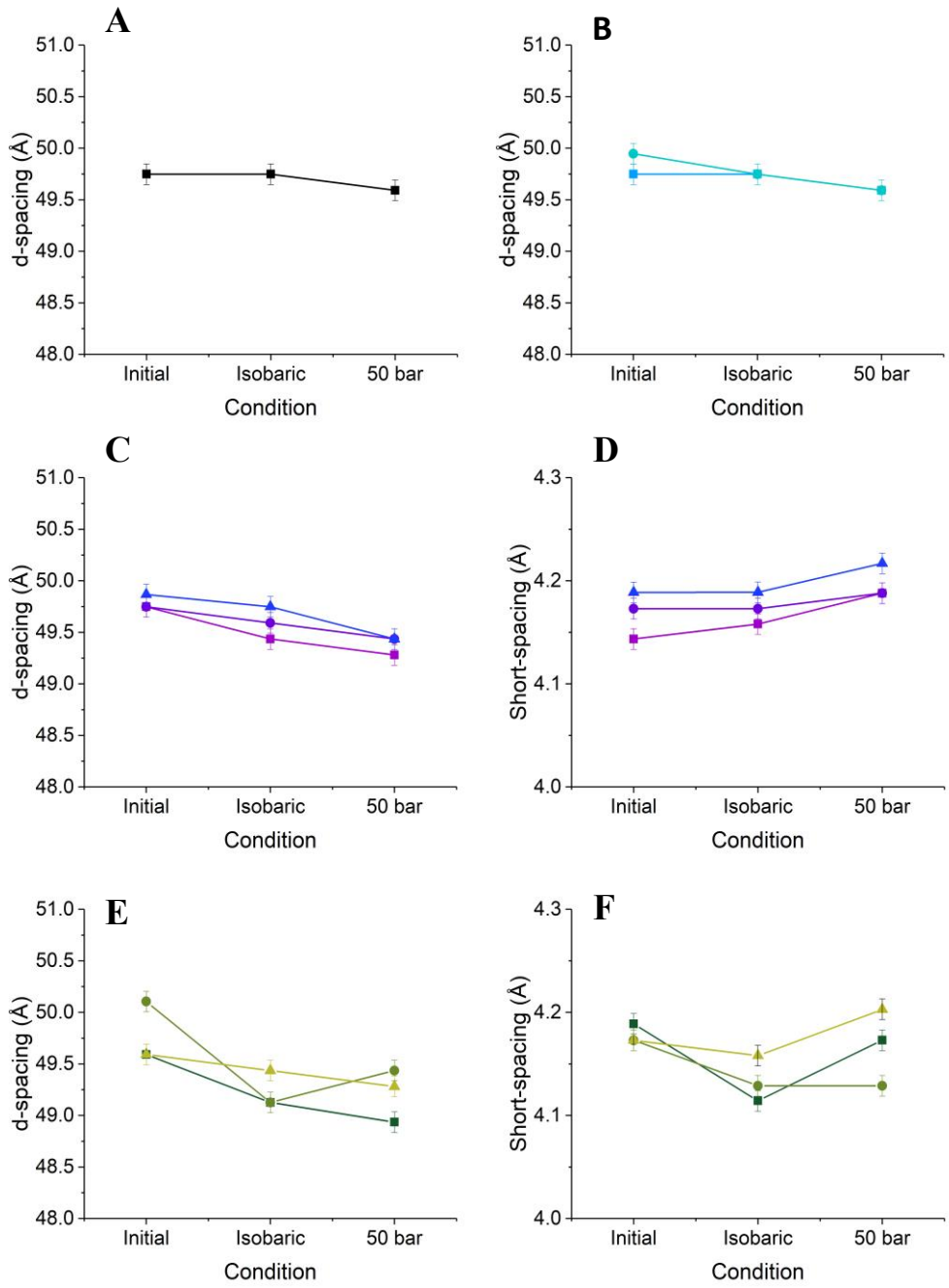

Figure 5.8 Evolution of the spacings of the pressure-treated CB, from the first well-developed peak, through the end of the isobaric period at P_{max}, and down to 50 bar. Panels A and B correspond to the d-spacing at atmospheric pressure and at 200 bar, respectively. Panels C and E, correspond to the d-spacings of the 400, and 600 treatment with a T_{imax} of 50 °C, respectively. Panels D and F show the short-spacings of the 400, and the 600 bar treatment with a T_{imax} of 50 °C, respectively. Squares refer to the 24 °C treatment, circles to 26 °C, and triangles to 28 °C.

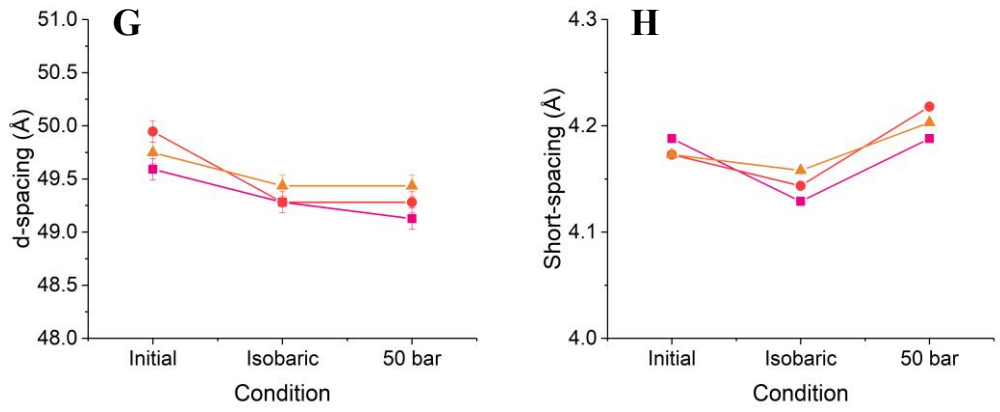

Figure 5.8 (Cont.) Evolution of the spacings of the pressure-treated CB, from the initial well-developed peak, through the end of the isobaric period at P_{max}, and down to 50 bar. Panel G corresponds to the d-spacings and panel H to the short-spacings of the 600 bar treatment with a T_{imax} of 100 °C, respectively. Squares refer to the 24 °C treatment, circles to 26 °C, and triangles to 28 °C.

Overall, pressure-treating CB resulted in a small reduction of the d-spacings of the α_1-form, especially at 28 °C. In the wide-angle region, larger overall variations were observed depending on all three parameters; however, on releasing the pressure a consistent increase of short-spacings, defined as the difference between the initial and final (50 bar) values, was evident in most treatments. The 600 bar treatment was an exception as an overall decrease was observed at a T_{cryst} 26 °C.

Despite the agreement between treatments on the decrease of the lamellar length (d-spacing), the specific values and their evolution at the different stages of the pressure protocol differed between treatments. At 200 bar, the 24 °C d-spacing remained stable during the isobaric period. This is in contrast with the 26 °C treatment where the d-spacing decreased (0.4%) during the isobaric time, eventually reaching the same d-spacing of the 24 °C treatment after releasing the pressure. Unfortunately, at 200 bar no peaks developed in the wide-angle, or were too broad to be positioned correctly, hence not allowing for further insight in the changes occuring in the FA chains. It is important to mention, regardless, that this treatment resulted in the exact same d-spacings and behaviour as the ambient pressure treatment, thus indicating that it did not impact the lamellar structure, but only the amount of crystallisation, as seen in the higher intensity of its peaks (Figure 5.9).

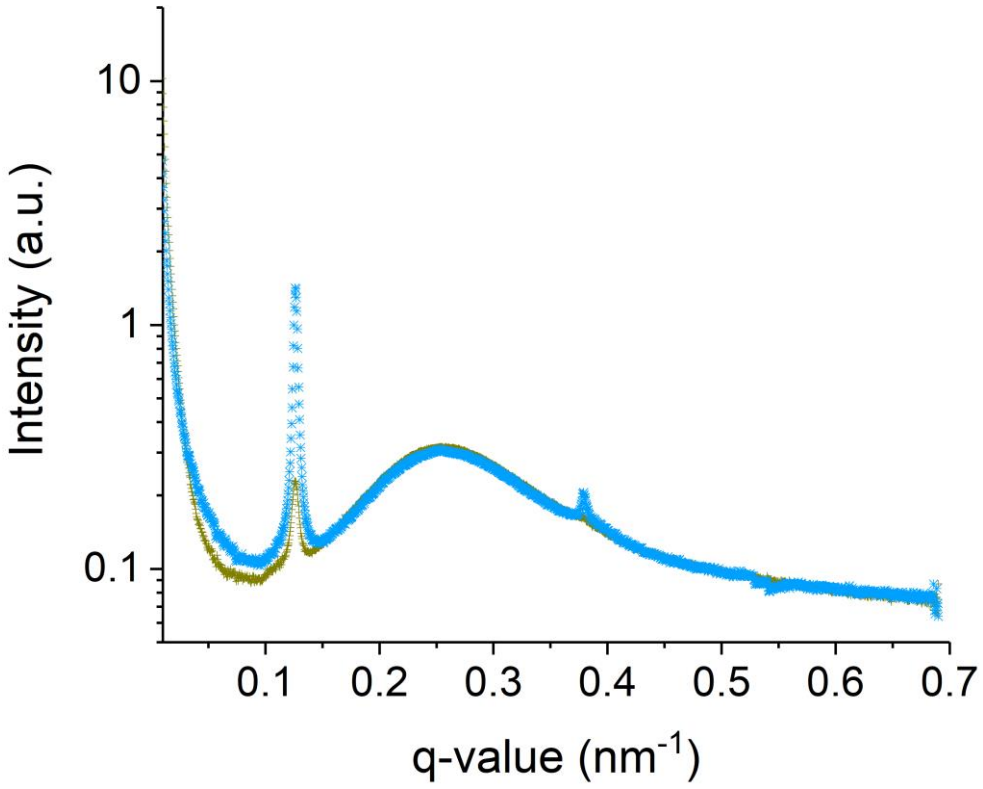

Figure 5.9 Scattering patterns of the 200 bar treatment at 24 °C after 80 s of isobaric time (green '+'), and its equivalent in time at atmospheric pressure (blue 'X')

At 400 bar, the initial d-spacings at all temperatures were very similar. At this pressure, the 28 °C treatment displayed the smallest decrease (0.24 %) in d-spacing upon reaching the maximum isobaric time at P_{max}. On releasing the pressure, however, the d-spacings continued to decrease at all T_{cryst}s used, especially at 28 °C (0.63 %).

Regarding the short-spacings of the 400 bar treatments, the initial values differed between the different T_{cryst}s in the following order 24 < 26 < 28 °C. Moreover, at all T_{cryst}, the short-spacings suffered an overall increase, especially in the 24 °C treatment (1.07 %). Interestingly, the short-spacings of the 26 °C and 28 °C treatments remained stable from the first sign of crystallisation to the end of the isobaric time, contrarily to the 24 °C treatment where a small increase was observed (0.35 %). Upon releasing the pressure, the 26 °C treatment was the one which displayed the smallest short-spacing increase (0.36 %), and the 24 °C treatment the largest (0.72 %).

At 600 bar, a larger overall decrease in the d-spacings is observed when compared to the other P_{max}, particularly at 24 °C and 26 °C (-1 and -1.34 %, respectively). The latter treatment also unexpectedly crystallised at a later stage than the 28 °C treatment, and developed the largest initial lamellar structure. Moreover, the 26 °C treatment developed the largest d-spacings of all treatments, and whilst it did result in a decrease of d-spacing during the isobaric period at P_{max} (2 %), on decreasing the pressure its d-spacing slightly increased (0.4 %). This last behaviour is in opposition to what was observed in the rest of the treatments.

Regarding the short-spacings, all treatments underwent a decrease under isobaric conditions (-1.78, -1.06 and -0.36 % in order of increasing T_{cryst}), as opposed to the 400 bar treatment where no change was observed except at 24 °C where a small increase was evident. On releasing the pressure, however, at 24 and 28 °C the short-spacings increased (1.43 and 1.8 % respectively), similarly to the 400 bar treatments. Contrastingly, at 26 °C the short-spacing remained stable. Henceforth, its final short-spacing was the smallest of the three T_{cryst}s used.

In contrast to the previous treatment, when a higher T_{imax} was used at a P_{max} of 600 bar, less fluctuations of the d-spacings were observed. Yet, similarly to the 50 °C treatment, at 26 °C the largest overall decrease was observed (-1.33 %), and at 28 °C the least (- 0.63 %). At a closer look, the initial d-spacings differed, once more, between the different T_{cryst} treatments 24>28>26 °C. Then, during the isobaric period at P_{max}, the d-spacing decreased at all T_{cryst}s, but more strongly at 26 °C (-1.33 %). On decreasing the pressure to 50 bar, only the 24 °C decreased in d-spacing (0.31 %), whilst the other two treatments remained stable, unlike any other treatment. The previous resulted in the 28 °C treatment having the largest final d-spacing, whilst the 24 °C treatment remained the lowest. The latter is comparable to the 600 and 400 bar treatments.

As mentioned before, fewer fluctuations in the short-spacings were also observed on applying a higher T_{imax}. This dampening effect of the T_{imax} on the effects of the application of pressure was stronger in the short-spacings, than in the d-spacings. Regardless, similarly to when applying a T_{imax} of 50 °C, the short-spacings decreased during the isobaric treatment at P_{max} (1.41, 0.71 and 0.36 % in order of increasing T_{cryst}). Upon reducing the pressure to 50 bar, the short-spacings at all T_{cryst}s increased,

in agreement with the other treatments. This behaviour, just as the initial reduction, was stronger at 24 and 26 °C (1.8 and 1.43 %, respectively). Hence, after the full pressure protocol, the short-spacings were larger than the initial ones, and with small variations between the different T_{cryst}s applied. The final short-spacings at 24 and 28 °C are comparable to those obtained on using a T_{imax} of 50 °C, whereas at 26 °C the short-spacing is larger (2 %) on applying a higher T_{imax}.

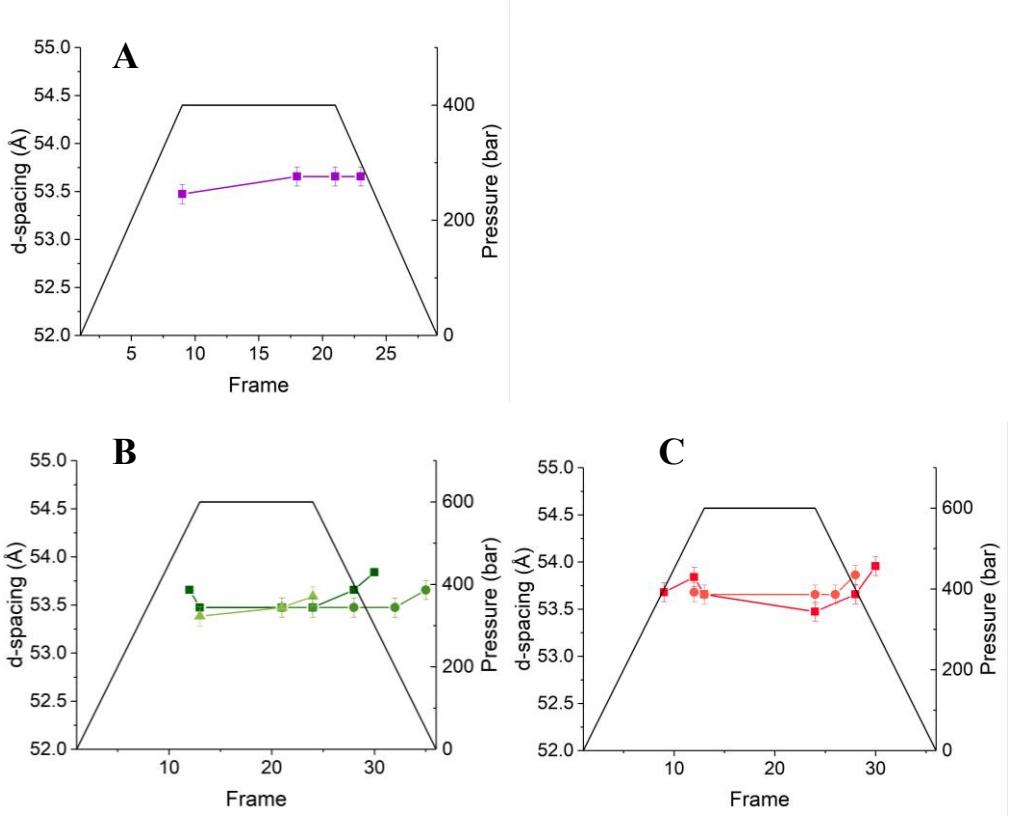

Figure 5.10 Evolution of the d-spacings of the α_2 form at 400 (A-purple), 600 (B-green), and 600 bar with a T_{imax} of 100 °C (C-red). The squares correspond to 24 °C treatments, the circles to 26 °C and the triangles to 28 °C treatments.

After describing the behaviour of the α_1-form in the small- and wide-angles, we can now turn to the α_2-form (Figure 5.10). Its evolution also depended on the different P_{max}, T_{cryst} and T_{imax} applied. Moreover, as has already been mentioned, only a few treatments developed this phase, namely the 24 and 28 °C treatments at 400 bar, all treatments at 600 bar, and the 24 and 26 °C treatments at 600 bar with a T_{imax} of 100 °C. The 400 bar treatment resulted in a small increase of d-spacing at 24 °C during the isobaric time (0.34 %), and remained stable on releasing the pressure. Similarly, the 28 °C treatment at 600 bar resulted in a small increase in d-spacing during the isobaric treatment (0.34 %). Contrastingly, the rest of the 600 bar treatments resulted in a small decrease of d-spacings on the application of pressure,

though on depressurising the system, the d-spacing increased (0.34 % and 0.20 % for the 24 and 26 °C treatments respectively) and reached a larger value than the initial one. On applying a higher T_{imax}, several effects were evident. Firstly, it hindered the development of the α_2-form at 28 °C. Secondly, it decreased the stability of the one formed at 26 °C, understood by its earlier disappearance and larger d-spacings. Thirdly, at 24 °C larger initial d-spacings were observed, though after the isobaric treatment at P_{max} the d-spacings are the same between the two T_{imax} treatments.

In summary, it can be said that regardless of the P_{max} used, an irreversible decrease of d-spacing was observable, whereas the opposite was evident in the short spacings. Moreover, at 600 bar, independently of the T_{imax}, a T_{cryst} of 26 °C resulted in the largest variations of spacings, whilst applying 28 °C resulted in the opposite effect. In contrast, at 400 bar, the 28 ° treatment was the one that induced a larger variation of spacings. Regardless, at this temperature a similar overall decrease was observed at all different P_{max}. As an additional note, the application of 200 bar did not impact the crystal structure at 24 °C, though it did enhance the degree of crystallisation. Finally, by increasing the T_{imax} from 50 °C to 100 °C, the effects of the application of pressure on molten CB were reduced.

Crystallisation behaviour of pressure-treated CB upon cooling

From Table 5.3, it is possible to observe that when using a T_{cryst} of 26 °C, pressure is indispensable to obtain crystals in less than 4 h as determined by van Malssen *et al.* [20]. This is evidenced by the pressure-treated samples still presenting Bragg peaks after depressurisation, whereas the one at ambient pressure required further cooling. However, at 28 °C, none of the treatments retained any Bragg peaks, therefore cooling was indispensable for crystallisation. However, all treatments developed the α_1-form SAXS peak at an average of 24 °C which is not unexpected as the 24 °C treatments crystallised without the need of the application of pressure. Nevertheless, it is tempting to say that as the applied pressure increased, the cooling required for re-crystallisation is slightly decreased, the 600 bar treatment with a T_{imax} of 50 °C being an outlier, as will be discussed further in the next section. Yet, further

experiments are needed to ascertain this behaviour as the temperature difference is small.

Table 5.3 Temperatures (°C) of appearance of the different crystalline peaks during the cooling protocols of the CB pre-treated at different P_{max}, T_{cryst} and T_{imax}.

Pressure (bar)	Polymorph	24 °C	26 °C	28 °C
Atmospheric	α_1	24	23.25	23.71
	α_2	16.49	16.37	16.85
	WAXS	22.48	20.93	21.59
200	α_1	24	26	23.25
	α_2	16.27	16.35	16.41
	WAXS	24	22.62	20.82
400	α_1	24	26	25.98
	α_2	15.21	15.98	16.46
	WAXS	24	23.06	21.83
600 (T_{imax}50 °C)	α_1	24	26	24.05
	α_2	18.80	18.62	---
	WAXS	24	26	21.47
600 (T_{imax}100 °C)	α_1	24	26	25.80
	α_2	15.37	15.74	16.68
	WAXS	24	23.07	22.80

From Table 5.3, it is possible to observe that when using a T_{cryst} of 26 °C, pressure is indispensable to obtain crystals in less than 4 h as determined by van Malssen *et al.* [20]. This is evidenced by the pressure-treated samples still presenting Bragg peaks after depressurisation, whereas the one at ambient pressure required further cooling. However, at 28 °C, none of the treatments retained any Bragg peaks, therefore cooling was indispensable for crystallisation. However, all treatments developed the α_1-form SAXS peak at an average of 24 °C which is not unexpected as the 24 °C treatments crystallised without the need of the application of pressure. Nevertheless, it is tempting to say that as the applied pressure increased, the cooling required for re-crystallisation is slightly decreased, the 600 bar treatment with a T_{imax} of 50 °C

being an outlier, as will be discussed further in the next section. Yet, further experiments are needed to ascertain this behaviour as the temperature difference is small.

Regarding the development of the WAXS peak, presumably belonging to the α_1-form, overall, it required more cooling than the small-angle peak, except at 24 °C of the pressure-treated samples as they retained their WAXS peak after releasing the pressure. At 26 °C, the temperature at which peaks developed in this region increased alongside the P_{max}, though this effect was dampened by the use of a T_{imax} of 100 °C. At 28 °C the temperatures of peak development are similar between treatments, suggesting that at this temperature, it is harder for the FA chains to pack in any sub-cell, regardless of the previous pressure treatment.

Regarding the α_2-form SAXS peak, it required a higher degree of cooling than the α_1-form, as would be expected from its later development under pressurised conditions. However, whilst most treatments required a similar degree of cooling, independently of the P_{max} or T_{cryst} used, the 600 bar treatment is the one that requires the least amount of cooling, irrespective of the T_{cryst} applied. This is particularly surprising at 24 °C treatment, for during the pressure treatment, the development of the α_2-form was comparable, thus, the earlier development on cooling cannot be directly associated to remaining structuring.

Just as the temperatures at which CB re-crystallised upon cooling varied depending on the treatment, so did the d-spacings as shown in Figure 5.11. As expected, the 28 °C treatment resulted in the largest d-spacings of the three T_{cryst} treatments, even after further cooling. This is because the other two treatments had visible (in the SAXS regime) remaining crystalline material after the pressure treatment, whereas the 28 °C treatment did not. Hence, at the two lower temperatures the crystals that have already started perfecting their structure, i.e. tilting, whereas the ones at 28 C are incipient, hence being comparable to the treatment at ambient pressure.

Furthermore, at 24 °C, treatments with a P_{max} of or above 400 bar had lower initial d-spacings than the other two treatments, and had little variation upon cooling. This suggests that the effect of pressure on crystal structure remains even after releasing the pressure. Moreover, the d-spacing of the 200 bar treatment remained stable after

cooling, whilst that of the ambient pressure sample decreased. This is interesting as both treatments had a similar d-spacing behaviour during the pre-treatment.

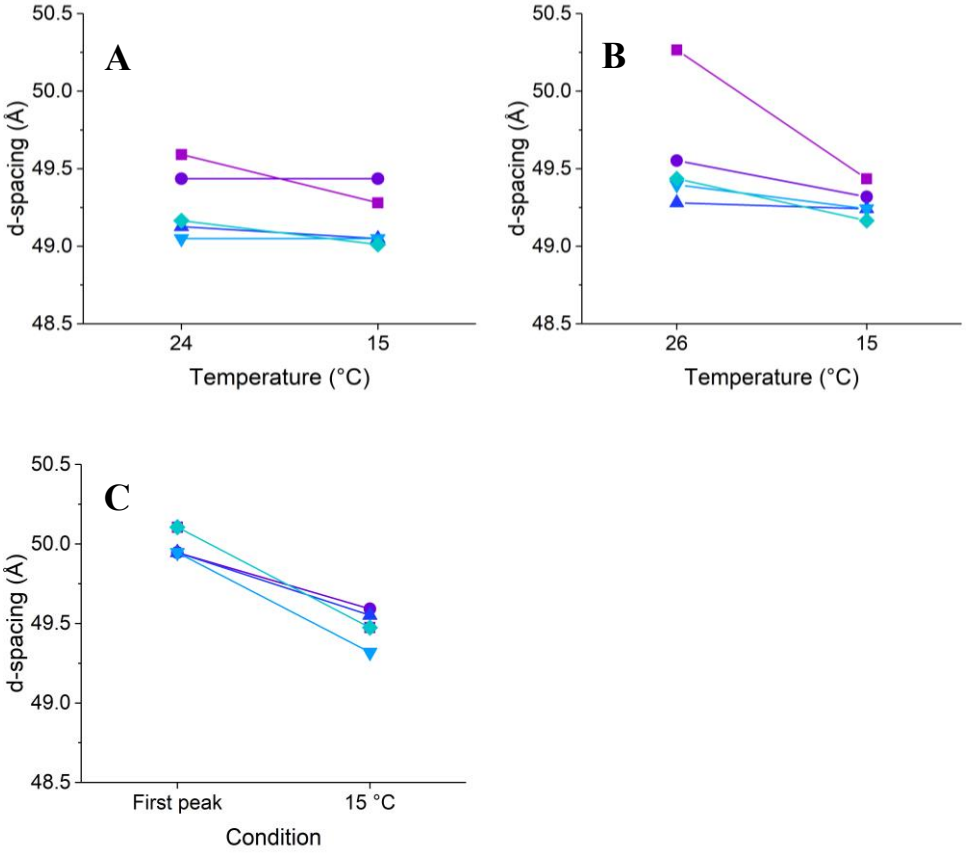

Figure 5.11 Observed d-spacings of the pressure treated samples observed at the first sign of crystallisation, which in the case of the 24 and 26 °C corresponds to the T_{cryst}, and after cooling to 15 °C at 24 (A), 26 (B), or 28 °C (C) after pressure was released. Violet squares refer to ambient pressure treatments, dark purple circles to 200 bar, blue upward triangles to 400 bar, light blue downward triangles to 600 bar, and cyan diamonds to 600 bar with a T_{imax} of 100 °C.

At 26 °C, most pressure-treated samples displayed the same d-spacing behaviour, i.e. a slight decrease upon cooling. The only treatment that had a different behaviour was the 400 bar one, which presented the smallest initial d-spacing, remaining stable after cooling to 15 °C. This is potentially related to this treatment being the first one to crystallise of the four different treatments, during the pressure processing (Table 5.2). As expected, the ambient pressure treatment has the largest d-spacings, for it did not crystallise during the previous treatment as no pressure was applied.

Lastly, the application of a T_{imax} of 100 °C had a strong effect on the crystallisation behaviour of the 600 bar treatment. Whilst when applying a T_{imax} of 50 °C, the 26 °C treatment resulted in a lower requirement of cooling for the α_1-form to crystallise in both SAXS and WAXS regimes, the 100 °C treatment resulted in different

behaviours depending on the region of the scattering pattern. In the small-angle, the cooling required decreased alongside the T_{cryst} used on the pressure pre-treatment. However, in the wide-angle, the 26 and 28 °C treatments require similar cooling conditions, whilst the 26 °C required further cooling. Regarding the α_2-form, a strong effect was evident when applying a T_{imax} of 100 °C. Once more, a lower cooling was necessary when a higher T_{cryst} was used during pre-treatment, similarly to the α_1-form. Regardless, the most striking difference was that the 28 °C treatment did result in the development of a peak, as opposed to when a T_{imax} of 50 °C was used, were no peak was observable. This is of particular relevance as the 50 °C treatment did develop a peak under pressurised conditions, and the 110 °C treatment did not.

Melting ranges of polymorphs developed during the pressure treatment

As mentioned in the methods section, in addition to the cooling protocol, another set of experiments was performed were the objective was to determine the melting points of the different peaks developed. Here, the samples were quenched to one of the three different T_{cryst}s, 24, 26 or 28 °C, pressurised to 600 bar, and held isobarically for two minutes after which the temperature was raised to 60 °C.

Table 5.4 Times and temperatures of the start and end of the melting process of the SAXS peaks developed during isobaric (600 bar) and isothermal crystallisation of CB. All values are in °C. When the starting and ending temperatures correspond to that of the T_{cryst} (*), this indicates that the event occurred during the isobaric period, and the specific time is identified between parenthesis.

Temperature	24 °			26 °C			28 °C		
Polymorph	α_2	α_1	WAXS	α_2	α_1	WAXS	α_2	α_1	WAXS
Start (°C)	24.12	32.91	25.88	26* (102 s)	32.14	27.26	28* (54 s)	33.31	30.39
End (°C)	30.90	45.03	42.51	29.70	42.29	40.87	28* (90 s)	43.46	41.24
T_{end}-T_{start}	6.78	12.12	16.63	NApp	10.15	13.60	NApp	10.15	10.85

Prior to the increase of temperature, all three 600 bar treatments had developed both α-forms in the SAXS region, as well as a WAXS peak, thus allowing the study of

their stabilities. The α_2-form, in the 24 °C treatment, started melting immediately on heating (24.1 °C), consequently, in the 26 °C treatment, it started decreasing in intensity within the isobaric period. In the case of the 28 °C treatment, the whole melting process occurred prior to the start of the heating ramp.

The α_1-form melted at higher temperatures than the α_2-form, suggesting a higher stability. In contrast, the temperature at which the melting finished decreased alongside T_{cryst}, the effect being more pronounced in the 26 °C treatment. The previous resulted in an enhanced melting rate, evaluated as T_{end} - T_{start}, when a T_{cryst} of 26 and 28 °C was used. Regarding the WAXS region, it behaved in a similar fashion to the α_1-form SAXS peak, though the actual melting temperatures were lower, which was expected as it developed at an earlier stage (Table 5.2).

5.1.4 Work done by pressure

From the melting points of CB at ambient pressure, 400 bar (Table 5.1) and 600 bar (Table 5.4), it was possible to estimate the change in molar volume in CB, when pressurised, following the Clausius equation (19)[264]

$$\frac{\Delta P}{\Delta T} = \frac{\Delta H_f}{T_f \, \Delta V} \qquad (19)$$

where ΔP is the change in pressure ($P_2 - P_1$), ΔT is the change in temperature of fusion ($T_2 - T_1$), ΔH_{fusion} is the enthalpy of fusion, T_f is the temperature of fusion at ambient pressure (in this case it is equivalent to T_1), and ΔV is the change in molar volume produced by the application of pressure ($V_2 - V_1$). A molecular weight of 861.04 g/mol was assumed for CB, corresponding to the one of StOSt, and an enthalpy of fusion for the alpha form (the one observed here) of 86.15 J/g. Volume differences of 0.04667 L/mol and 0.043416 L/mol were obtained at 400 and 600 bar, respectively.

From these volume changes, the work applied (ΔW) to the system, i.e. CB, was calculated from equation 20[265].

$$\Delta W = P\Delta \qquad (20)$$

where the term on the right is negative as the change in volume is assumed to be negative as the material gets compressed. Thus, the work applied at 400 bar is of

1866.80 J/mol, and at 600 bar its 2604.96 J/mol. Thus, whilst the difference between the ΔV terms is minimal, the work applied per mol increases almost 40 %.

5.2 Discussion

The post-processing analyses, although they did not provide direct evidence on the mechanisms through which pressure effects CB crystallisation, they were useful as the results gave the first evidence that the application of pressures below 1000 bar on cooled CB promoted crystallisation. Yet, the results obtained are mostly in opposition to the *in-situ* measurements, as will be discussed below. Nevertheless, the post-processing observations are valuable as they allowed to identify critical parameters that need to be considered for the industrial crystallisation of CB, which can be extended to that of other vegetable fats, namely the temperature to which the fat needs to be heated, and insights into the efficiency of the heat-transfer unit were obtained.

Before discussing the inconsistent post-processing results further, it is important to highlight the ambient pressure treatment results observed at 26 °C. This treatment commonly leads to an initial crystallisation into the formation the β'-polymorph (Figure 5.1b), and only after a holding time of 4 hours[20]. Thus, the presence of the β-V polymorph post-processing suggests that a contamination with small seed crystals occurred. Based on the T_{imax} results from Chapter 4, it is likely that this contamination came from some small crystalline clusters remaining within the machine, as it was only heated to 50 °C prior to any treatment. The second possible origin of such contamination is the depositing nozzle, as its tip is in direct contact with the surrounding air, the residual material present might not melt completely on heating.

As mentioned earlier, it is not only the treatment at ambient pressure which showed surprising results, but most of the post-processing results obtained do not agree with those obtained from the *in*-situ measurements. The main difference is that in all treatments, the two polymorphs that developed were the β'- and the β-V forms, whereas in the Synchrotron experiments only the development of the α-form was evident, even after cooling the CB. It is noted, that comparing different sample

volumes used in synchrotron SAXS, and PLM measurements did not significantly influence the crystallisation behaviour of CB. From these experiments, it was determined that no crystallisation occurred when treating CB at 100 bar (Table 5.2), especially at 28 °C. Hence a similar crystallisation behaviour to the treatment at atmospheric pressure would be expected, i.e. no presence of the β-V form. Furthermore, at 200 bar, once more the β-V form was identified in both T_{cryst} treatments (Table 5.2), whereas the *in-situ* experiments did not show evidence of crystallisation at 28 °C, and only a minor fraction of solid CB at 26 °C was observed (Table 5.2). This supports the notion that the pressure-processed β-V crystals have been induced by seeds, especially as their presence would explain the inconsistency in the behaviour at the different temperatures and pressures.

Moreover, it was also noted during processing, that the temperature of CB on depositing was two or three degrees higher than the set-temperature of the heat exchanger. Whilst it could be tempting to explain this result by a heat-release on nucleation, the lack of consistent temperature variations suggests otherwise. Therefore, it is concluded that the heat-exchanger efficiency was not optimal, skewing the results.

A particularly striking result was that the 600 bar treatment displayed the lowest amount of β-V crystals of all pressure-treated samples. This was evidenced by SWAXS experiments, which confirmed a predominance of the β'-form instead (Figure 5.1). Noteworthy, this was the only consistent behaviour observed at both T_{cryst}, and yet the one that contrasts the most with the *in-situ* measurement, as in the latter, the 600 bar treatment led only to the formation of the α_2-form at all temperatures (Table 5.3).

Additional DSC analyses did not provide further insights into the polymorphs present in the post-processing, as all treatments behaved in a similar fashion. They solely confirmed that a mix of β'-III and β-V was present in all samples with the β-V form being predominant. This differs from the results in the X-ray Scattering experiments, where the β' and β-V dominance varied between samples. The main difference in the experimental protocol concerns the transfer of CB to the X-ray Scattering and DSC instruments, respectively. The X-ray Scattering measurements were performed within minutes of taking the samples out of the freezer, whereas the

DSC measurements were performed after transporting the sample from Leeds to York, thus allowing further crystal growth and transformation of the crystals into more stable forms. Another difference that needs to be considered is that of sample size, as the moulds from which the DSC samples were taken contained a larger amount of CB (ca. 8 g) than the samples for the X-ray Scattering analysis, which inherently results in slower cooling rates, further increasing the transformation into more stable forms[44, 47, 49, 50, 53].

In brief, the post-processing experiments did not show any trend in terms of the induced polymorphs at the different pressures applied, most likely due to remaining seeds. Thus, no conclusion can be drawn in terms of determining if the application of pressures below 1000 bar does induce crystallisation of CB into the more stable polymorphs. Nevertheless, it was evident that the bespoke machine requires a more efficient cooling system (heat exchanger). More importantly, the machine needs to allow higher T_{imax}, at least 80 °C, in order to exclude the contamination with β-V seeds remaining from previous treatments. This seeding effect is considered undesirable, for it is not controllable and causes a high variability between treatments.

In conclusion, the post-processing measurements were not representative of the effects of pressure on crystallisation. Henceforth, the PLM and the *in-situ* X-ray studies are the only ones that provide an insight into what happens throughout the pressure treatments on CB. The PLM studies did not allow for unambiguous determination of the polymorph developed[67, 221], given that only small granular specks were observed. However, given their similarity to those usually seen during the initial crystallisation stages of the α-form[64, 67, 127, 237], this is considered to be the primary polymorph present, in agreement with the X-ray studies. Moreover, the overall behaviour was also comparable to the synchrotron X-ray studies (Table 5.2). At 26 °C, crystallisation was induced at pressures as low as 200 bar (Table 5.3). As expected, when using a higher T_{cryst}, 28 °C, higher pressures were required, i.e. at least 400 bar. Furthermore, no crystals were observed to remain on releasing the pressure (Figure 5.4 and 1.6) with either method applied (manual or pressure-jump). Nevertheless, microscopy[181] has a lower resolution than X-ray scattering.

In turn, the X-ray scattering measurements did allow for the accurate determination of the polymorphic forms developed at the different stages of the pressure treatment: a mix of the α_1- and α_2-forms was observed throughout. From these treatments it was evidenced that the best treatment for crystallisation induction was the one at 600 bar as it was the only one to develop the α_1- and α_2-forms at any of the temperatures used (Table 5.2). Also, its potential of inducing transformation into the β'-form may be enhanced, since its final long and short spacings are smaller than at lower pressures, indicating a higher degree of chain tilt and a closer packing of the FA chains in agreement with literature[266-269].

Conversely, the short-spacings, though they decreased under pressurised conditions, upon releasing the pressure they displayed a reversible behaviour of the chain packing (see synchrotron WAXS data in Figure 5.8), i.e. a slightly less dense chain packing was re-established. However, the SAXS data did not show the same reversibility, but in contrast, the *d*-spacings kept decreasing with time. While the overall lattice changes are minimal (in the order of 0.02 to 0.05 nm, see Figure 5.8), this trend was not expected. Most likely, the CB system's trend to transform with time from the α- to the β'-form is slightly more dominant than the effect of pressure release, for which a complete reversibility of the *d*-spacing back to a slightly higher lattice spacing would have been expected. Nevertheless, these lattice spacing effects under the combined influence of elapsing time and decreasing pressure are almost negligible (see above). It is therefore considered that experiments designed for following the CB nanostructure for a longer time frame after the final depressurising step, would allow to clarify this minute, but clearly observed monotonous trend.

An exception of this behaviour was the 600 bar treatment, at 26 °C and with a T_{imax} of 50 °C. Here, an increase of d-spacing was observed upon releasing the pressure. However, considering that this treatment resulted in a slower crystallisation than at 28 °C, and developed an initial d-spacing larger than the 100 °C treatment, it is considered to be an outlier originated, most likely, to inherent variations in the amount of heterogeneous nuclei between the samples. The observed delay in the onset of crystallisation is associated with the development of less stable structures with higher mobility, thus allowing for further deformation under pressure (-1.95% , see Figure 5.8) which is not retained after releasing the pressure.

Furthermore, at 28 °C, irrespective of the P_{max} used, a lower reduction of d-spacing under pressurised conditions was observed. This indicates that the application of a higher T_{cryst} leads to more stable structures, in agreement with literature[20, 32, 122, 154, 270]. Notably, whereas in previous studies a higher crystallisation temperature is related to the development of higher polymorphs, such as the β'-form[20, 32, 122, 154, 270], here it is suggested that a higher degree of tilt is indicative of a higher stability. This is because it is considered the first step towards transformation into the β'-form, which still possesses a 2L lamellar structure but a shorter d-spacing. Moreover, it is important to note that treatments at this temperature, surprisingly, resulted in a slight retention of crystallinity after the release of pressure, as evident by small broad peaks in the range of both 2L and 3L structures that, prior to recrystallisation during the cooling profile, they kept coming in and out of existence. This instability can be considered the reason behind the different re-crystallisation temperatures observed between the different pressure treatments (see Table 5.3), as it suggests a stochastic mechanism. However, it is proposed that a longer holding time might help with the stabilisation of these small lamellar clusters.

It is important to note, that the 600 bar treatments with a T_{imax} of 100 °C had a similar behaviour to the 50 °C treatments. However, the long and short-spacings developed were larger, suggesting the formation of less stable crystalline structures. This is reinforced further by the treatments at 26 and 28 °C where upon pressure release, the d-spacings did not follow the decreasing trend as other treatments, and displayed a slightly higher increase of the short-spacings

So far, this chapter has focused on the crystallisation of the α_1-form which is the primary polymorph observed in all crystallising treatments. Nonetheless, as mentioned earlier, an additional polymorph was observed, similar to the α_2-form identified by Mykhaylyk, *et al.*[96-98, 271]. The development of this phase was not a by-product of the application of pressure, as it was also observable in the treatment under atmospheric conditions. This polymorph displayed a highly transient nature. In the treatments with a higher T_{cryst} it started melting prior to the increase of temperature, and at 28 °C it even disappeared before full depressurisation (Table 5.2). This full melting at 28 °C is not unexpected, considering that the melting temperature range obtained from the 24 °C treatment is from 24 to 30.90 °C (Table 5.4). Hence, 28 °C does not supply sufficient supercooling to stabilise this structure, and possibly only

the longer chain TAGs are the ones that form the ephemeral α_2-phase and in a smaller proportion than at a lower T_{cryst}.

Surprisingly though, even if this form is less stable than the α_1-form it still required higher supercooling, or higher pressure, in contrast with the findings of Mykhaylyk, O. *et al*. [98]. However, this could be related to the apparent lack of a wide-angle peak, which suggests that at least under these conditions, this phase is a liquid crystal which retains a lamellar structure, but where the FA chains have high mobility, hence destabilising the structure.

Furthermore, in all treatments, upon depressurisation, the d-spacings of the α_2-form increased. Thus suggesting that any tilting caused by the application of pressure is lost, hence underlining the instability of this form. However, it is notable, that as its intensity decreased alongside pressure release, the intensity of the α_1-form increased (see contour plots in Appendix A), i.e. the latter grows at the expense of the former. Based on the proposed mixed 2L and 3L structure, it could be assumed that the α_2-form separates, similarly to what has been previously observed on increasing the temperature[96-98, 271].

As a final comment it is noted that crystallisation is assumed to start, not only from heterogeneous nuclei, but also from the back-to-back TAG clusters proposed in Chapter 3. In the particular case of CB, by applying pressure, the mobility of the TAG molecules is reduced. Consequently, the degree of occupation of the outer shell of the clusters is increased as molecules which had interdigitated with the core of the TAG clusters, are stabilised and can no longer go back into the isotropic liquid, thus aiding to the onset of crystallisation.

5.3 Conclusions

Based on the *in-situ* experiments performed, it was possible to determine that treating cooled CB to pressures in the range of 200 to 600 bar, at 24 to 28 °C, crystallisation is induced, but only in the α_1- and α_2-phases form. Moreover, these crystalline forms melt partially or totally on depressurising and, after cooling to 15 °C, they recrystallise, but do not transform into more stable polymorphs. Consequently, the observed development of the β'- and β-V-forms in the post-processing is only

attributable to the maturation of crystals, and more importantly, to residual seed crystalline material in the bespoke machine. This highlights the need for the use of a higher melting temperature in between treatments. Additionally, further studies are suggested to evaluate the effect of pressure on post-processing maturation, particularly, polymorphic transformation.

The *in-situ* experiments also helped to determine that the application of 600 bar is preferable over all other pressures used, as it induced crystallisation under all T_{cryst} applied. The observed *d*-spacing reduction is expected to promote further polymorphic transformation. Moreover, the 28 °C treatment, at this pressure, resulted in the most stable lattice spacings.

In conclusion, the application of pressures below 1000 bar does induce crystallisation, following the Le Chatelier principle, which states that the reduction of specific volume leads to a transition from liquid to solid. Regardless, when using temperatures above 24 °C and 28 °C, pressures above 100 and 200 bar, respectively, are required to enhance the thermodynamic driver of crystallisation. The advantage of using low pressures is that the kinetic factor does not start to hamper crystallisation. Nevertheless, given that only the α-forms developed, and for chocolate production it is the β-V polymorph which is desired, further studies are suggested to determine if during crystal maturation polymorphic transformation can be accelerated by applying pressure pre-treatments of CB, or if a different combination of pressure-temperature conditions could induce such polymorph.

Chapter 6 General conclusions and future work

Two parameters have been explored in this thesis, one more related to fundamental research, attempting to elucidate the effects of the initial maximum (melting) temperature, T_{imax}, and another related to a potential alternative to current chocolate tempering, i.e. the application of medium pressures (1-1000 bar). The first parameter is relevant from a fundamental point of view because of the need to establish the adequate temperature at which to melt CB prior to any crystallisation studies, to avoid any memory or kinetic effects. From a practical point of view, it is important, as the chocolate mass can reach temperatures above 80 °C during conching, therefore, studies using lower melting temperatures are not fully representative of what occurs during processing. Regarding the second parameter, pressure, it has a more evident practical application, as new processing methods are always being sought to make chocolate tempering more efficient. However, the study here presented provides a glimpse not only in terms of the processing technique, but more importantly, about the way that medium pressure affects the crystallisation induction times, and the crystalline structures promoted.

CB is known to crystallise in six forms at ambient pressure: γ, α, β'-III, β'-IV, β-V and β-VI. In this thesis, under the applied conditions, only forms α, β'-IV, β-V and β-VI were observed. From the T_{imax} results, it was determined that this parameter is critical for crystallisation studies, as the application of higher temperatures delayed the α-phase induction, the α→β'-form and β-V→β-VI form transformations, combined with a faster transformation into the β-V form. Additionally, developments of new morphologies, as observed by PLM, occurred at an earlier stage with the application of higher temperatures, and consequently, their melting temperatures were slightly increased, as the crystals had more time to perfect.

Differences between the different T_{imax} treatments were initially thought to be related to differences in the self-diffusion of the molecules. However, this was disproved by

the FFC-NMR measurements. Regardless, it is plausible that rather than "bulk" self-diffusion, some differences might be present in local diffusion or microviscosity, as observed by Dibildox-Alvarado, *et al.*[149], thus, further studies are required to confirm this hypothesis. These studies are relevant as they are performed on the basis of a single Browning probe (molecule)[272] being driven through the fluid and motion tracked. This motion modifies the medium's microstructure, thus allowing for the measurement of its physical properties at the microscale which are expected to change as the liquid starts transitioning into a solid, due to the increase of anisotropy.

Another plausible hypothesis is derived from the liquid structure model, as the application of higher T_{imax} is thought to cause an increased stripping of the outer layer of the back-to-back TAG clusters in the liquid, thus delaying the onset of crystallisation upon cooling, by requiring further time for the outer shell of the clusters to be filled again. Nevertheless, combining the previous hypotheses, the main mechanism at play is thought to be a crystal memory effect originated from the presence of higher melting acylglycerol species in CB. At 50 °C, fully saturated TAGs, such as tripalmitin and tristearin are thought to remain solid as their melting points are above 65 °C, and are suspected to not go completely into solution, whilst at 80 °C, fully saturated DAGs and MAGs cannot be expected to have fully melted as this temperature coincides with their melting points. Hence, it would be advisable to perform further experiments in the range between 80 and 110 °C, as well as varying holding times to determine at which combination of the two the crystallisation kinetics no longer change.

The memory effects are of relevance as potentially the first layers of the back-to-back layers are constructed of the higher melting acylglycerol species, which would then take longer to relax and undergo full transformation from solid to liquid, thus requiring for longer holding times at the highest temperatures. These would then impact the time required for concentrations of the different components reach an equilibrium in the bulk as well due to the possible differences in the microviscosity in different regions of the product.

Whilst the use of different time-temperature combinations would provide indirect evidence of the presence of higher melting crystallites, a more direct approach could be used. Pure samples of the three main TAGs of CB could be evaluated, followed by their combination, and potentially adding fully saturated TAGs and DAGs in a representative proportion. As an alternative approach, the polar compounds of CB

could be removed through solid phase extraction, thus serving as a baseline for comparison with the model lipid system. However, this alternative is not deemed ideal as full removal cannot be secured.

The aforementioned tests relate only to the lipid molecules present in CB. Nevertheless, CB is known to still have some water molecules present. These would be expected to be bound to the PLs polar headgroups, therefore, even if in this thesis a temperature above the boiling point of water was used, significant water loss is not anticipated. However, to confirm this, moisture analysis would be required before and after the heat treatment. This is of importance as it could be the origin of changes in the structure of CB crystals as the PLs present might change their organisation due to changes in their hydration.

The fact that crystallisation kinetics were modified by increasing the T_{imax} is of relevance in the production of chocolate, as mentioned earlier, as these higher temperatures are sometimes used during conching. Also, the faster transformation into the β-V polymorph is of interest, as it is what the chocolate industry pursues. Nevertheless, the studies here presented only used 10 min as holding time, and were performed in small samples. Therefore, longer holding times would be advisable, though keeping them below the 10 h mark based on the OSI analysis. More importantly, however, would be to perform bulk measurements as well as dynamic (shear) crystallisation studies, as in industry fats are usually kept in constant agitation to ensure an efficient heat transfer. The effect of shear would then need to be evaluated first during the application of T_{imax}, and secondly upon cooling. Shear is of relevance, not only for making experiments closer to real applications, but also because it has been observed to enhance transformation into the β-phase in fat systems[270, 273, 274], whilst in polymers, the application of shear to the melt led to the formation of smectic structures from which crystallisation would start[275]. The latter is of interest, as it is possible to hypothesise that the proposed structures for the liquid CB, could then align and form a stronger scaffolding for crystallisation.

Though the driving force behind this thesis was the applicability of the studies within the scope of the chocolate industry, CB also serves as a model fat for other industries. Given that higher melting points were observed in the PLM studies, and that crystallisation kinetics were slower when a higher T_{imax} was used, it is likely that the separation of the higher melting TAG species is promoted. Thus making these studies

relevant for fat fractionation, a processing method that is of importance in the palm oil industry, for example. Therefore, it would be relevant to assess the effect of different T_{imax} on such a system, as it would help understand in more detail if fractionation is truly enhanced by modifying this parameter. If this were the case, it would provide the fat industry with an aid for such process, provided no oxidative processes were enhanced.

An increased T_{imax} not only affected isothermal crystallisation at ambient pressure, but also when applying pressures of 600 bar on CB quenched to 26 and 28 °C. Here, no polymorphic transformations were observable, as the pressure-temperature-time combination used was not sufficient. The main effects observed on CB, when pressure-treated, were related to the spacings of the developed polymorphs (α_1 and α_2), which after the full treatment, were larger than those of the 600 bar treatment using a T_{imax} of 50 °C. Thus, it was possible to determine that a higher T_{imax} has an effect even under pressurised conditions.

The pressure studies were driven by the previously reported promotion of the crystallisation of acylglycerol species under pressurised conditions[87, 90, 162, 164, 276], as well as the initial post-processing analyses which showed promising results for the application of medium pressure as an alternative to traditional tempering. However, *in-situ* measurements disproved the results from the post-processing analyses, i.e that applying pressures of 200 to 600 bar induced the crystallisation of the β-V form, as only the α_1- and α_2-forms were observable under the applied conditions. Nevertheless, it would be of interest to measure the samples after holding the final temperature for at least two hours, to evaluate polymorphic transformation. The latter is proposed, as it is hypothesised that the 600 bar treatment is likely to induce a faster transformation into more stable polymorphs, as upon cooling it developed the α_2-form at an earlier stage. This polymorph is thought to be an early precursor of the β-polymorphs because of its lamellar structure, which is thought to be either a mix of 2-L and 3-L lamellar structures or a quasi 3-L structure.

Regarding the crystalline structures developed in molten CB under pressurised conditions, it is considered that the 28 °C treatment is of particular interest as it developed the most stable structures, thus defined from the decreased variation of their long and short spacings which suffered less variation throughout the full treatment. However, given that this temperature corresponds to the high-end of the melting range

of the crystalline structures, upon full depressurisation it suffered the largest decrease of crystallinity, observed as a decreased intensity in the SAXS region and a complete loss of the sub-cell packing. Nevertheless, it is thought that by prolonging the holding times, and thus, the size of the crystals, an increased retention of crystallinity, at least of the lamellar stacking, could be obtained.

Returning to the polymorphs observed during the pressure treatments, including the blank at ambient temperature, the development of the α_2-form in CB is notable, as this form has only been clearly identified during the crystallisation of StOSt, which is one of the main TAG components of CB. Therefore, further SAXS and WAXS experiments would be required to understand its role, if any, in polymorphic transformations, initially at ambient pressure only. A singularity of the α_2-form here observed is that it developed after the α_1-form, in contrast to the StOSt studies, though this could be related to the mixed composition of CB which adds another hurdle for its crystallisation.

In summary, the application of a higher T_{imax} and P_{max}, especially 600 bar, have an impact on CB crystallisation, yet the specific mechanisms through which this occurs are yet to be fully understood. Particularly those of T_{imax}, as the effect of pressure is partially explainable by thermodynamic principles (Le Chatelier, and Clausius-Clapeyron). This thesis has made it possible to conclude that CB, as humble as it may seem, when compared to other fat systems with a larger compositional variation, it has a highly complex crystallisation behaviour. Once more answers are obtained regarding the mechanisms, or at least the drivers for the observed effects, it should be possible to make full use of the parameters studied to improve processing conditions. These conditions are not thought to be limited only to the tempering of chocolate, but have the potential to be applied in other areas of the fat industry, particularly that of fat fractionation. However, at this stage it is mere speculation as confirmation of differences in composition is needed.

Finally, based on what Prof Eckhard Flöter from the Technical University of Berlin (Berlin, Germany) said in one of our discussions, that a PhD is about opening the door for further research by raising even more questions than when it started, then I believe that this one has fulfilled its objective. Whilst it did provide insights on the effects of parameters or conditions not previously reported in literature, it has also raised

questions as to why these effects were observed, and prompt me to dig deeper to grasp further understanding.

References

1. S. T. Beckett, in *The Science of Chocolate*, ed. S. T. Beckett, The Royal Society of Chemistry, 2000, DOI: 10.1039/9781847552143-00001, pp. 1-7.
2. J. Garthwaite, What We Know About the Earliest History of Chocolate, https://www.smithsonianmag.com/history/archaeology-chocolate-180954243/, 2018).
3. A. Fiegl, A Brief History of Chocolate, https://www.smithsonianmag.com/arts-culture/a-brief-history-of-chocolate-21860917/, 2018).
4. O. B. Waxman, The Bittersweet History of Chocolate, http://time.com/4693048/chocolate-history-museum/, 2018).
5. B. Callebaut, History of chocolate, https://www.barry-callebaut.com/about-us/media/press-kit/history-chocolate).
6. *Guidance on the Cocoa and Chocolate Products Regulations* 2009. United Kingdom: Food Standards Agency.
7. S. T. Beckett, *Science of Chocolate*, The Royal Society of Chemistry, United Kingdom, 2000.
8. S. T. Beckett, in *Industrial Chocolate Manufacture and Use*, ed. S. T. Beckett, Blackwell Publishing, Ltd, Oxford, United Kingdom, 3rd edn., 2009, ch. 9, pp. 192-223.
9. S. T. Beckett, in *Science and Technology of Enrobed and Filled Chocolate, Confectionery and Bakery Products*, ed. G. Talbot, Woodhead Publishing, 2009, ch. 2, pp. 11-28.
10. E. O. Afoakwa, A. Paterson and M. Fowler, *Trends in Food Science & Technology*, 2007, **18**, 290-298.
11. O. Nieburg, The new world of chocolate: How is consumption in emergin markets developing?, http://www.confectionerynews.com/Markets/Chocolate-consumption-in-emerging-markets-2014, (accessed 25/08/2016, 2016).
12. H. Tan, Dark times for cocoa as prices hit 4-year lows, https://www.cnbc.com/2017/02/05/cocoa-prices-at-4-year-lows-health-conscious-consumers-slowing-global-appetite-for-chocolate.html, 2017).
13. K. Barnato and L. Graham, Future of the chocolate industry looks sticky, https://www.cnbc.com/2016/03/24/future-of-the-chocolate-industry-looks-sticky.html).

14. E. Terazono, Asian chocolate demand set to outstrip global growth, https://www.ft.com/content/3cb2e488-a8f8-11e7-ab55-27219df83c97, 2018).

15. I. Foubert, P. A. Vanrolleghem, O. Thas and K. Dewettinck, *Journal of Food Science*, 2004, **69**, E478-E487.

16. S. Chaiseri and P. S. Dimick, *Journal of the American Oil Chemists' Society*, 1995, **72**, 1491-1496.

17. S. Chaiseri and P. Dimick, *Journal of the American Oil Chemists' Society*, 1989, **66**, 1771-1776.

18. E. J. Windhab, in *Industrial Chocolate Manufacture and Use*, ed. S. T.Becket, Wiley-Blackwell, United Kindom, 2007, ch. 13, pp. 276-319.

19. E. O. Afoakwa, A. Paterson, M. Fowler and J. Vieira, *Journal of Food Engineering*, 2008, **89**, 128-136.

20. K. van Malssen, R. Peschar and H. Schenk, *Journal of the American Oil Chemists' Society*, 1996, **73**, 1209-1215.

21. A. G. a. W. Marangoni, L.H . , in *Structure and Properties of Fat Crystal Networks, Second Edition*, CRC Press, 2012, DOI: doi:10.1201/b12883-2, pp. 19-44.

22. J. W. Mullin, *Crystallization*, Butterworth-Heinemann, Oxford, 4th edn., 2001.

23. C. Himawan, V. M. Starov and A. G. F. Stapley, *Advances in Colloid and Interface Science*, 2006, **122**, 3-33.

24. M. J. Povey, *Food Hydrocolloids*, 2014, **42**, 118-129.

25. J. Coupland, *An introduction to the physical chemistry of food*, Springer, Berlin, 2014.

26. H. Schnablegger, Singh, Y., *The SAXS Guide: Getting acquainted with the principles*, Anton Paar GmbH, Austria, 3rd edn., 2013.

27. R. E. Timms, *Progress in Lipid Research*, 1984, **23**, 1-38.

28. F. Lavigne, C. Bourgaux and M. Ollivon, *Le Journal de Physique IV*, 1993, **3**, C8-137-C138-140.

29. K. Sato, L. Bayes-Garcia, T. Calvet, M. Angel Cuevas-Diarte and S. Ueno, *European Journal of Lipid Science and Technology*, 2013, **115**, 1224-1238.

30. T. Threlfall, *Organic Process Research & Development*, 2003, **7**, 1017-1027.

31. C. Himawan, V. M. Starov and A. G. F. Stapley, *Advances in Colloid and Interface Science*, 2006, **122**, 3-33.

32. K. Sato, *Chemical Engineering Science*, 2001, **56**, 2255-2265.

33. S. Verstringe, K. Dewettinck, S. Ueno and K. Sato, *Cryst. Growth Des.*, 2014, **14**, 5219.

34. N. C. Acevedo and A. G. Marangoni, *Crystal Growth & Design*, 2010, **10**, 3327-3333.

35. E. S. Lutton, *Journal of the American Oil Chemists' Society*, 1955, **32**, 49-53.

36. Q. Bonnie, P. Fernanda, G. Tyler, M. Alejandro, B. H. Charles and A. P. David, *Journal of Physics: Condensed Matter*, 2014, **26**, 464108.

37. A. G. Marangoni, N. Acevedo, F. Maleky, E. Co, F. Peyronel, G. Mazzanti, B. Quinn and D. Pink, *Soft Matter*, 2012, **8**, 1275.

38. D. A. Pink, B. Quinn, F. Peyronel and A. G. Marangoni, *Journal of Applied Physics*, 2013, **114**, 234901.

39. F. Peyronel, D. a. Pink and A. G. Marangoni, *Curr. Opin. Colloid Interface Sci.*, 2014, **19**, 459.

40. P. R. Ramel, E. D. Co, N. C. Acevedo and A. G. Marangoni, *Progress in Lipid Research*, 2016, **64**, 231-242.

41. D. A. Pink, B. Townsend, F. Peyronel, E. D. Co and A. G. Marangoni, *Food & Function*, 2017, **8**, 3621-3635.

42. A. P. B. Ribeiro, M. H. Masuchi, E. K. Miyasaki, M. A. F. Domingues, V. L. Z. Stroppa, G. M. de Oliveira and T. G. Kieckbusch, *Journal of Food Science and Technology*, 2015, **52**, 3925-3946.

43. M. R. Baker, L. Bouzidi, N. Garti and S. S. Narine, *JAOCS, Journal of the American Oil Chemists' Society*, 2014, **91**, 1685-1694.

44. L. Bouzidi and S. S. Narine, *Chemistry and Physics of Lipids*, 2012, **165**, 105-119.

45. L. Bayes-Garcia, T. Calvet, M. Angel Cuevas-Diarte, S. Ueno and K. Sato, *CrystEngComm*, 2013, **15**, 302-314.

46. L. Bayes-Garcia, T. Calvet, M. A. Cuevas-Diarte, S. Ueno and K. Sato, *CrystEngComm*, 2011, **13**, 3592-3599.

47. C. Himawan, W. MacNaughtan, I. A. Farhat and A. G. F. Stapley, *European Journal of Lipid Science and Technology*, 2007, **109**, 49-60.

48. K. W. Smith, F. W. Cain and G. Talbot, *European Journal of Lipid Science and Technology*, 2005, **107**, 583-593.

49. S. Martini, M. L. Herrera and R. W. Hartel, *Journal of the American Oil Chemists' Society*, 2002, **79**, 1055-1062.

50. R. Campos, S. S. Narine and A. G. Marangoni, *Food Research International*, 2002, **35**, 971-981.

51. C. Lopez, P. Lesieur, C. Bourgaux and M. Ollivon, *Journal of Dairy Science*, 2005, **88**, 511-526.

52. D. Pérez-Martínez, C. Alvarez-Salas, J. A. Morales-Rueda, J. F. Toro-Vazquez, M. Charó-Alonso and E. Dibildox-Alvarado, *Journal of the American Oil Chemists' Society*, 2005, **82**, 471-479.

53. C. L. Chong, Z. Kamarudin, P. Lesieur, A. Marangoni, C. Bourgaux and M. Ollivon, *European Journal of Lipid Science and Technology*, 2007, **109**, 410-421.

54. N. C. Acevedo and A. G. Marangoni, *Crystal Growth & Design*, 2010, **10**, 3334-3339.

55. F. Maleky, N. C. Acevedo and A. G. Marangoni, *European Journal of Lipid Science and Technology*, 2012, **114**, 748-759.

56. G. Mazzanti, S. E. Guthrie, E. B. Sirota, A. G. Marangoni and S. H. J. Idziak, *Crystal Growth & Design*, 2004, **4**, 1303-1309.

57. D. Kalnin, P. Lesieur, F. Artzner, G. Keller and M. Ollivon, *European Journal of Lipid Science and Technology*, 2005, **107**, 594-606.

58. A. G. Marangoni, T. C. Aurand, S. Martini and M. Ollivon, *Crystal Growth & Design*, 2006, **6**, 1199-1205.

59. A. G. Marangoni and S. E. McGauley, *Cryst. Growth Des.*, 2003, **3**, 95.

60. J. W. Mullin, *Journal*, 2001.

61. C. Bourlieu, V. Guillard, M. Ferreira, H. Powell, B. Vallès-Pàmies, S. Guilbert and N. Gontard, *Journal of the American Oil Chemists' Society*, 2010, **87**, 133-145.

62. H. Yao, I. Hatta, R. Koynova and B. Tenchov, *Biophysical Journal*, 1992, **61**, 683-693.

63. K. Sato, *Chemical Engineering Science*, 2001, **56**, 2255.

64. J. Ray, W. MacNaughtan, P. S. Chong, J. Vieira and B. Wolf, *Journal of the American Oil Chemists' Society*, 2012, **89**, 437-445.

65. S. D. MacMillan, K. J. Roberts, M. A. Wells, M. C. Polgreen and I. H. Smith, *Cryst. Growth Des.*, 2003, **3**, 117.

66. I. Foubert, 2003.

67. A. G. Marangoni and S. E. McGauley, *Crystal Growth & Design*, 2002, **3**, 95-108.

68. K. F. van Malssen, R. Peschar and H. Schenk, *Journal of the American Oil Chemists Society*, 1996, **73**, 1209.

69. A. Kos, D. Tefelski, R. M. Siegoczyński, R. Rutkowski, W. Ejchart and R. Wiśniewski, *High Pressure Research*, 2005, **25**, 51-56.

70. R. M. Siegoczyński, A. Kos, D. B. Tefelski, R. Kościesza and W. Ejchart, *High Pressure Research*, 2007, **27**, 47-50.

71. D. B. Tefelski, L. Kulisiewicz, A. Wierschem, A. Delgado, A. J. Rostocki and R. M. Siegoczyński, *High Pressure Research*, 2011, **31**, 178-185.

72. R. Kościesza, L. Kulisiewicz and A. Delgado, *High Pressure Research*, 2010, **30**, 118-123.

73. P. Kiełczyński, M. Szalewski, A. Balcerzak, A. Malanowski, R. M. Siegoczyński and S. Ptasznik, *Food Research International*, 2012, **49**, 60-64.

74. P. Kiełczyński, M. Szalewski, A. Balcerzak, K. Wieja, A. Malanowski, R. Kościesza, R. Tarakowski, A. J. Rostocki and R. M. Siegoczyński, *Ultrasonics*, 2014, **54**, 2134-2140.

75. P. Kiełczyński, M. Szalewski, A. Balcerzak, A. J. Rostocki and D. B. Tefelski, *Ultrasonics*, 2011, **51**, 921-924.

76. R. M. Siegoczyński, A. J. Rostocki, P. Kielczyński and M. Szalewski, *Journal of Physics: Conference Series*, 2008, **121**, 142010.

77. B. Guignon, C. Aparicio and P. D. Sanz, *High Pressure Research*, 2009, **29**, 38-45.

78. P. Ferstl, S. Gillig, C. Kaufmann, C. Dürr, C. Eder, A. Wierschem and W. Ruß, *Annals of the New York Academy of Sciences*, 2010, **1189**, 62-67.

79. C. Yokoyama, Y. Tamura and Y. Nishiyama, *Journal of Crystal Growth*, 1998, **191**, 827-833.

80. D. B. Tefelski, C. Jastrzębski, M. Wierzbicki, R. M. Siegoczyński, A. J. Rostocki, K. Wieja and R. Kościesza, *High Pressure Research*, 2010, **30**, 124-129.

81. H. G. Brittain, in *Polymorphism in pharmaceutical solids*, ed. H. G. Brittain, Informa Healthcare USA, Inc., New York, U.S.A., 2007, ch. 3, pp. 35-72.

82. I. Gutzow, B. Durschang and C. Russel, *Journal of Materials Science*, 1997, **32**, 5389-5403.

83. P. d. P. Atkins, Julio, in *Elements of Physical Chemistry*, Oxford University Press, Oxford, 5th edn., 2009, ch. 5, pp. 105-152.

84. K. Adrjanowicz, A. Grzybowski, K. Grzybowska, J. Pionteck and M. Paluch, *Crystal Growth & Design*, 2013, **13**, 4648-4654.

85. K. Adrjanowicz, A. Grzybowski, K. Grzybowska, J. Pionteck and M. Paluch, *Crystal Growth & Design*, 2014, **14**, 2097-2104.

86. M. Greiner, A. M. Reilly and H. Briesen, *Journal of Agricultural and Food Chemistry*, 2012, **60**, 5243-5249.

87. P. Ferstl, C. Eder, W. Ruß and A. Wierschem, *High Pressure Research*, 2011, **31**, 339-349.

88. G. M. Acosta, R. L. Smith and K. Arai, *Journal of Chemical and Engineering Data*, 1996, **41**, 961-969.

89. A. Yasuda and K. Mochizuki, *High Pressure and Biotechnology*, 1992, **224**, 255-259.

90. J.-H. Oh and B. G. Swanson, *Journal of the American Oil Chemists' Society*, 2006, **83**, 1007-1014.

91. M. Nic, J. Jiri and B. Kosata, *IUPAC Compendium of Chemical Terminology (Gold Book)*, IUPAC, Prague, Czechia, 2014.

92. K. Sato, T. Arishima, Z. H. Wang, K. Ojima, N. Sagi and H. Mori, *Journal of the American Oil Chemists' Society*, 1989, **66**, 664-674.

93. P. Rousset and M. Rappaz, *Journal of the American Oil Chemists' Society*, 1996, **73**, 1051-1057.

94. P. Rousset, M. Rappaz and E. Minner, *Journal of the American Oil Chemists' Society*, 1998, **75**, 857-864.

95. S. Ueno, A. Minato, H. Seto, Y. Amemiya and K. Sato, *The Journal of Physical Chemistry B*, 1997, **101**, 6847-6854.

96. O. O. Mykhaylyk, V. Castelletto, I. W. Hamley and M. J. W. Povey, *European Journal of Lipid Science and Technology*, 2004, **106**, 319-324.

97. O. O. Mykhaylyk and I. W. Hamley, *The Journal of Physical Chemistry B*, 2004, **108**, 8069-8083.

98. O. O. Mykhaylyk, K. W. Smith, C. M. Martin and A. J. Ryan, *Journal of Applied Crystallography*, 2007, **40**, s297-s302.

99. T. Koyano, I. Hachiya, T. Arishima, K. Sato and N. Sagi, *Journal of the American Oil Chemists Society*, 1989, **66**, 675-679.

100. E. S. Lutton and F. L. Jackson, *Journal of the American Chemical Society*, 1950, **72**, 3254-3257.

101. E. S. Lutton, *Journal of the American Chemical Society*, 1951, **73**, 5595-5598.

102. T. Arishima, N. Sagi, H. Mori and K. Sato, *Journal of the American Oil Chemists Society*, 1991, **68**, 710-715.

103. W. Landmann, R. O. Feuge and N. V. Lovegren, *Journal of the American Oil Chemists Society*, 1960, **37**, 638-643.

104. T. Davis and P. Dimick, *Journal of the American Oil Chemists Society*, 1989, **66**, 1494-1498.

105. M. Kellens, W. Meeussen, R. Gehrke and H. Reynaers, *Chemistry and Physics of Lipids*, 1991, **58**, 131-144.

106. A. Minato, S. Ueno, J. Yano, Z. H. Wang, H. Seto, Y. Amemiya and K. Sato, *Journal of the American Oil Chemists' Society*, 1996, **73**, 1567-1572.

107. L. Zhang, S. Ueno, K. Sato, R. Adlof and G. List, *Journal of Thermal Analysis and Calorimetry*, 2009, **98**, 105-111.

108. L. Bayés-García, T. Calvet, M. À. Cuevas-Diarte, S. Ueno and K. Sato, *The Journal of Physical Chemistry B*, 2015, **119**, 4417-4427.

109. L. Zhang, S. Ueno, S. Miura and K. Sato, *Journal of the American Oil Chemists' Society*, 2007, **84**, 219-227.

110. L. Zhang, S. Ueno and K. Sato, *Journal of Oleo Science*, 2018, **67**, 679-687.

111. G. R. Desiraju, *CrystEngComm*, 2003, **5**, 466-467.

112. J. D. Dunitz, *CrystEngComm*, 2003, **5**, 506-506.

113. P. Dimick and D. Manning, *Journal of the American Oil Chemists' Society*, 1987, **64**, 1663-1669.

114. M. Lipp and E. Anklam, *Food Chemistry*, 1998, **62**, 73-97.

115. M. H. Gordon and I. A. Rahman, *J. Am. Oil Chem. Soc.*, 1991, **68**, 577.

116. A. J. Wright, R. W. Hartel, S. S. Narine and A. G. Marangoni, *J. Am. Oil Chem. Soc.*, 2000, **77**, 463.

117. A. J. Wright, R. W. Hartel, S. S. Narine and A. G. Marangoni, *J. Am. Oil Chem. Soc.*, 2000, **77**, 463.

118. A. J. Wright and A. G. Marangoni, *JAOCS, Journal of the American Oil Chemists' Society*, 2002, **79**, 395-402.

119. K. Smith, K. Bhaggan, G. Talbot and K. van Malssen, *Journal of the American Oil Chemists' Society*, 2011, **88**, 1085-1101.

120. P. R. Smith, I. Furó, K. W. Smith and F. Cain, *Journal of the American Oil Chemists' Society*, 2007, **84**, 325-329.

121. R. L. Wille and E. S. Lutton, *Journal of the American Oil Chemists Society*, 1966, **43**, 491-496.

122. K. van Malssen, A. van Langevelde, R. Peschar and H. Schenk, *Journal of the American Oil Chemists' Society*, 1999, **76**, 669-676.

123. G. M. Chapman, E. E. Akehurst and W. B. Wright, *Journal of the American Oil Chemists Society*, 1971, **48**, 824-830.

124. C. Loisel, G. Keller, G. Lecq, C. Bourgaux and M. Ollivon, *Journal of the American Oil Chemists' Society*, 1998, **75**, 425-439.

125. A. van Langevelde, R. Driessen, W. Molleman, R. Peschar and H. Schenk, *Journal of the American Oil Chemists' Society*, 2001, **78**, 911-918.

126. C. Loisel, G. Lecq, G. Keller and M. Ollivon, *Journal of Food Science*, 1998, **63**, 73-79.

127. J. F. Toro-Vazquez, E. Rangel-Vargas, E. Dibildox-Alvarado and M. A. Charó-Alonso, *European Journal of Lipid Science and Technology*, 2005, **107**, 641-655.

128. C. Savage and P. Dimick, *The Manufacturing Confectioner*, 1995, **75**, 127-132.

129. A. Tardieu, V. Luzzati and F. C. Reman, *Journal of Molecular Biology*, 1973, **75**, 711-733.

130. I. Hachiya, T. Koyano and K. Sato, *Journal of the American Oil Chemists' Society*, 1989, **66**, 1757-1762.

131. D. Arruda and P. Dimick, *Journal of the American Oil Chemists' Society*, 1991, **68**, 385-390.

132. N. Widlak, *Physical properties of fats, oils, and emulsifiers*, AOCS Press, Champaign, Ill, 1999.

133. J. A. Hamilton, *Biochemistry*, 1989, **28**, 2514-2520.

134. S. A. Hindle, M. J. W. Povey and K. W. Smith, *Journal of the American Oil Chemists Society*, 2002, **79**, 993-1002.

135. S. Hindle, M. J. W. Povey and K. Smith, *Journal of Colloid and Interface Science*, 2000, **232**, 370-380.

136. T. Davis and P. Dimick, *Journal of the American Oil Chemists Society*, 1989, **66**, 1488-1493.

137. I. Foubert, P. A. Vanrolleghem and K. Dewettinck, *Thermochimica Acta*, 2003, **400**, 131-142.

138. N. Yoshimoto and K. Sato, *Japanese Journal of Applied Physics*, 1994, **33**, 2746.

139. Y. Wang, Masters in Science, Dalhousie University, 2016.

140. R. W. Corkery, D. Rousseau, P. Smith, D. A. Pink and C. B. Hanna, *Langmuir*, 2007, **23**, 7241-7246.

141. K. Larsson, *Journal of the American Oil Chemists Society*, 1992, **69**, 835-836.

142. D. Cebula, D. J. McClements, M. W. Povey and P. Smith, *Journal of the American Oil Chemists' Society*, 1992, **69**, 130-136.

143. D. A. Pink, C. B. Hanna, C. Sandt, A. J. MacDonald, R. MacEachern, R. Corkery and D. Rousseau, *The Journal of Chemical Physics*, 2010, **132**, 054502.

144. L. Lin, MSc, Dalhousie University, 2014.

145. W.-D. Hsu and A. Violi, *The Journal of Physical Chemistry B*, 2009, **113**, 887-893.

146. A. S. Tascini, M. G. Noro, R. Chen, J. M. Seddon and F. Bresme, *Physical Chemistry Chemical Physics*, 2018, **20**, 1848-1860.

147. E. Dibildox-Alvarado, A. G. Marangoni and J. F. Toro-Vazquez, *Food Biophysics*, 2010, **5**, 218-226.

148. E. Dibildox-Alvarado, T. Laredo, J. F. Toro-Vazquez and A. G. Marangoni, *J. Am. Oil Chem. Soc.*, 2010, **87**, 1115.

149. E. Dibildox-Alvarado, T. Laredo, J. F. Toro-Vazquez and A. G. Marangoni, *Journal of the American Oil Chemists' Society*, 2010, **87**, 1115-1125.

150. K. Sato, *Lipid / Fett*, 1999, **101**, 467-474.

151. R. H. Ferguson and E. S. Lutton, *Chemical Reviews*, 1941, **29**, 355-384.

152. A. van Langevelde, K. Van Malssen, R. Peschar and H. Schenk, *Journal of the American Oil Chemists' Society*, 2001, **78**, 919-925.

153. K. Van Malssen, R. Peschar, C. Brito and H. Schenk, *JAOCS, Journal of the American Oil Chemists' Society*, 1996, **73**, 1225-1230.

154. I. Foubert, PhD, Universiteit Gent, 2003.

155. M. Cerdeira, R. J. Candal and M. L. Herrera, *Journal of Food Science*, 2004, **69**, R185-R191.

156. L. Hernqvist, *Fette, Seifen, Anstrichmittel*, 1984, **86**, 297-300.

157. U. o. Muenster, *Diffusion measurements by Nuclear Magnetic Resonance (NMR)*.

158. I. f. P. Chemie, Diffusion measurements by Nuclear Magnetic Resonance (NMR), https://www.uni-muenster.de/imperia/md/content/physikalische_chemie/nmr_pfg_diffusion.pdf, (accessed 01/05/2018).

159. N. Hiramatsu, T. Inoue, M. Suzuki and K. Sato, *Chemistry and Physics of Lipids*, 1989, **51**, 47-53.

160. M. Zulkurnain, V. M. Balasubramaniam and F. Maleky, *Crystal Growth & Design*, 2017, DOI: 10.1021/acs.cgd.7b00768.

161. M. Zulkurnain, F. Maleky and V. M. Balasubramaniam, *Food Engineering Reviews*, 2016, DOI: 10.1007/s12393-016-9144-4, 1-21.

162. A. J. Rostocki, R. Kościesza, D. B. Tefelski, A. Kos, R. M. Siegoczyński and Ł. Chruściński, *High Pressure Research*, 2007, **27**, 43-45.

163. R. M. Siegoczyński, R. Kościesza, D. B. Tefelski and A. Kos, *High Pressure Research*, 2009, **29**, 61-66.

164. M. Zulkurnain, F. Maleky and V. M. Balasubramaniam, *Innovative Food Science & Emerging Technologies*, 2016, **38, Part B**, 302-311.

165. P. Kiełczyński, M. Szalewski, A. J. Rostocki, M. Zduniak, R. M. Siegoczyński and A. Balcerzak, 2009.

166. A. Sadeghpour, M. Ladd Parada, J. Vieira, M. J. W. Povey and M. Rappolt, *The Journal of Physical Chemistry B*, 2018, DOI: 10.1021/acs.jpcb.8b06704.

167. E. S. Lutton, *Journal of the American Chemical Society*, 1945, **67**, 524-527.

168. I. T. Norton, C. D. Lee-Tuffnell, S. Ablett and S. M. Bociek, *Journal of the American Oil Chemists' Society*, 1985, **62**, 1237-1244.

169. K. Van Malssen, R. Peschar, C. Brito and H. Schenk, *Journal of the American Oil Chemists' Society*, 1996, **73**, 1225-1230.

170. S. Chaiseri and P. Dimick, *Journal of the American Oil Chemists' Society*, 1995, **72**, 1491-1496.

171. S. H. J. Idziak, in *Structure-Function Analysis of Edible Fats*, ed. A. G. Marangoni, AOCS Press, Urbana, IL, USA, 2012, ch. 3, pp. 79-106.

172. H. K. D. M., T. Maryjane and K. B. M., *Angewandte Chemie International Edition*, 2001, **40**, 1626-1651.

173. B. E. Warren, *X-ray Diffraction*, Addison-Wesley, Reading, 1969.

174. M. Rappolt, *Journal of Applied Physics*, 2010, **107**, 084701.

175. C. M. Savage and P. S. Dimick, *The Manufacturing Confectioner*, 1995, **75**, 127.

176. PerkinElmer, Differential Scanning Calorimetry (DSC) A beginners guide, http://www.perkinelmer.co.uk/CMSResources/Images/44-74542GDE_DSCBeginnersGuide.pdf, (accessed 26 October 2017).

177. K. van Malssen, R. Peschar and H. Schenk, *Journal of the American Oil Chemists' Society*, 1996, **73**, 1217-1223.

178. J. Schlichter Aronhime, S. Sarig and N. Garti, *Journal of the American Oil Chemists' Society*, 1988, **65**, 1140-1143.

179. W. Kloek, P. Walstra and T. van Vliet, *Journal of the American Oil Chemists' Society*, 2000, **77**, 389-398.

180. P. A. Gunning, in *Food Microstructures - Microscopy, Measurement and Modelling*, eds. V. J. Morris and K. Groves, Elsevier, Philadelphia, USA, 2013, ch. 3, pp. 62-95.

181. C. P. Robinson and M. W. Davidson, Polarised Microscopy, https://www.microscopyu.com/techniques/polarized-light/polarized-light-microscopy, (accessed 12/04/2018).

182. R. Hoffman and M. W. Davidson, Michel-Levy Birefringence Chart, http://olympus.magnet.fsu.edu/primer/techniques/polarized/michel.html, (accessed 13 April 2018).

183. B. Crist and J. M. Schultz, *Progress in Polymer Science*, 2016, **56**, 1-63.

184. A. G. Shtukenberg, Y. O. Punin, E. Gunn and B. Kahr, *Chemical Reviews*, 2012, **112**, 1805-1838.

185. E. A. Woo, G. Lugito, C. Yang, S. Chang and T. Lee, *Journal of Advanced Chemical Engineer*, 2015, **5**.

186. *Official methods and recommended practices of the AOCS* 1998. Champaign, Ill: AOCS.

187. K. P. A. M. v. Putte and J. v. d. Enden, *Journal of Physics E: Scientific Instruments*, 1973, **6**, 910.

188. K. Van Putte and J. Van Den Enden, *Journal of the American Oil Chemists Society*, 1974, **51**, 316-320.

189. K. Van Putte, L. Vermaas, J. Van Den Enden and C. Den Hollander, *Journal of the American Oil Chemists' Society*, 1975, **52**, 179-181.

190. B. BioSpin, Solid Fat Content (SFC) Analysis, https://www.bruker.com/fileadmin/user_upload/8-PDF-Docs/MagneticResonance/TD-NMR/SFC_AppNote_T151922.pdf, 2017).

191. s. r. l. Stelar, Fast Field Cyclying NMR, http://www.stelar.it/ffc_nmr.htm, (accessed 29 September 2016).

192. P. Conte, V. Mineo, S. Bubici, C. De Pasquale, F. Aboud, A. Maccotta, D. Planeta and G. Alonzo, *Analytical and Bioanalytical Chemistry*, 2011, **400**, 1443-1450.

193. P. d. P. Atkins, Julio, in *Elements of Physical Chemistry*, oxford University Press, Oxford, 5 th edn., 2009, ch. 11.

194. K. Nicolay, K. P. J. Braun, R. A. d. Graaf, R. M. Dijkhuizen and M. J. Kruiskamp, *NMR in Biomedicine*, 2001, **14**, 94-111.

195. J. G. Calvert, *Glossary of atmospheric chemistry terms (Recommendations 1990)*, 1990.

196. H. Y. Carr and E. M. Purcell, *Physical Review*, 1954, **94**.

197. K. Zick, *Diffusion NMR User manual*, Bruker Corporation, Germany, 2016.

198. E. O. Stejskal and J. E. Tanner, *The Journal of Chemical Physics*, 1965, **42**, 288-292.

199. K.-C. Chung, H.-Y. Yu and S. Ahn, *Convection Effects on PGSE-NMR Self-Diffusion Measurements at Low Temperature: Investigation into Sources of Induced Convective Flows*, 1970.

200. W. J. Goux, L. A. Verkruyse and S. J. Saltert, *Journal of Magnetic Resonance (1969)*, 1990, **88**, 609-614.

201. N. Klaas, K. P. J. Braun, R. A. d. Graaf, R. M. Dijkhuizen and M. J. Kruiskamp, *NMR in Biomedicine*, 2001, **14**, 94-111.

202. D. Kruk, R. Meier and E. A. Rössler, *The Journal of Physical Chemistry B*, 2011, **115**, 951-957.

203. R. Meier, D. Kruk, J. Gmeiner and E. A. Rössler, *The Journal of Chemical Physics*, 2012, **136**, 034508.

204. B. Angelov, A. Angelova, R. Mutafchieva, S. Lesieur, U. Vainio, V. M. Garamus, G. V. Jensen and J. S. Pedersen, *Physical Chemistry Chemical Physics*, 2011, **13**, 3073-3081.

205. R. Kimmich and E. Anoardo, *Progress in Nuclear Magnetic Resonance Spectroscopy*, 2004, **44**, 257-320.

206. D. Kruk, R. Meier and E. A. Rössler, *Physical Review E*, 2012, **85**, 020201.

207. J. Rault, *Journal of Non-Crystalline Solids*, 2000, **271**, 177-217.

208. J. Brillo, A. I. Pommrich and A. Meyer, *Physical Review Letters*, 2011, **107**, 165902.

209. A. Takeuchi and A. Inoue, *Materials Transactions*, 2002, **43**, 1205-1213.

210. TF-Instruments, *ResoScan(R) Help Documents*, Germany, 2002.

211. V. Smirnovas, PhD, Technischen Universität Dortmund, 2007.

212. M. E. Tat and J. H. Van Gerpen, *Journal of the American Oil Chemists' Society*, 2003, **80**, 1127-1130.

213. *Edible human foods - Vegetable or animal fats and oils - Determination of OSI oil stability index- Test method* 2010. Mexico: Secretaria de comercio y fomento industrial.

214. L. M. Nightingale, S. Y. Lee and N. J. Engeseth, *Journal of Food Science*, 2011, **76**, C142-C153.

215. N. J. Brooks, B. L. L. E. Gauthe, N. J. Terrill, S. E. Rogers, R. H. Templer, O. Ces and J. M. Seddon, *Review of Scientific Instruments*, 2010, **81**, 064103.

216. K. Dewettinck, I. Foubert, M. Basiura and B. Goderis, *Crystal Growth & Design*, 2004, **4**, 1295-1302.

217. M. Ladd Parada, A. Sadeghpour, J. Vieira, M. J. W. Povey and M. Rappolt, *The Journal of Physical Chemistry B*, 2018, DOI: 10.1021/acs.jpcb.8b06708.

218. R. Peschar, M. M. Pop, D. J. A. De Ridder, J. B. van Mechelen, R. A. J. Driessen and H. Schenk, *The Journal of Physical Chemistry B*, 2004, **108**, 15450-15453.

219. A. Rigolle, B. Goderis, K. Van Den Abeele and I. Foubert, *Journal of Agricultural and Food Chemistry*, 2016, **64**, 3405-3416.

220. D. Manning and P. Dimick, *Food Structure*, 1985, **4**, 9.

221. A. G. Marangoni and S. E. McGauley, in *Physical Properties of Lipids*, CRC Press, 2002, DOI: doi:10.1201/9780203909171.ch4.

222. M.-L. Xue, J. Sheng, Y.-L. Yu and H. H. Chuah, *European Polymer Journal*, 2004, **40**, 811-818.

223. E. Araneda, A. Leiva, L. Gargallo, N. Hadjichristidis, I. Mondragon and D. Radic, *Polymer Engineering & Science*, 2012, **52**, 1128-1136.

224. A. Keller, *Die Makromolekulare Chemie*, 1959, **34**, 1-28.

225. B. Lotz, *Nuclear Instruments and Methods in Physics Research Section B: Beam Interactions with Materials and Atoms*, 1997, **131**, 13-21.

226. M. Ladd-Parada, M. J. Povey, J. Vieira and M. E. Ries, *Molecular Physics*, 2018, DOI: 10.1080/00268976.2018.1508784, 1-8.

227. G. C. Alfonso and P. Scardigli, *Macromolecular Symposia*, 1997, **118**, 323-328.

228. P. Supaphol and J. E. Spruiell, *Journal of Applied Polymer Science*, 2000, **75**, 337-346.

229. A. Maus, E. Hempel, T. Thurn-Albrecht and K. Saalwächter, *The European Physical Journal E*, 2007, **23**, 91.

230. J. A. Martins, W. Zhang and A. M. Brito, *Polymer*, 2010, **51**, 4185-4194.

231. B. O. Reid, M. Vadlamudi, A. Mamun, H. Janani, H. Gao, W. Hu and R. G. Alamo, *Macromolecules*, 2013, **46**, 6485-6497.

232. M. Muthukumar, *The Journal of Chemical Physics*, 2016, **145**, 031105.

233. A. Noda, K. Hayamizu and M. Watanabe, *The Journal of Physical Chemistry B*, 2001, **105**, 4603-4610.

234. P. T. Callaghan and K. W. Jolley, *Chemistry and Physics of Lipids*, 1980, **27**, 49-56.

235. A. Van Langevelde, R. Peschar and H. Schenk, *Acta Crystallographica Section B*, 2001, **57**, 372-377.

236. P. D. I. Fletcher, N. A. Roberts and C. Urquhart, *Journal of Industrial and Engineering Chemistry*, 2016, **34**, 382-389.

237. P. D. Harrison, K. W. Smith, K. Bhaggan and A. G. F. Stapley, *Journal of Crystal Growth*, 2016, **444**, 28-38.

238. S. Ueno, A. Minato, J. Yano and K. Sato, *Journal of Crystal Growth*, 1999, **198–199, Part 2**, 1326-1329.

239. G. Talbot, in *Industrial Chocolate Manufacture and Use*, ed. S. T. Becket, Blackwell Publishing, Ltd, Oxford, United Kingdom, 4th edn., 2009, ch. 12, pp. 261-275.

240. J. Yano, K. Sato, F. Kaneko, D. M. Small and D. R. Kodali, *Journal of Lipid Research*, 1999, **40**, 140-151.

241. M. R. Dent, I. Lopez-Duarte, C. J. Dickson, N. D. Geoghegan, J. M. Cooper, I. R. Gould, R. Krams, J. A. Bull, N. J. Brooks and M. K. Kuimova, *Physical Chemistry Chemical Physics*, 2015, **17**, 18393-18402.

242. J. J. Stankus, R. Torre and M. Fayer, *The Journal of Physical Chemistry*, 1993, **97**, 9478-9487.

243. N. Garti and N. R. Widlak, in *Cocoa Butter and Related Compounds*, AOCS Press.

244. R. A. Tietz and R. W. Hartel, *Journal of the American Oil Chemists' Society*, 2000, **77**, 763-771.

245. T. Malkin, M. R. El Shurbagy and M. L. Meara, *Journal of the Chemical Society (Resumed)*, 1937, DOI: 10.1039/JR9370001409, 1409-1413.

246. T. Malkin and M. R. E. Shurbagy, *Journal of the Chemical Society (Resumed)*, 1936, DOI: 10.1039/JR9360001628, 1628-1634.

247. W. Curatolo, *Biochimica et Biophysica Acta (BBA) - Reviews on Biomembranes*, 1987, **906**, 111-136.

248. R. C. da Silva, F. A. S. D. M. Soares, J. M. Maruyama, N. R. Dagostinho, Y. A. Silva, J. N. R. Ract and L. A. Gioielli, *International Journal of Food Properties*, 2017, **20**, S385-S398.

249. R. C. Silva, F. A. S. D. M. Soares, J. M. Maruyama, N. R. Dagostinho, Y. A. Silva, G. A. Calligaris, A. P. B. Ribeiro, L. P. Cardoso and L. A. Gioielli, *Food Research International*, 2014, **55**, 436-444.

250. D. J. Cebula and K. W. Smith, *Journal of the American Oil Chemists' Society*, 1992, **69**, 992-998.

251. X. Chen, A. Mamun and R. G. Alamo, *Macromolecular Chemistry and Physics*, 2015, **216**, 1220-1226.

252. J. D Hoffman and J. J Weeks, *Melting Process and Equilibrium Melting Temperature of Poly(chlorotrifluoroethylene)*, 1962.

253. J. F. Toro-Vazquez, M. Briceño-Montelongo, E. Dibildox-Alvarado, M. Charó-Alonso and J. Reyes-Hernández, *Journal of the American Oil Chemists' Society*, 2000, **77**, 297-310.

254. T. Sonoda, Y. Takata, S. Ueno and K. Sato, *Journal of the American Oil Chemists' Society*, 2004, **81**, 365-373.

255. H. Marand, J. Xu and S. Srinivas, *Macromolecules*, 1998, **31**, 8219-8229.

256. J. Xu, S. Srinivas, H. Marand and P. Agarwal, *Macromolecules*, 1998, **31**, 8230-8242.

257. K. M. G. Taylor and R. M. Morris, *Thermochimica Acta*, 1995, **248**, 289-301.

258. W. MacNaughtan, I. A. Farhat, C. Himawan, V. M. Starov and A. G. F. Stapley, *JAOCS, Journal of the American Oil Chemists' Society*, 2006, **83**, 1-9.

259. J. Bricknell and R. W. Hartel, *Journal of the American Oil Chemists' Society*, 1998, **75**, 1609-1615.

260. M. Greiner, E. Elts and H. Briesen, 7th International Conference on Simulation and Modelling in the Food and Bio-Industry 2012, FOODSIM 2012, Freising, 2012.

261. C. P. Tan and Y. B. C. Man, *Phytochemical Analysis*, 2002, **13**, 129-141.

262. D. J. Cebula and K. W. Smith, *Journal of the American Oil Chemists Society*, 1991, **68**, 591-595.

263. C. P. Tan and Y. B. Che Man, *Food Chemistry*, 2002, **76**, 89-102.

264. P. d. P. Atkins, Julio, in *Elements of Physical Chemistry*, Oxford University Press, Oxford, 5 th edn., 2009, ch. 5.

265. P. d. P. Atkins, Julio, in *Elements of Physical Chemistry*, Oxford University Press, Oxford, 5 th edn., 2009, ch. 1.

266. R. Winter, *Current Opinion in Colloid & Interface Science*, 2001, **6**, 303-312.

267. R. Winter and C. Jeworrek, *Soft Matter*, 2009, **5**, 3157-3173.

268. N. J. Brooks, O. Ces, R. H. Templer and J. M. Seddon, *Chemistry and Physics of Lipids*, 2011, **164**, 89-98.

269. A. I. I. Tyler, G. C. Shearman, N. J. Brooks, H. Delacroix, R. V. Law, R. H. Templer, O. Ces and J. M. Seddon, *Physical Chemistry Chemical Physics*, 2011, **13**, 3033-3038.

270. D. Dhonsi and A. G. F. Stapley, *Journal of Food Engineering*, 2006, **77**, 936-942.

271. O. O. Mykhaylyk and C. M. Martin, *European Journal of Lipid Science and Technology*, 2009, **111**, 227-235.

272. R. N. Zia, *Journal of Rheology*, 2012, **56**, 1175-1208.

273. T. V. J. F., P. M. David, D. A. Elena, C. A. Miriam and R. H. Jaime, *Journal of the American Oil Chemists' Society*, 2004, **81**, 195-202.

274. E. Tarabukina, F. Jego, J. M. Haudin, P. Navard and E. Peuvrel-Disdier, *J. Food Sci.*, 2009, **74**, 616.

275. L. Li and W. H. de Jeu, *Faraday Discussions*, 2005, **128**, 299-319.

276. D. B. Tefelski, R. M. Siegoczyński, A. J. Rostocki, A. Kos, R. Kościesza and K. Wieja, *Journal of Physics: Conference Series*, 2008, **121**, 142004.

Appendix A Contour plots of the SAXS and WAXS scattering patterns of pressure-treated CB

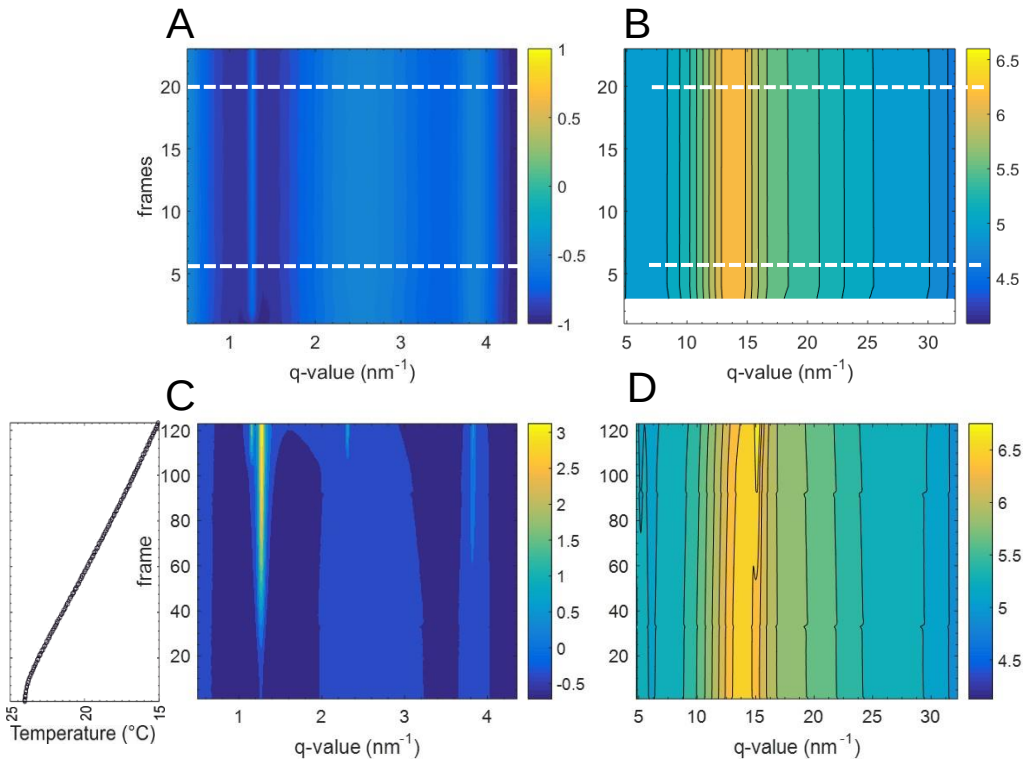

Figure A. 1 Contour plots of the SAXS (A and C) and WAXS (B and D) scattering patterns of CB treated at ambient pressure and 24 °C. In plots A and B, the white dashed lines indicate the frames equivalent to when the 200 bar pressure would have been reached (bottom line), and when the pressure would have been decreased to 50 bar (top line). On the left hand side of panels C and D, the temperature profile during the post-processing cooling to 15 °C is displayed. The white area observed in panel B was caused by problems with the detector which caused loss of data. Regardless, they are not deemed problematic as they are frames occurring prior to the start of crystallisation.

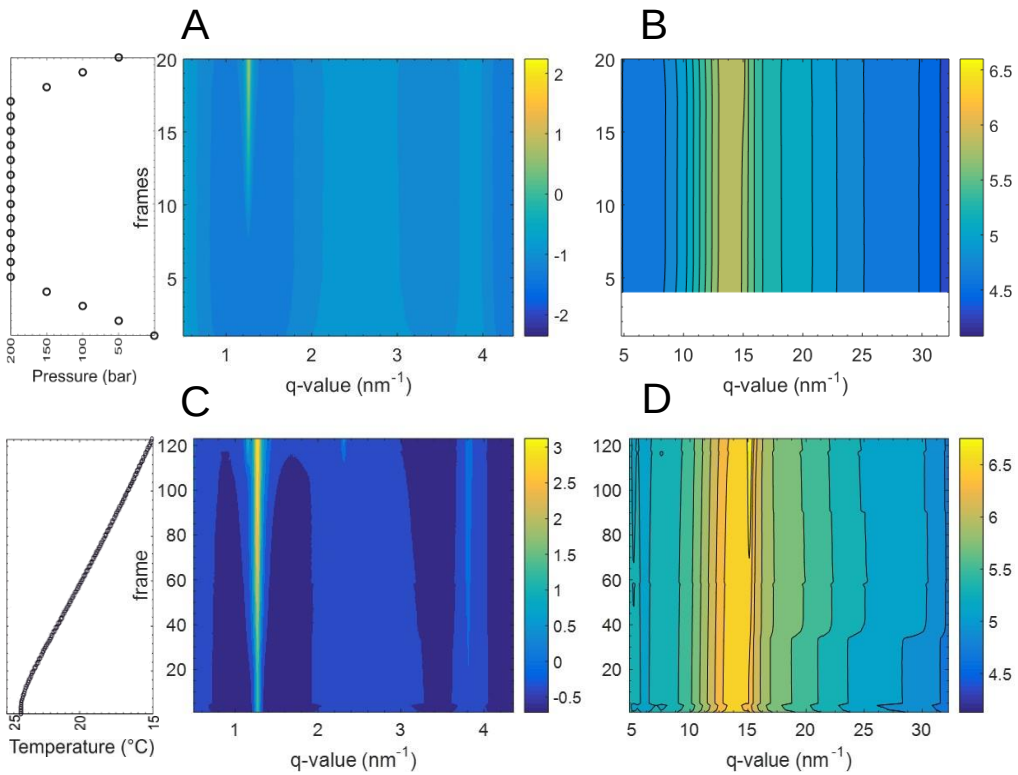

Figure A. 2 Contour plots of the SAXS (A and C) and WAXS (B and D) scattering patterns of CB treated to 200 bar and 24 °C. On the left hand side of panels A and B, the pressure profile during the pressure treatment is displayed, it is not shown as a continuous line as it was performed in a step-wise manner (see Materials and methods). On the left hand side of panels C and D, the temperature profile during the post-processing cooling to 15 °C is displayed. The white area observed in panel B was caused by problems with the detector which caused loss of data. Regardless, they are not deemed problematic as they are frames occurring prior to the start of crystallisation.

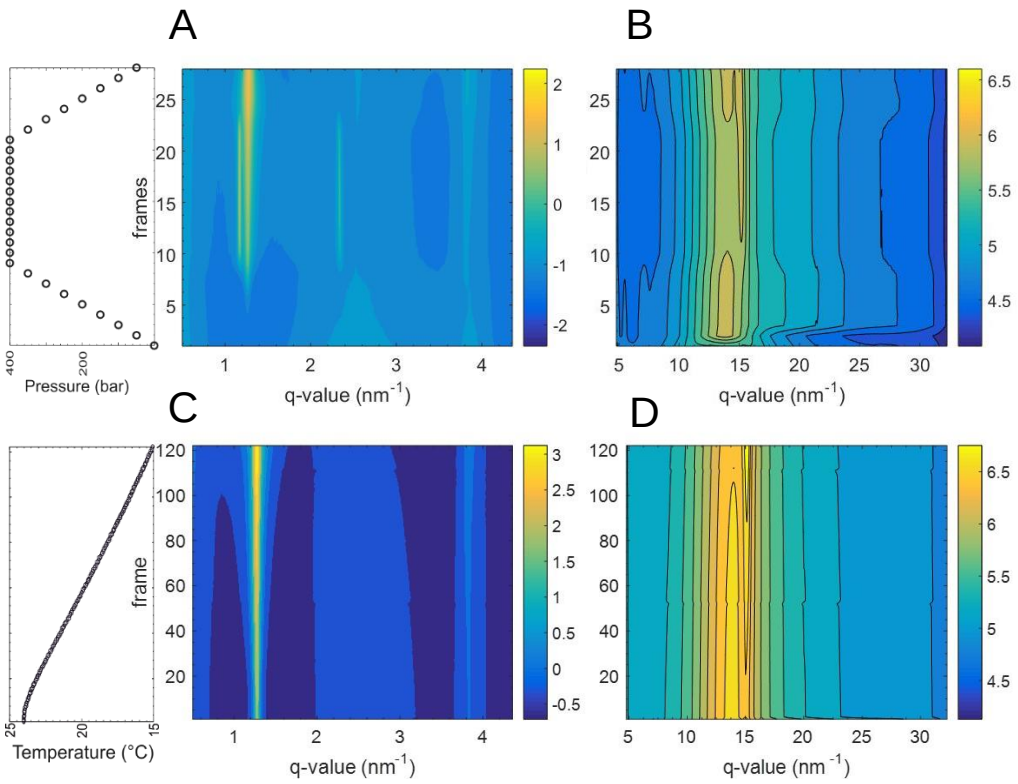

Figure A. 3 Contour plots of the SAXS (A and C) and WAXS (B and D) scattering patterns of CB treated to 400 bar and 24 °C. On the left hand side of panels A and B, the pressure profile during the pressure treatment is displayed, it is not shown as a continuous line as it was performed in a step-wise manner (see Materials and methods). On the left hand side of panels C and D, the temperature profile during the post-processing cooling to 15 °C is displayed.

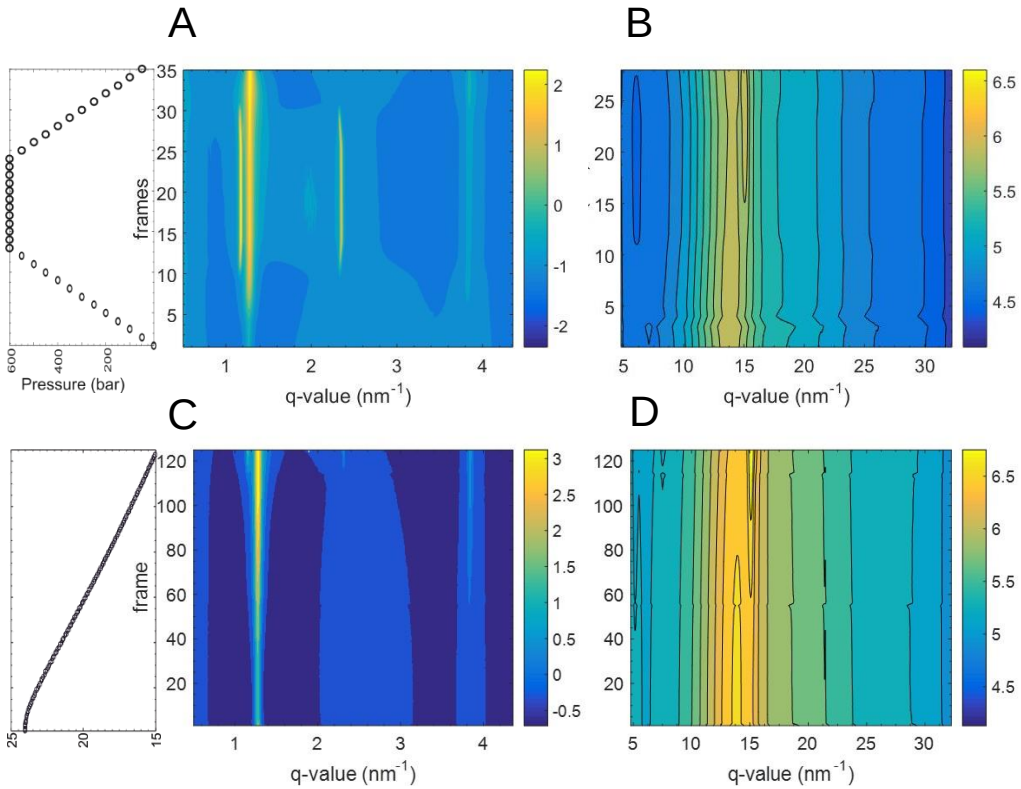

Figure A. 4 Contour plots of the SAXS (A and C) and WAXS (B and D) scattering patterns of CB treated to 400 bar and 24 °C. On the left hand side of panels A and B, the pressure profile during the pressure treatment is displayed, it is not shown as a continuous line as it was performed in a step-wise manner (see Materials and methods). On the left hand side of panels C and D, the temperature profile during the post-processing cooling to 15 °C is displayed.

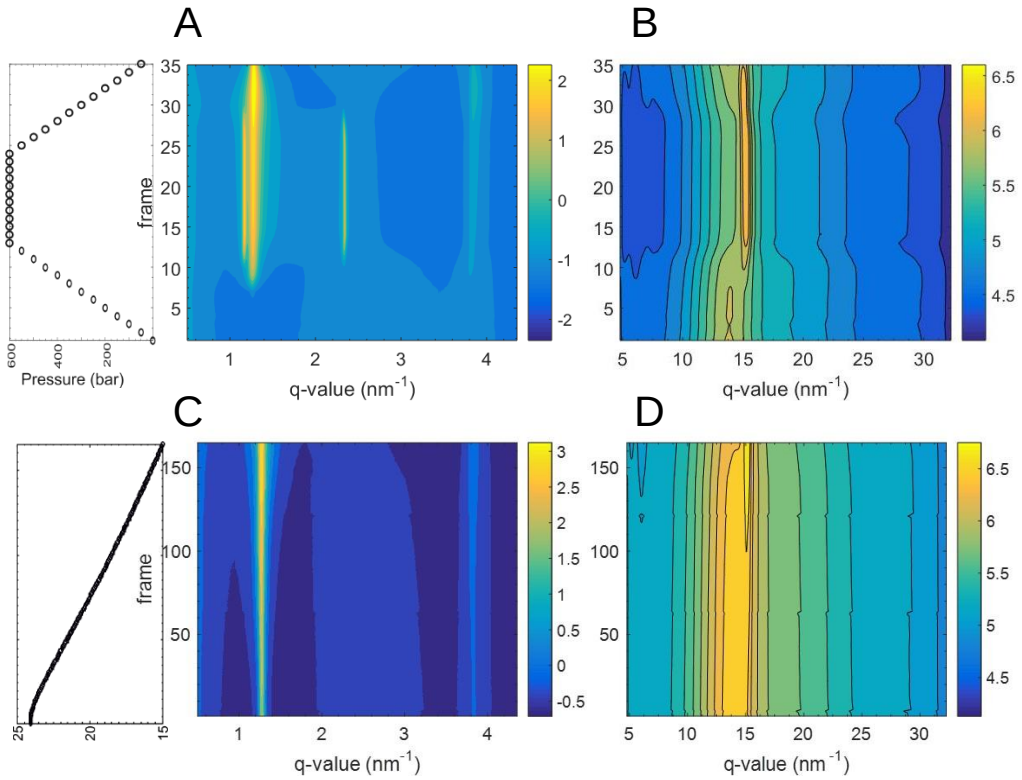

Figure A. 5 Contour plots of the SAXS (A and C) and WAXS (B and D) scattering patterns of CB treated with a T_{imax} of 100 °C, a P_{max} of 600 bar and a T_{cryst} of 24 °C. On the left hand side of panels A and B, the pressure profile during the pressure treatment is displayed, it is not shown as a continuous line as it was performed in a step-wise manner (see Materials and methods). On the left hand side of panels C and D, the temperature profile during the post-processing cooling to 15 °C is displayed.

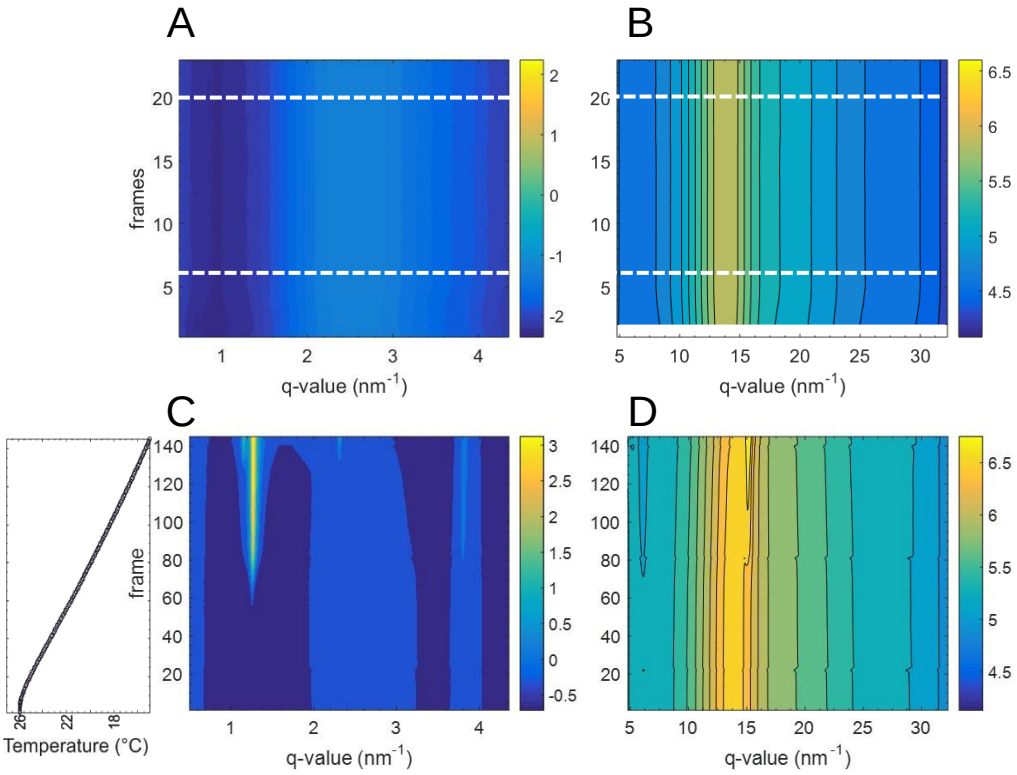

Figure A. 6 Contour plots of the SAXS (A and C) and WAXS (B and D) scattering patterns of CB treated at ambient pressure and 26 °C. In plots A and B, the white dashed lines indicate the frames equivalent to when the 200 bar pressure would have been reached (bottom line), and when the pressure would have been decreased to 50 bar (top line). On the left hand side of panels C and D, the temperature profile during the post-processing cooling to 15 °C is displayed. The white area observed in panel B was caused by problems with the detector which caused loss of data. Regardless, they are not deemed problematic as they are frames occurring prior to the start of crystallisation.

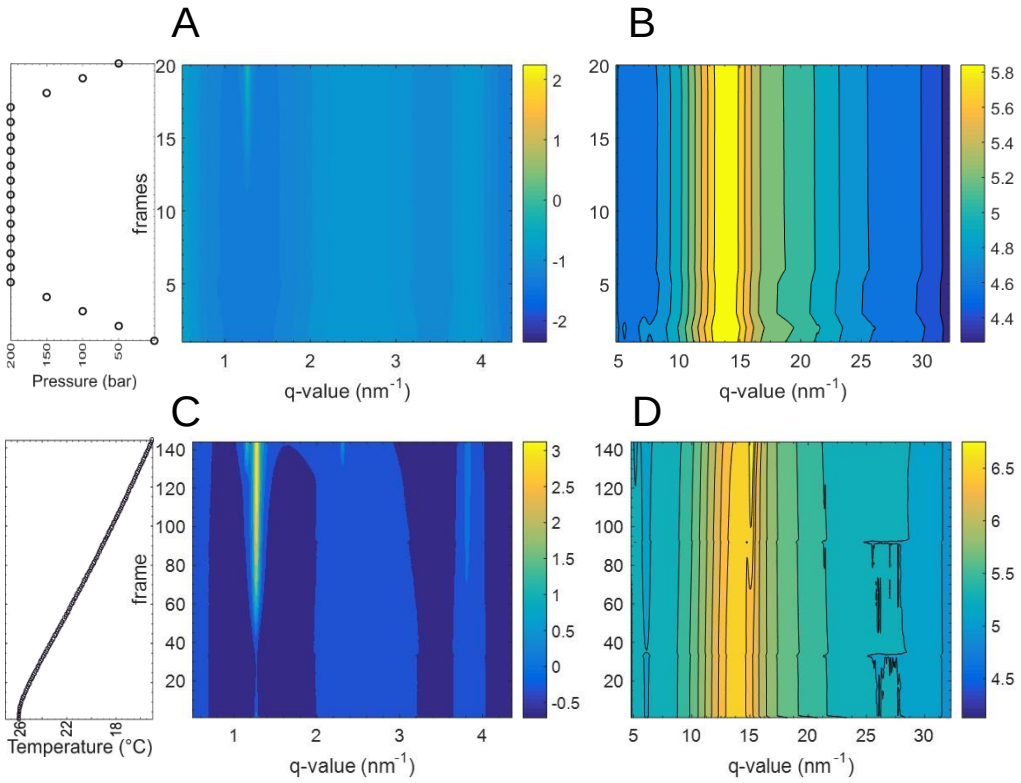

Figure A. 7 Contour plots of the SAXS (A and C) and WAXS (B and D) scattering patterns of CB treated to 200 bar and 26 °C. On the left hand side of panels A and B, the pressure profile during the pressure treatment is displayed, it is not shown as a continuous line as it was performed in a step-wise manner (see Materials and methods). On the left hand side of panels C and D, the temperature profile during the post-processing cooling to 15 °C is displayed.

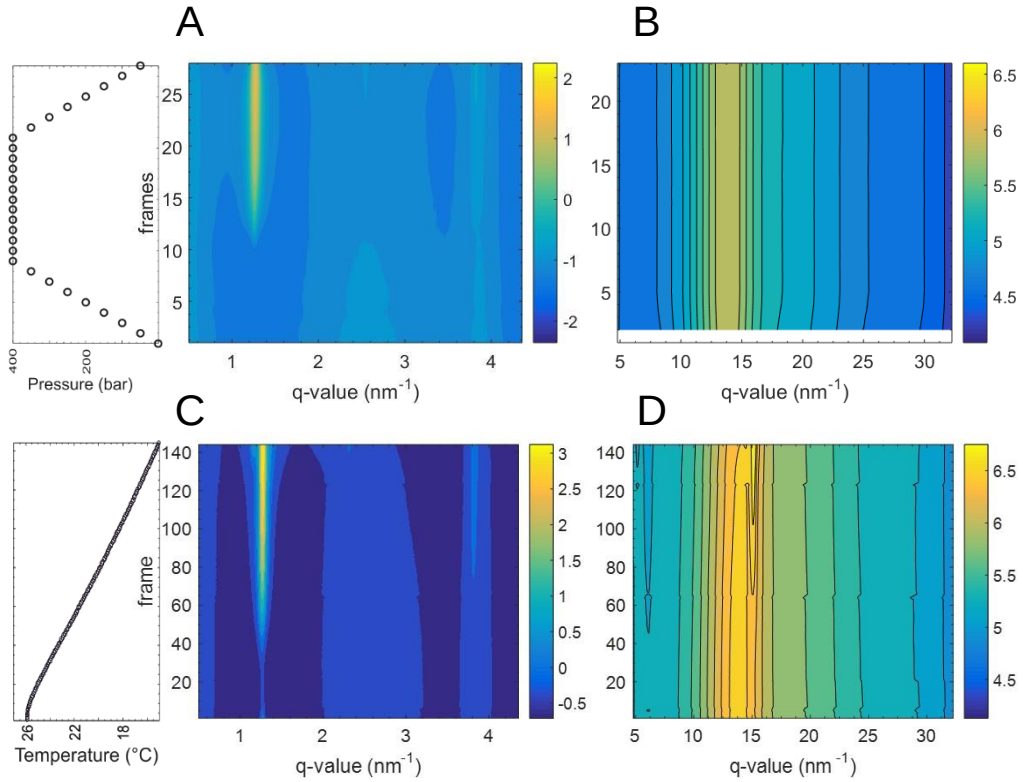

Figure A. 8 Contour plots of the SAXS (A and C) and WAXS (B and D) scattering patterns of CB treated to 400 bar and 24 °C. On the left hand side of panels A and B, the pressure profile during the pressure treatment is displayed, it is not shown as a continuous line as it was performed in a step-wise manner (see Materials and methods). On the left hand side of panels C and D, the temperature profile during the post-processing cooling to 15 °C is displayed. The white area observed in panel B was caused by problems with the detector which caused loss of data. Regardless, they are not deemed problematic as they are frames occurring prior to the start of crystallisation.

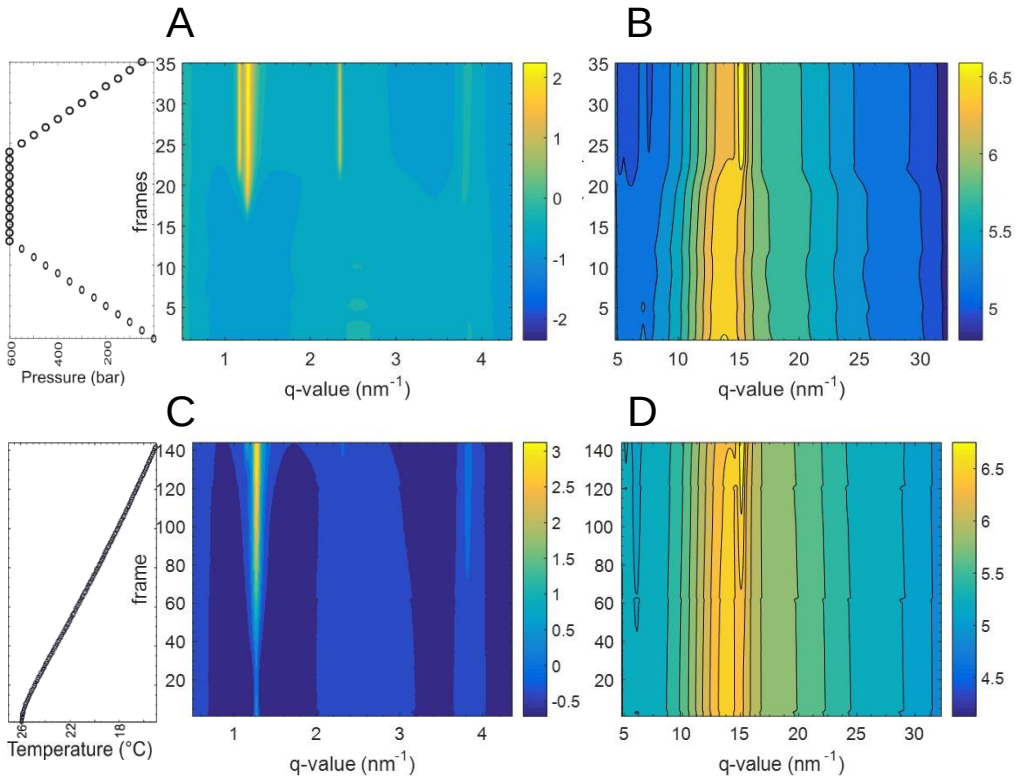

Figure A. 9 Contour plots of the SAXS (A and C) and WAXS (B and D) scattering patterns of CB treated to 600 bar and 26 °C. On the left hand side of panels A and B, the pressure profile during the pressure treatment is displayed, it is not shown as a continuous line as it was performed in a step-wise manner (see Materials and methods). On the left hand side of panels C and D, the temperature profile during the post-processing cooling to 15 °C is displayed.

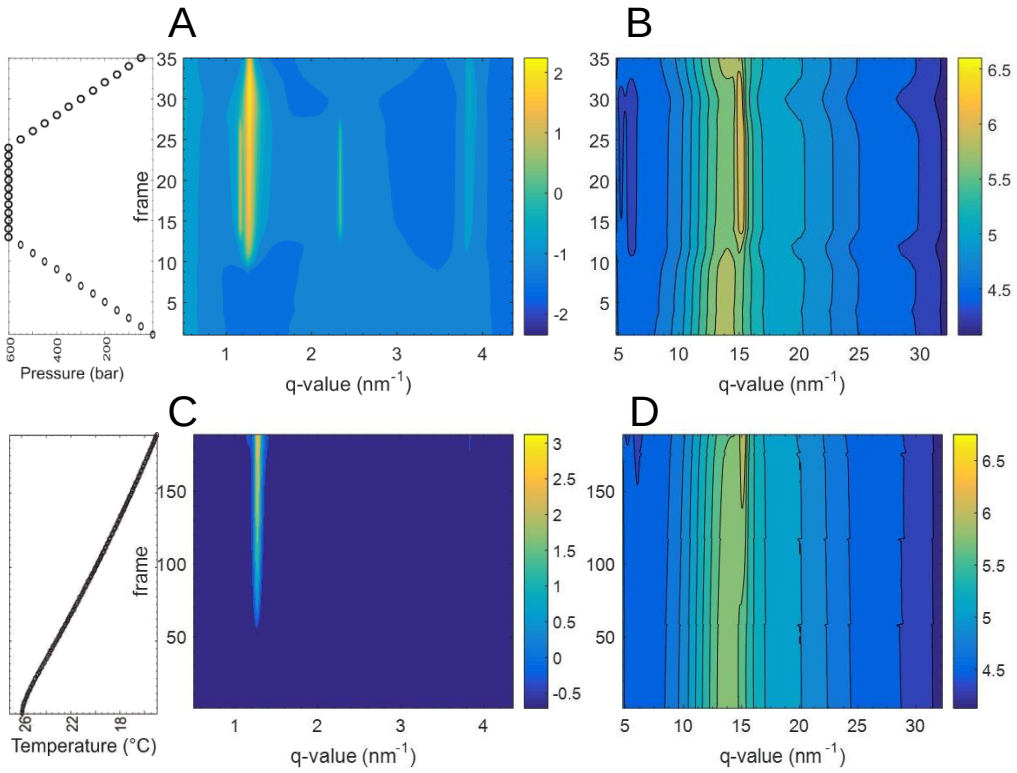

Figure A. 10 Contour plots of the SAXS (A and C) and WAXS (B and D) scattering patterns of CB treated with a T_{imax} of 100 °C, a P_{max} of 600 bar and a T_{cryst} of 26 °C. On the left hand side of panels A and B, the pressure profile during the pressure treatment is displayed, it is not shown as a continuous line as it was performed in a step-wise manner (see Materials and methods). On the left hand side of panels C and D, the temperature profile during the post-processing cooling to 15 °C is displayed.

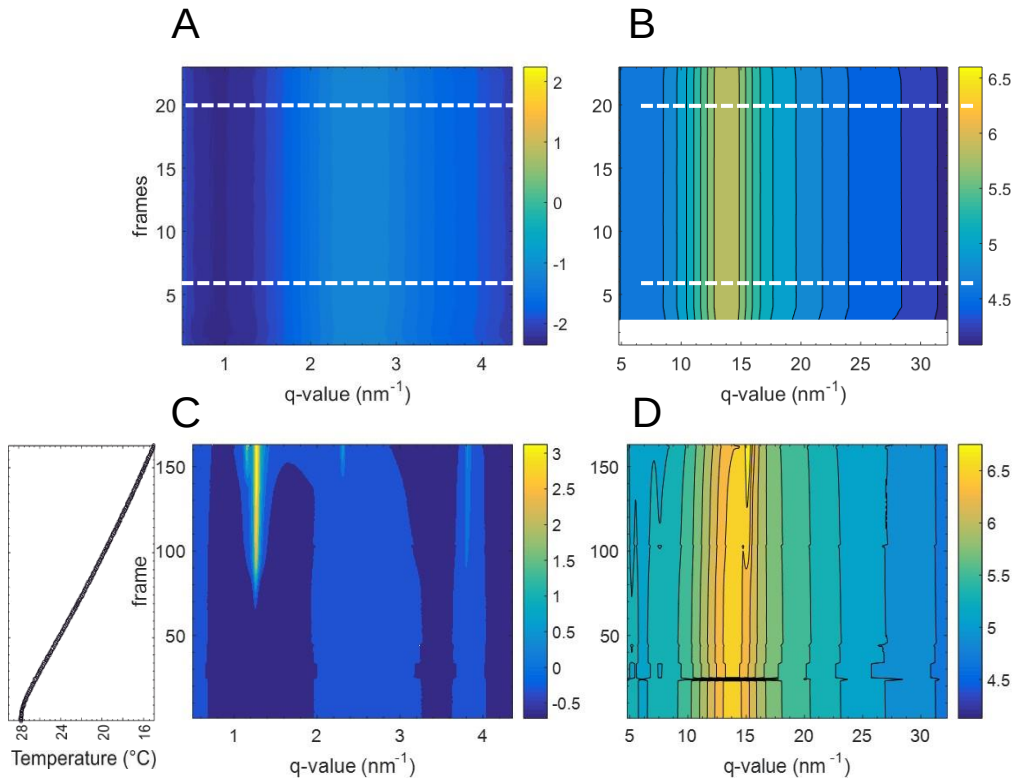

Figure A. 11 Contour plots of the SAXS (A and C) and WAXS (B and D) scattering patterns of CB treated at ambient pressure and 28 °C. In plots A and B, the white dashed lines indicate the frames equivalent to when the 200 bar pressure would have been reached (bottom line), and when the pressure would have been decreased to 50 bar (top line). On the left hand side of panels C and D, the temperature profile during the post-processing cooling to 15 °C is displayed. The white area observed in panel B was caused by problems with the detector which caused loss of data. Regardless, they are not deemed problematic as they are frames occurring prior to the start of crystallisation.

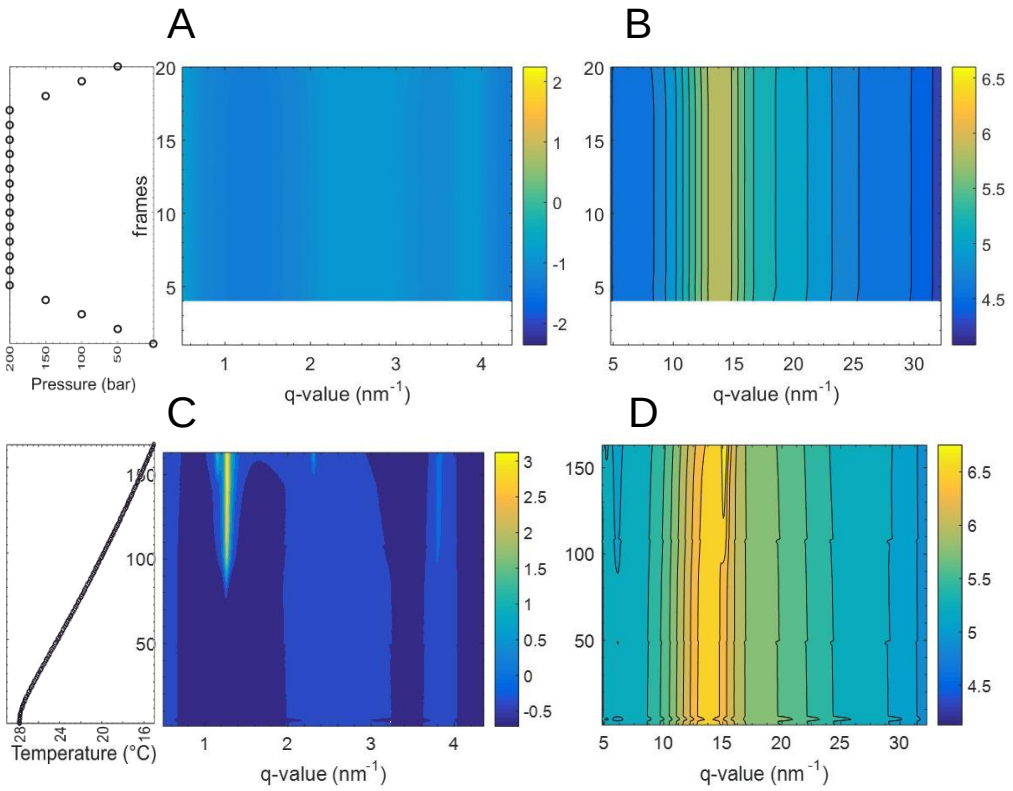

Figure A. 12 Contour plots of the SAXS (A and C) and WAXS (B and D) scattering patterns of CB treated to 200 bar and 28 °C. On the left hand side of panels A and B, the pressure profile during the pressure treatment is displayed, it is not shown as a continuous line as it was performed in a step-wise manner (see Materials and methods). On the left hand side of panels C and D, the temperature profile during the post-processing cooling to 15 °C is displayed. The white areas observed in panel A were caused by problems with the detector which caused loss of data. Regardless, they are not deemed problematic as they are frames occurring prior to the start of crystallisation.

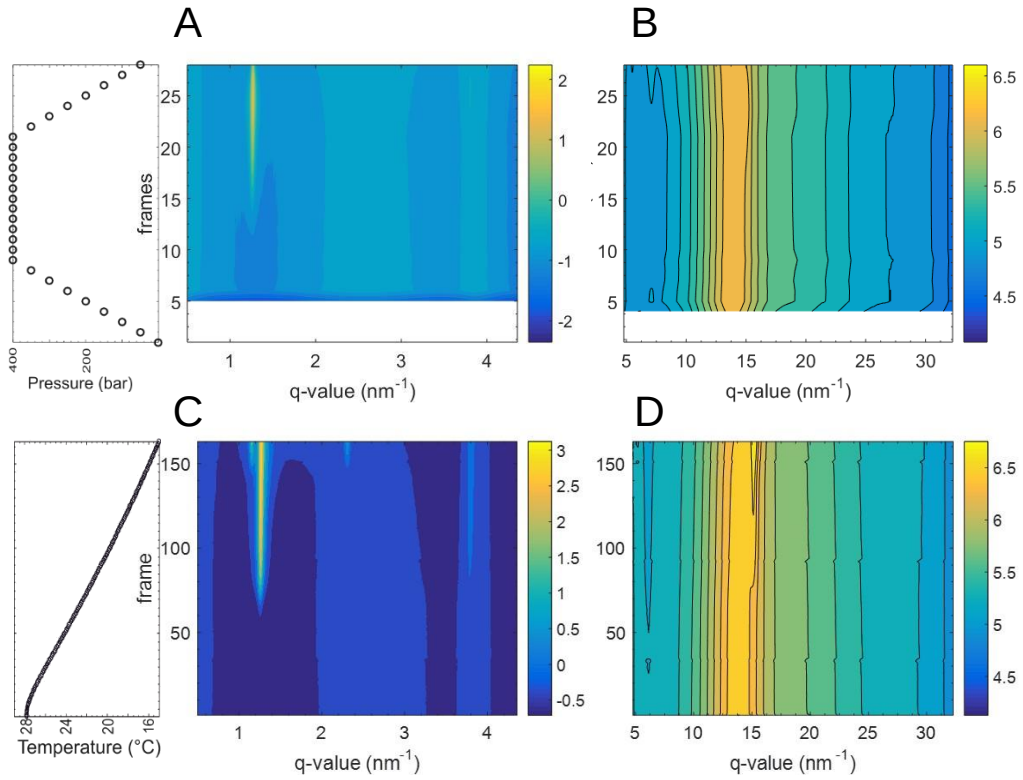

Figure A. 13 Contour plots of the SAXS (A and C) and WAXS (B and D) scattering patterns of CB treated to 400 bar and 28 °C. On the left hand side of panels A and B, the pressure profile during the pressure treatment is displayed, it is not shown as a continuous line as it was performed in a step-wise manner (see Materials and methods). On the left hand side of panels C and D, the temperature profile during the post-processing cooling to 15 °C is displayed. The white areas observed in panels A and B were caused by problems with the detector which caused loss of data. Regardless, they are not deemed problematic as they are frames occuring prior to the start of crystallisation.

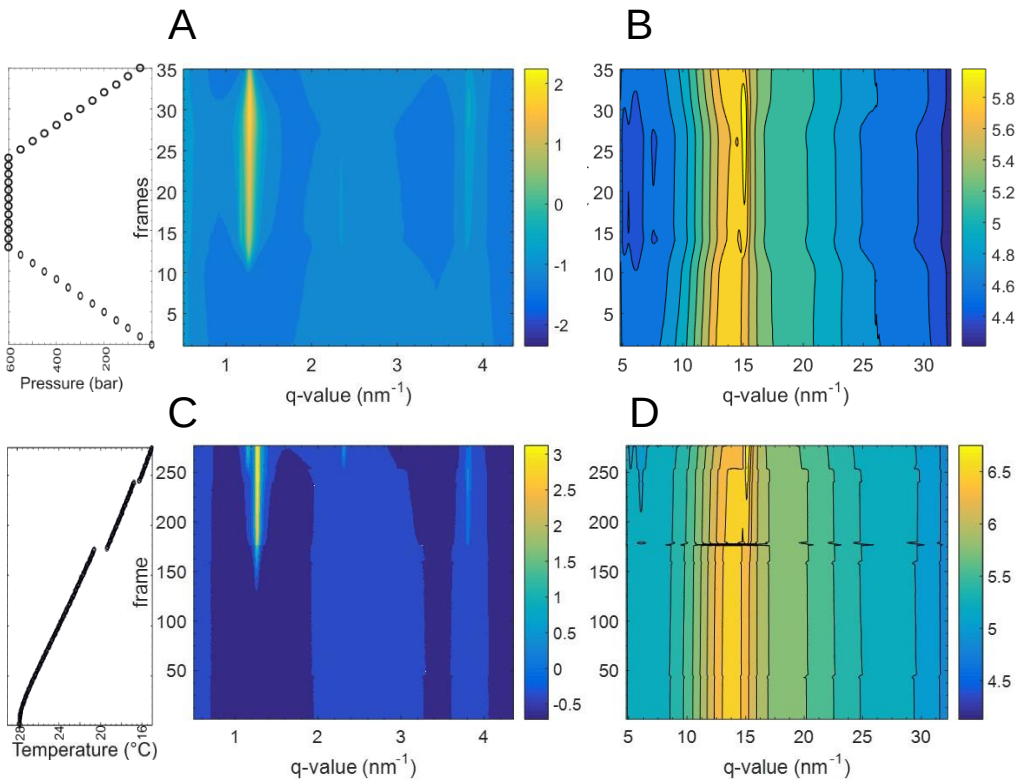

Figure A. 14 Contour plots of the SAXS (A and C) and WAXS (B and D) scattering patterns of CB treated to 600 bar and 28 °C. On the left hand side of panels A and B, the pressure profile during the pressure treatment is displayed, it is not shown as a continuous line as it was performed in a step-wise manner (see Materials and methods). On the left hand side of panels C and D, the temperature profile during the post-processing cooling to 15 °C is displayed. Note should be taken that the temperature profile is not continuous, as compared to the rest of the treatments. This is because measurements stopped and had to be restarted; however, the cooling process continued independently of the acquisition.

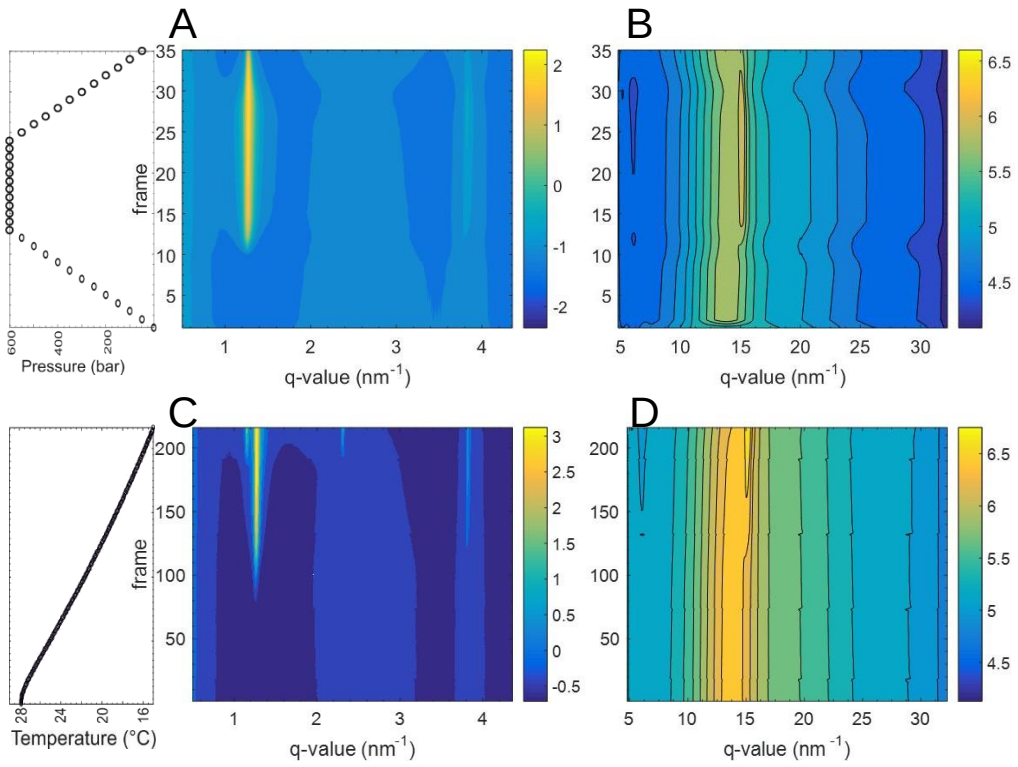

Figure A. 15 Contour plots of the SAXS (A and C) and WAXS (B and D) scattering patterns of CB treated with a T_{imax} of 100 °C, a P_{max} of 600 bar and a T_{cryst} of 28 °C. On the left hand side of panels A and B, the pressure profile during the pressure treatment is displayed, it is not shown as a continuous line as it was performed in a step-wise manner (see Materials and methods). On the left hand side of panels C and D, the temperature profile during the post-processing cooling to 15 °C is displayed.